Calibration Report for the Solar Aureole Camera of the Descent Imager/Spectral Radiometer aboard the Huygens Probe of the Cassini Mission

27 April 2006

(Rev. 17 Jan. 2007)

By

M. G. Tomasko and L. E. Dafoe

Table of Contents

Table of Figures

Table of Tables

1 Introduction

This document describes the Solar Aureole (SA) system on the flight model (SN03) of the Descent Imager/Spectral Radiometer (DISR) flown on the Huygens Probe of the Cassini Mission. An overview of the SA system is given, followed by a section on the actual Titan descent. Next follows the overall methodology of the reduction of Solar Aureole data to measured calibrated intensity and degree of polarization and the verification of that calibration. The following sections provide detail necessary to reduce the Solar Aureole data, including tables of values. Finally, the Appendices include reports on different aspects of the Solar Aureole system, often deriving the equations used in the analysis, describing test setups for the calibration, and noting the quality of modeling fits to the measured calibration data.

2 System Overview

The Solar Aureole system uses four channels to measure the brightness of a vertical strip of sky some 6 degrees wide by 50 degrees long within a few degrees of the sun and opposite to the sun in the sky. The field of view is centered at 50 degrees zenith angle, the zenith angle of the sun in the sky of Titan during the nominal entry. Each of the four channels includes a linear sheet polarizer and an interference filter. The four channels thus consist of measurements centered at 500 or 935 nm in both vertically and horizontally polarized light.

The schematic layout of the optical system is shown in Figure 2-1 . Lens elements in each of the four channels focus light onto the ends of fiber optic ribbons that bring the light to four 6 by 50 pixel arrays on the CCD sensor. The optical system also includes a beamsplitter that permits light from an onboard calibration source to illuminate the SA system through all optical elements except the outside window.

Figure 2-2 shows the field of view of the SA system relative to the shadow bar on the DISR sensor head. The field is centered at 50 degrees zenith angle and is tipped 6 degrees toward the direction of increasing azimuth. The shadow bar prevents direct light from the sun from illuminating the SA window during the SA integrations. The software permits integrations to begin at azimuth angles between about 2.5 and 2.9 degrees. Thus the 6 degree-wide field of view of the SA system includes measurements from at least 6 – 3 + 2.5 or 5.5 degrees to 11.5 degrees azimuth from the sun at the start of the integration. The azimuth at the end of the integration depends on the integration time and the rotation rate, but the rotation during the integration is limited to a maximum of 3.5 degrees. In these measurements near the sun, all 300 elements in each of the four Solar Aureole channels are included in the telemetry stream.

In addition to the measurements near the sun, the SA system makes a measurement centered at an azimuth angle between 172 and 176 degrees from the sun. In these measurements, the signals in all six columns in each SA channel are summed before transmission to the ground. The integration time for these measurements is limited so that the probe rotates through no more than 20 degrees during the exposure.

The measurements through two orthogonal linear polarizers are not sufficient to uniquely determine the position angle and degree of linear polarization for light of an arbitrary state of

linear polarization. Rather, we will assume that the light in Titan's atmosphere is partially linearly polarized with the position angle perpendicular to the scattering plane. This is sufficient to determine both the total intensity and the degree of polarization from the measurements made opposite to the sun. We plan to simply add the horizontal and vertical components of intensity near the sun to obtain the total intensity as a function of angular distance from the sun.

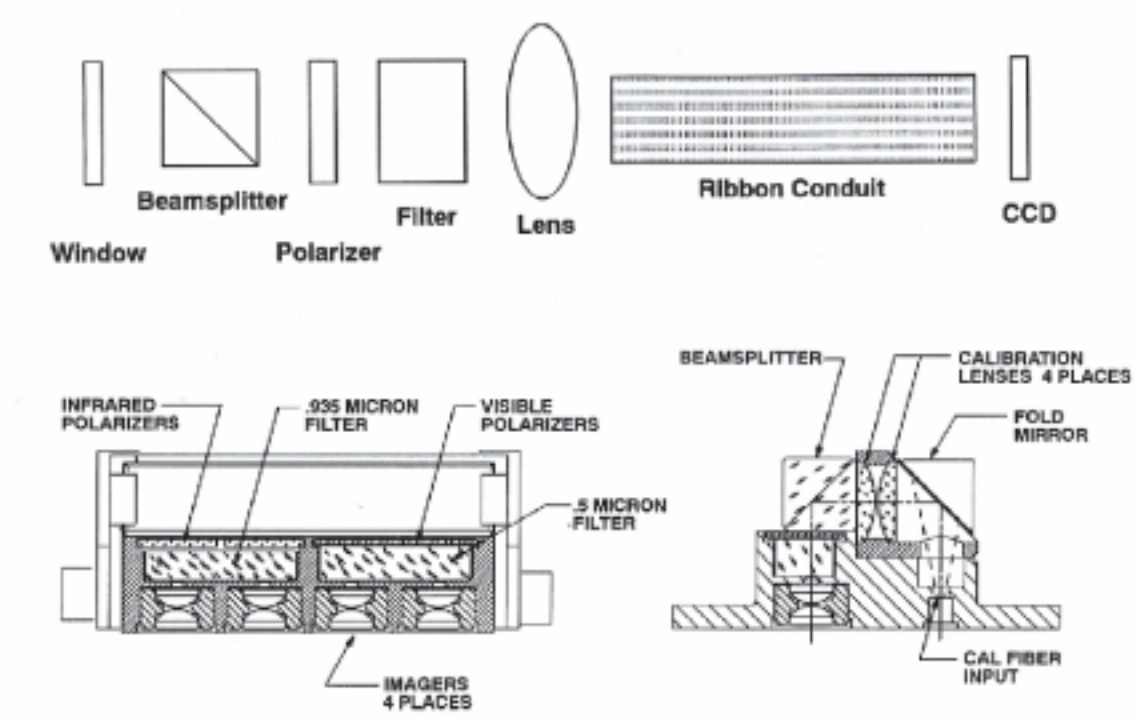

Figure 2-1 The schematic layout of the components of the Solar Aureole system. The beamsplitter is used to introduce light from the inflight calibration system into the four channels of the Solar Aureole system.

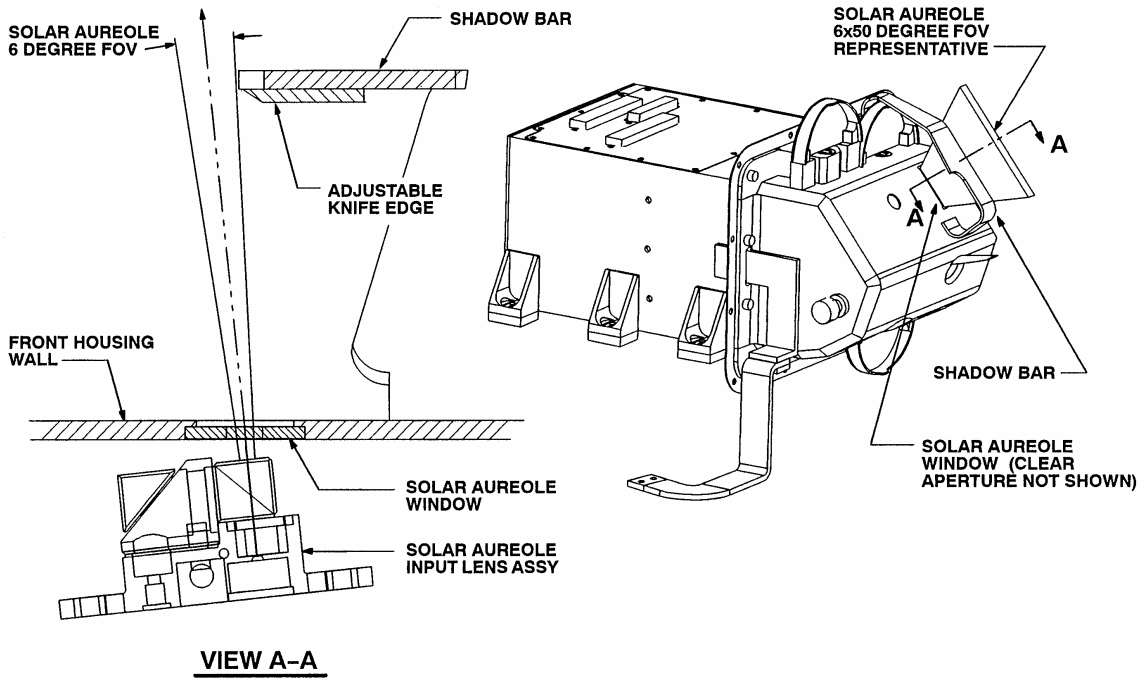

Figure 2-2 The field of view of the Solar Aureole camera is shown relative to the shadow bar of the sensor head. The center of the field of view is tipped by 6 degrees in the direction of increasing azimuth. The shadow bar shades the entire window of the Solar Aureole system when the Solar Aureole makes its measurement, since the measurement starts at an azimuth of about 2.5 degrees and extends to increasing azimuth.

As described above, the Solar Aureole system consists of four 6 by 50 pixel cameras. These cameras have focal planes on the CCD detector array. The following table shows the row and column numbers of each camera. The data from the cameras is delivered in one of two data set types, Solar Aureole data sets or part of the Full CCD data sets. The table addresses both instances. Note also that rows 0:49 in a Solar Aureole data set correspond to rows 204:253 in a Full data set. In the DISRsoft files, the header entries that designate CCD column and row numbers for the lower left corner designate row 203 instead of 204, but this is incorrect.

Table 2-1 Solar Aureole CCD Row and Column Designations

SA data set columns	0:5	6:11	12:17	18:23
Full data set columns	40:45	31:36	23:28	14:19
Filter	Blue	Blue	Red	Red
Polarization	Horizontal	Vertical	Vertical	Horizontal
Designation sometimes used	Blue Perpendicular	Blue Parallel	Red Parallel	Red Perpendicular

3 The Titan Descent As It Occurred

While much of the Huygens mission went as planned, the actual descent yielded some surprises.

The most significant impact on the Solar Aureole measurements of the actual descent relative to what was expected was that the real time knowledge of azimuth failed throughout the descent. This was caused by the DISR Sun Sensor failing to lock onto the solar signal as the

probe rotated. Its locking on the sun was intended to provide an effective trigger for scheduling all DISR measurements in azimuth, but the Solar Aureole measurement was particularly dependent on the Sun Sensor because of the desire to measure the aureole adjacent to the sun, but not including the solar disk. The timing on this measurement is especially critical. The Sun Sensor failed because of probe dynamics and the detector reaching colder than expected temperatures.

Because real time azimuthal knowledge was not available, the Solar Aureole measurements were taken at random azimuths rather than at 2.5 degrees and 174 degrees as planned. Because the azimuths were random, the auto-exposure algorithm did not work as designed, and saturation occurred in some data sets. There is a single red unsaturated data set near the sun over the course of the mission. It occurs at around 60 km altitude and around 8.5 degrees from the sun. There are more blue data sets near the sun that are unsaturated.

However, one can be grateful that the Sun Sensor detection failed because if it had succeeded, the Solar Aureole measurements near the sun would all have had the direct solar beam in them. The probe rotated backwards over most of the descent. The Shadow Bar was designed to shield the SA field from the direct solar beam as the probe rotated counter clockwise as viewed from above. This was the spin direction for the first roughly 10 minutes of the descent, but then the direction reversed and stayed clockwise throughout. Therefore, if the Sun Sensor had given stable and reliable triggers, which are not dependent on the direction of probe rotation, all the near sun measurements would have been taken with the sun in the field.

Another difference between the Solar Aureole measurements as planned and the measurements achieved relates to the absolute calibration of edge rows and columns. Recall that the Solar Aureole is comprised of four optical channels, each fed via a fiber ribbon conduit to a CCD detector. The fiber ribbons are thin (under 140 microns thick) and delicate. The fiber polishing on the end of the ribbon resulted in small chips and fractures on the ribbon edges. The effect of these chips is to cause the edge columns of several of the four channels to have structure in their absolute response along the column. It becomes clear upon observing the computed absolute intensity over the course of the descent for each column that a slight shift in fiber location over the CCD array occurred. This shift is not seen in the cruise phase data (which includes active optical stimulation of the SA system). It is believed that the shift occurred during entry into Titan's atmosphere. The result is that several columns (not pixels) of the Solar Aureole system should be omitted from the data reduction. Additionally, row 0 has not had sufficient illumination to be useful throughout the program, so this row should be deleted. The columns and rows to be omitted are indicated below.

Table 3-1 Solar Aureole CCD Row and Column Designations for Columns that Should Be Omitted From Analysis

Instrument	Blue Horizontal	Blue Vertical	Red Vertical	Red Horizontal
SA data set designation	Column 0 Column 5 Row 0	Column 6 Row 0	Column 12 Column 17 Row 0	Column 18 Row 0
CCD data set designation	Column 40 Column 45 Row 204	Column 31 Row 204	Column 23 Column 28 Row 204	Column 14 Row 204
SA channel designation (columns 0 to 5 and rows 0 to 49)	Column 0 Column 5 Row 0	Column 0 Row 0	Column 0 Column 5 Row 0	Column 0 Row 0

Note that the following methodology and plans for data analysis assume the measurements will be taken as planned, and that all the SA pixels have accurate calibration. Special care should be taken in reducing the actual mission data regarding saturation, correct geometric viewing angles including probe tip and tilt, and careful combination of the two SA channels in each color because of field of view overlap and polarization/retarder effects using only the good columns.

4 Methodology for Analyzing Solar Aureole Data

4.1 Generation of Solar Aureole Data Numbers

For every SA pixel, the number of counts generated at temperature T and exposure time t_i in the presence of intensity $I(\lambda,\theta,\phi,altitude)$ is given by

$$DN = t_i * Abs\_Resp(T)\int\int I(\lambda,\theta,\phi,altitude)RSR(\lambda,T)d\lambda d\Omega + DN_{dark}(T,t_i) + Noise(T,t_i,DN_{nom}) \quad 1.$$

where:

$Abs\_Resp(T)$ is absolute responsivity of the SA pixel in (DN/sec) / Watts/(m^2-μm-str);

$I(\lambda,\theta,\phi,altitude)$ is the intensity (Watts/(m^2-μm-str)) in the atmosphere at wavelength λ, zenith angle θ, azimuth angle ϕ, and the specified altitude in the Titan atmosphere;

$RSR(\lambda,T)$ is the relative spectral response of the SA pixel at wavelength λ and temperature T;

$\int(*)d\Omega$ is the integral of the intensity times the RSR over the spectral band integrated over the field of view of the SA pixel over the course of the exposure time;

$DN_{dark}(T,t_i)$ is the dark current of the SA pixel at that temperature and for that integration time, plus the CCD bias;

$Noise(T,t_i,DN_{nom})$ is the noise in the measurement at that temperature, integration time, and nominal incident energy.

The absolute response, relative spectral response, dark current, and noise are all models as described later in this document.

4.2 Computing Solar Aureole Calibrated Intensities in Each Pixel

Consider the above equation with the following substitution,

$$I(\lambda,\theta,\phi,altitude) = I\_std\_wave(\lambda_0,\theta,\phi,altitude) * I\_shape(\lambda_0,\theta,\phi,altitude) \qquad 2.$$

where $I\_std\_wave(\lambda_0,\theta,\phi,altitude)$ is the intensity at wavelength λ_0 at zenith angle θ, azimuth angle ϕ, and the specified altitude and I_shape is the normalized spectral shape of the intensity at that location where I_shape equals 1.0 at λ_0. This substitution results in the following:

$$DN = t_i * Abs\_Resp(T) * I\_std\_wave(\lambda_0,\theta,\phi,altitude) \int\int I\_shape(\lambda_0,\theta,\phi,altitude) RSR(\lambda,T) d\lambda d\Omega + DN_{dark}(T,t_i) + Noise(T,t_i,DN_{nom}) \qquad 3.$$

For every SA pixel (or row in the case of summed data sets), the intensity $I\_std\_wave(\lambda_0,\theta,\phi,altitude)$ in units of Watts/(m^2-μm-str) at wavelength λ_0, zenith angle θ, azimuth angle ϕ, and the altitude in the Titan atmosphere is computed from the number of counts generated at temperature T and exposure time t_i by:

$$I\_std\_wave(\lambda_0,\theta,\phi,altitude) = \frac{DN - DN_{dark}(T,t_i)}{t_i * Abs\_Resp(T) \int I\_shape(\lambda_0,\theta,\phi,altitude) RSR(\lambda,T) d\lambda} \qquad 4.$$

where:

DN is the measured counts for that Solar Aureole measurement;

$DN_{dark}(T,t_i)$ is the dark current of the SA pixel at that temperature and for that integration time, plus the CCD bias;

$Abs\_Resp(T)$ is absolute responsivity of the SA pixel in (DN/sec) / Watts/(m^2-μm-str);

$RSR(\lambda,T)$ is the relative spectral response of the SA pixel at wavelength λ and temperature T;

$I\_shape(\lambda_0, \theta, \phi, altitude)$ is the spectral shape of the intensity (unitless and normalized to 1.0 by definition) at the specified altitude in the Titan atmosphere. It is defined by dividing the Titan model by the intensity at that wavelength as in equation 2.

It is important to note that the computation of calibrated intensities at a specific wavelength is an iterative process. The I_shape is model dependent, so a proposed model must be introduced, which creates an I_shape, which then must result in correct SA intensity predictions. This I_shape must be consistent with the polarizing affects of both Titan's atmosphere and the SA instrument as noted in the next section.

4.3 Combining Intensities in Each Pixel to Result in Total Absolute Calibrated Intensities and Degree of Polarization

Recall that each pixel includes only the intensity in one polarization state. Therefore, the total Titan intensity and the degree of polarization measured in one data set must be computed using both polarization channels in each color. As can be seen in the sections and appendices regarding field of view and polarization, the combination of the intensities in each color is complex.

First note that the four Solar Aureole channels do not have aligned fields of view – each channel looks at a slightly different angle and thus has a slightly different field of view. Therefore, the calibrated I_std_wave which has been computed for every pixel in a data set must be interpolated in space to some internal standard grid that has data from both polarization states (where the fields of view overlap). Care must be taken to omit columns and rows that have faulty calibration due to fiber ribbon shift upon Titan entry. Care must also be taken to ensure one knows where in Titan's sky each theoretic grid point is pointed.

Second, note that the in flight calibration beamsplitter at the front of the optical train of the SA system acts as a retarder, with a different retardance and a different optical axis position angle for each row in each channel. The book Polarimeters for Optical Astronomy by K. Serkowski contains on pages 144 and 145 an excellent section on detection of light through a retarder and analyzer. If one defines the Stokes parameters of elliptically polarized light by

$$
\begin{aligned}
&I \\
&Q = Ip\cos 2\theta \\
&U = Ip\sin 2\theta \\
&V = Iq \\
&\textit{where:} \\
&I = \text{Intensity} \\
&p = \text{degree of linear polarization} \\
&\theta = \text{position angle in the equatorial coordinate system} \\
&q = \text{degree of circular polarization}
\end{aligned}
$$

then the intensity of light transmitted through a retarder with the optical axis at position angle ψ followed by an analyzer with the principal plane at position φ=0 (upper signs, horizontal Solar Aureole channels) or φ=0 (lower signs, vertical Solar Aureole channels) can be obtained by:

$$I' = \frac{1}{2}\left[I \pm Q\left(G + H\cos 4\psi\right) \pm UH \sin 4\psi \mp V \sin\tau \sin 2\psi\right]$$

where:

$$G = \frac{1}{2}\left(1 + \cos\tau\right)$$

$$H = \frac{1}{2}\left(1 - \cos\tau\right)$$

$$\tau = \text{retardance of the retarder}$$

Note that these retardances and retarder optical axes must be interpolated to the internal standard grid defined by the field of view overlap and carefully combined with the I_std_wave functions for each data set for accurate calculation of the intensity and degree of polarization.

Because this combination can be complex, some correct IDL code lines are added here for user's verification of their understanding.

```
; First, consider the data sets that are summed across the rows.
; These have their own geometries since all 6 rows are included in
; each data set before telemetering to earth.

for i=0,num_summed-1 do begin

 ; Interpolate to internal standard zenith angles
 b_per_interp=interpol(I_std_wave(sum_idx(i),0,*),mean_blu_per_ze,blu_za)
 b_par_interp=interpol(I_std_wave(sum_idx(i),1,*),mean_blu_par_ze,blu_za)
 r_par_interp=interpol(I_std_wave(sum_idx(i),2,*),mean_red_par_ze,red_za)
 r_per_interp=interpol(I_std_wave(sum_idx(i),3,*),mean_red_per_ze,red_za)

 ; Compute intensity
 blue(sum_idx(i),*)=2.0*(b_per_interp+b_par_interp+b_per_interp* $
  cos(4.*b_par_psi)+b_par_interp*cos(4.*b_per_psi))/ $
  (2.+cos(4.*b_per_psi)+cos(4.*b_par_psi))
 red(sum_idx(i),*)=r_per_interp+r_par_interp+ $
  (r_per_interp-r_par_interp)* $
  (Gv+Hv*cos(4.*r_par_psi)-Gh-Hh*cos(4.*r_per_psi))/ $
  (Gv+Hv*cos(4.*r_par_psi)+Gh+Hh*cos(4.*r_per_psi))

 ; Compute degree of polarization
 blu_deg_pol(i,*)=2.*(b_per_interp-b_par_interp)/ $
  (b_per_interp+b_par_interp+b_per_interp*cos(4.*b_par_psi)+ $
  b_par_interp*cos(4.*b_per_psi))
 red_deg_pol(i,*)=(r_per_interp-r_par_interp)/ $
  (r_per_interp*(Gv+Hv*cos(4.*r_par_psi))+ $
  r_par_interp*(Gh+Hh*cos(4.*r_per_psi)))
endfor

; Next consider the data sets that are contour, with 6x50 pixel aspects.

for z=0,49 do begin
 for i=0,num_unsummed-1 do begin

  ; Interpolate to internal standard zenith angles, blue first
  blu_per_cont= $
   interpol(unsum_data(i,0:5,z),blu_per_az_cont(*,z),blu_az(*,z))
  blu_par_cont= $
   interpol(unsum_data(i,6:11,z),blu_par_az_cont(*,z),blu_az(*,z))
  b_per_interp=mean(blu_per_cont)
  b_par_interp=mean(blu_par_cont)
```

```
  ; Compute intensity for both contour and summed geometries
  blue(unsum_idx(i),z)=2.0*(b_per_interp+b_par_interp+b_per_interp* $
   cos(4.*b_par_psi(z))+b_par_interp*cos(4.*b_per_psi(z)))/ $
   (2.+cos(4.*b_per_psi(z))+cos(4.*b_par_psi(z)))
  blu_contour(i,*,z)=2.0*(blu_per_cont+blu_par_cont+blu_per_cont* $
   cos(4.*b_par_psi(z))+blu_par_cont*cos(4.*b_per_psi(z)))/ $
   (2.+cos(4.*b_per_psi(z))+cos(4.*b_par_psi(z)))
 endfor

 ; Interpolate to internal standard zenith angles, red next
 for i=0,num_unsummed-1 do begin
 red_par_cont= $
  interpol(unsum_data(i,12:17,z),red_par_az_cont(*,z),red_az(*,z))
 red_per_cont= $
  interpol(unsum_data(i,18:23,z),red_per_az_cont(*,z),red_az(*,z))
 r_per_interp=mean(red_per_cont)
 r_par_interp=mean(red_par_cont)
 red(unsum_idx(i),z)=r_per_interp+r_par_interp+ $
  (r_per_interp-r_par_interp)* $
  (Gv(z)+Hv(z)*cos(4.*r_par_psi(z))-Gh(z)-Hh(z)*cos(4.*r_per_psi(z)))/$
  (Gv(z)+Hv(z)*cos(4.*r_par_psi(z))+Gh(z)+Hh(z)*cos(4.*r_per_psi(z)))
 red_contour(i,*,z)=red_per_cont+red_par_cont+ $
  (red_per_cont-red_par_cont)* $
  (Gv(z)+Hv(z)*cos(4.*r_par_psi(z))-Gh(z)-Hh(z)*cos(4.*r_per_psi(z)))/$
  (Gv(z)+Hv(z)*cos(4.*r_par_psi(z))+Gh(z)+Hh(z)*cos(4.*r_per_psi(z)))
 endfor
endfor
```

Also note that the effects of the retarder on the I_shapes used in the basic calculation of intensity falling on each SA pixel must also be included. Because Titan's atmosphere is polarized, the spectral shape of the intensity field falling on a SA pixel will vary over the SA field of view dependent on the direction the pixel is looking, the shape of the intensity field, and the shape of the Q intensity affected by the retarder in the appropriate manner.

5 Calibration Verification

As may be becoming apparent, the calibration of the Solar Aureole system is quite involved, including careful combination of the geometric fields of the different instruments, variations of relative spectral response over the spatial field and temperature, variation of the absolute response on a pixel by pixel basis with temperature, variation of polarization qualities over the instrument field, and accurate handling of dark current and the basics of instrument performance.

Therefore, verification of the calibration effort was desired. This was achieved using a simulated Titan descent performed in the lab using the flight model DISR inside a calibrated integrating sphere, with varying CCD temperature along the expected thermal profile for the descent. The Solar Aureole data created in this calibrated environment was reduced to result in computed intensities in the integrating sphere (which had spatial inhomogeneities which had been previously mapped). These computed intensities were then compared to the known intensity and found to be within 2% over all temperatures and every pixel. This is fully documented in an appendix.

6 Stability of SA Response with Time from Cruise Measurements

Over the seven year cruise phase, sixteen instrument checkouts were performed. In each checkout, the In Flight Calibration System was used to stimulate the Solar Aureole cameras. The resulting measurements were tracked over time to detect any optical or electronic changes after the lab calibration. The changes in Solar Aureole response were less than 2% throughout cruise. These checkouts are all reported in detail in the In Flight Checkout documents that were submitted for each test. The latest, most complete Solar Aureole Responsivity verification was from F13.

7 Some Operational Points of Note

Some operational points of note are included in an appendix.

8 Geometry and Field of View

As mentioned above, the four Solar Aureole channels point at slightly different angles. Below is a figure of the fields of view for the four channels. Derivations of these angles and equations for converting from DISR to Titan coordinates are in an appendix.

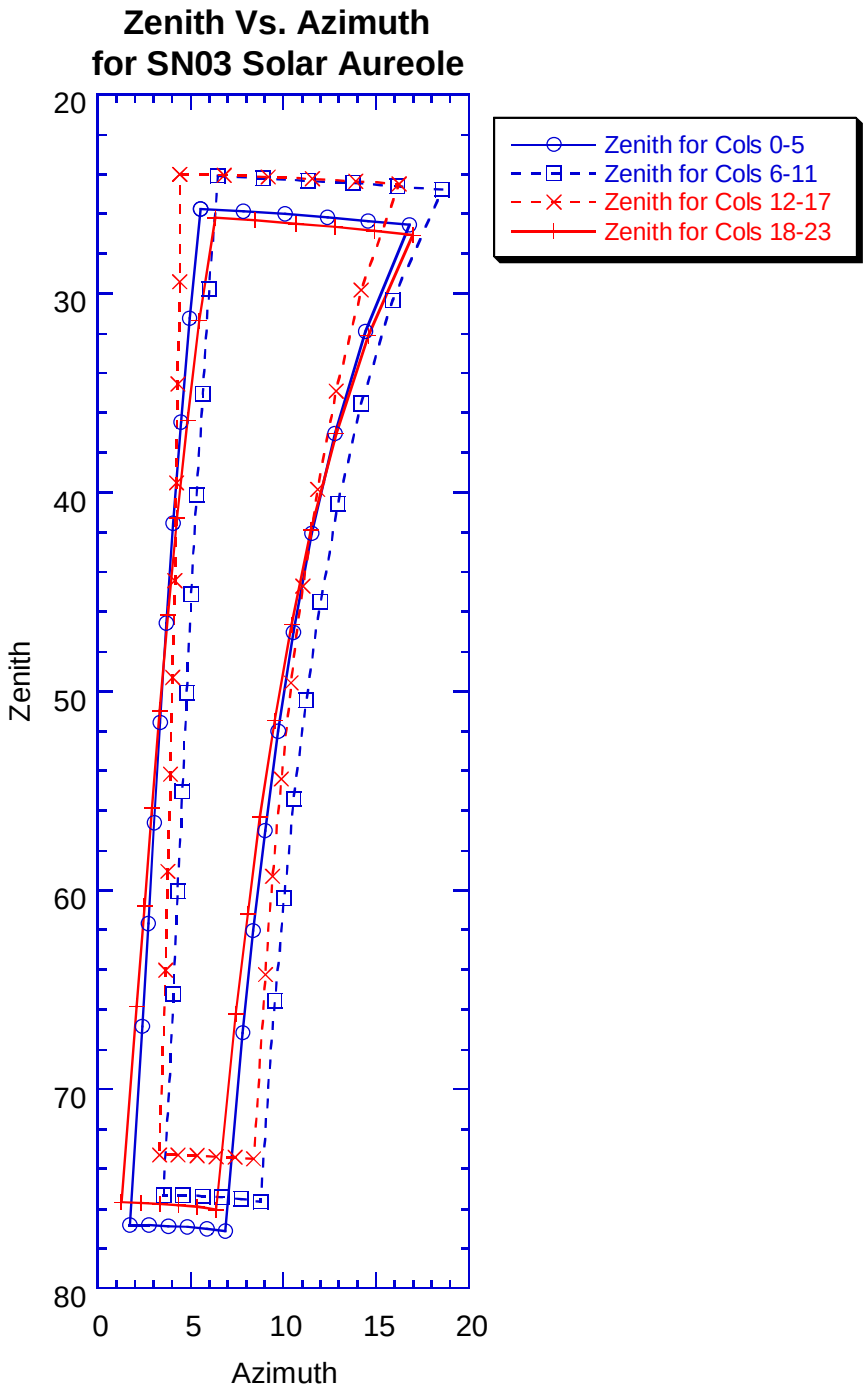

Figure 8-1 The centers of the pixels at the edge of the four solar arrays are shown in azimuth and zenith angle. Note that the arrays do not overlap exactly, and that care will have to be taken in interpolation in an array at one polarization state to obtain the intensity in the other polarization state at the same location. The azimuths shown are relative to the sun if the data were obtained when the instrument crossed the exact azimuth of the sun. In fact, Solar Aureole exposures begin when the instrument is 2.5 to 2.9 degrees past the azimuth of the sun and will continue for a maximum of 3.5 degrees of rotation.

The azimuth and zenith angles for each SA pixel are given in the following four tables.

Table 8-1 Blue Horizontal Solar Aureole Azimuth and Zenith Angles for Every Pixel

Table 8-2 Blue Vertical Solar Aureole Azimuth and Zenith Angles for Every Pixel

Table 8-3 Red Horizontal Solar Aureole Azimuth and Zenith Angles for Every Pixel

Table 8-4 Red Vertical Solar Aureole Azimuth and Zenith Angles for Every Pixel

Because the physical quantities measured by the Solar Aureole combine data from both polarization states, there is an effective field of view created by the intersection of the two fields of view for each color. This effective field of view is smaller than 6 by 50 degrees, and it can have an irregular shape. The following two figures show the effective fields of view for the blue and red SA channels if all pixels can be used. As discussed in the section about the Titan descent, several columns must be omitted, which further constrains the effective field of view.

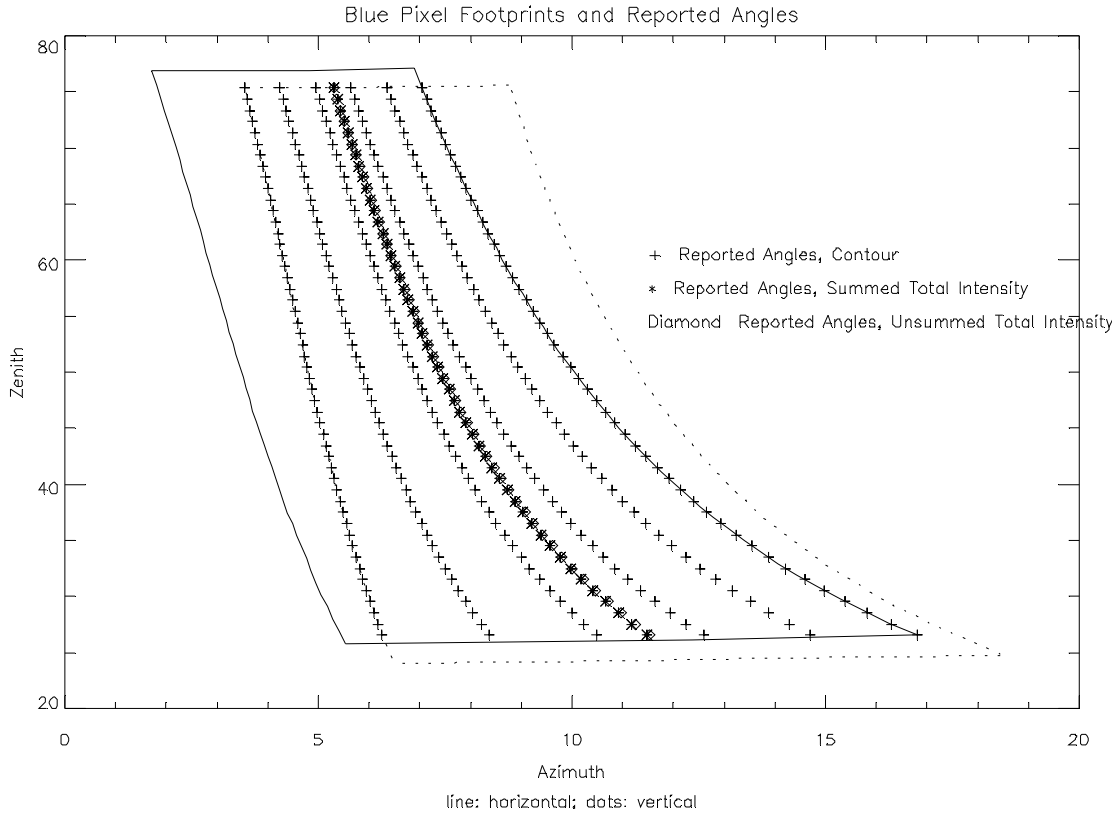

Figure 8-2 The effective field of view for the blue Solar Aureole channels if all columns are used. The horizontal and vertical channels do not overlap perfectly, so a smaller field is used to combine the intensities from both channels to result in total intensity and polarization. The + signs indicate locations where physical quantities are reported in the University of Arizona Lunar and Planetary Lab analysis for data sets that are delivered in full 24 by 50 pixel format. The diamonds indicate locations where physical quantities are reported for data sets that are summed on board before sending them to earth. Care must be taken to exclude pixels where the absolute responsivity is poorly known as mentioned in the section on the Titan descent.

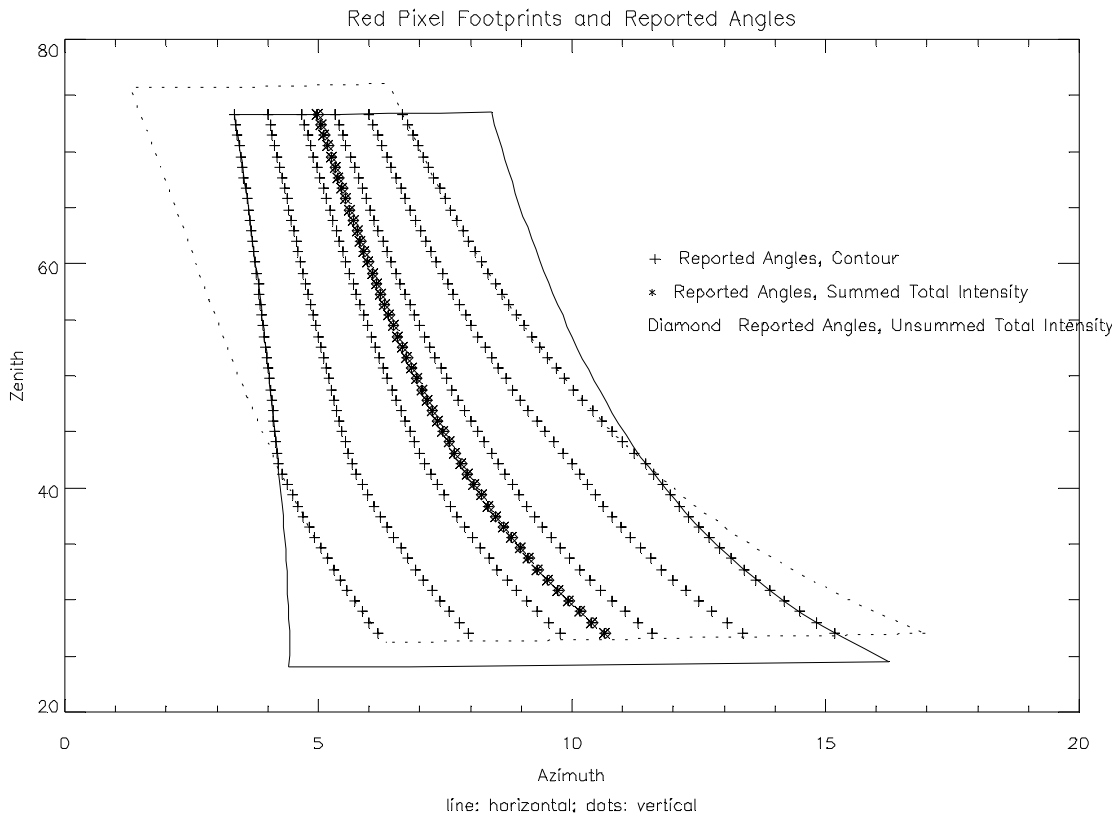

Figure 8-3 Same as previous figure, but for the red.

9 Relative Spectral Response

9.1 The Form of Relative Spectral Response Model

A model of the Relative Spectral Response (RSR) was derived from measured DISR Solar Aureole data. The details of the model derivation, as well as the quality of the model fits, are shown in an appendix.

The form of the RSR model includes a foundational set of spectrally varying curves, *filter*, whose characteristics are largely due to the interference filters in each channel but also have contributions from the beamsplitter. The filter curves are functions of the row number (angle of incidence) for each pixel. To result in the RSR model, the filter curves are multiplied by a polynomial function that includes all thermally varying effects and some spatial effects, all of which are presumed to reside in the CCD chip and fiber bundle since the filters have been shown to have no temperature dependence (see appendix). This latter function is called the "non-filter model", or NFM, because it is derived analytically by eliminating the interference filter effects from the measured relative spectral response. It includes some spatial variation on a columnwise basis.

As derived, the RSR for each of the four SA channels can be found by the following equation.

$$SA\_RSR(T,\lambda,c,r) = filter(\lambda,r) * NFM(T,\lambda,c)$$

where:

$filter$ = scaled model of interference filter transmission

NFM = everything in the SA channel contributing to relative spectral response except the interference filter

T = temperature

λ = wavelength

c = column

r = row

5.

The form of the NFM is the following polynomial equation, where the thermal coefficients, a, b, c, and d, are properties of the SA channel, and the column coefficients, M0 through M3, are column dependent for each channel.

$$NFM(T,\lambda,c) = NFM_{ini}(\lambda) * (M0(c) + M1(c)*\lambda + M2(c)*\lambda^2 + M3(c)*\lambda^3) + (293K - T) * (a + b*\lambda + c*\lambda^2 + d*\lambda^3)$$

where:

$NFM_{ini}(\lambda)$ = an initial spectral non filter model

6.

Due to fiber ribbon/CCD misalignments, a few columns do not match their neighbors in RSR shape. These columns are treated in the manner described above, but with their own set of filters and coefficients. Additional localized spatial effects are found throughout the system – the CCD has some pixel to pixel variation and the optical train has obvious illumination variations over the field due to the cameras and fiber ribbon underfilling the CCD – but the number of pixels affected and the degree of modeling error are small.

The initial NFM, $NFM_{ini}(\lambda)$, is an underlying spectrally varying function which includes structure in the CCD quantum efficiency. The blue channels have no underlying structure, so NFM_{ini} is defined to be unity. The red channels, on the other hand, do have some structure over the SA bandpass, and this structure can be modeled as follows.

A known bump in the CCD quantum efficiency can be seen in the red SA RSR, so it is modeled empirically in the initial NFM as a lorentzian function with a center wavelength of 854 nm, a full-width at half maximum response of 15 nm, and a peak amplitude of 0.4, as follows.

$$Bump(\lambda) = 1 + \frac{0.4}{1 + \left(2 * \frac{(854 - \lambda)}{15}\right)^2}$$

7.

The coefficients of the initial NFM quadratic fit of the quantum efficiency rolloff for the red horizontal and vertical channels are as follows.

Table 9-1 Table of NFM_{ini} Quadratic Coefficients

	Red Horizontal	Red Vertical
nfm0	67.900400	25.311233
nfm1	-0.13372830	-0.043105799
nfm2	6.6157520e-005	1.8006592e-005

Thus, the initial NFM is as follows for the blue or red channels.

$$NFM_{ini}(\lambda) = \left\{ \begin{array}{c} 1.0 \\ or \\ Bump(\lambda) * \left(nfm0 + nfm1 * \lambda + nfm2 * \lambda^2 \right) \end{array} \right\} \qquad 8.$$

Thus, the Solar Aureole Relative Spectral Response is modeled in the following forms. For the blue channels, the final equation is as follows,

$$SA\_RSR(T,\lambda,c,r) = filter(\lambda,r) * \left\{ \begin{array}{l} \left(M0(c) + M1(c) * \lambda + M2(c) * \lambda^2 + M3(c) * \lambda^3 \right) + \\ (224.7 - T) * \left(a + b * \lambda + c * \lambda^2 + d * \lambda^3 \right) \end{array} \right\} \qquad 9.$$

where the filter and the coefficients M0 through M3 and a through d are in the tables below.

For the red channels, the final equation is as follows,

$$SA\_RSR(T,\lambda,c,r) = filter(\lambda,r) * Bump(\lambda) * \left(nfm0 + nfm1 * \lambda + nfm2 * \lambda^2 \right) * \left\{ \begin{array}{l} \left(M0(c) + M1(c) * \lambda + M2(c) * \lambda^2 + M3(c) * \lambda^3 \right) + \\ (224.7 - T) * \left(a + b * \lambda + c * \lambda^2 + d * \lambda^3 \right) \end{array} \right\} \qquad 10.$$

where the filter and the coefficients M0 through M3 and a through d are in the tables below, and the *Bump* function and nfm0 through nfm2 are in this section. Care must be taken to use the correct filters and coefficients for the columns 0 and 1 as appropriate.

It should be noted that the complexity of the modeling is due to both systematic effects such as the filter transmission variation with angle of incidence and the CCD quantum efficiency changing with temperature, and to pixel to pixel variations largely caused by the fiber ribbons. These ribbons have imperfections throughout their thin "bulk" and along their edges. It is these effects that create such model complexity.

9.2 The SA Interference Filter Transmissions

Recall that while these are designated "filter transmissions," they include effects from the filters and the beamsplitters and possibly other sources. Therefore, the full zenith angle field of view is characterized rather than just angles from the optic axis.

Table 9-2 Table of Blue Horizontal Filter Curves

Table 9-3 Table of Blue Vertical Filter Curves

Table 9-4 Table of Red Horizontal Filter Curves

Table 9-5 Table of Red Vertical Filter Curves

Table 9-6 Table of Red Horizontal Filter Curves, Column 0

Table 9-7 Table of Red Horizontal Filter Curves, Column 1

Table 9-8 Table of Red Vertical Filter Curves, Column 0

9.3 The SA RSR Thermal Coefficients, a, b, c, and d

The thermal variations in the RSR are modeled using polynomials as shown in the equation for the NFM (non filter model). These polynomials are characteristic of each SA channel, with two columns requiring their own temperature dependence because of edge chips on the fiber ribbon. The coefficients are as follows.

Table 9-9 Thermal Coefficients for All SA Channels

Channel	a	b	c	d
Blue Hor	2.0519205	-0.012112786	2.3854392e-005	-1.5672918e-008
Blue Ver	2.6717794	-0.015919638	3.1632590e-005	-2.0960937e-008
Red Hor	4.1627853	-0.013355480	1.4316606e-005	-5.1278929e-009
Red Ver	0.46694120	-0.0014621260	1.5654954e-006	-5.7336477e-010
Red Hor, col 0	5.2851043	-0.016804565	1.7844364e-005	-6.3286793e-009
Red Hor, col 1	4.9409769	-0.015830010	1.6938123e-005	-6.0531465e-009

9.4 The SA RSR Column Variation Coefficients, M0, M1, M2, and M3

Given the initial NFM and filter models, and the thermal variations represented by the polynomials in the previous section, there remain column to column variations in the non filter models. These are mapped by other polynomials, as shown in the NFM model equation in Section 9.1

The column coefficients M0 through M3 for each channel are in the following tables.

Table 9-10 Blue Horizontal Column Coefficients

	M0	M1	M2	M3
Column 0	-1.576161E+01	6.991217E-02	-7.261663E-05	0.000000E+00
Column 1	-1.120476E+02	6.776472E-01	-1.348858E-03	8.917191E-07
Column 2	-5.451464E+01	3.371992E-01	-6.802498E-04	4.559225E-07
Column 3	1.0	0.0	0.0	0.0
Column 4	7.670377E+01	-4.607676E-01	9.324273E-04	-6.274879E-07
Column 5	1.279626E+02	-7.734728E-01	1.566727E-03	-1.055404E-06

Table 9-11 Blue Vertical Column Coefficients

	M0	M1	M2	M3
Column 0	1.287794E+02	-7.803157E-01	1.587449E-03	-1.075872E-06
Column 1	1.076329E+02	-6.419133E-01	1.287519E-03	-8.604670E-07
Column 2	1.0	0.0	0.0	0.0
Column 3	1.033230E+01	-5.103488E-02	9.152373E-05	-5.362022E-08
Column 4	4.158349E+01	-2.413895E-01	4.777937E-04	-3.147463E-07
Column 5	1.067493E+02	-6.317197E-01	1.256640E-03	-8.324925E-07

Table 9-12 Red Horizontal Column Coefficients

	M0	M1	M2	M3
Column 0	-6.951670E+01	2.272747E-01	-2.440805E-04	8.734615E-08
Column 1	9.833868E+00	-2.762700E-02	2.874322E-05	-9.946730E-09
Column 2	1.0	0.0	0.0	0.0
Column 3	-8.488152E+01	2.770449E-01	-2.980202E-04	1.069016E-07
Column 4	-1.488555E+02	4.824542E-01	-5.178775E-04	1.853475E-07
Column 5	-9.319383E+01	3.022677E-01	-3.235209E-04	1.154941E-07

Table 9-13 Red Vertical Column Coefficients

	M0	M1	M2	M3
Column 0	9.037937E+00	-2.485048E-02	2.555993E-05	-8.744530E-09
Column 1	3.750232E+02	-1.205694E+00	1.293924E-03	-4.622855E-07
Column 2	9.085585E+01	-2.906646E-01	3.126092E-04	-1.117840E-07
Column 3	1.0	0.0	0.0	0.0
Column 4	1.899895E+01	-6.003125E-02	6.722727E-05	-2.525717E-08
Column 5	2.436124E+01	-7.513855E-02	8.203623E-05	-3.038352E-08

10 Absolute Response

The absolute responsivity of the SA cameras was measured in the lab as described in an appendix. Once this absolute response was measured, a model could be generated that would be a general representation of the absolute response. The details of the model derivation, as well as the quality of the model fits, are shown in an appendix.

10.1 Mean Absolute Response

Because the absolute response varies with temperature, it is helpful to have a thermal model. As a base for the model, the mean absolute response for each channel is computed versus CCD chip temperature, and it is fit with a fifth or sixth order polynomial. Column 0 is excluded from the mean because it lies at the edge of the fiber ribbon illumination and is impacted by mechanical changes with temperature that are different from the rest of the array. Creating a thermal model using the detector temperature for the mean and initial pixel map derivation, but using the optics temperature for pixel-to-pixel variations over temperature (which makes more physical intuitive sense), resulted in a model with poorer performance than just using CCD temperature. The pixel-to-pixel variation with temperature is likely due to thermal variance of the separation between the CCD and the fiber ribbon, which is better

modeled by the CCD temperature than the optics temperature since that temperature sensor is closer than the one on the optical bench.

The results are in the following plot and table.

Table 10-1 Polynomial Coefficients for the Mean Absolute Response versus CCD Temperature

	Blue Horizontal	Blue Vertical	Red Horizontal	Red Vertical
A0	-1.320628900000e+8	-1.043157230000e+8	-6.342293175000e+7	-4.764707846875e+7
A1	3.439118281250e+6	2.708450062500e+6	1.392982078125e+6	1.053106603516e+6
A2	-3.693190771484e+4	-2.898806738281e+4	-1.200406482697e+4	-9.126064826965e+3
A3	2.100620784760e+2	1.643101100922e+2	5.120302107930e+1	3.914550912380e+1
A4	-6.678061112761e-1	-5.205441340804e-1	-1.080477217911e-1	-8.309265802382e-2
A5	1.125490496634e-3	8.742839563638e-4	9.032962566380e-5	6.989951356218e-5
A6	-7.858712436359e-7	-6.084150783181e-7	0.000000000000e+0	0.000000000000e+0

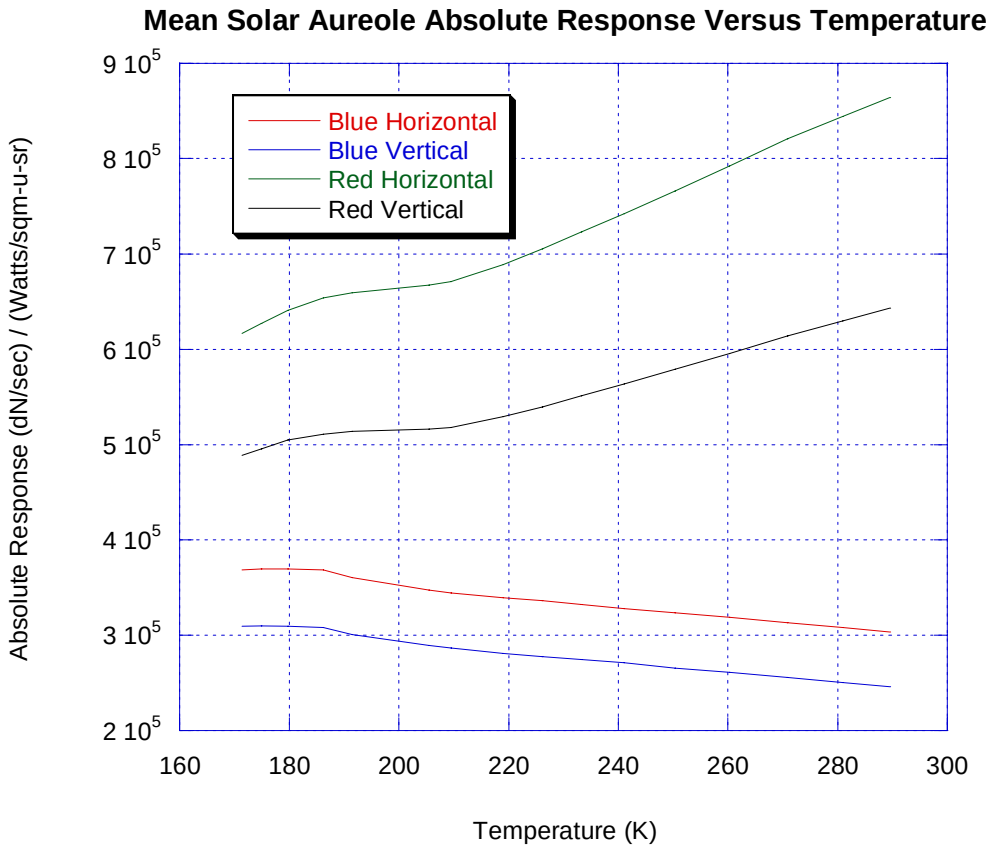

Figure 10-1 Mean Absolute Response versus Temperature

10.2 Thermal Variation in Pixel Maps

The next step in the generation of a thermal model is the formation of a pixel map at the coldest temperature. This map is the computed absolute response from the previous sections

divided by the polynomial fit at the coldest temperature. This map then represents the pixel-to-pixel variations.

$$Map(col,row) = \frac{Abs(T_0,col,row)}{A0 + A1*T_0 + A2*T_0^2 + A3*T_0^3 + A4*T_0^4 + A5*T_0^5 + A6*T_0^6} \quad 11.$$

If the pixel-to-pixel variations were thermally invariant, one could then compute the absolute response of any pixel at any temperature by the following equation.

$$Abs(T,col,row) = Map(col,row)* \left(A0 + A1*T_0 + A2*T_0^2 + A3*T_0^3 + A4*T_0^4 + A5*T_0^5 + A6*T_0^6\right) \quad 12.$$

Unfortunately, this is not the case. The pixel-to-pixel variations do vary also with temperature. Several physical mechanisms may be contributing to this variation, but one effect is that the separation between the fiber ribbon bundle and the CCD appears to vary slightly with temperature.

The pixel-to-pixel variation with temperature is modeled by an additional set of polynomial coefficients for each pixel in the map. Two temperatures were considered in this polynomial fit – the detector temperature and the optics temperature. The detector temperature yields the better performance, probably because the detector temperature sensor is closer to the gap between the fiber ribbon and CCD and thus models the temperature of that gap more accurately. In this way, the absolute response for any pixel at any temperature can be computed by the following equation.

$$Abs(T,col,row) = Map(col,row)* (p0(col,row) + p1(col,row)*T + p2(col,row)*T^2 + p3(col,row)*T^3)* \left(A0 + A1*T_0 + A2*T_0^2 + A3*T_0^3 + A4*T_0^4 + A5*T_0^5 + A6*T_0^6\right) \quad 13.$$

This equation can be simplified by multiplying the Map and the "p" polynomial coefficients to result in the final model for the thermal variation of the absolute response.

$$Abs(T,col,row) = \left(M0(col,row) + M1(col,row)*T + M2(col,row)*T^2 + M3(col,row)*T^3\right)* \left(A0 + A1*T_0 + A2*T_0^2 + A3*T_0^3 + A4*T_0^4 + A5*T_0^5 + A6*T_0^6\right) \quad 14.$$

The "M" coefficients for the thermal variation of the pixel map are in the following tables. Care should be taken not to confuse these M coefficients with those for the Relative Spectral Response model.

Table 10-2 Coefficients for Thermal Variation of Pixel Map: Blue Horizontal M0 Coefficients

Table 10-3 Coefficients for Thermal Variation of Pixel Map: Blue Horizontal M1 Coefficients

Table 10-4 Coefficients for Thermal Variation of Pixel Map: Blue Horizontal M2 Coefficients

Table 10-5 Coefficients for Thermal Variation of Pixel Map: Blue Horizontal M3 Coefficients

Table 10-6 Coefficients for Thermal Variation of Pixel Map: Blue Vertical M0 Coefficients

11 Polarization Sensitivity

The four Solar Aureole channels include two channels in each of two colors. The two channels for a given color are identical with the exception of the orientation of polarizers in the optical path, one parallel to the Shadow Bar (vertical) and one perpendicular to the Shadow Bar (horizontal). During the test and calibration phase of the DISR program, several unexpected effects were noticed regarding the polarization sensitivity of the SA cameras. The details of these effects and their cause are included in an appendix.

The bottom line result is that the beamsplitter prism which introduces calibration light into the SA optical train acts as a retarder in the system. It re-orients the principal plane over the field of view of each SA channel. The action of this retarder must be included in the SA data analysis.

It is interesting to understand how the instrument came to have these properties. One requirement of the in flight calibration system was that it pass light through all the optical elements of a system except for the front window. This requirement allowed for accurate tracking of any radiation darkening of optics or changes in alignments over the launch or cruise environments. However, because of the design of the Solar Aureole optical system, it implied a beamsplitter to introduce the calibration signal.

The blue beamsplitter acts nearly as a quarter-wave retarder. Its position angle as a function of row number is given in the following figure. The retardance is taken as 90 degrees for the blue prism.

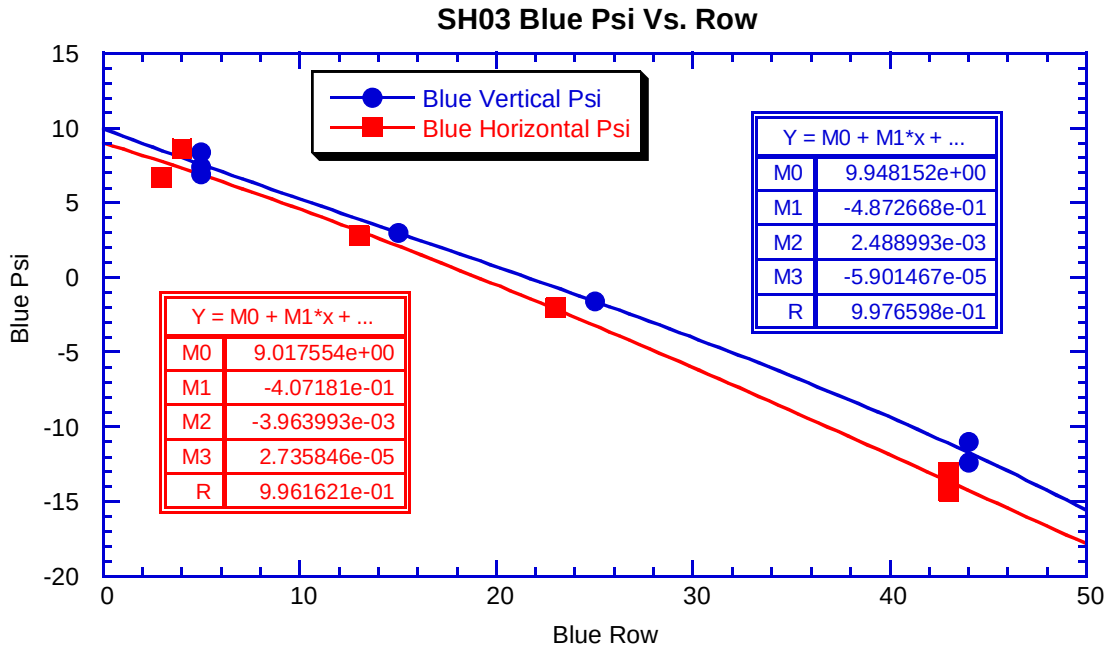

Figure 11-1 We show the position angle as a function of row number for the Blue Vertical and Horizontal channels in the SH03 flight Solar Aureole system. The retardance is taken as 90 degrees for the flight prism in the blue channel.

The retardance of the flight prism is less in the red than in the blue channel. Note that the retardance of the prism alone in the red channels is approximately 30 degrees compared to the 90 degrees measured in the blue channel. Since the dichroic beam splitter is much more reflective in the blue than in the red, this is not surprising. Below are two figures which include the retardance and the angle of the principal plane in both channels of the red Solar Aureole system.

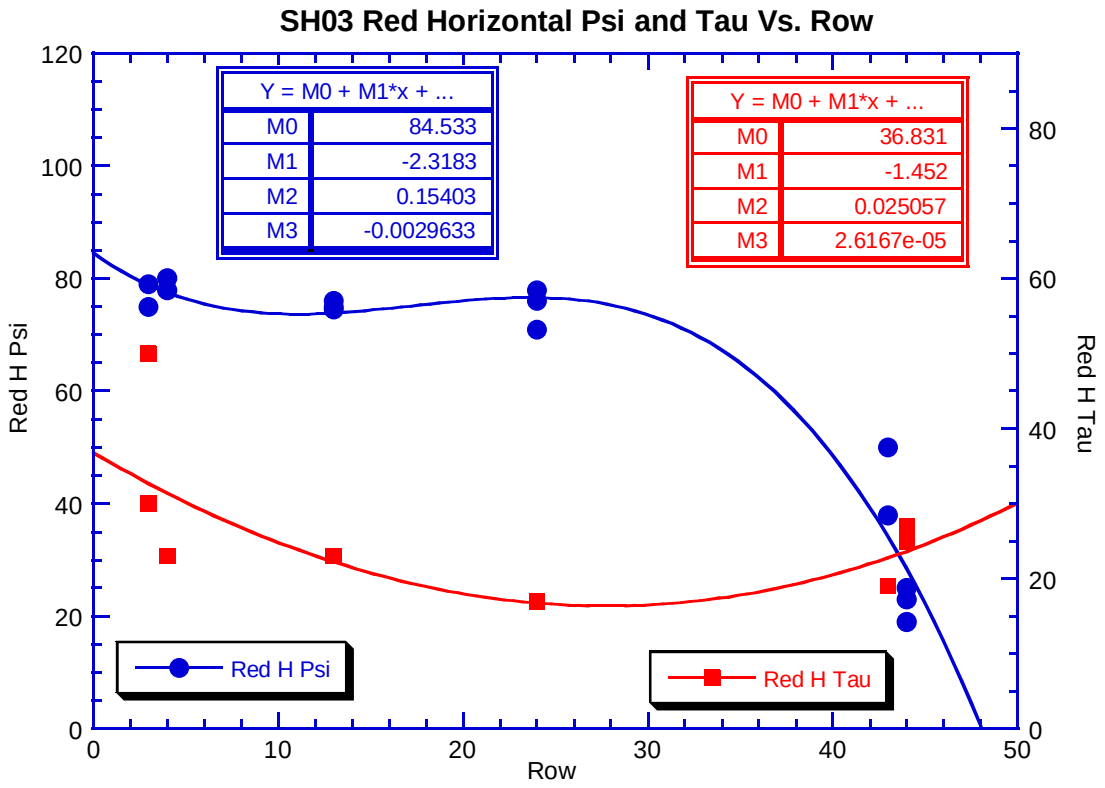

Figure 11-2 The position angle (Psi, left scale, blue dots) and the degree of retardance (tau, right scale, red squares) as functions of row in the horizontal channel of the flight sensor head.

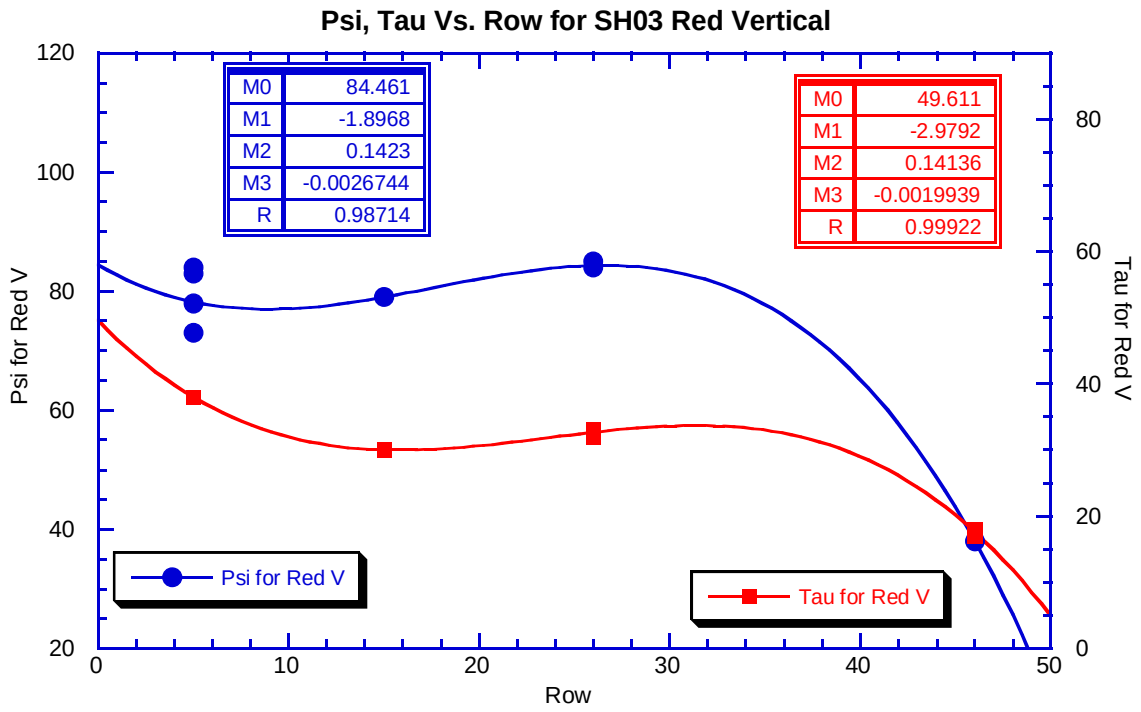

Figure 11-3 Like Figure 11-2 but for the vertical channel of the flight SA in the red.

12 Temperature Dependence of Dark Current

The CCD has a temperature dependent dark current which must be removed from all measurements. This dark current can be computed in the following manner:

1.) Read in matrices mapping pixel to pixel variations for the Solar Aureole portion of the CCD. These are designated f1 and f2, and are attached as Table 12-1 and Table 12-2.
2.) Read the file with Mission Time, Mean CCD Dark, Bias + Serial Register. This is often designated CC_MST_MDK_BSR.dat, and is listed as Table 12-3.
3.) Interpolate the mean dark to the specific mission time of a data set.
4.) Interpolate the bias+sr to the specific mission time of a data set.
5.) Change bias+sr to spectral read mode using mbias = ((bias-8.9)*(0.976/8.384))+8.9 > 0.0.
6.) Calculate memory zone dwell time array (mz) array for each row according to mz = (row+1)*0.000976 seconds where "row" is in Full CCD units (i.e. 204 through 253).
7.) Change the exposure time of data set to seconds.
8.) Calculate dark + bias pixel value for data set's specific mission time and exposure time using:

dark + bias = (exptime * f1 * mdark) + (mz * mdark * f2) + mbias

Table 12-1 Solar Aureole CCD Image Section Map of Dark Current Rates

Table 12-2 Solar Aureole CCD Memory Section Map of Dark Current Rates

Table 12-3 Mean CCD Dark Rate, Bias, Serial Register

The derivation of the CCD dark current for all CCD measurements is contained in a separate report.

13 Appendices

13.1 Calibration Verification – Simulation Descent Reduction Paper

13.1.1 Introduction

After the recent revelation that the Solar Aureole absolute response model needed refinement, the model was updated and a simulated descent was analyzed. This document describes the results from the recent simulated descent analysis.

The simulated descent analyzed is that performed on August 7, 1996. It is the best descent to study for the SA because its window was not covered with alumalloy.

13.1.2 Approach

The basic approach to this analysis is to compute the predicted intensity given the SA counts and the models derived elsewhere, followed by computation of the true intensity in the integrating sphere derived from the calibration files. The ratio of the predicted intensity to the true intensity is the figure of merit for this analysis, and we would hope this ratio would be unity over the descent and thus over temperature.

The code descent_analysis, which inputs an entire descent's worth of Solar Aureole data and computes calibrated intensities at specific locations on the sky over the descent, is used to compute the predicted intensity. Total intensity cuts across zenith angle are computed for every data set returned in the descent, and contour maps are computed where the full format data is available.

To compute the predicted intensity, we input the counts measured in the SA, subtract the dark counts and CCD bias using Andrew Eibl's dark model, and then divide this by the product of the integration time, model absolute response, and integral of the model relative spectral response times the shape of the monochromator scan (During the mission, the base shape for the input intensity will be derived from the ULVS measurements.). This quantity, I_{std_wave}, is the calibrated intensity at a specific wavelength: 492nm in the blue and 934nm in the red. Mathematically, we do the following:

$$I_{std\_wave} = \frac{dN - (dark + bias)}{t_i * Abs\,\mathrm{Re}sp * \int RSR * I_{shape} d\lambda}$$

To compute the true intensity in the sphere, we take the monochromator scan performed for this log, correct for lamp drift during the scan and during the descent, and correct for spatial variations in the integrating sphere. For comparison with the data produced by the descent_analysis code, which sums the two polarization states, the effects of pixel registration must be carefully performed since the interior of the integrating sphere is not perfectly uniform.

13.1.3 Results – Absolute Calibration

Before describing the results in detail, we consider the overall results in the table below. This table indicates that for the total intensity data, the ratio of the predicted intensity at a specific zenith angle to the measured intensity at that angle, averaged over every data set in the descent is 0.997 for the blue and 1.005 for the red. This corresponds to an average model fidelity of a fraction of a percent. The minimum and maximum ratios for every zenith angle over the descent are also given. They indicate a maximum dispersion of 5% in the blue and 4% in the red. The contour data results in larger dispersion around nominal, which is expected due to noise.

	Minimum	Maximum	Mean
Blue Total Intensity	0.953	1.052	0.997
Red Total Intensity	0.981	1.042	1.005
Blue Contour	0.898	1.077	0.996
Red Contour	0.967	1.076	1.005

It should be noted that the SNR has not been incorporated explicitly in these results. The SNR for data that has not been summed increases to around 100 for the blues and around 230 for the reds in the central pixels.

It should also be noted that the lamp used for the test failed for a short period of the descent. This causes the lamp drift equation to yield unrealistic values. Data taken during this period is not included in this analysis, nor is the data from three instances of saturation which occurred due to auto-exposure when the lamp came back on.

As will be seen later, the lamp failure contributes to an overall question to the true accuracy of the absolute response calibration for this test, but it is useful to see how well the Solar Aureole models perform even in this condition.

Consider the following two plots of model performance for the total intensity cuts. These plots show the ratio of predicted to measured intensities in the blue and red channels. They include every zenith angle in every appropriate data set in the descent. One can note the minima and maxima as described in the table above.

The three plotting styles (asterisks, diamonds, and plus signs) indicate regions of model performance, which will now be addressed. Note that for historical reasons there are three plotting styles. There are actually only two regions of performance. The third “region” was an artifact of incorrect handling of the bias in the CCD. After correction of this error, the three regions collapsed into two.

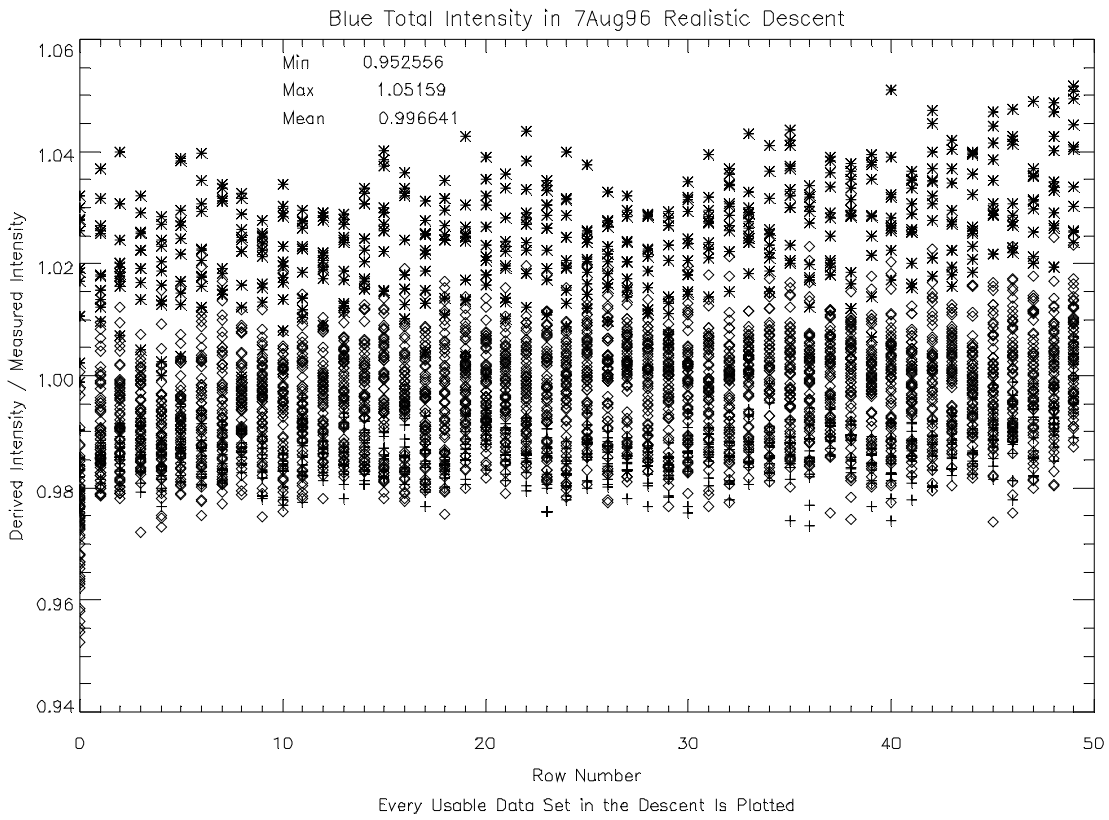
Blue Total Intensity in 7Aug96 Realistic Descent
Min 0.952556
Max 1.05159
Mean 0.996641
Derived Intensity / Measured Intensity
1.06
1.04
1.02
1.00
0.98
0.96
0.94
0
10
20
30
40
50
Row Number
Every Usable Data Set in the Descent Is Plotted

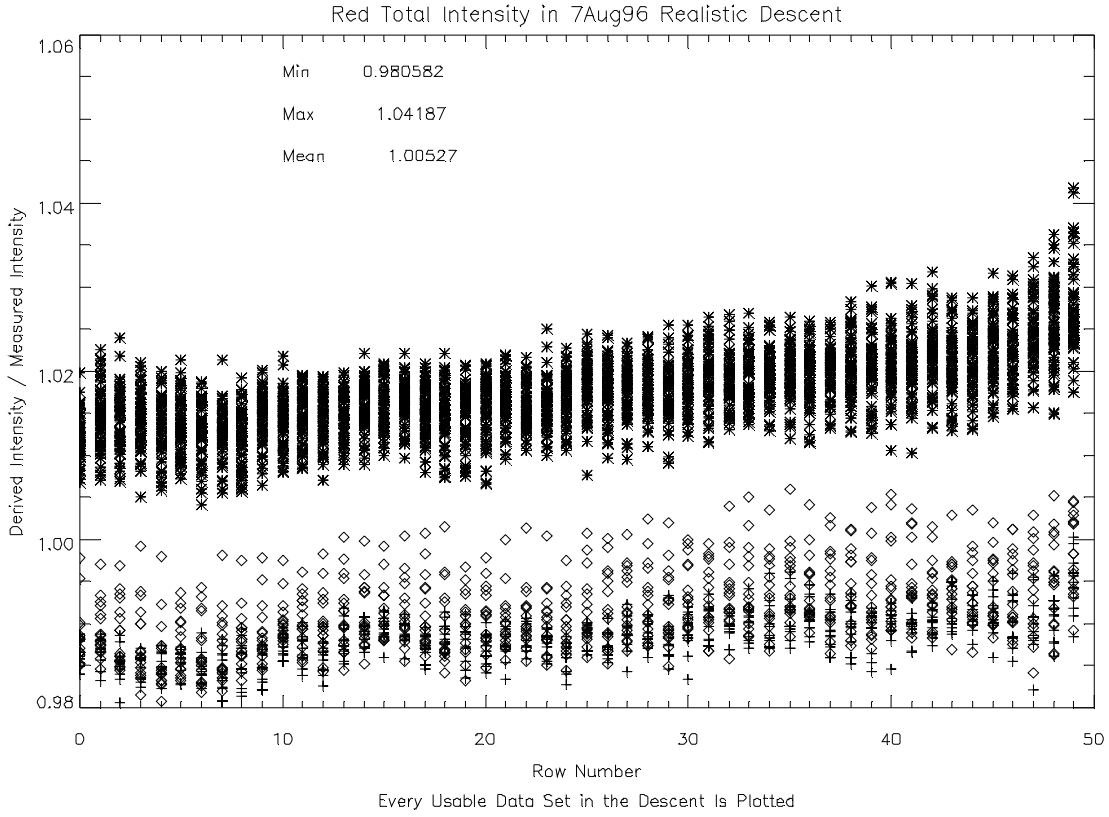
Red Total Intensity in 7Aug96 Realistic Descent
Min 0.980582
Max 1.04187
Mean 1.00527
Derived Intensity / Measured Intensity
1.06
1.04
1.02
1.00
0.98
0
10
20
30
40
50
Row Number
Every Usable Data Set in the Descent Is Plotted

13.1.3.1 Red Summed Data

The red channel shows the most obvious splitting of performance, so it is addressed first. It was found that the regions of performance related to periods of time during the descent. The CCD temperature is plotted versus mission time below. The plotting styles here correspond to those in the model performance plot above.

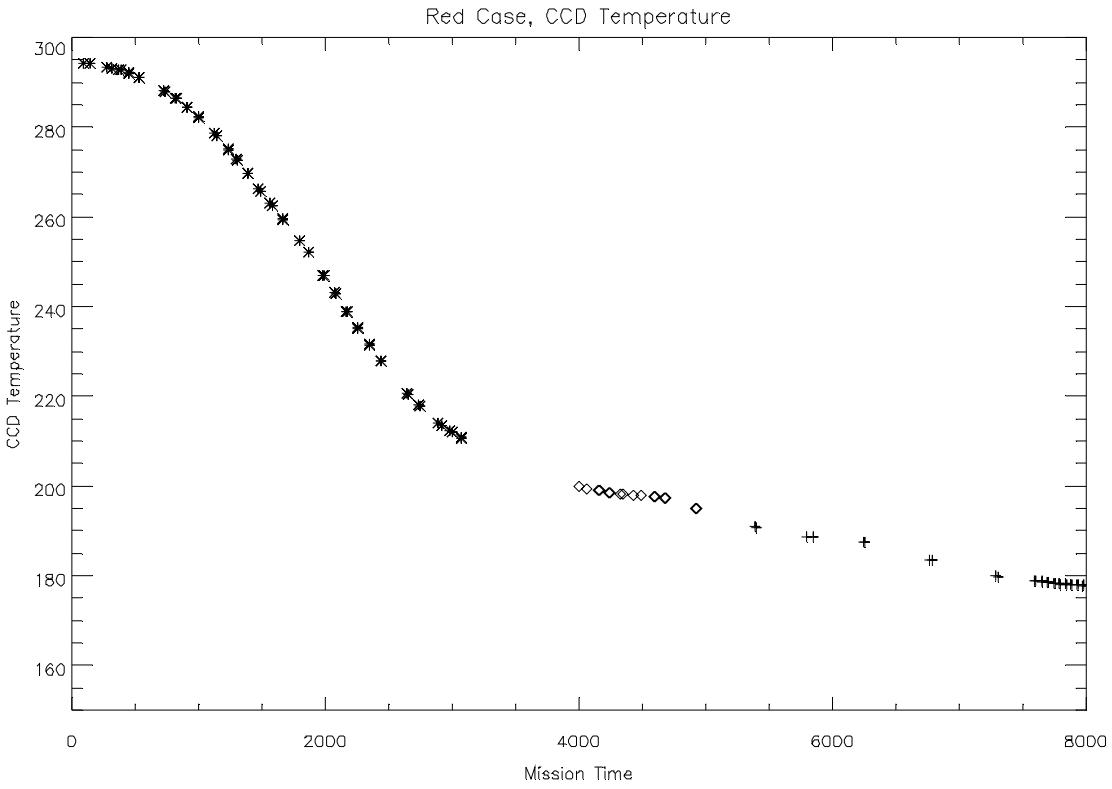

It is seen that the majority of the temperature range is in the first of the three regions. While the splitting of performance could in fact be due to poor thermal modeling of the SA response, another explanation is more convincing.

The measured calibrated intensity in the integrating sphere at the location seen by the red horizontal channel central pixel is plotted versus mission time below. Again, the plotting styles here correspond to those in the model performance plot above. The large gap between the asterisks and the line is when the light failed and then came on again. One can see that the lamp does not really become stable again until later in the descent. It is clear that the model performance correlates with the lamp regions of operation.

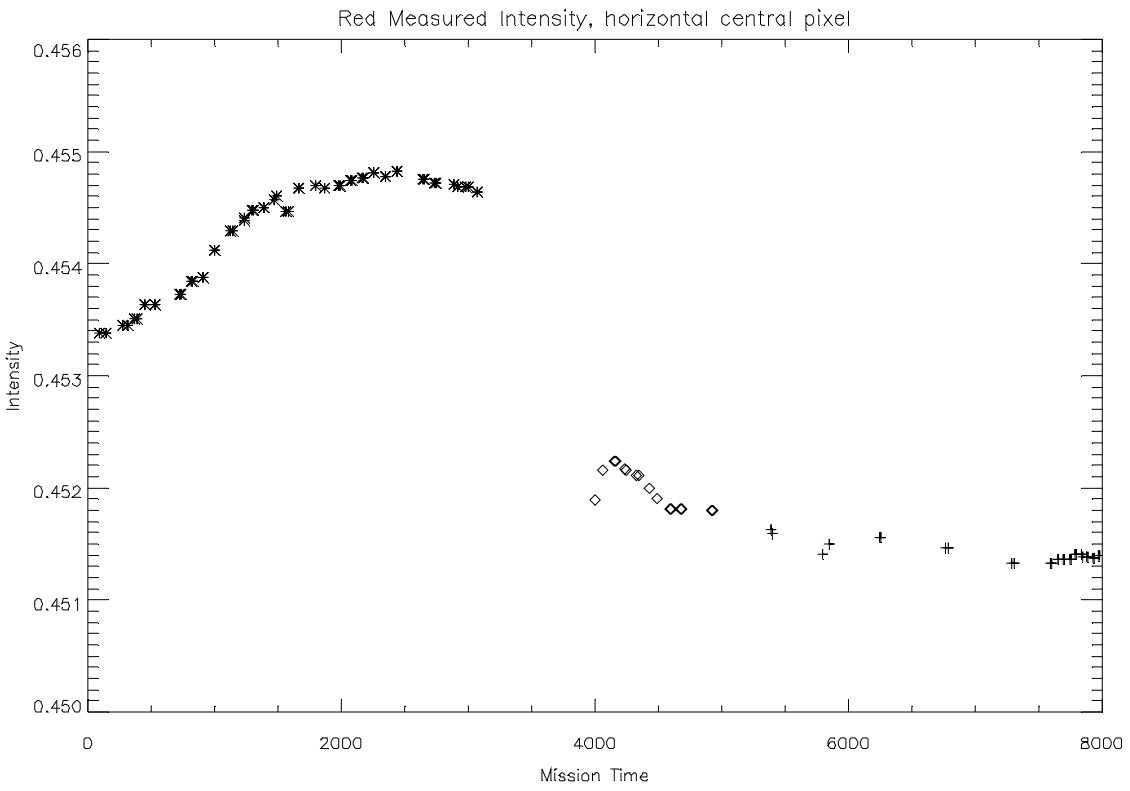

The question arises, then, about the fidelity of the measured calibrated intensity values for this particular descent run. The measured intensity values are derived from two monochromator scans, one for the blue and one for the red, which were performed at 14:40 and 15:02 hours respectively, on 7 Aug 96. The descent occurred between 10:54 and 13:28 hours, and it included a lamp failure. The notes file from this log also indicates some "cal crashes" prior to the actual descent, and the dark readings for the calibrated detector system are very difficult to find through that entire day's work. Therefore, it could be argued fairly convincingly that the values taken for the true intensities for the descent could be off by a couple of percent due to lamp variations over a period of almost 5 hours which was known to include a lamp failure, and due to possible recent power cycles in the calibration equipment and due to misrepresentation of the dark readings in the calibration detector.

13.1.3.2 Blue Summed Data

Switching to the blue channel, the plots of CCD temperature and measured intensity versus mission time are below. The boundary between the first and second performance regions occurs at a different place for the blue than the red. The boundary between the second and third regions occurs at the same time as the red (the red data point is not plotted because of saturation in that data set).

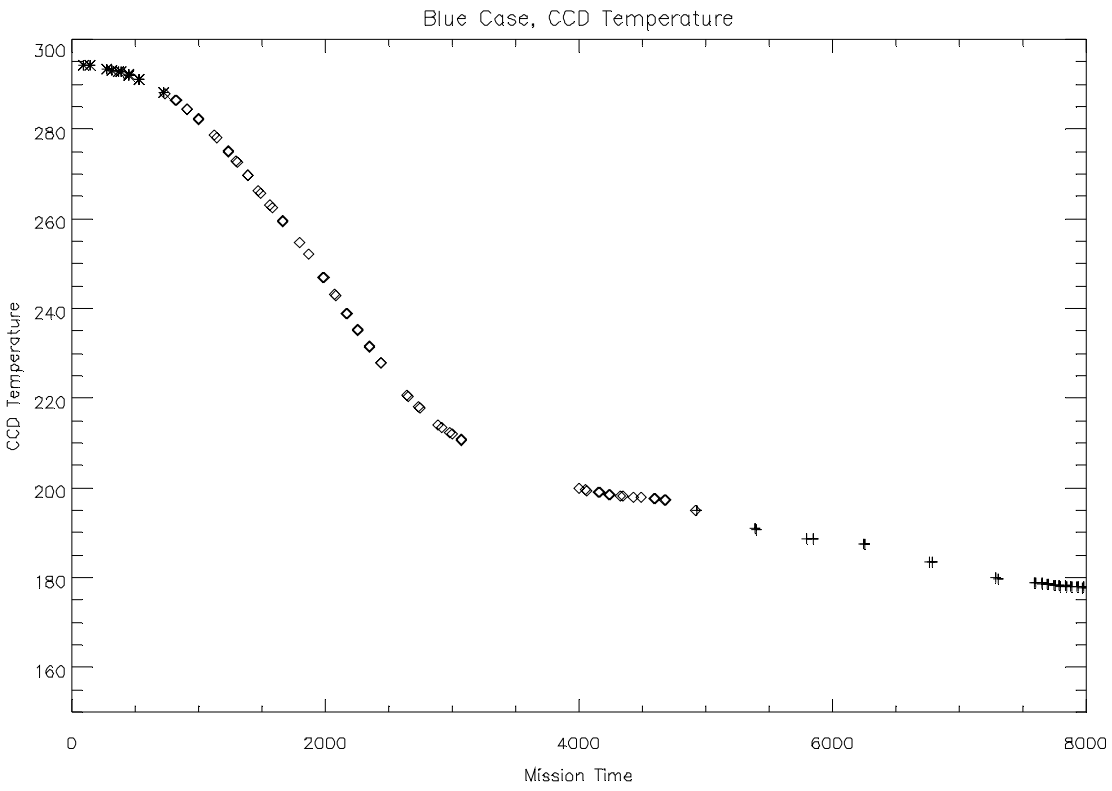
Blue Case, CCD Temperature
CCD Temperature
300
280
260
240
220
200
180
160
0
2000
4000
6000
8000
Mission Time

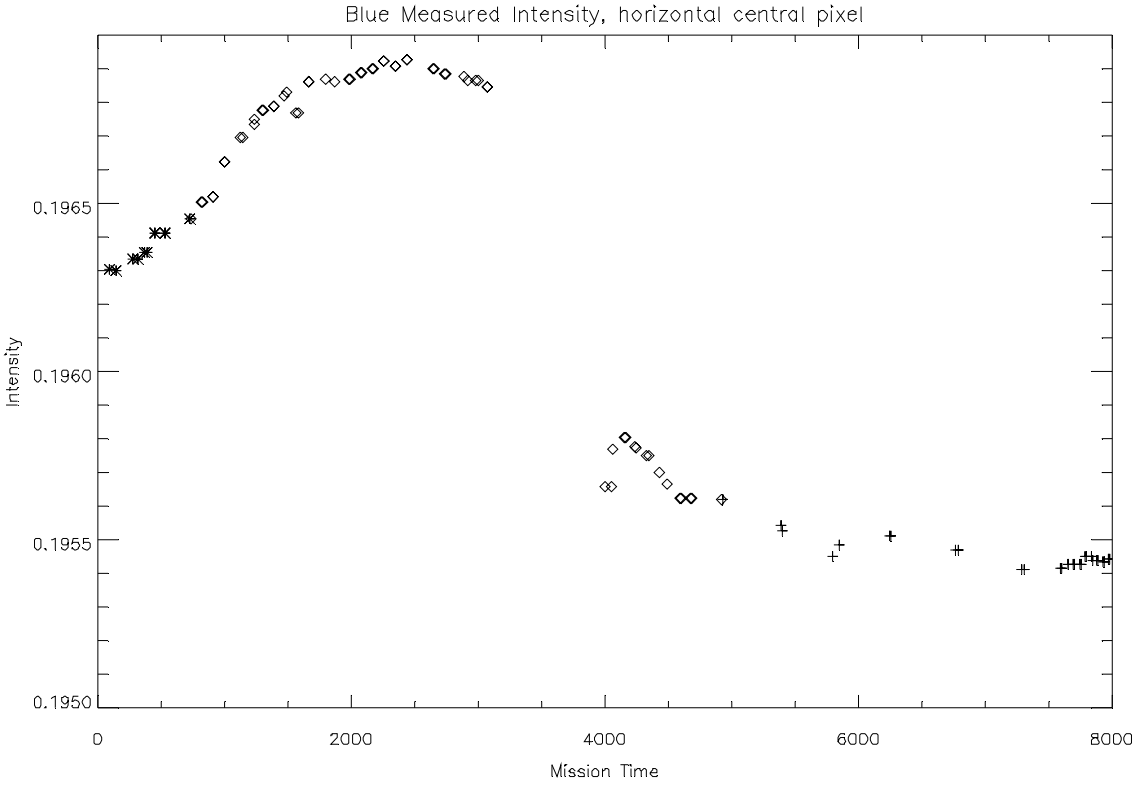
Blue Measured Intensity, horizontal central pixel
Intensity
0.1965
0.1960
0.1955
0.1950
0
2000
4000
6000
8000
Mission Time

In the blue case, it could be argued more convincingly that the variation in model performance is in fact due to the thermal modeling. The first region corresponds to temperatures over about 290K. The highest temperature for the absolute response original data is 289K. Therefore, it is reasonable that the model performance above 290K could diverge from the true response. Fortunately, the flight instrument is not expected to see this high temperature during its remaining lifetime.

While the lower performance region could be due to poor models as well, its correlation with the red channel and the lamp re-stabilization makes it more likely that this third region is due to lamp effects. Therefore, the blue model appears to be working fairly well over its temperature region, within about 2%, 0.4% of which is due to noise (SNR in un-summed data rises to 100 over the descent.).

13.1.3.3 Blue Un-Summed Data

Now that the summed data resulting in total intensity cuts has been analyzed, attention can be turned to the un-summed data, whose model performance is plotted below. Like the total intensity data, every appropriate data set in the descent is represented. For the contour data, only one column is plotted at a time for simplicity. However, the numerical data values in the table at the beginning of this section and duplicated on the plots for column 2 do include every pixel from every data set. Therefore, the minima and maxima are not necessarily included in the plotted lines since they could be from columns other than column 2.

Turning first to the blue, the performance for column 2 is plotted below. Six different plotting points are included, with 10 consecutive data sets in each plot style. The order of the plot styles in the descent is: +, *, diamond, triangle, square, X.

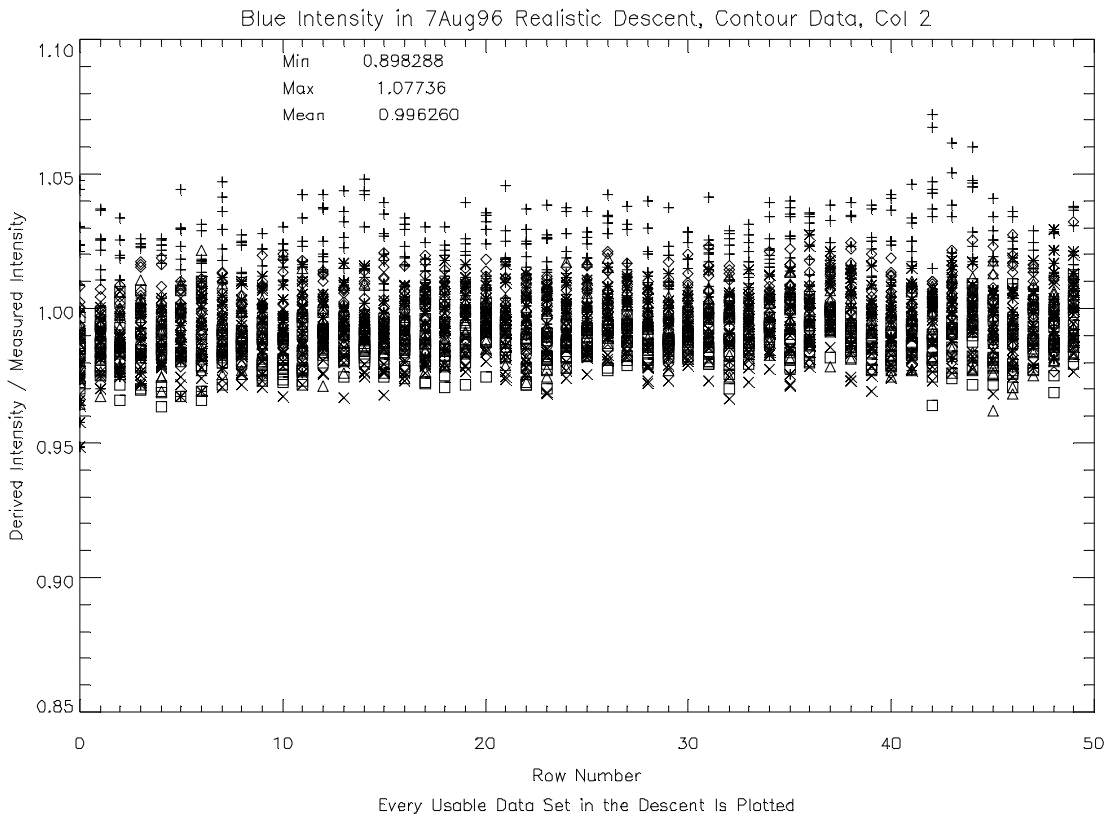

We see that the blue intensity model for this central column is good to roughly 2% over temperature, with 1% of that error due to measurement noise in the original data. The other 5 columns in the blue are plotted below. We see that columns 1 through 4 show the same 2% error, with 1% due to noise. Column 0 has a slightly larger variation, roughly 3%. However, the SNR for this column at row 23 starts at 75 and rises to 90, so its measurement noise will be larger than the 1% seen in the central columns. Column 5 has the most variation of performance, but its SNR starts down around 60, so this makes sense. Column 5 has significant features due to fiber ribbon chips.

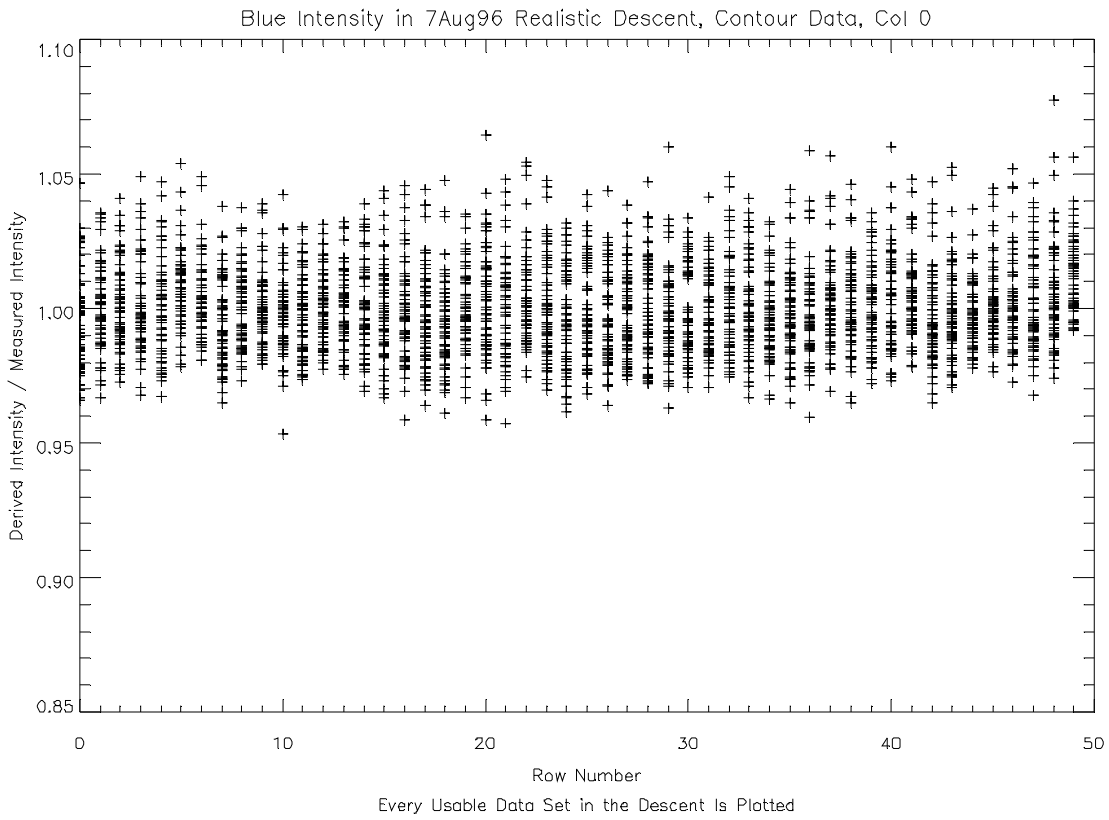
Blue Intensity in 7Aug96 Realistic Descent, Contour Data, Col 0
Derived Intensity / Measured Intensity
1.10
1.05
1.00
0.95
0.90
0.85
0
10
20
30
40
50
Row Number
Every Usable Data Set in the Descent Is Plotted

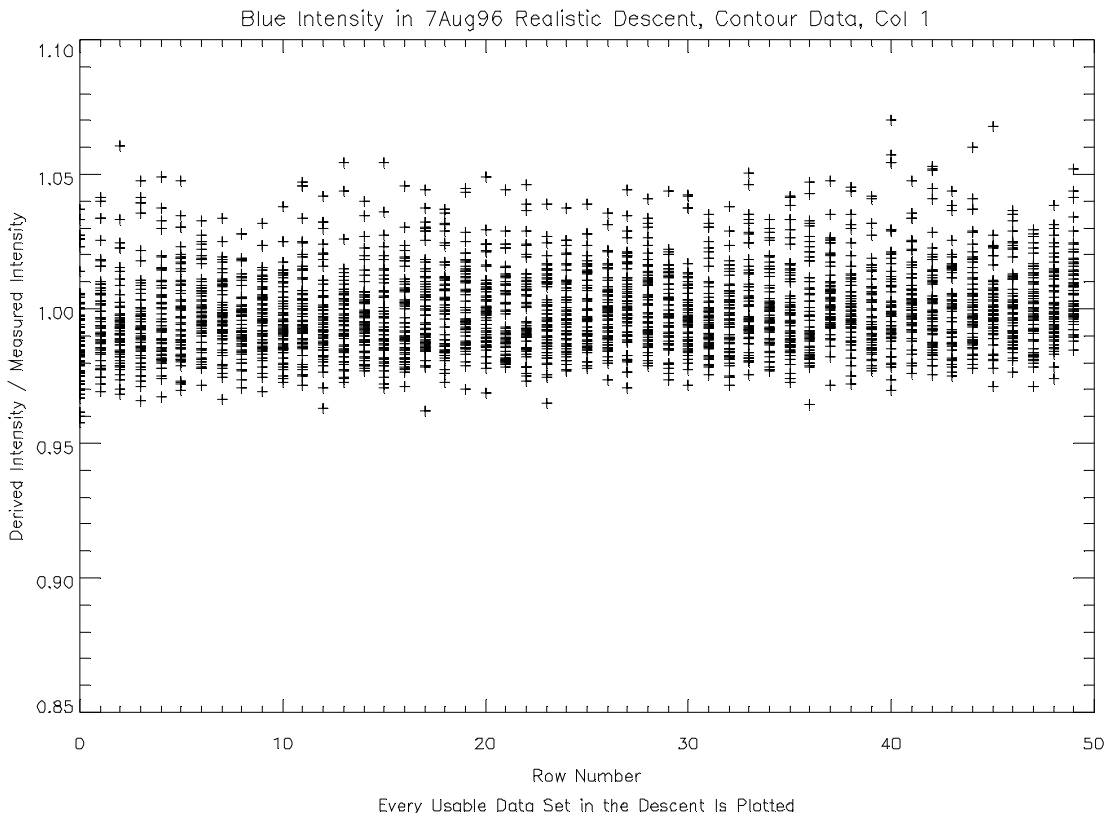
Blue Intensity in 7Aug96 Realistic Descent, Contour Data, Col 1
Derived Intensity / Measured Intensity
1.10
1.05
1.00
0.95
0.90
0.85
0
10
20
30
40
50
Row Number
Every Usable Data Set in the Descent Is Plotted

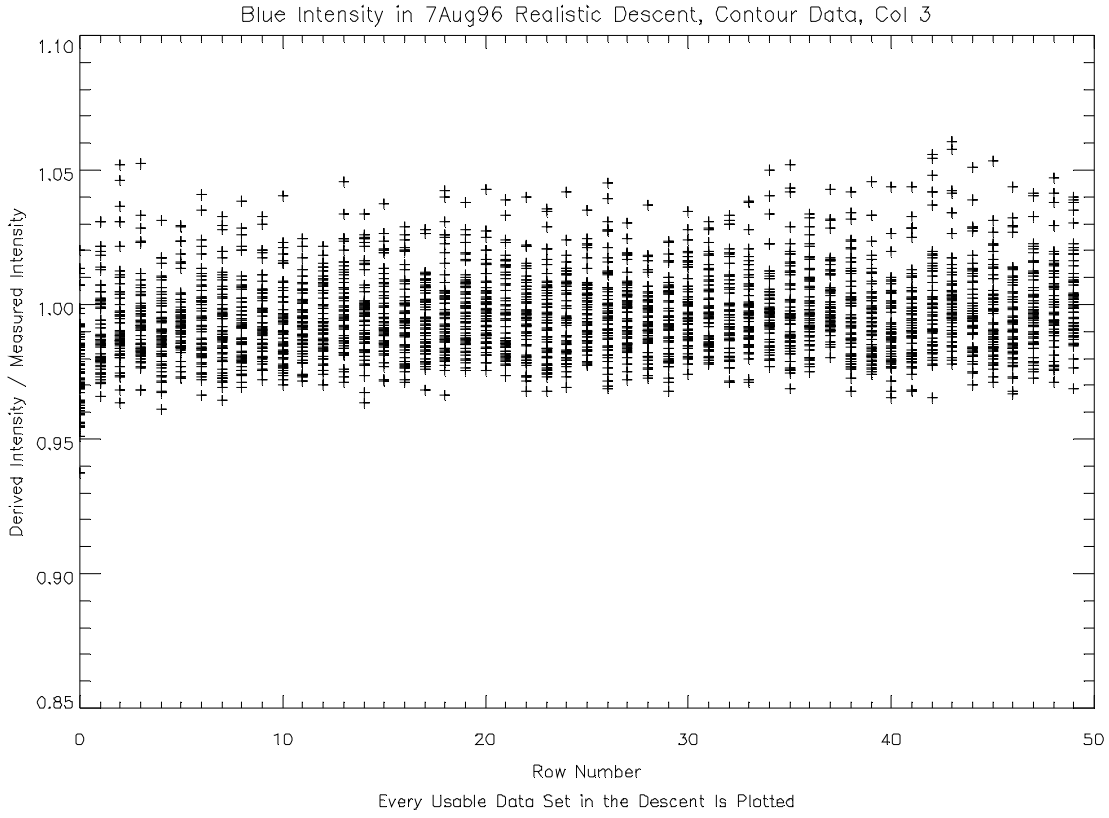
Blue Intensity in 7Aug96 Realistic Descent, Contour Data, Col 3
Derived Intensity / Measured Intensity
1.10
1.05
1.00
0.95
0.90
0.85
0
10
20
30
40
50
Row Number
Every Usable Data Set in the Descent Is Plotted

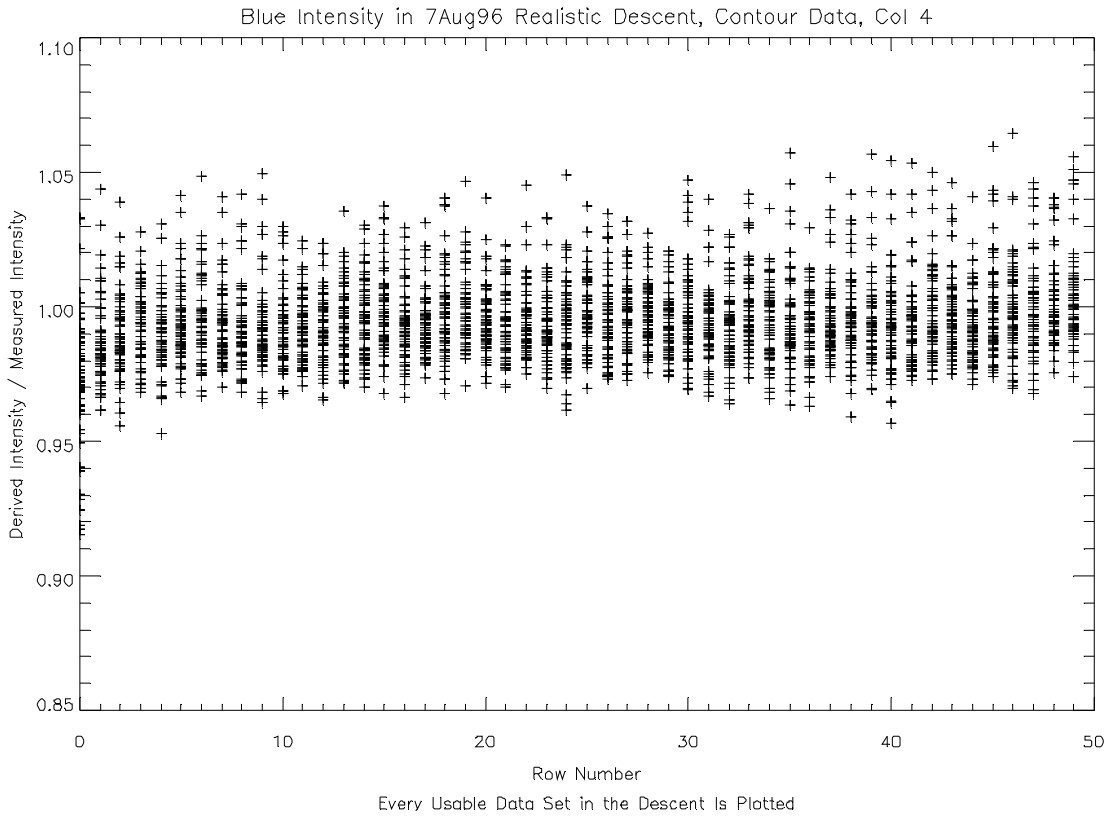

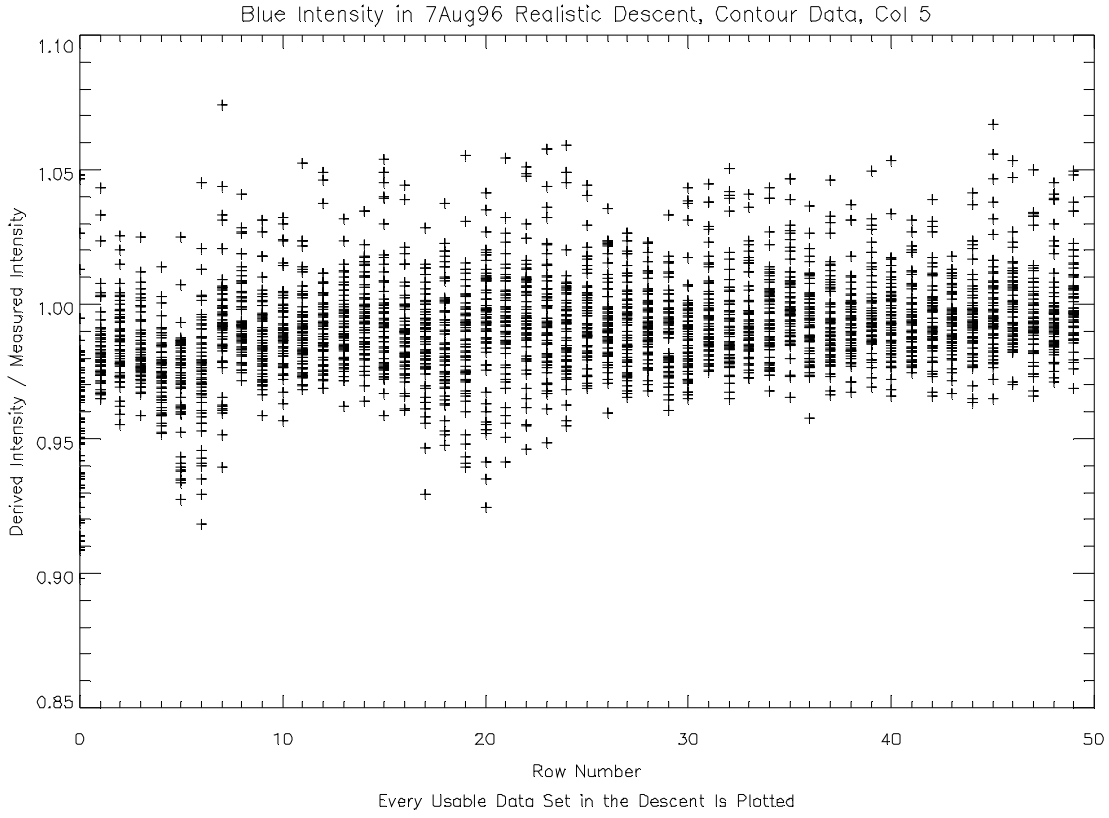

If we average over the rows and plot this mean ratio versus CCD temperature, we get the following result. There appears to be some systematic variation on the order of +/-2%.

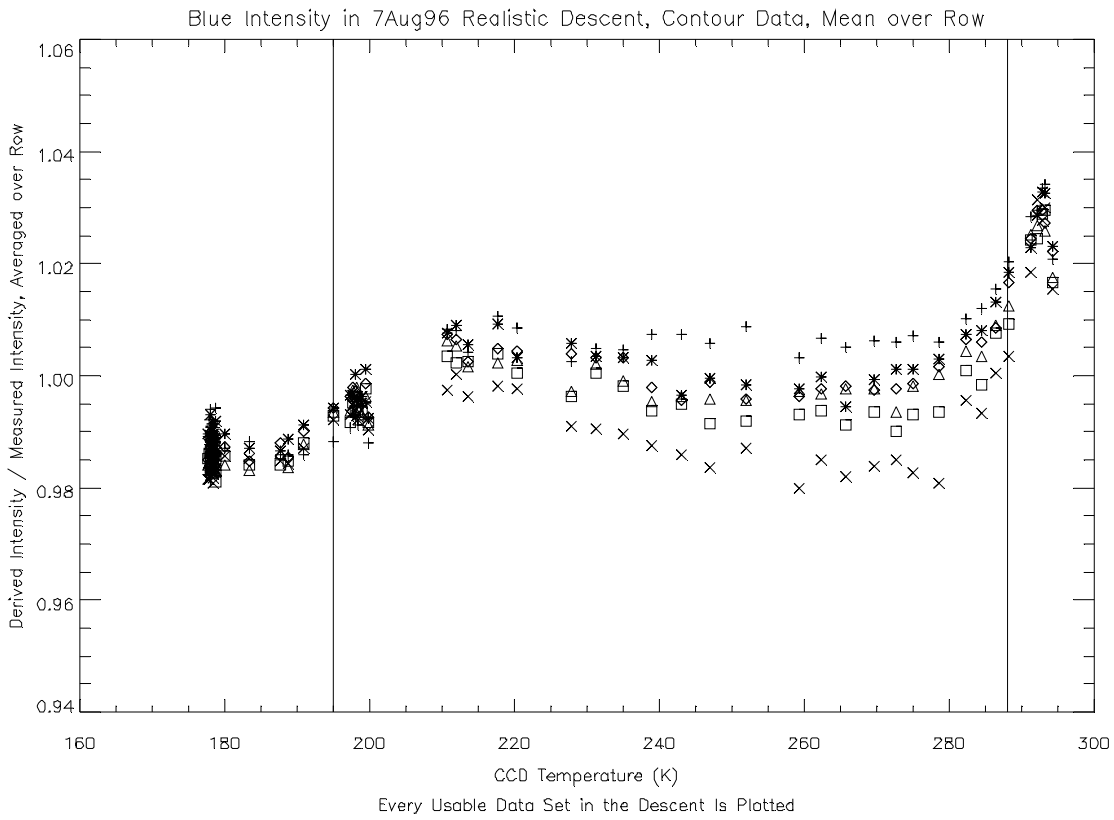

The plot styles are as follows:

Column Number	Plot Symbol
0	+
1	*
2	Diamond
3	Triangle
4	Square
5	X

The two vertical lines delineate the regions of performance noted in the discussion of total intensity results.

13.1.3.4 Red Un-Summed Data

Now attention is turned to the red channel. Column 2 performance is plotted below. Again, six different plotting points are included, with 10 consecutive data sets in each plot style. The order of the plot styles in the descent is: +, *, diamond, triangle, square, X.

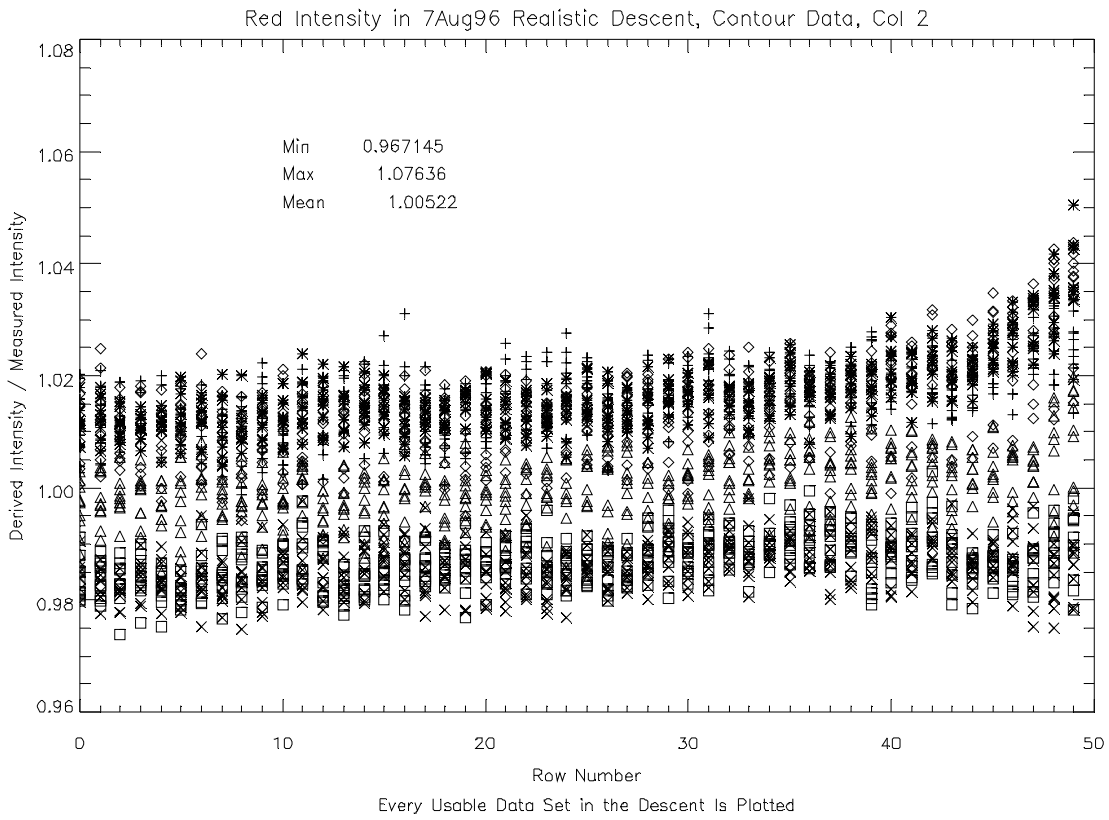

Fewer data sets are appropriate for the contour plotting than for the total intensity plots, but nevertheless, the performance regions are still visible. The same effects due to the lamp and calibration system would logically affect this data as well, and the model performance for the red column 2 is believed to be better than 2% overall.

The other columns are plotted in the next 5 plots. Columns 2 through 5 show roughly the same 2% performance, but columns 0 and 1 have slightly worse performance. Column 0 has lower SNR than the others, starting at about 180 and falling to 130. This can explain some of the poorer performance, but not all.

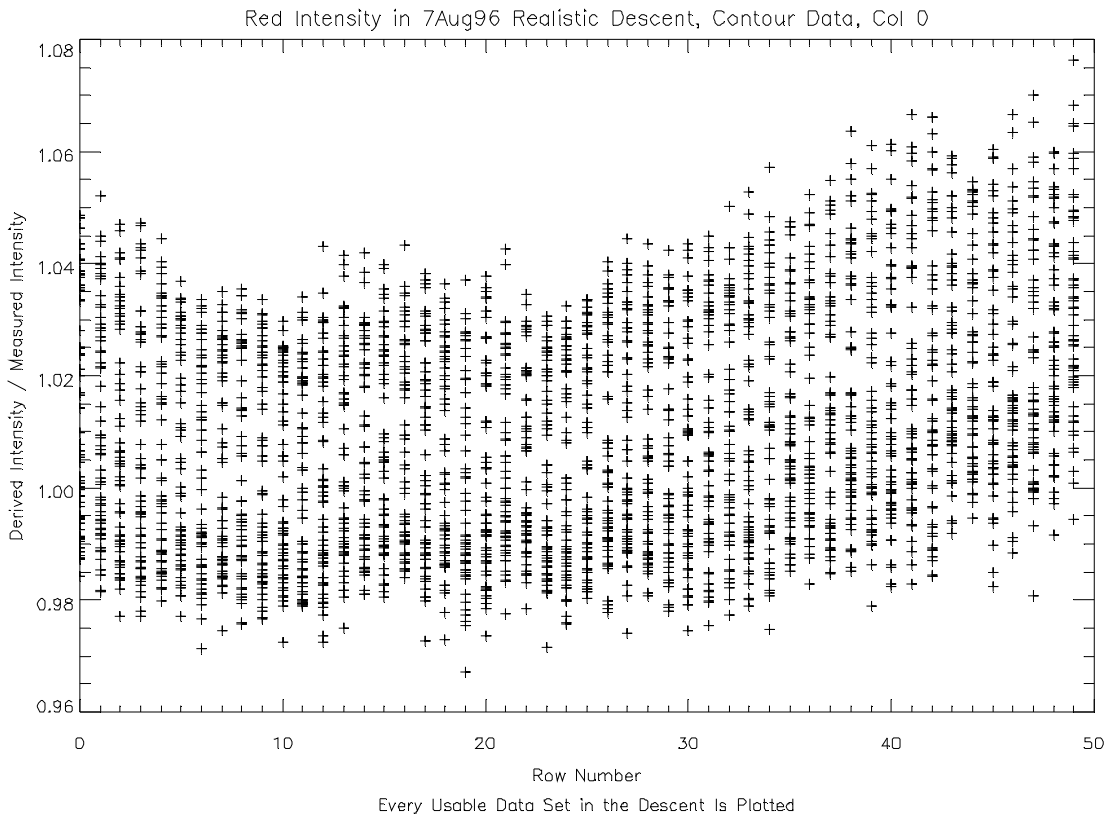
Red Intensity in 7Aug96 Realistic Descent, Contour Data, Col 0
Derived Intensity / Measured Intensity
1.08
1.06
1.04
1.02
1.00
0.98
0.96
0
10
20
30
40
50
Row Number
Every Usable Data Set in the Descent Is Plotted

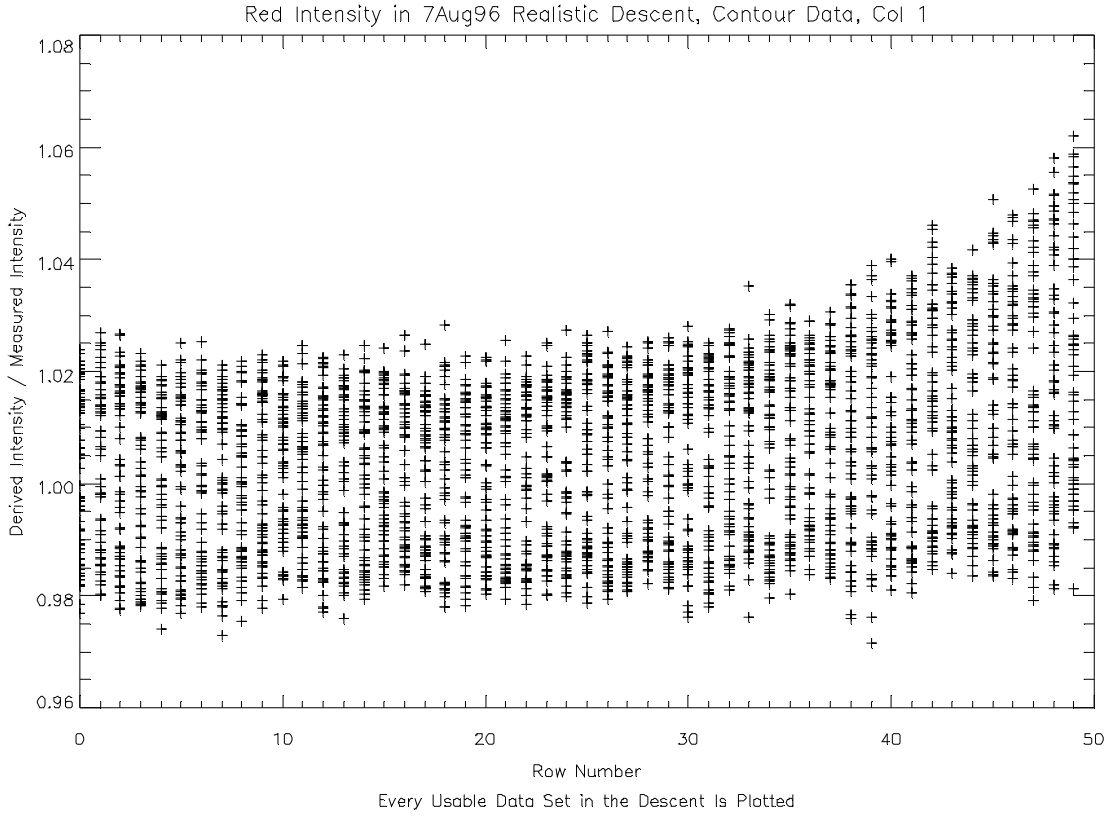
Red Intensity in 7Aug96 Realistic Descent, Contour Data, Col 1
Derived Intensity / Measured Intensity
1.08
1.06
1.04
1.02
1.00
0.98
0.96
0
10
20
30
40
50
Row Number
Every Usable Data Set in the Descent Is Plotted

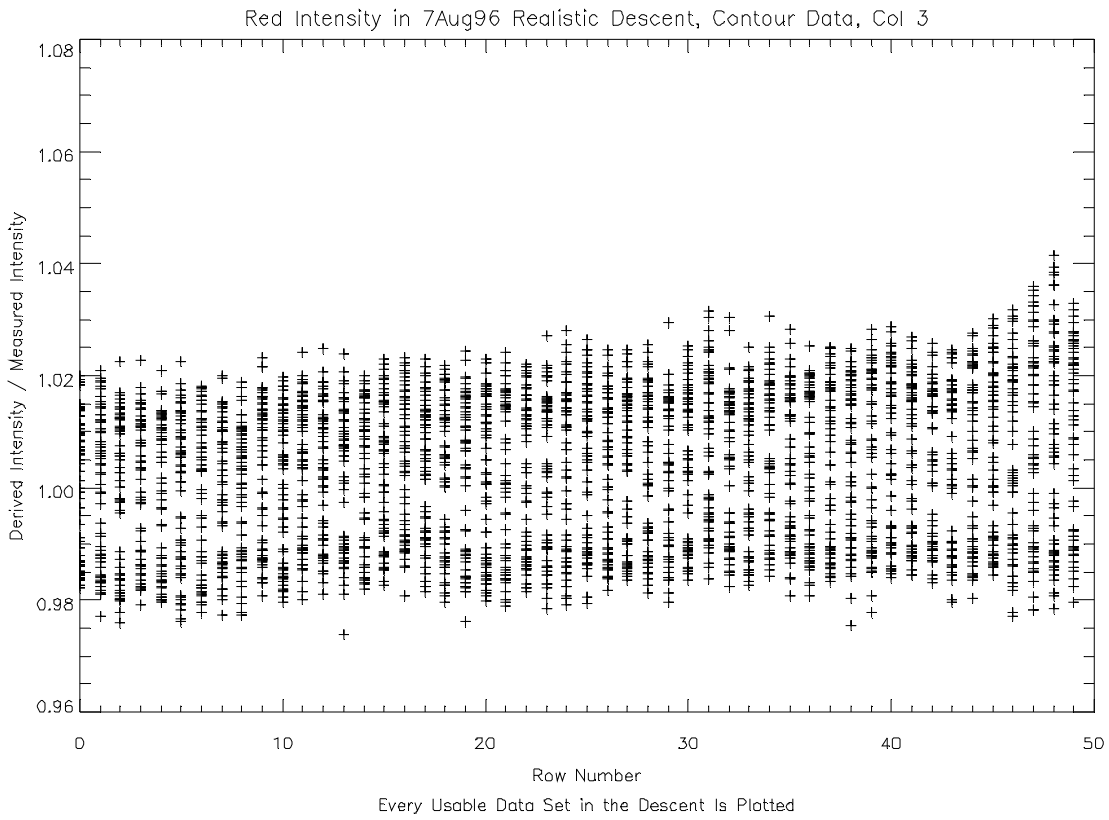
Red Intensity in 7Aug96 Realistic Descent, Contour Data, Col 3
Derived Intensity / Measured Intensity
1.08
1.06
1.04
1.02
1.00
0.98
0.96
0
10
20
30
40
50
Row Number
Every Usable Data Set in the Descent Is Plotted

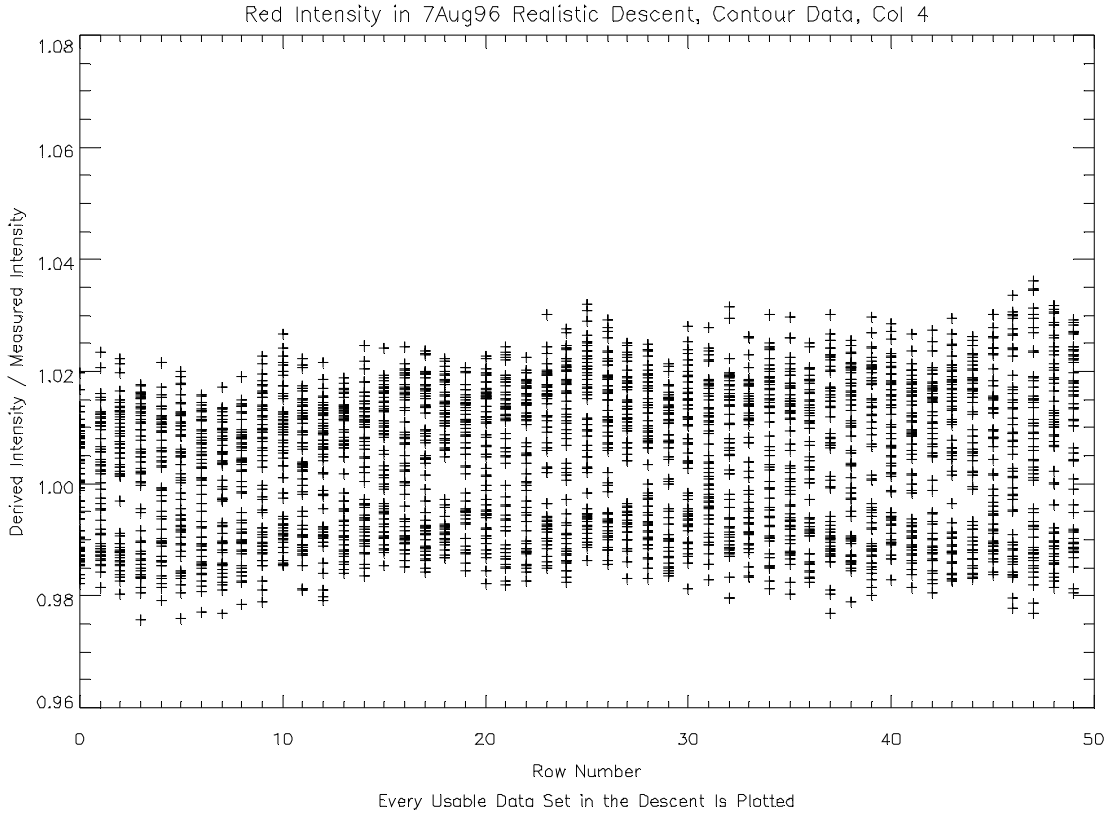
Red Intensity in 7Aug96 Realistic Descent, Contour Data, Col 4
Derived Intensity / Measured Intensity
1.08
1.06
1.04
1.02
1.00
0.98
0.96
0
10
20
30
40
50
Row Number
Every Usable Data Set in the Descent Is Plotted

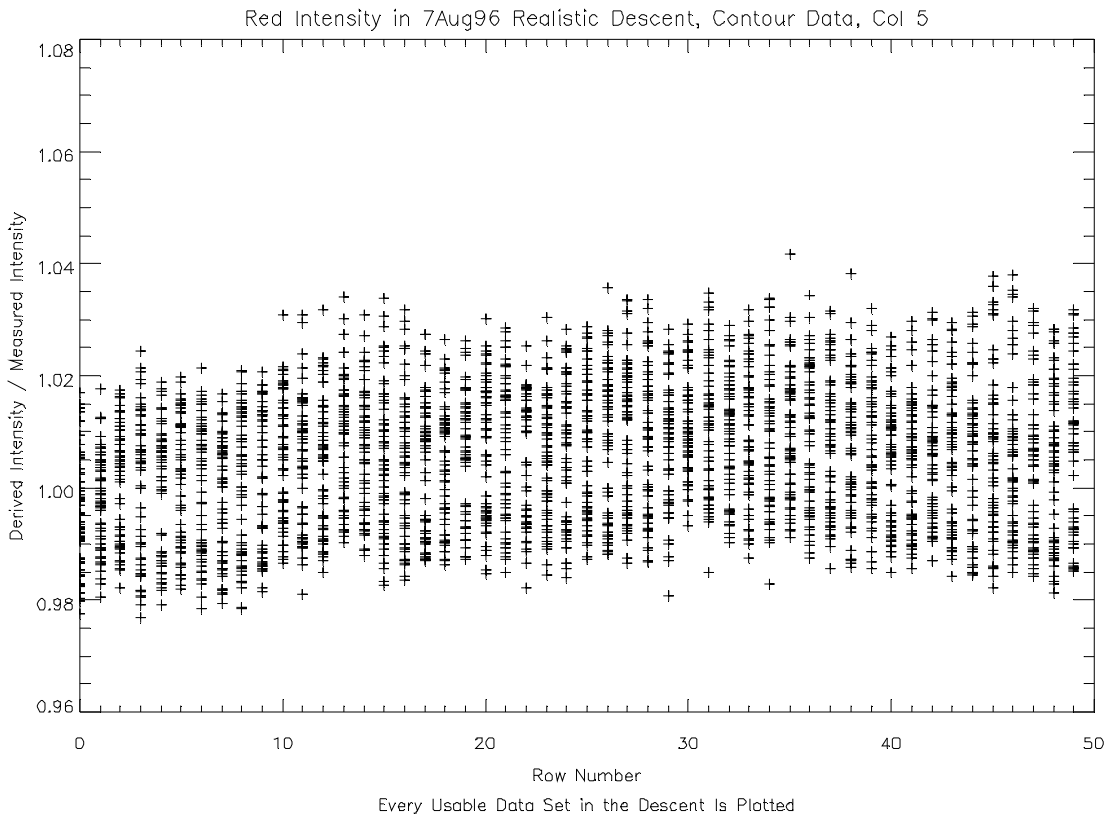

Again, averaging the ratios over the rows, we see the following. The vertical lines delineate the performance regions, and the column symbols are like those used in the similar blue plot. Recall that the lamp failed when the CCD was roughly 210K. There appears to be some systematic variation on the order of +/-2% for most columns, with a larger deviation for column 0.

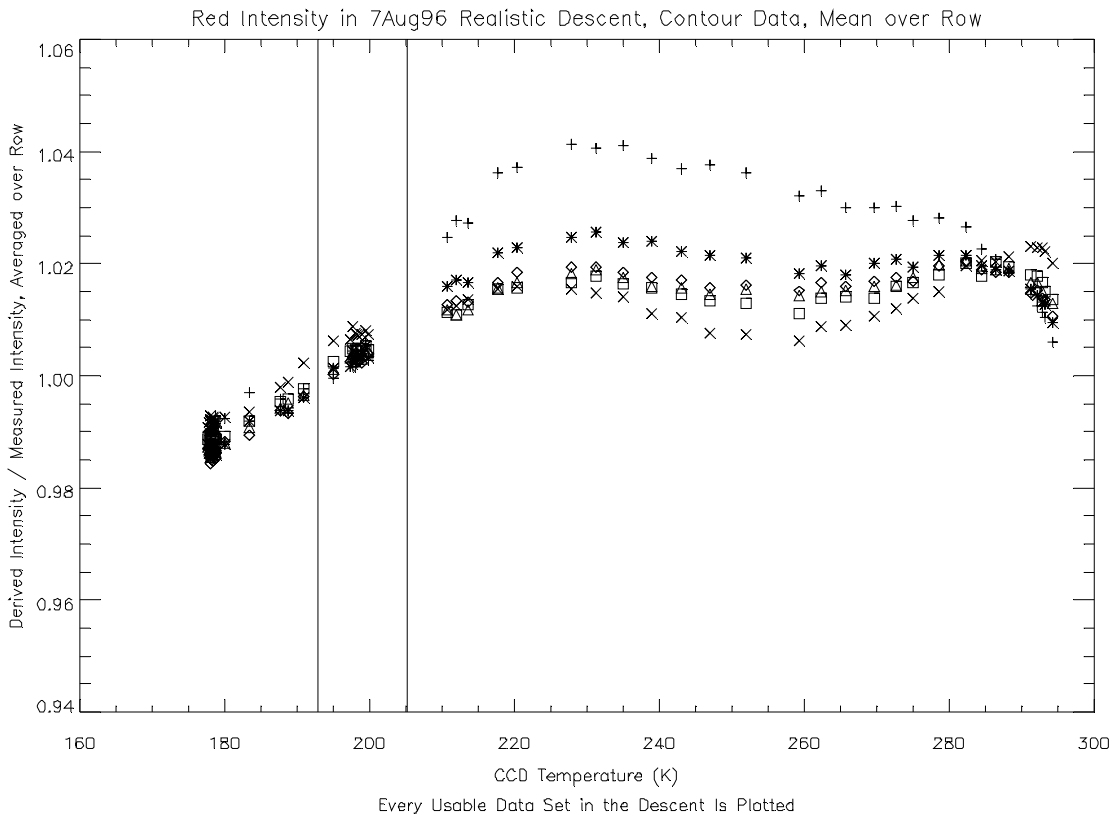

There is a slight upward slope in most red plots of performance. This could be due to model errors in the zenith direction, to variations in the relative brightness in the integrating sphere in the zenith direction, or to errors in the pixel registration code in descent_analysis. These errors are slight, but worth noting. If the error is in the pixel registration, the test cases using the constant and the "ramp zenith" input intensities will indicate the errors, which will then be corrected.

13.1.3.5 Conclusion – Absolute Calibration

The test results of the DISR undergoing a thermally accurate simulated descent while placed in the calibrated integrating sphere indicate response models accurate to 2% in both the red and blue channels for un-summed data in almost all pixels.

Column 0 in the red results in poorer performance than the other cases. Both the horizontal and vertical red channels have dark regions in column 0 due to fiber ribbon misalignments. The absolute response model for the red horizontal channel column 0 is worse than all other models. Consideration could be made to exclude it from the summed data returned in DISR telemetry. Care should also be taken in using this extreme column toward the sun in the contour analyses.

A slight variation in red performance with zenith angle will be monitored.

13.1.4 Results – Relative Calibration across Columns

Another interesting figure of merit is the relative calibration from pixel to pixel in a Solar Aureole channel. One would hope that although the absolute calibration may be off by several percent, the relative response of the pixels within a single data set would be closer.

13.1.4.1 Blue Summed Data

Summed data implies the relative calibration will be along the column direction only. Consider the following 5 plots of the blue relative calibration. These plots are taken throughout the descent. There are roughly 100 data sets, and every 20th data set is plotted below.

Each plot consists of the following.

Plot Symbol	Definition
+	Solar Aureole predicted calibrated intensity
*	Measured sphere calibrated intensity
lines	SNR 1-sigma band around the SA data
diamond	Measured sphere calibrated intensity normalized to the mean of the SA data

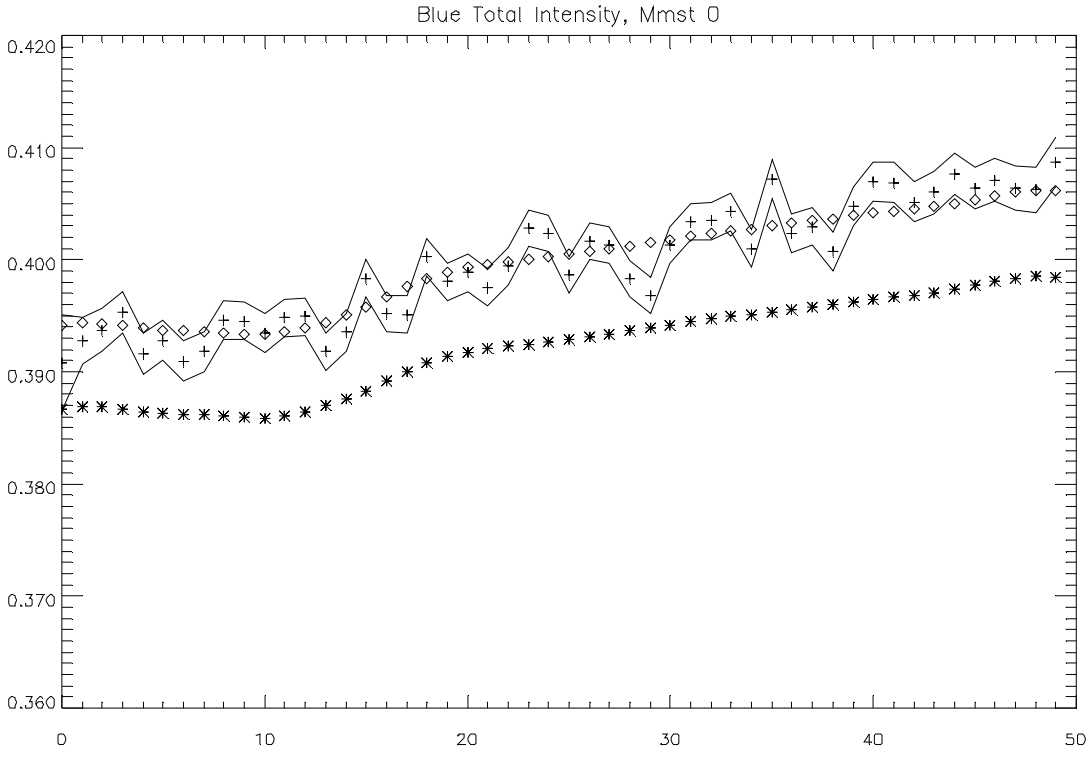

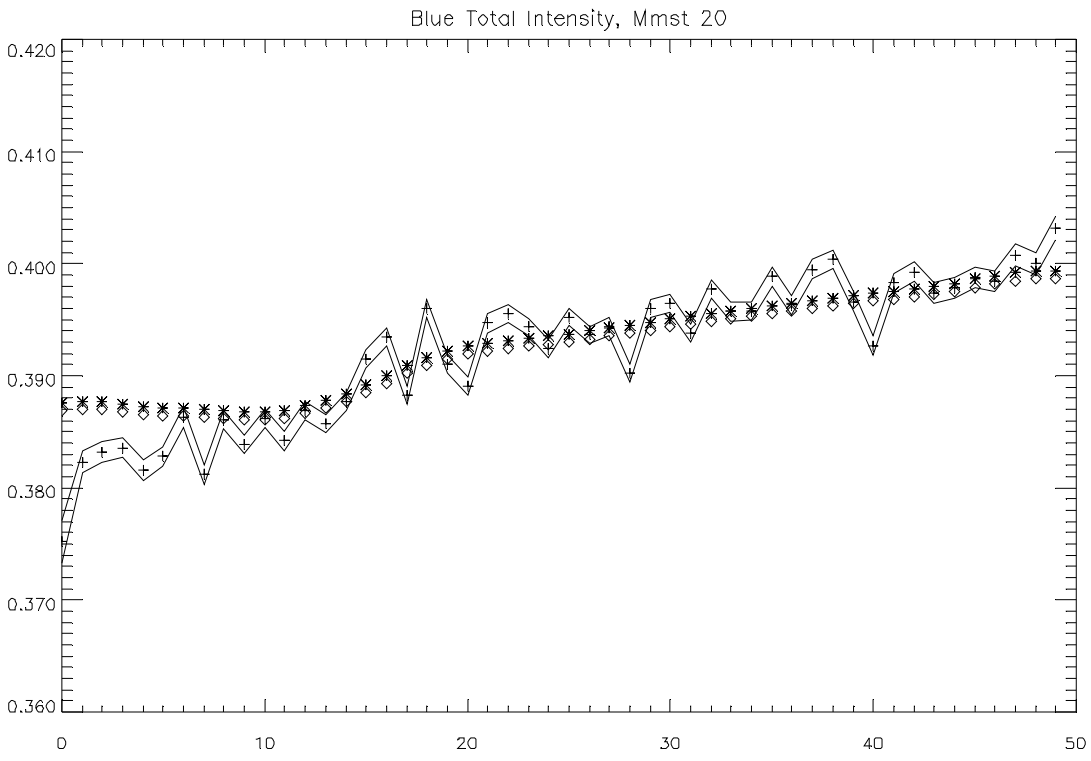
Blue Total Intensity, Mmst 20
0.420
0.410
0.400
0.390
0.380
0.370
0.360
0
10
20
30
40
50

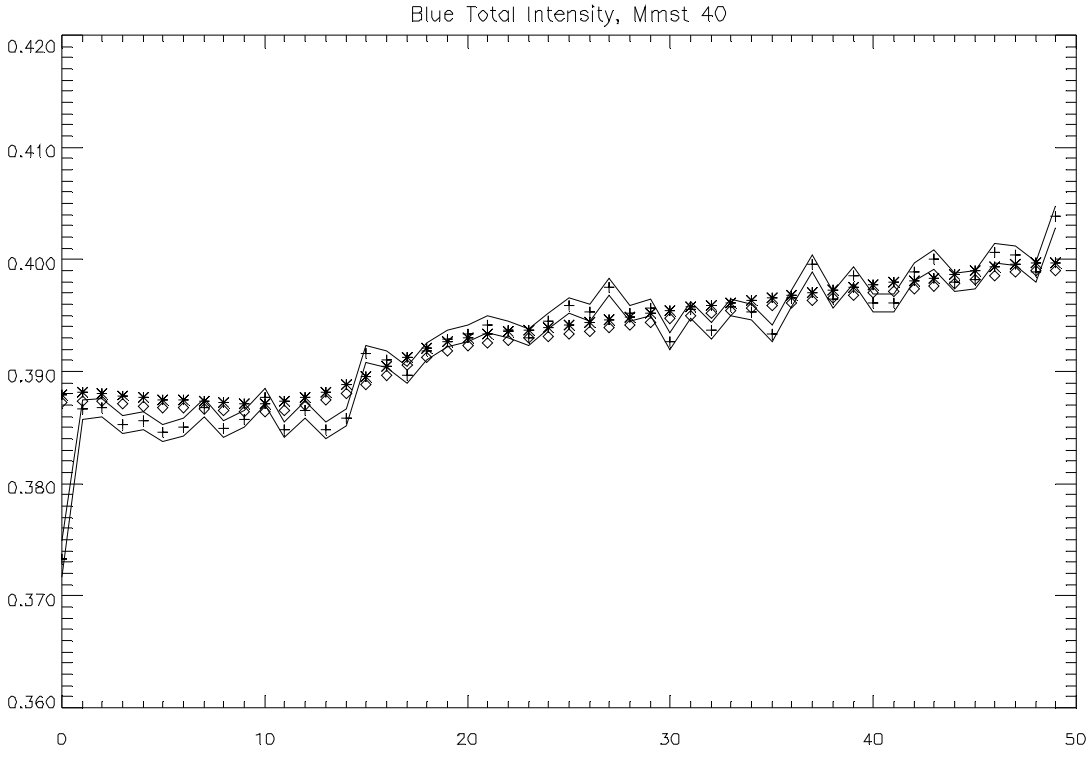
Blue Total Intensity, Mmst 40
0.420
0.410
0.400
0.390
0.380
0.370
0.360
0
10
20
30
40
50

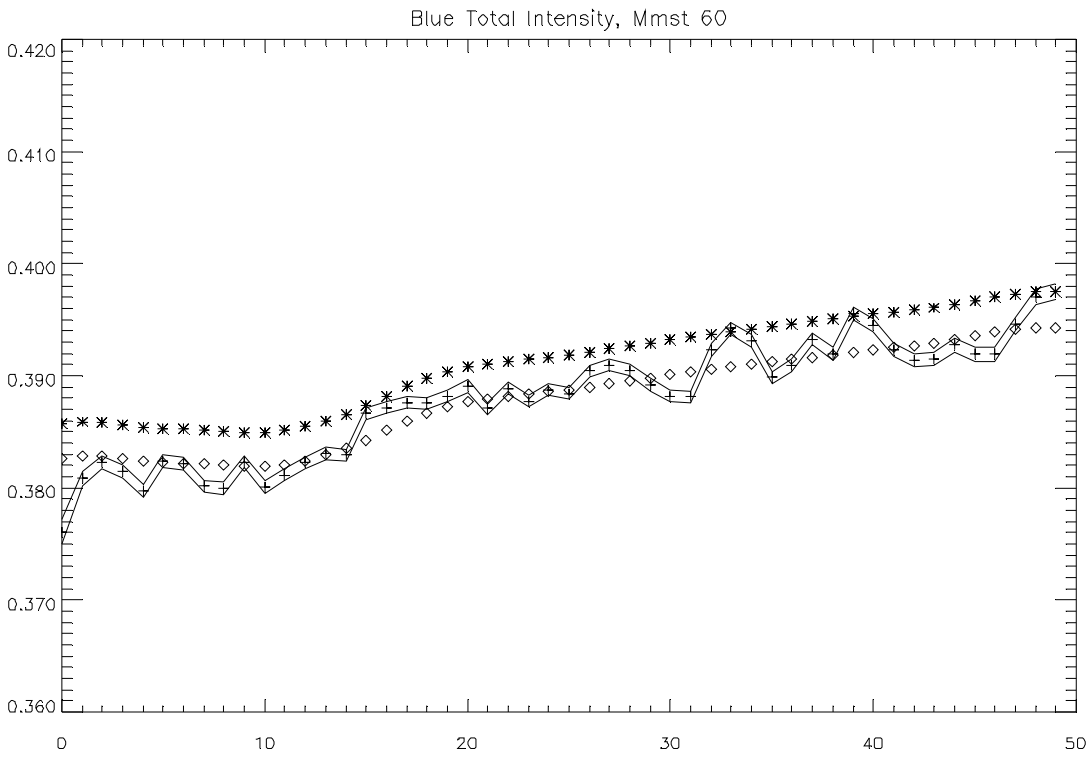
Blue Total Intensity, Mmst 60
0.420
0.410
0.400
0.390
0.380
0.370
0.360
0
10
20
30
40
50

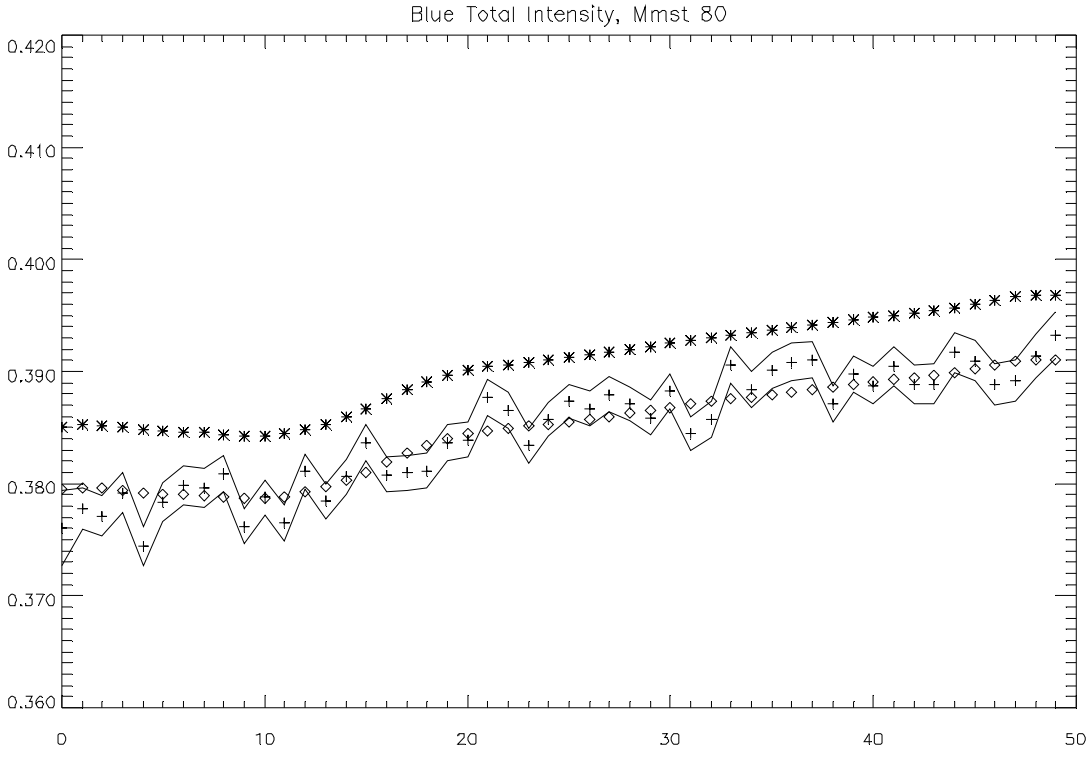
Blue Total Intensity, Mmst 80
0.420
0.410
0.400
0.390
0.380
0.370
0.360
0
10
20
30
40
50

We can see that in most cases, the relative calibration is within about 1%, and there are no systematic variations over column number.

13.1.4.2 Red Summed Data

Turning now to similar plots in the red, we see the same results, relative calibration within 1%, though there does seem to be a slight systematic trend toward lower measured values for lower row numbers, and higher measured values for higher row numbers.

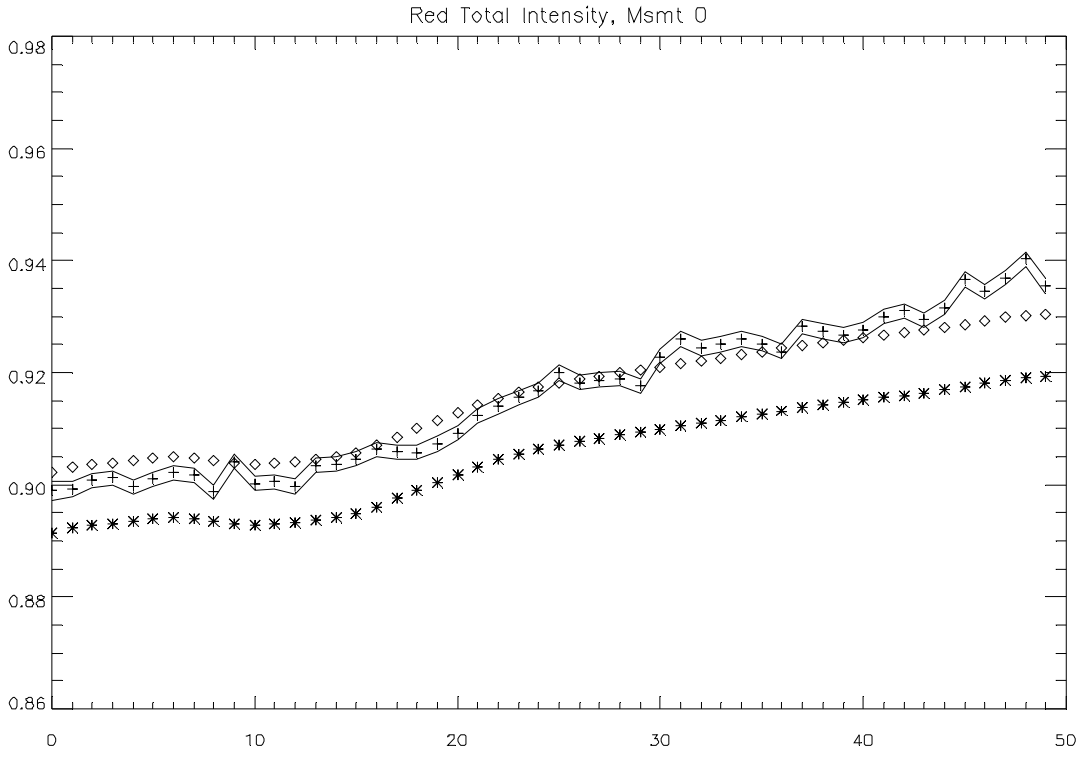

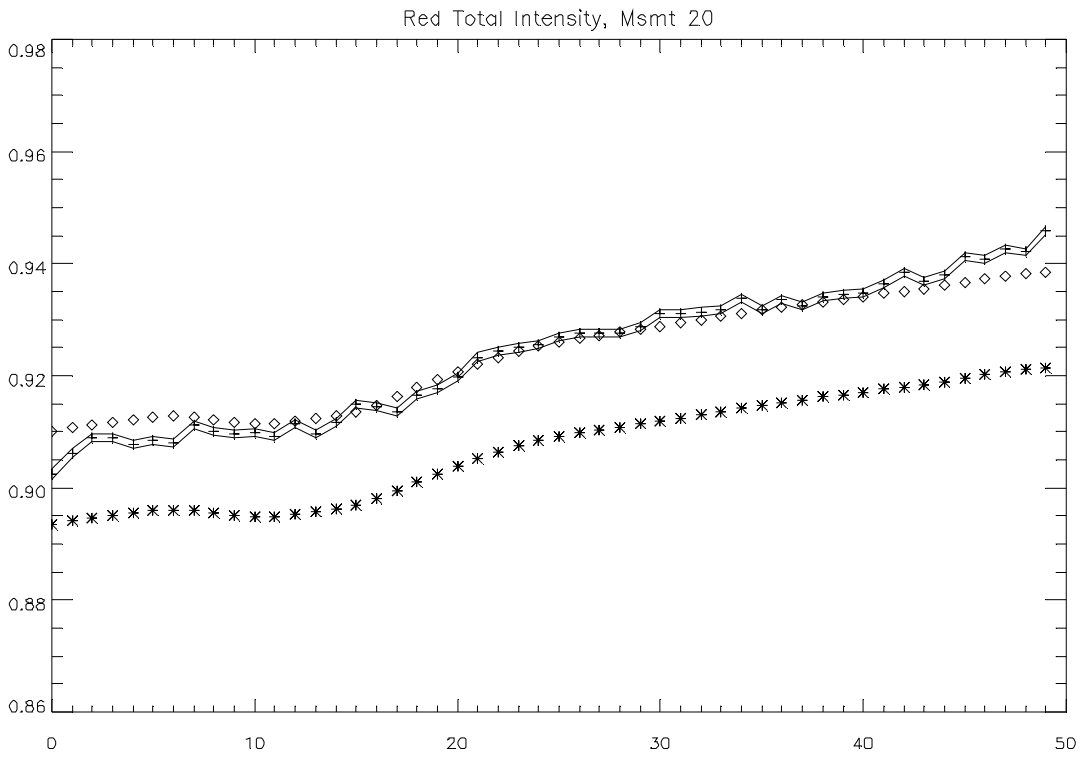
Red Total Intensity, Msmt 20
0.98
0.96
0.94
0.92
0.90
0.88
0.86
0
10
20
30
40
50

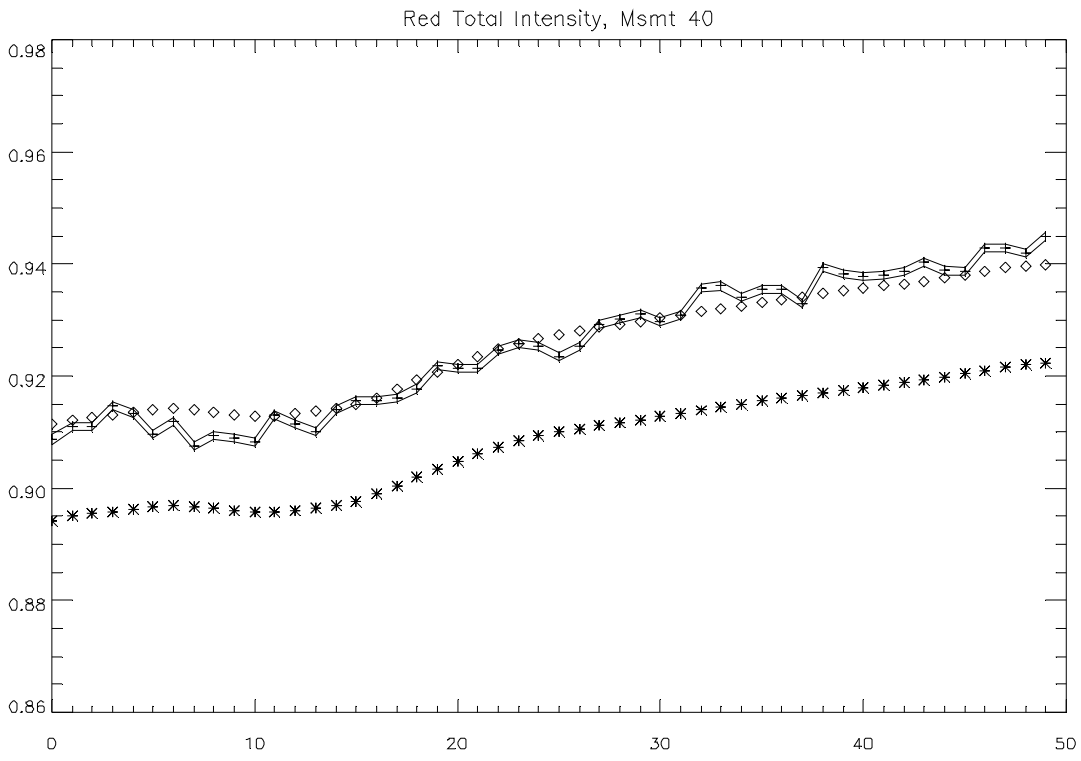
Red Total Intensity, Msmt 40
0.98
0.96
0.94
0.92
0.90
0.88
0.86
0
10
20
30
40
50

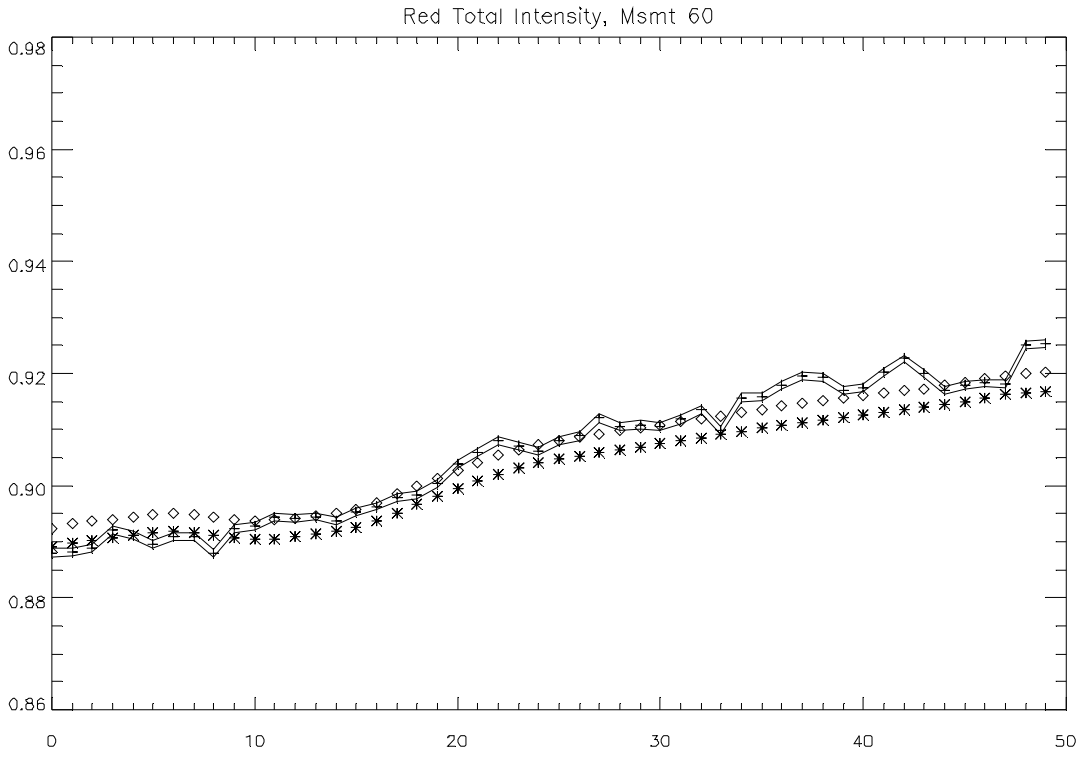
Red Total Intensity, Msmt 60
0.98
0.96
0.94
0.92
0.90
0.88
0.86
0
10
20
30
40
50

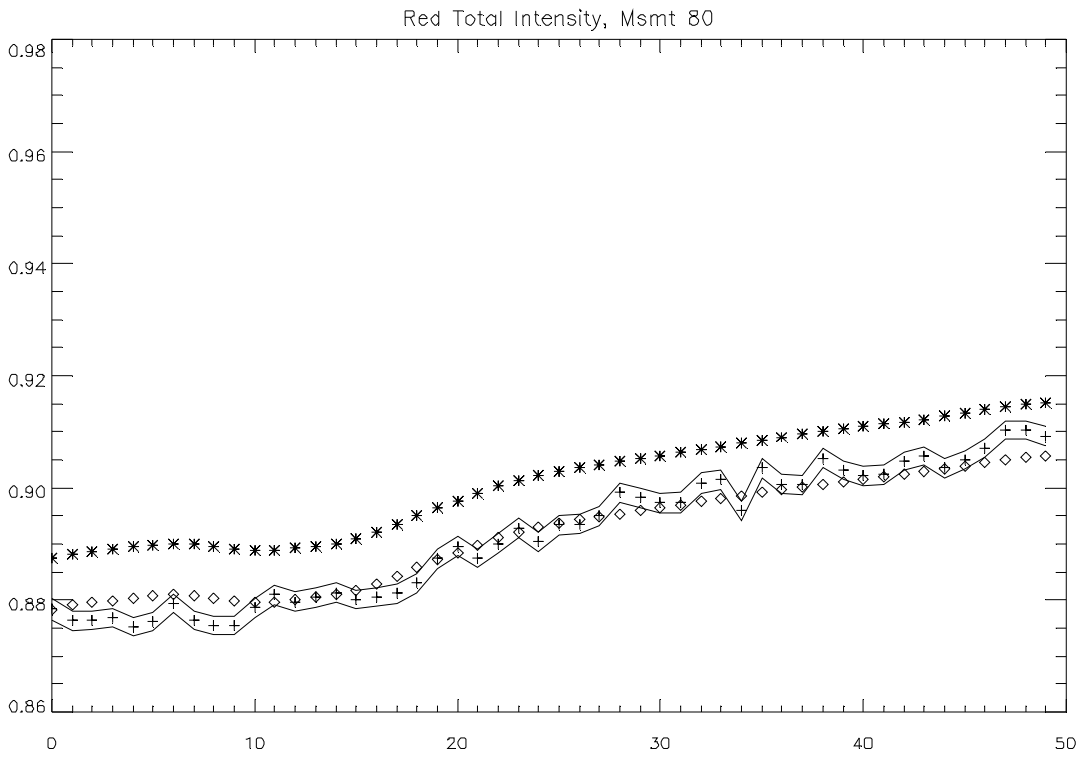

13.1.4.3 Blue Un-Summed Data

Now we turn to the un-summed data. First, consider the relative response along the column direction for column 2 for the blue channel. The plotting styles are the same as in the previous sections. There are roughly 60 contour data sets in the descent. A plot of every 10th one follows:

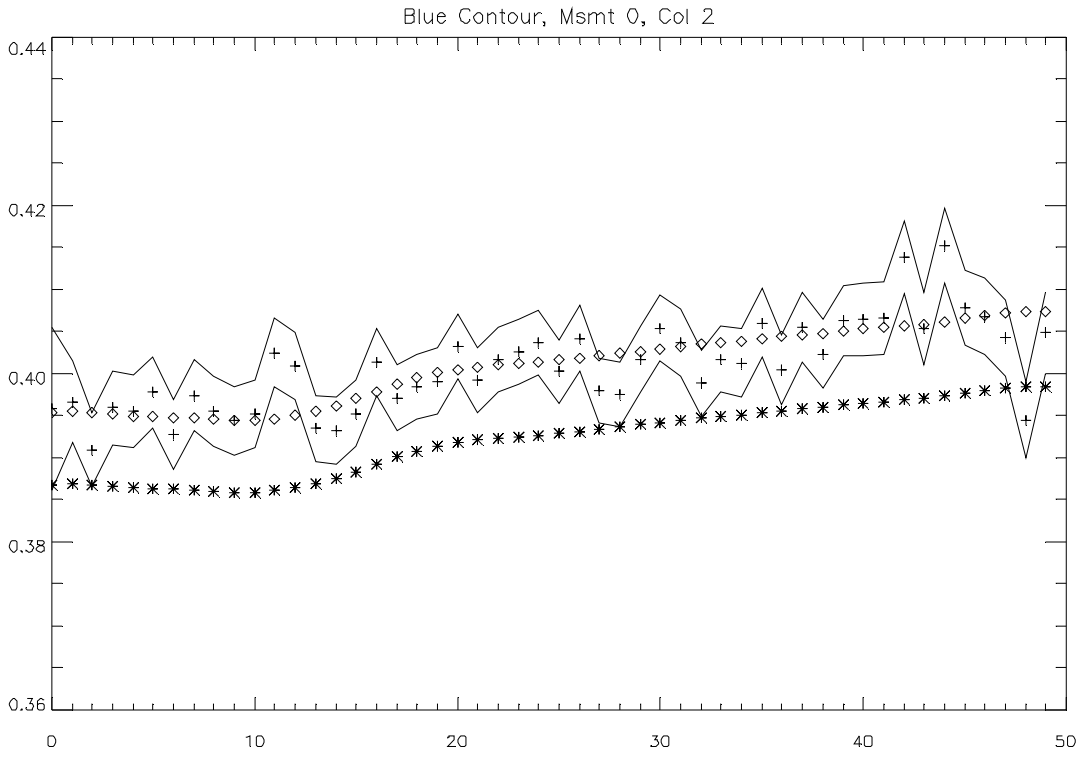
Blue Contour, Msmt 0, Col 2
0.44
0.42
0.40
0.38
0.36
0
10
20
30
40
50

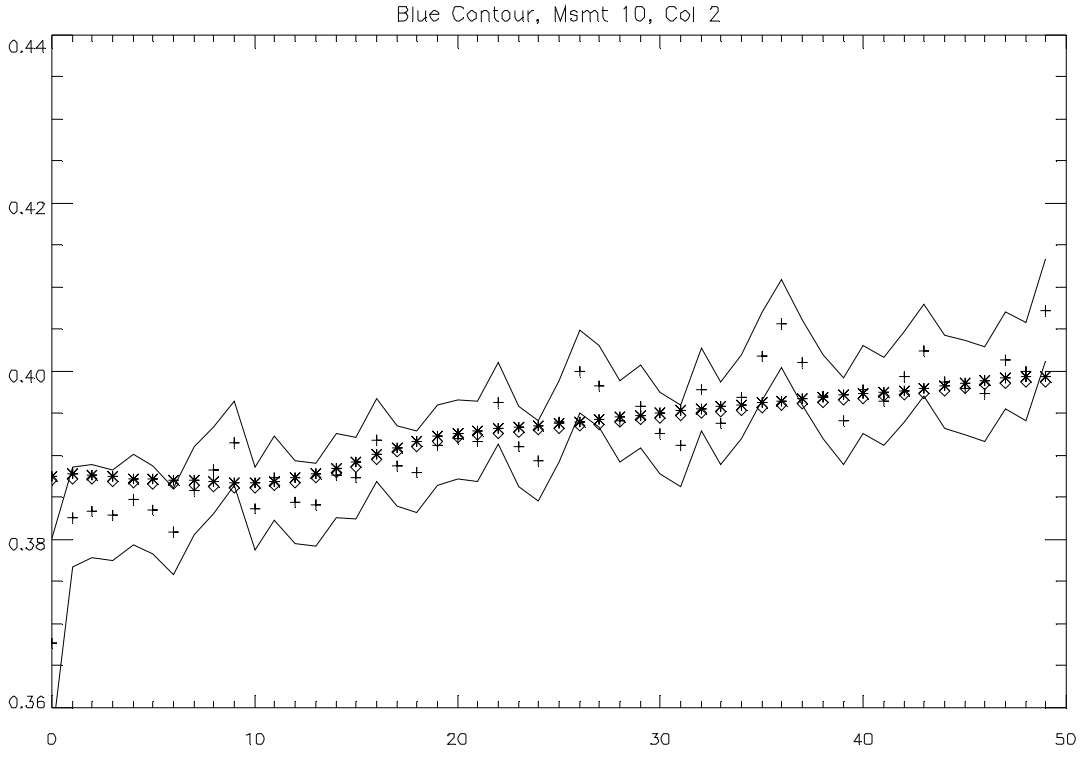
Blue Contour, Msmt 10, Col 2
0.44
0.42
0.40
0.38
0.36
0
10
20
30
40
50

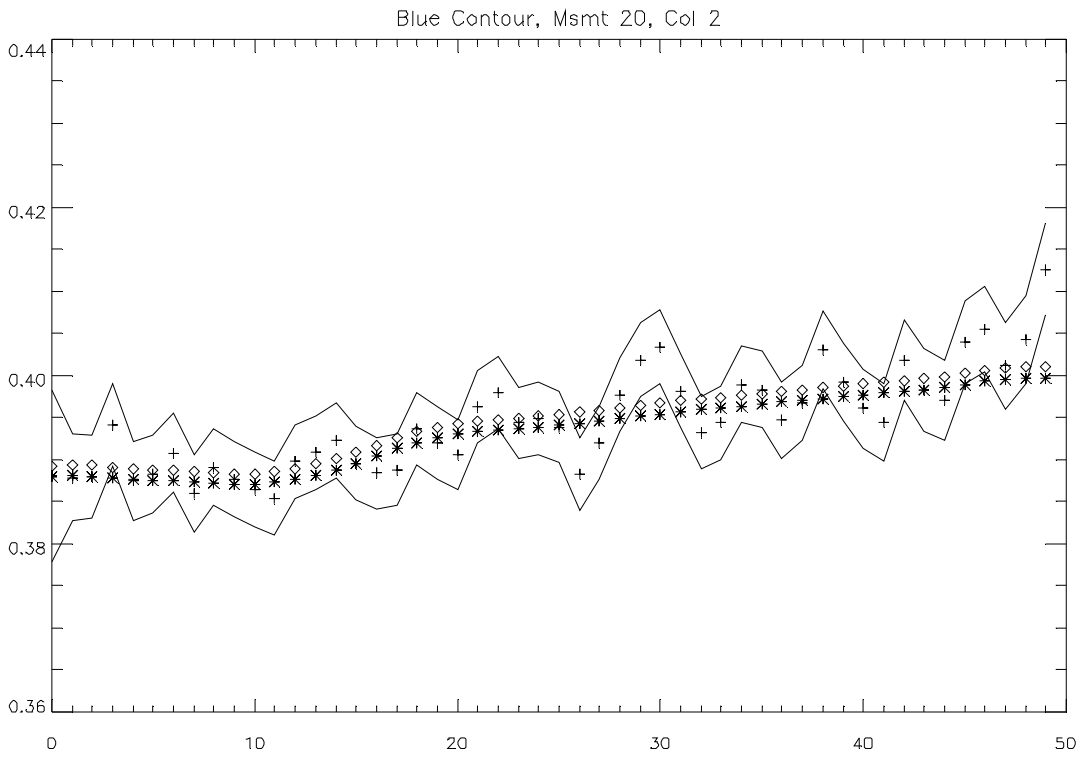
Blue Contour, Msmt 20, Col 2
0.44
0.42
0.40
0.38
0.36
0
10
20
30
40
50

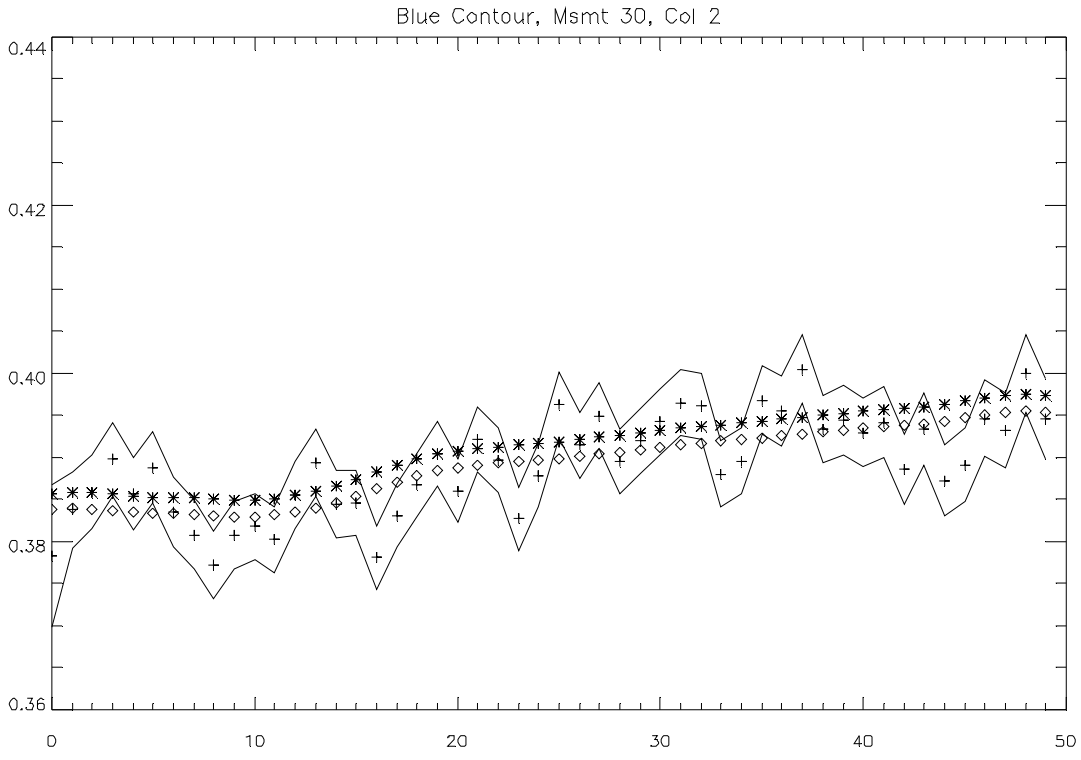
Blue Contour, Msmt 30, Col 2
0.44
0.42
0.40
0.38
0.36
0
10
20
30
40
50

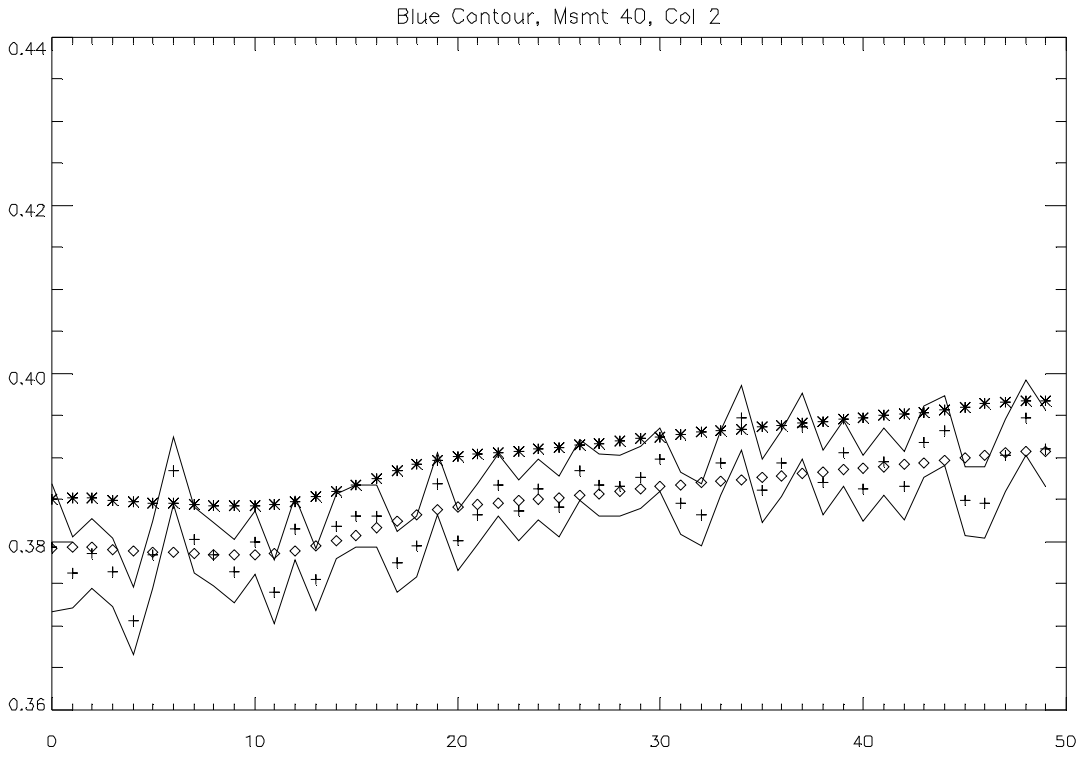
Blue Contour, Msmt 40, Col 2
0.44
0.42
0.40
0.38
0.36
0
10
20
30
40
50

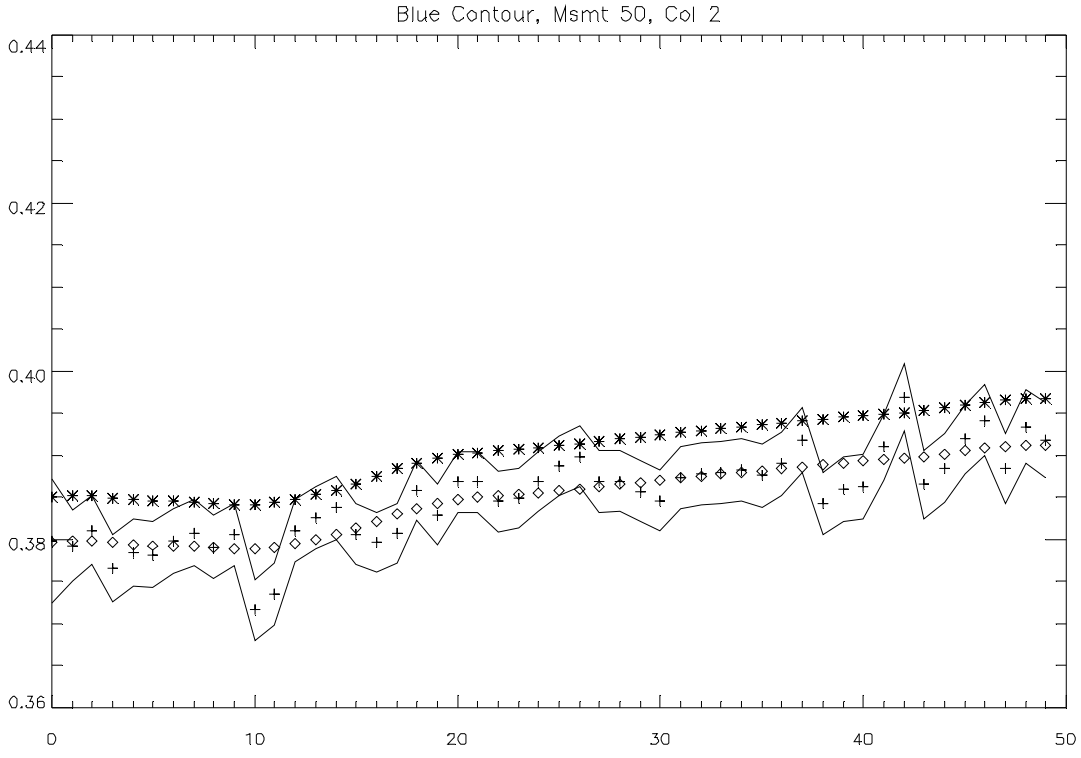
Blue Contour, Msmt 50, Col 2
0.44
0.42
0.40
0.38
0.36
0
10
20
30
40
50

We see that in the blue channel, the normalized response falls almost entirely in the noise band of the SA measurement. This implies a good relative calibration of the blue channel in column 2.

13.1.4.4 Red Un-Summed Data

Turning to the red, we see the following plots along column 2.

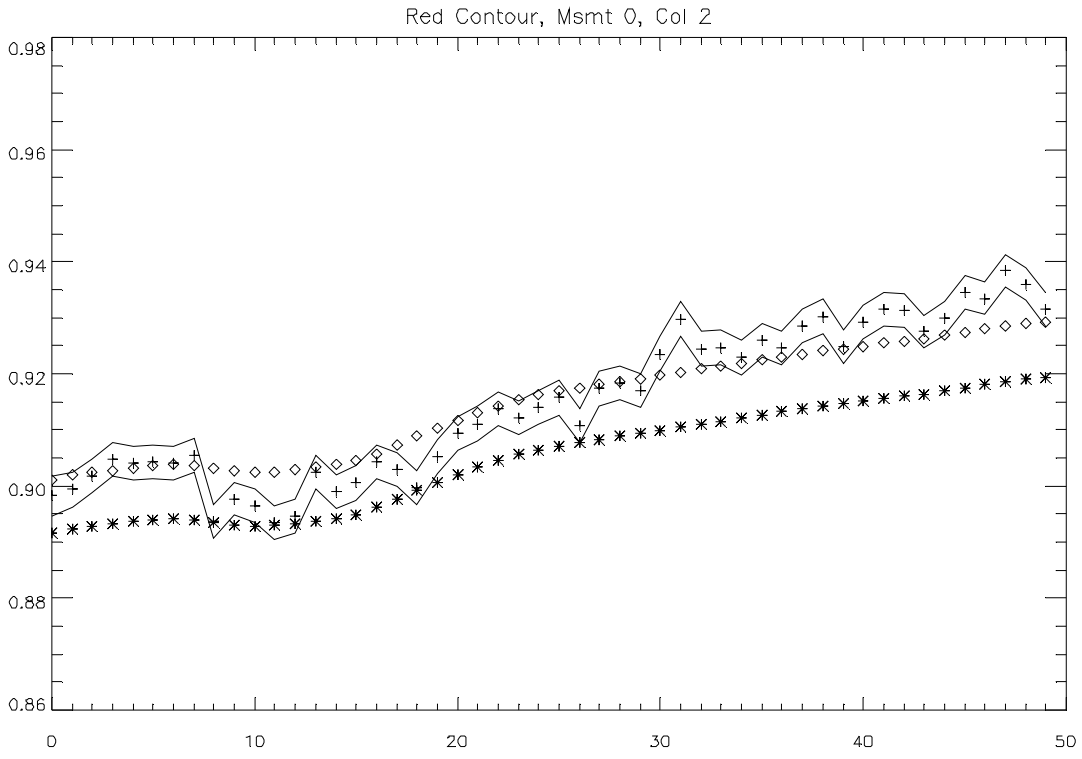

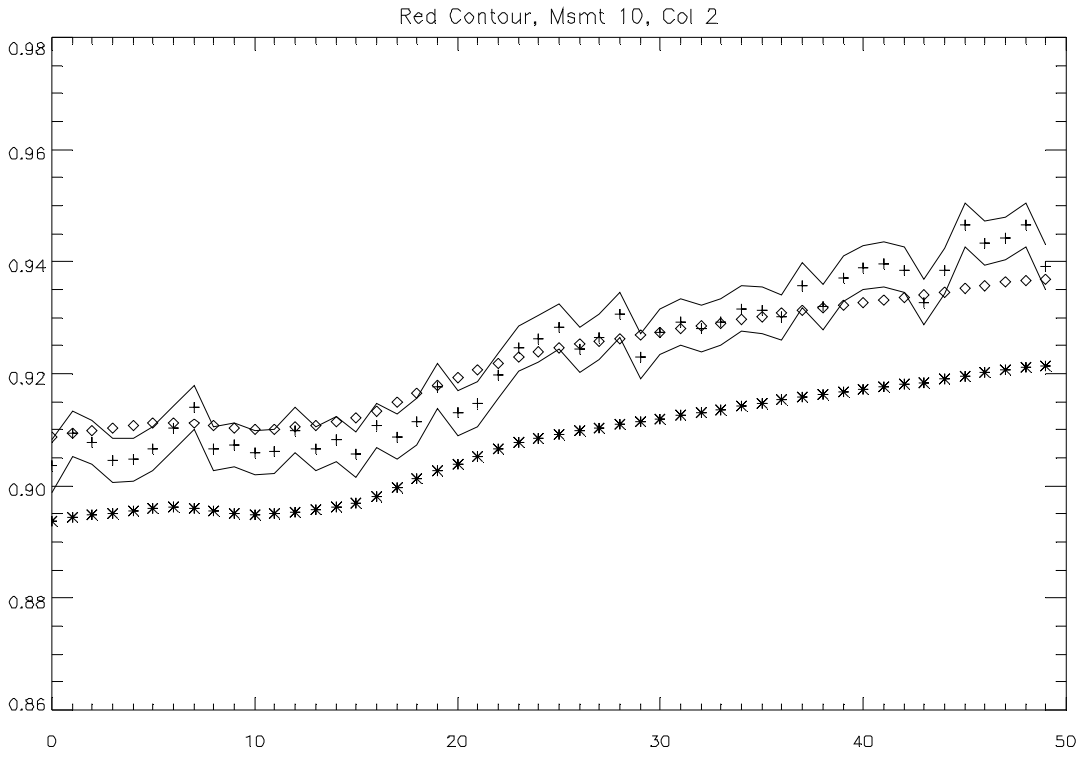
Red Contour, Msmt 10, Col 2
0.98
0.96
0.94
0.92
0.90
0.88
0.86
0
10
20
30
40
50

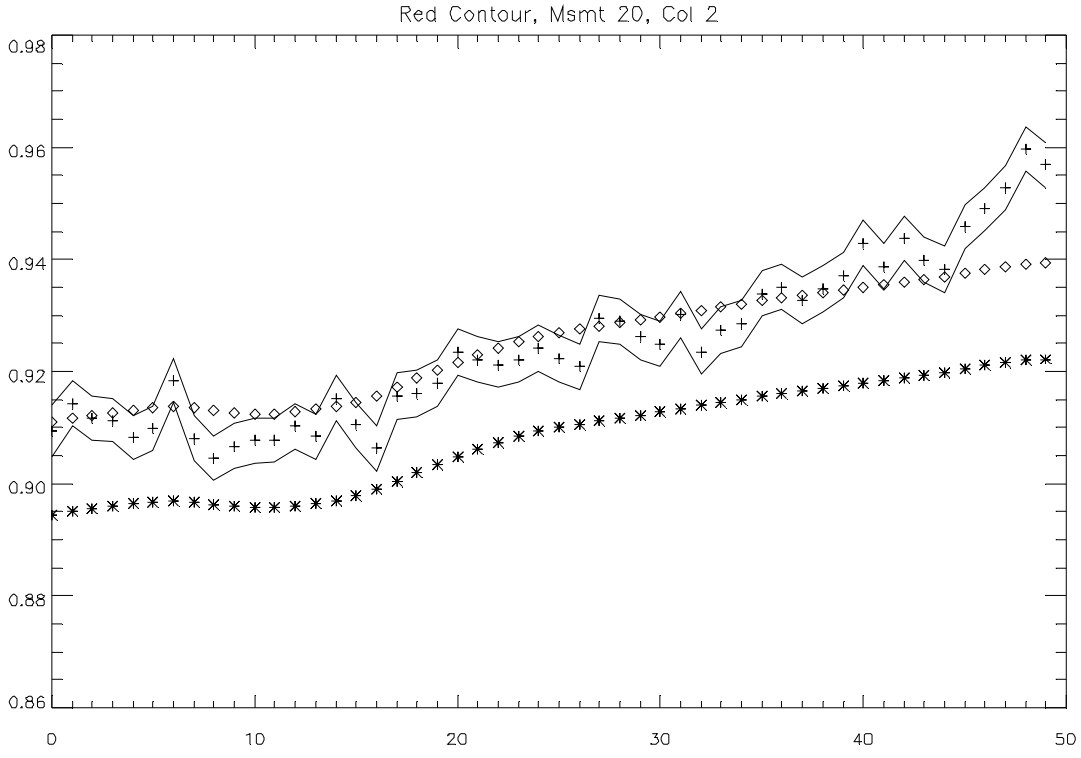
Red Contour, Msmt 20, Col 2
0.98
0.96
0.94
0.92
0.90
0.88
0.86
0
10
20
30
40
50

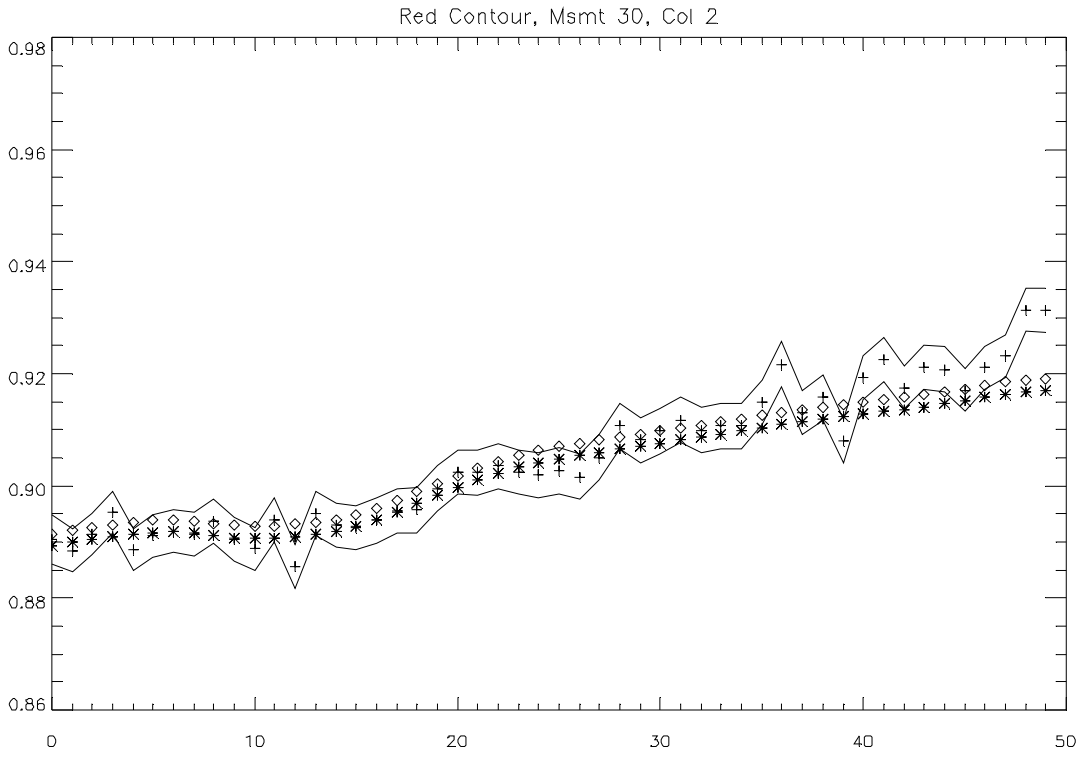
Red Contour, Msmt 30, Col 2
0.98
0.96
0.94
0.92
0.90
0.88
0.86
0
10
20
30
40
50

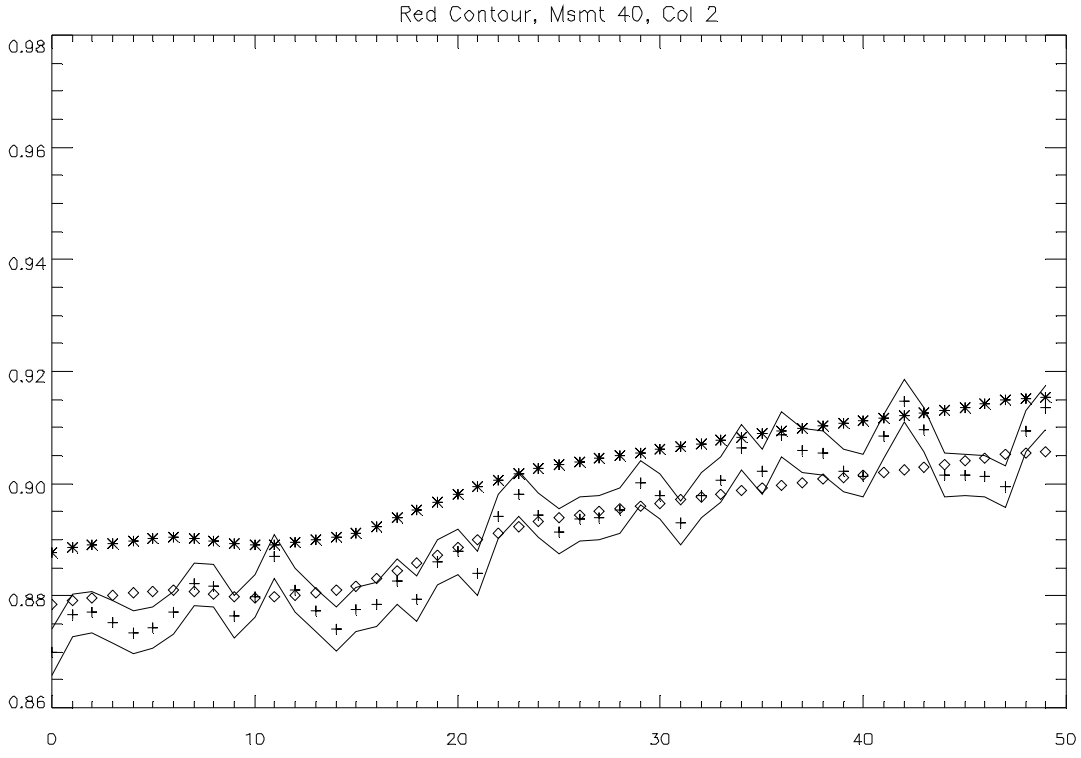
Red Contour, Msmt 40, Col 2
0.98
0.96
0.94
0.92
0.90
0.88
0.86
0
10
20
30
40
50

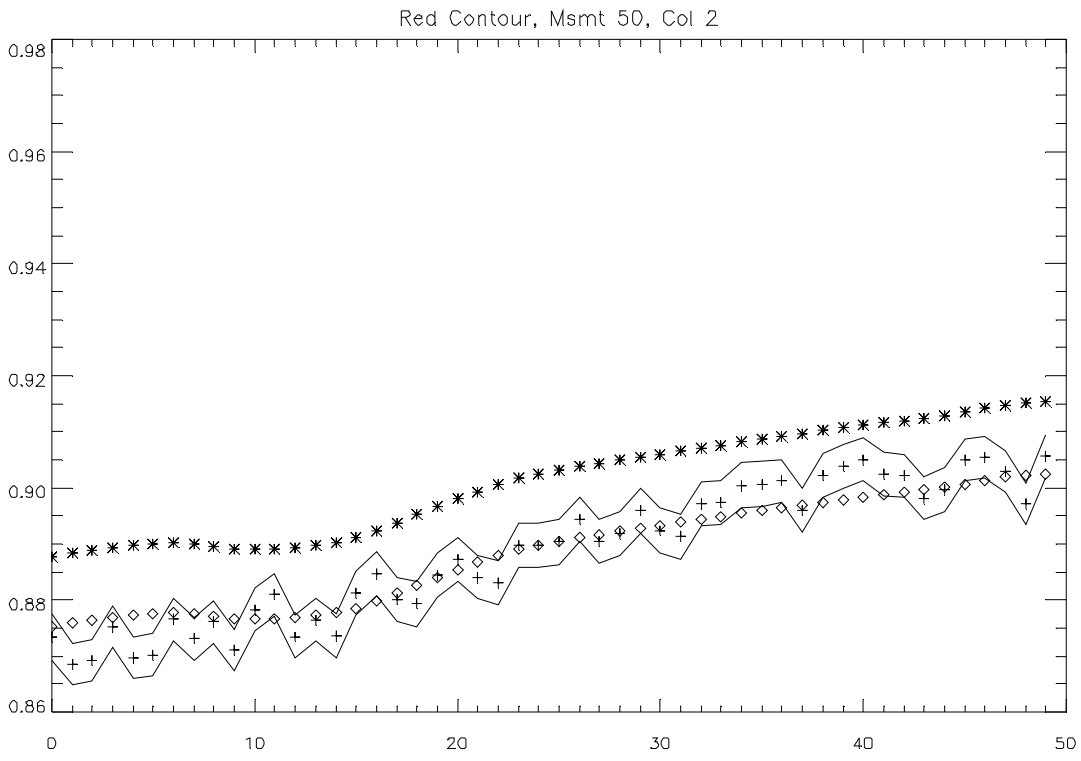

We see that much of the time, the normalized intensity is within the noise band of the measured data, which indicates a good relative calibration. Occasionally, a few pixels could be off by as much as 2%. The higher row numbers often have higher measured intensities than the true intensities.

Because column 0 in the red has poorer performance in absolute calibration, this same set of plots is given below for column 0. This column has poorer results, sometimes as bad as 3%.

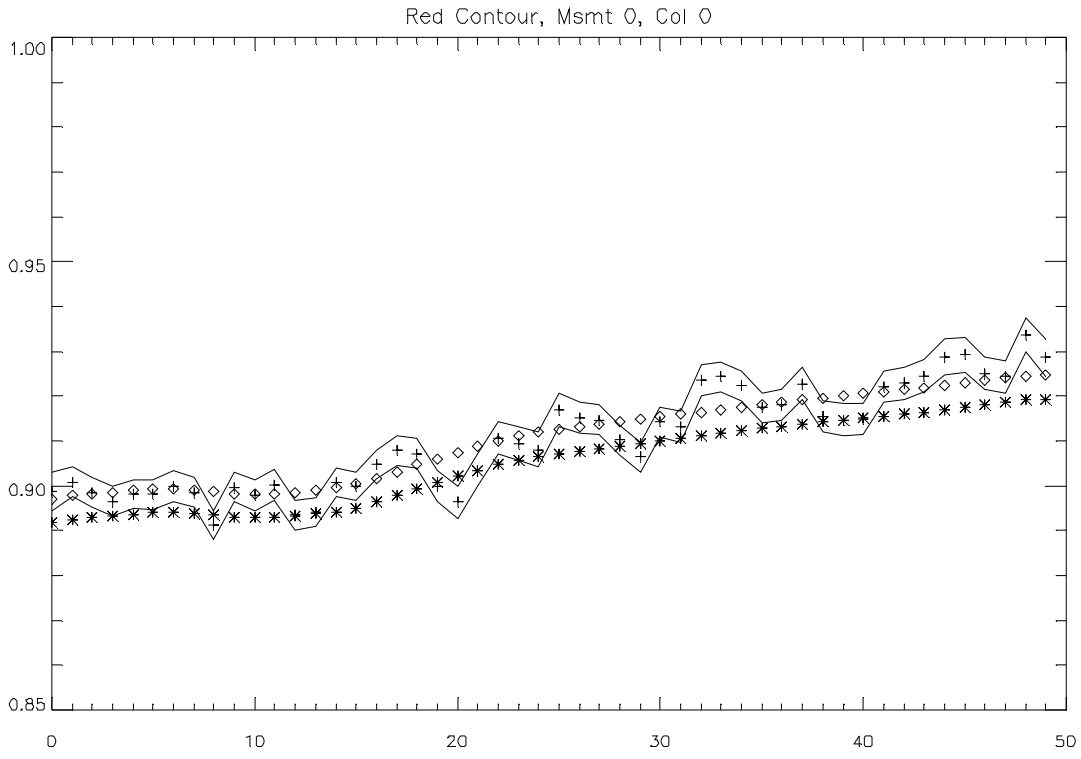
Red Contour, Msmt 0, Col 0
1.00
0.95
0.90
0.85
0
10
20
30
40
50

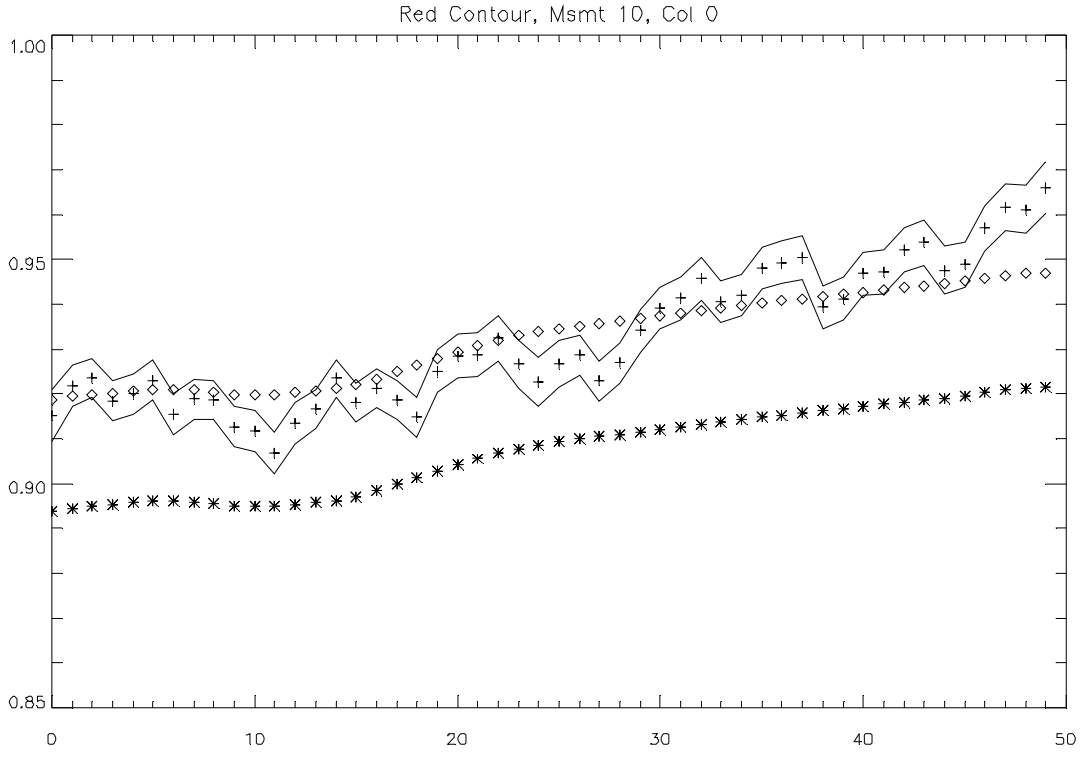
Red Contour, Msmt 10, Col 0
1.00
0.95
0.90
0.85
0
10
20
30
40
50

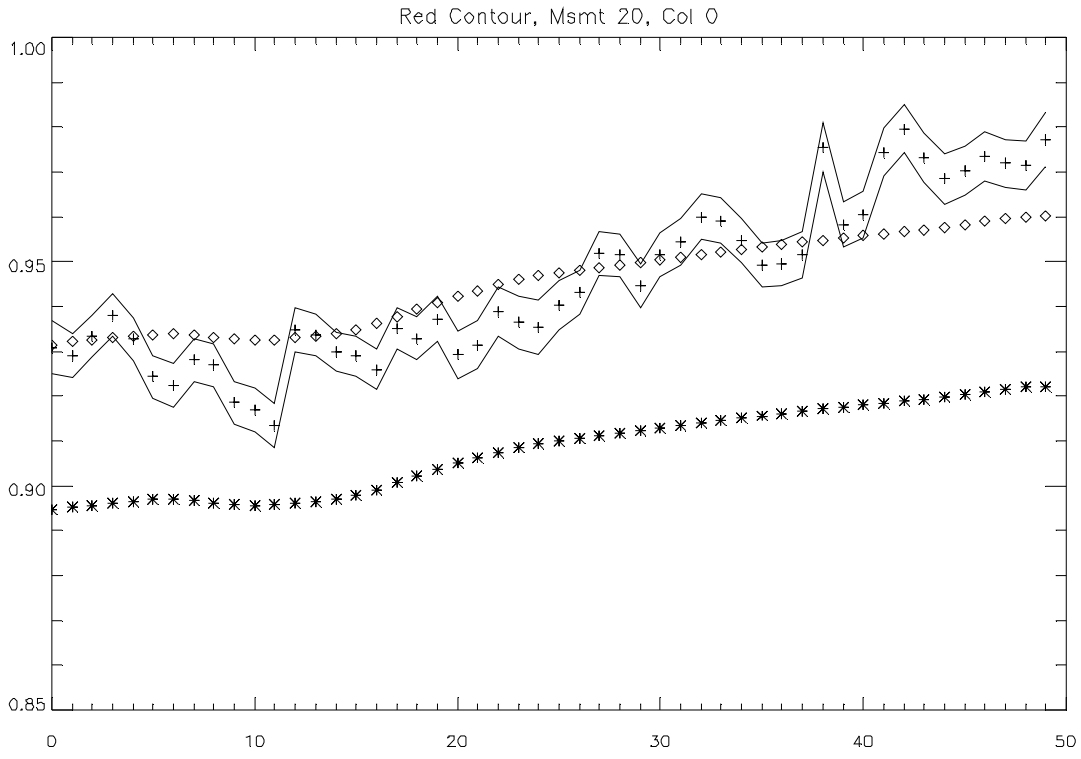
Red Contour, Msmt 20, Col 0
1.00
0.95
0.90
0.85
0
10
20
30
40
50

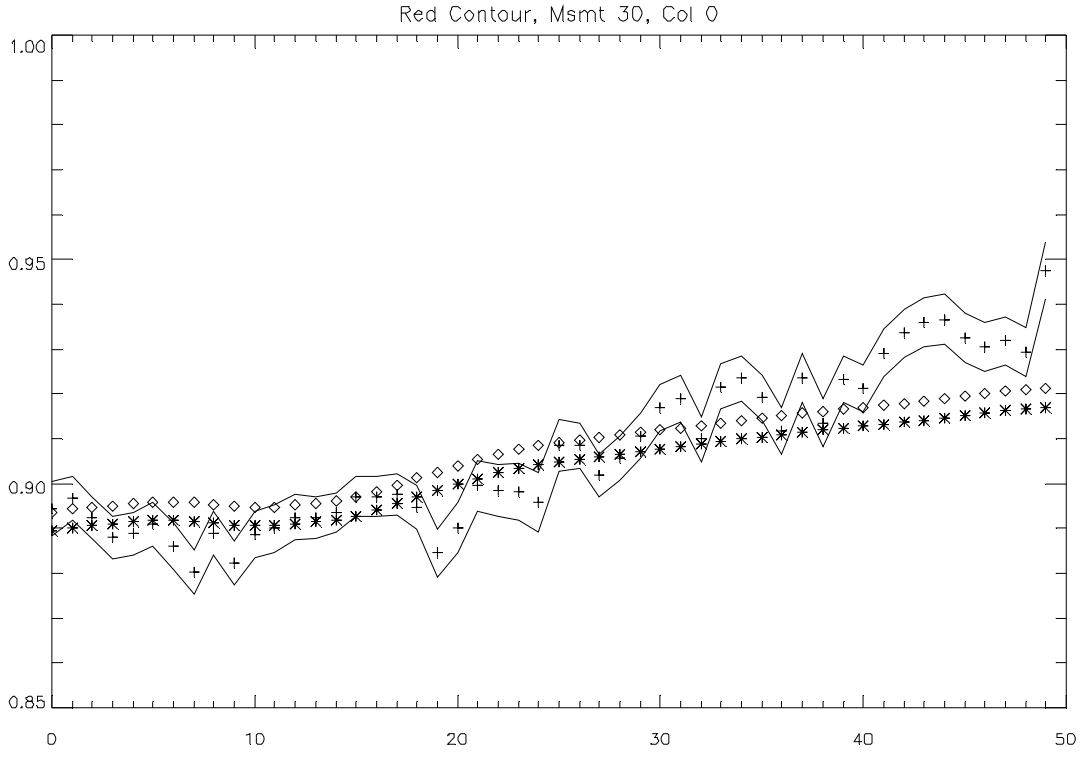
Red Contour, Msmt 30, Col 0
1.00
0.95
0.90
0.85
0
10
20
30
40
50

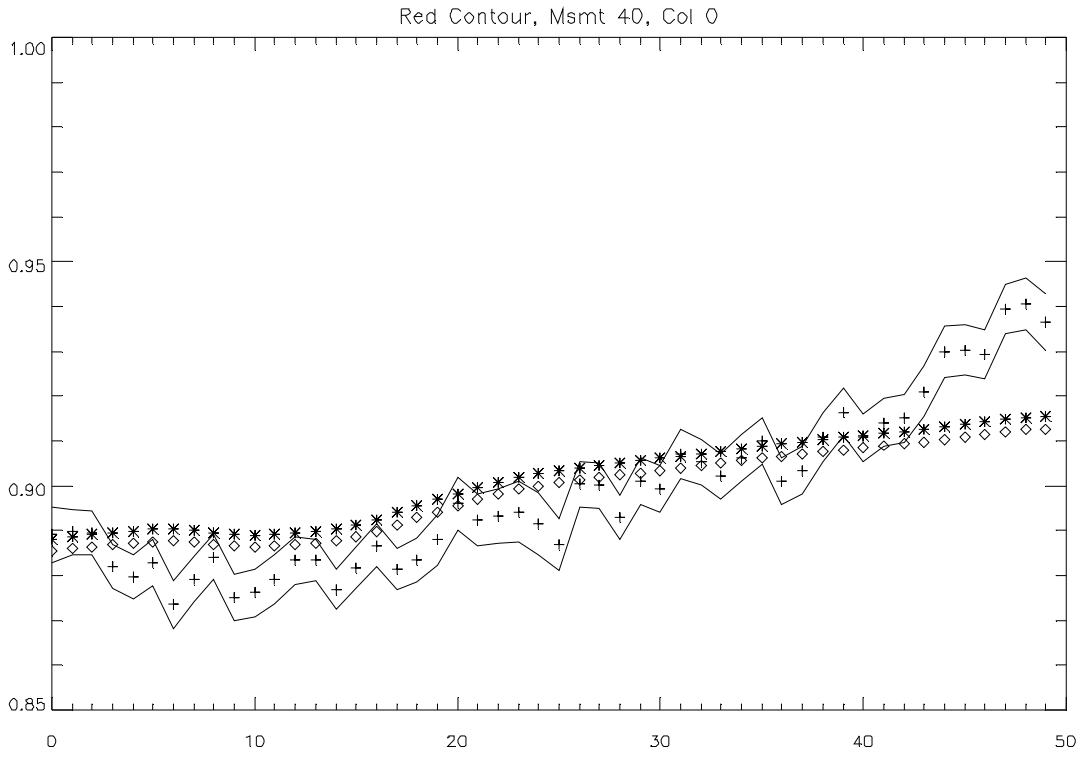
Red Contour, Msmt 40, Col 0
1.00
0.95
0.90
0.85
0
10
20
30
40
50

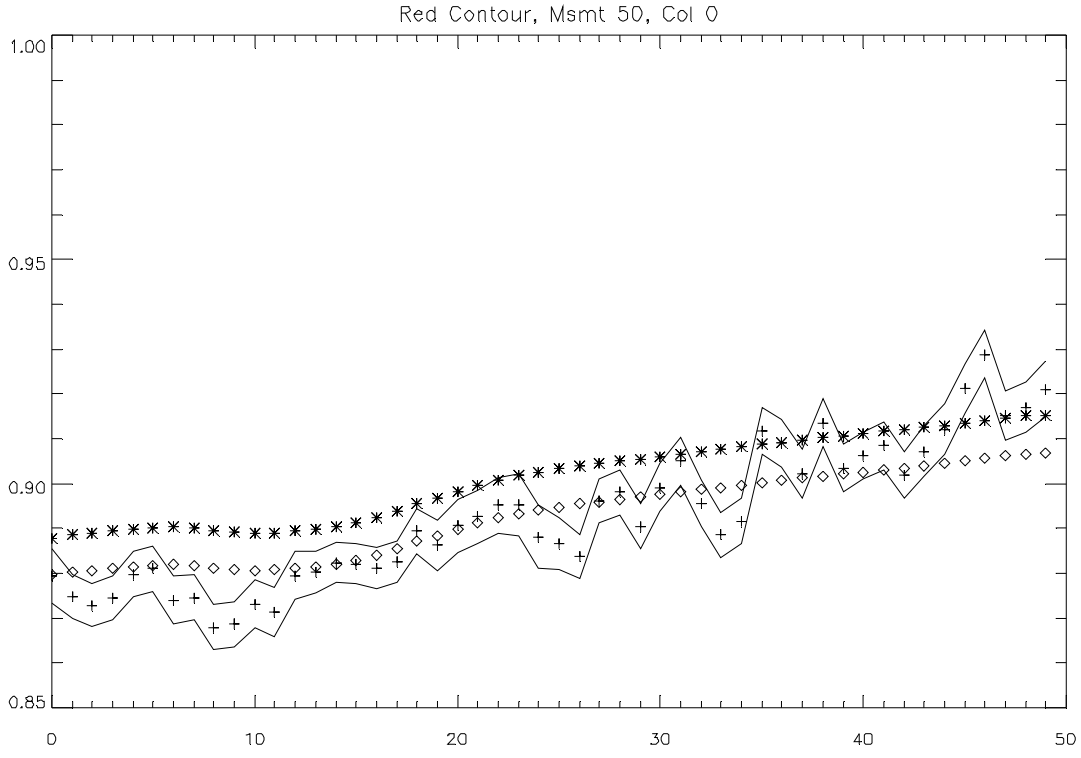
Red Contour, Msmt 50, Col 0
1.00
0.95
0.90
0.85
0
10
20
30
40
50

13.1.5 Results – Relative Calibration across Rows

Now we turn to relative calibration across the rows instead of the columns. The summed data does not lend itself to this section, so we consider only the data returned in full format.

13.1.5.1 Blue Un-Summed Data

We make similar plots to those above for different rows. Consider row 23 near the center. The plots over the course of the descent are as follows. Note that in some cases, although the measured data may not be significantly out of the bounds of the noise band, the measured shape of the intensity field across those six pixels can be significantly different from the actual flat shape. Having only six pixels in this direction makes curve fitting difficult. There does not appear to be any systematic variation across the six pixels.

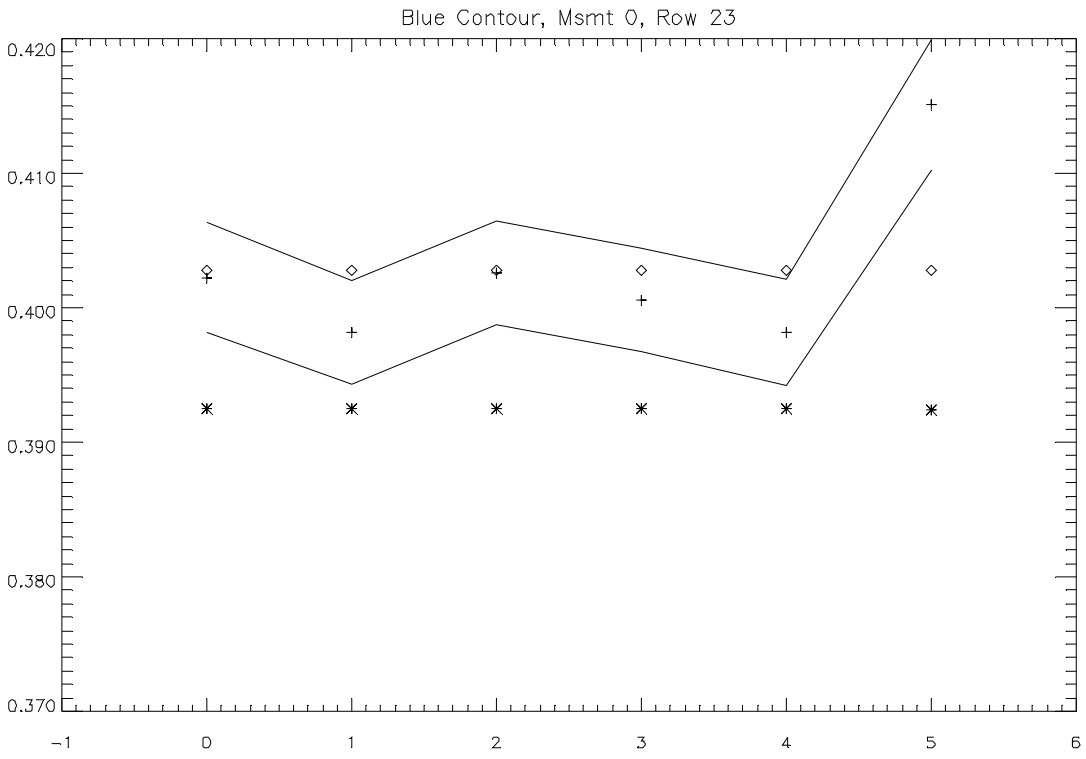

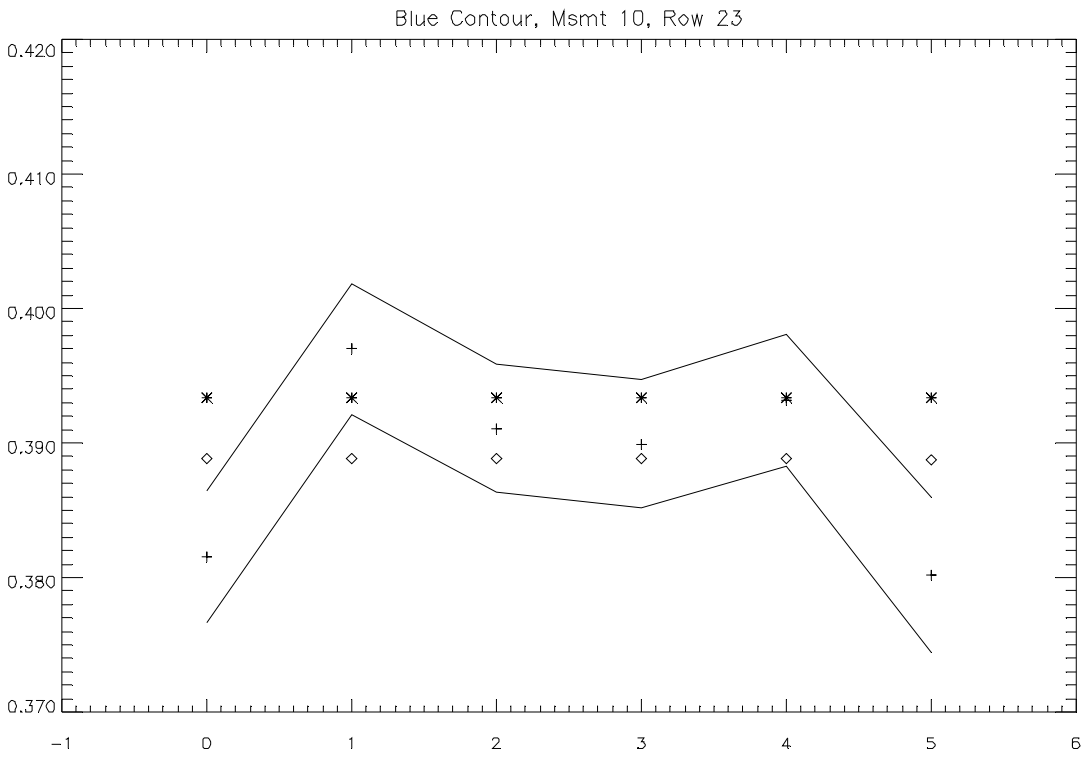
Blue Contour, Msmt 10, Row 23
0.420
0.410
0.400
0.390
0.380
0.370
−1
0
1
2
3
4
5
6

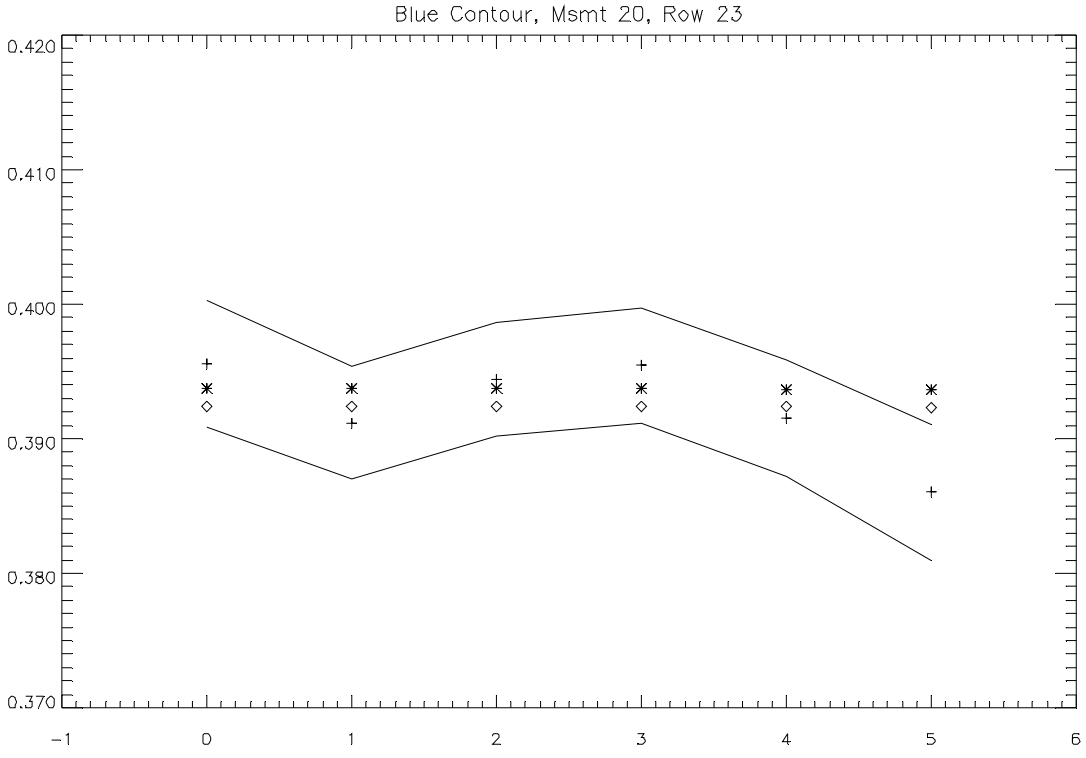
Blue Contour, Msmt 20, Row 23
0.420
0.410
0.400
0.390
0.380
0.370
−1
0
1
2
3
4
5
6

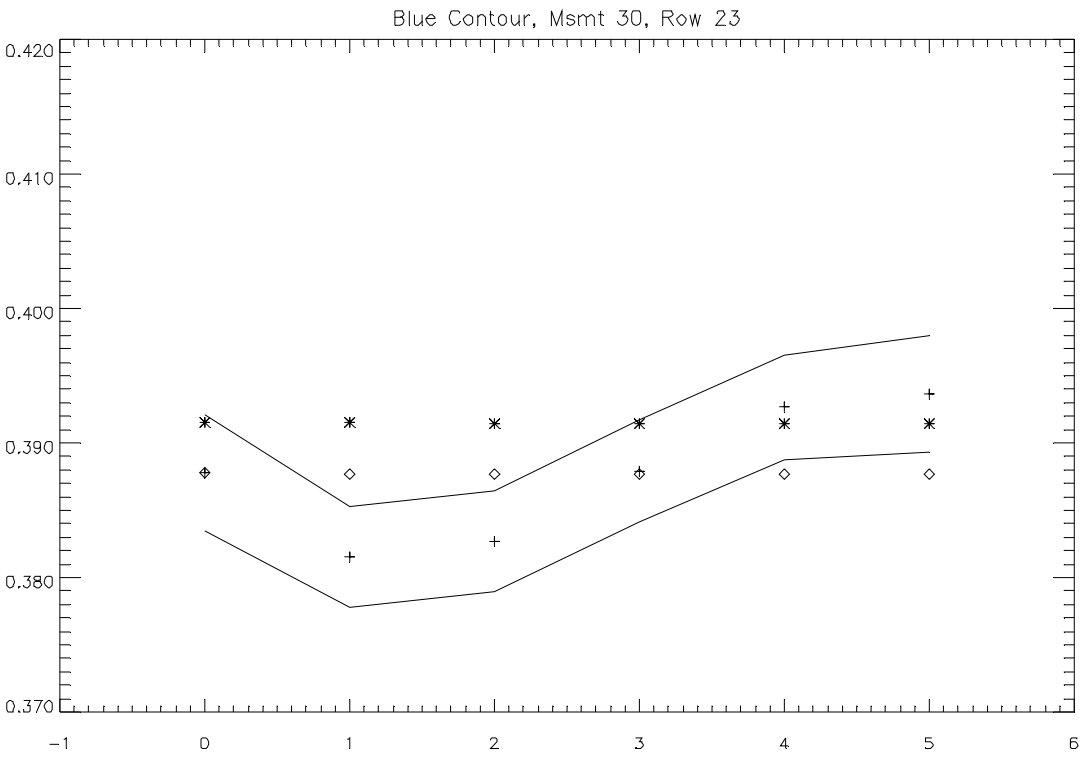
Blue Contour, Msmt 30, Row 23
0.420
0.410
0.400
0.390
0.380
0.370
−1
0
1
2
3
4
5
6

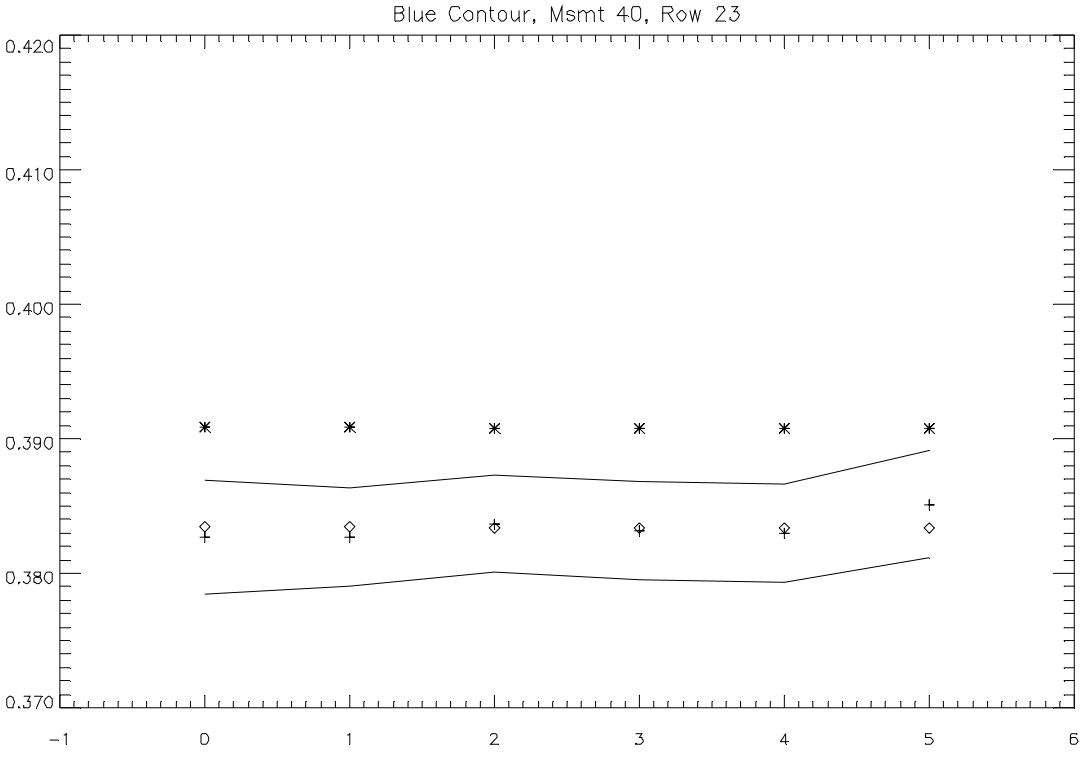
Blue Contour, Msmt 40, Row 23
0.420
0.410
0.400
0.390
0.380
0.370
−1
0
1
2
3
4
5
6

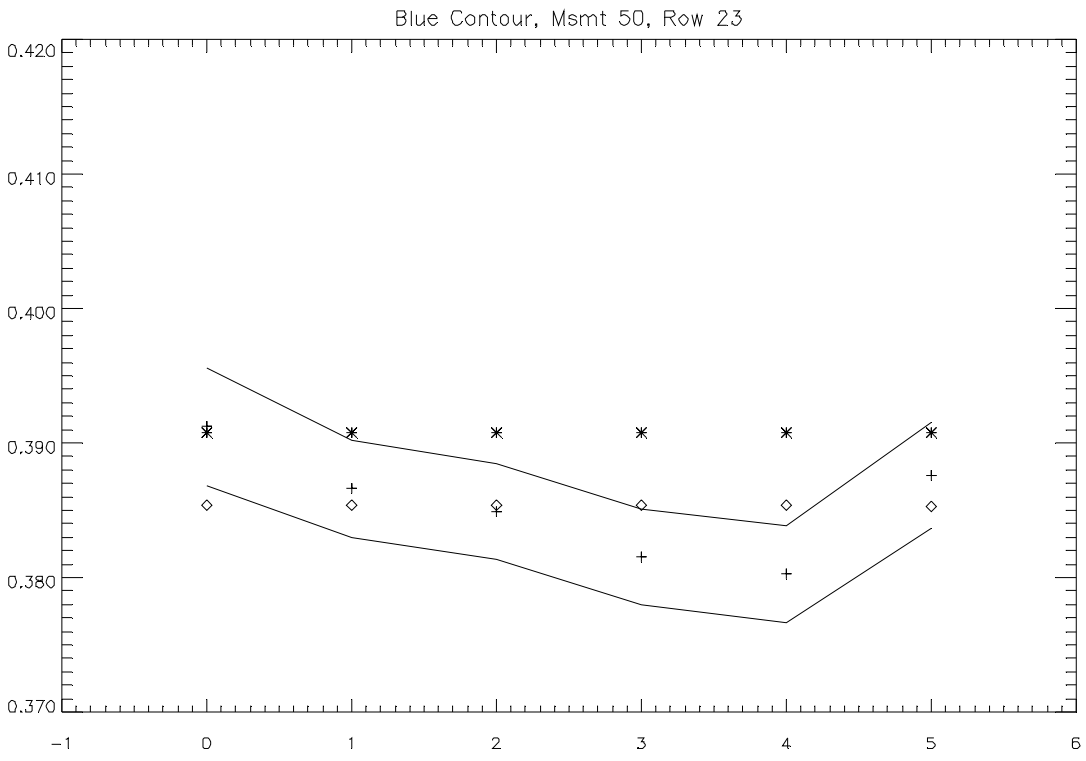

Also considering an extreme row is helpful to bound the performance. Here are the plots for row 48. Again, we sometimes see the possibility of vastly different measured shapes from the true ones, but there are no systematic errors. While the errors are not systematic, it is difficult to advertise greater than 2% relative calibration accuracy in this case.

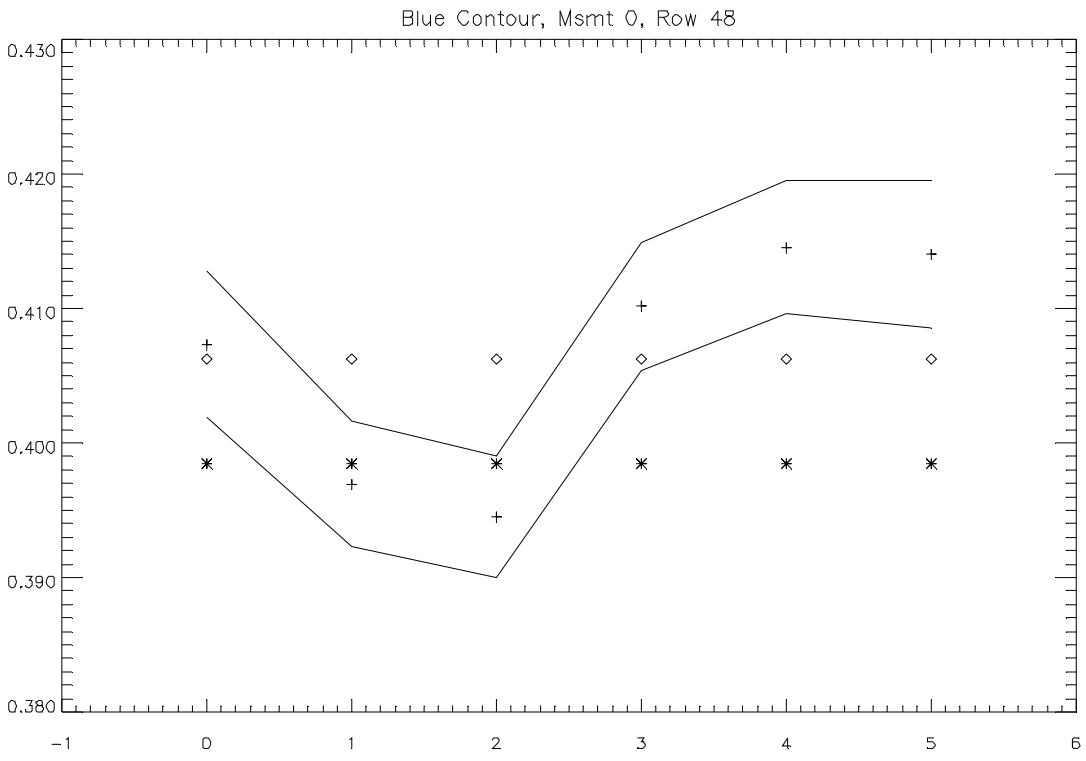
Blue Contour, Msmt 0, Row 48
0.430
0.420
0.410
0.400
0.390
0.380
−1
0
1
2
3
4
5
6

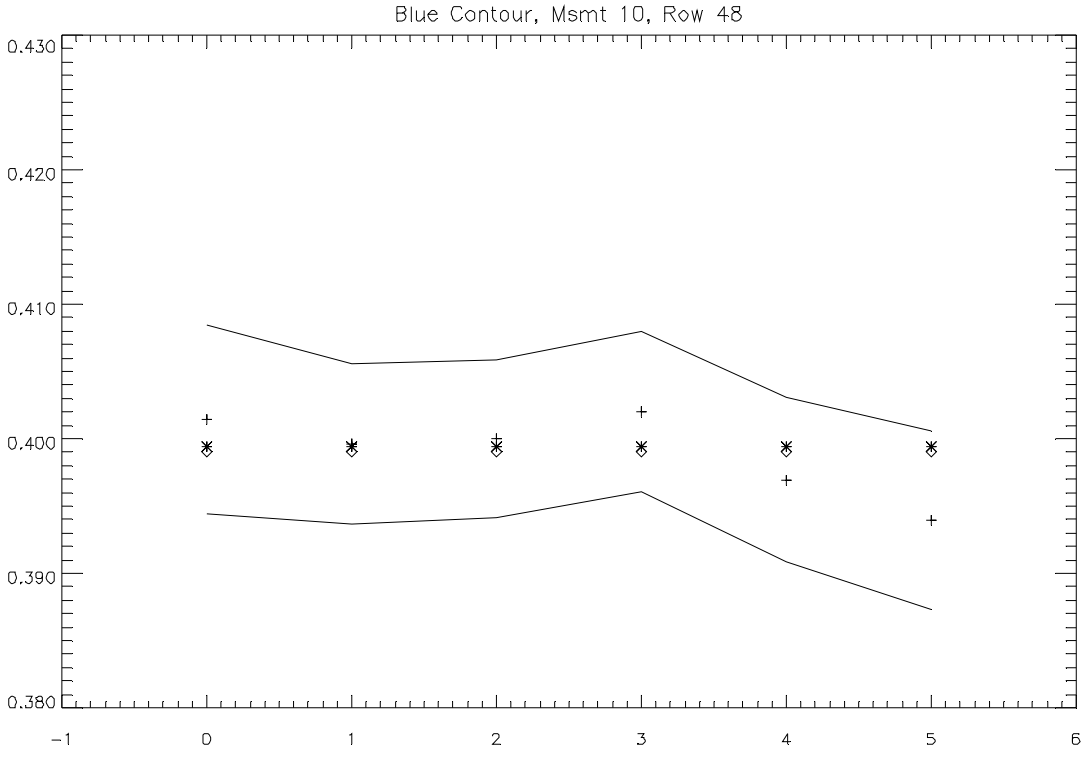
Blue Contour, Msmt 10, Row 48
0.430
0.420
0.410
0.400
0.390
0.380
−1
0
1
2
3
4
5
6

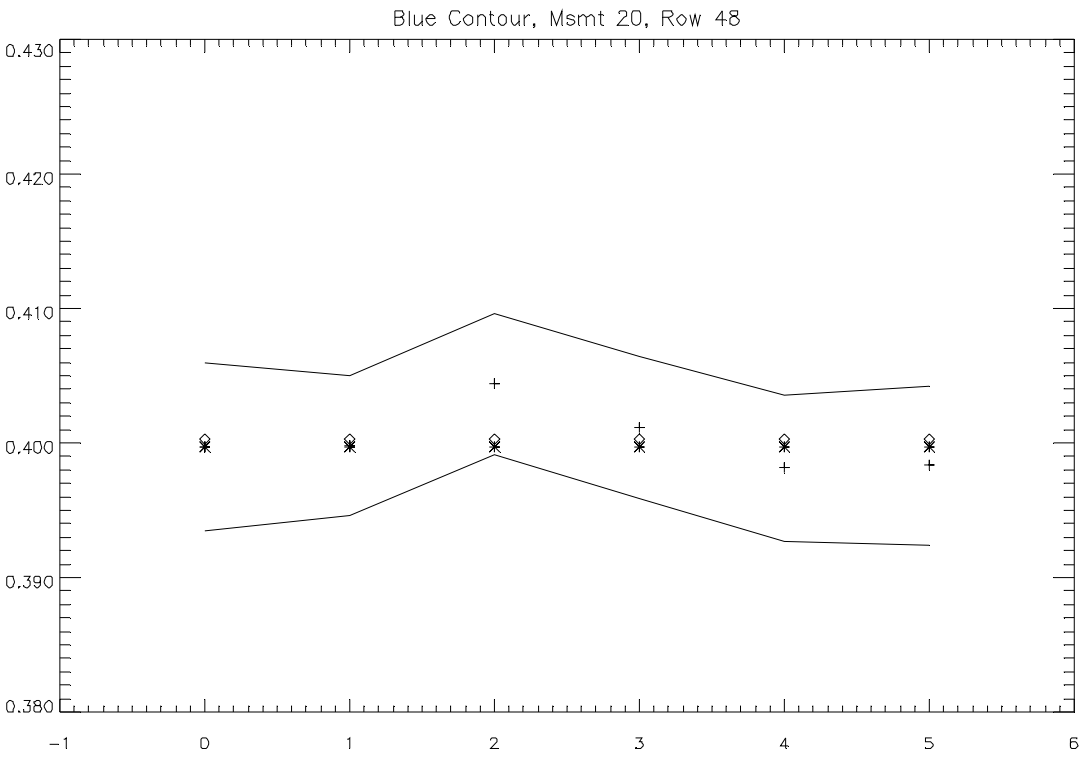
Blue Contour, Msmt 20, Row 48
0.430
0.420
0.410
0.400
0.390
0.380
−1
0
1
2
3
4
5
6

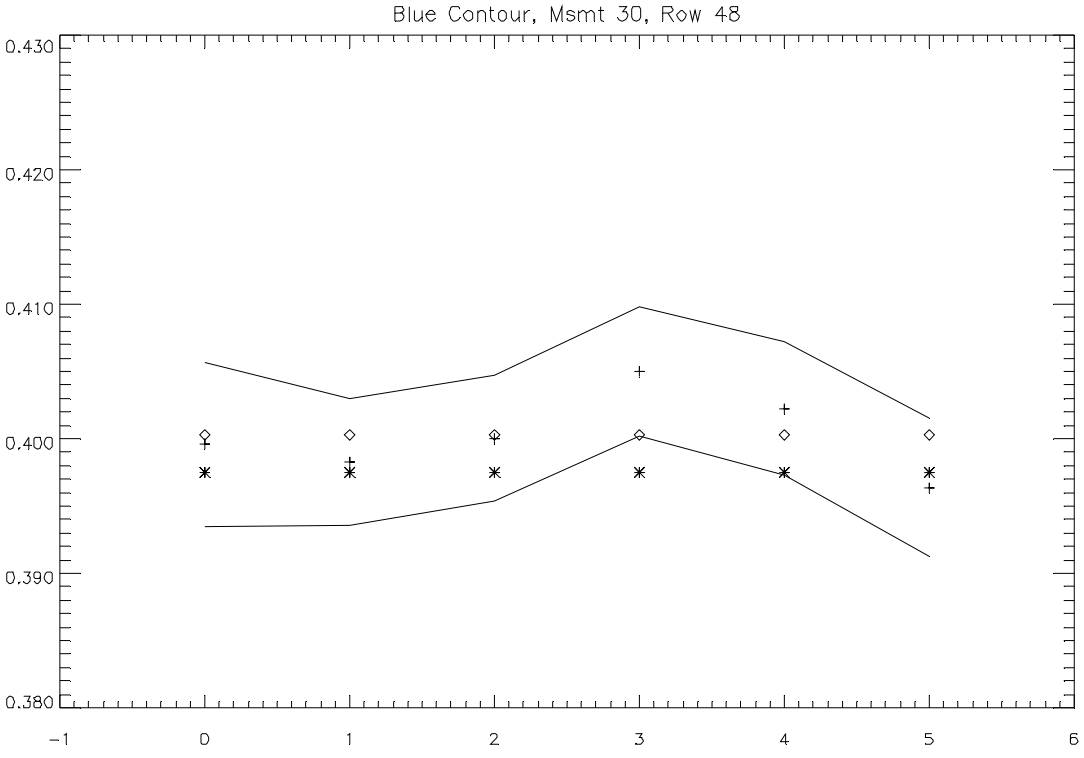
Blue Contour, Msmt 30, Row 48
0.430
0.420
0.410
0.400
0.390
0.380
−1
0
1
2
3
4
5
6

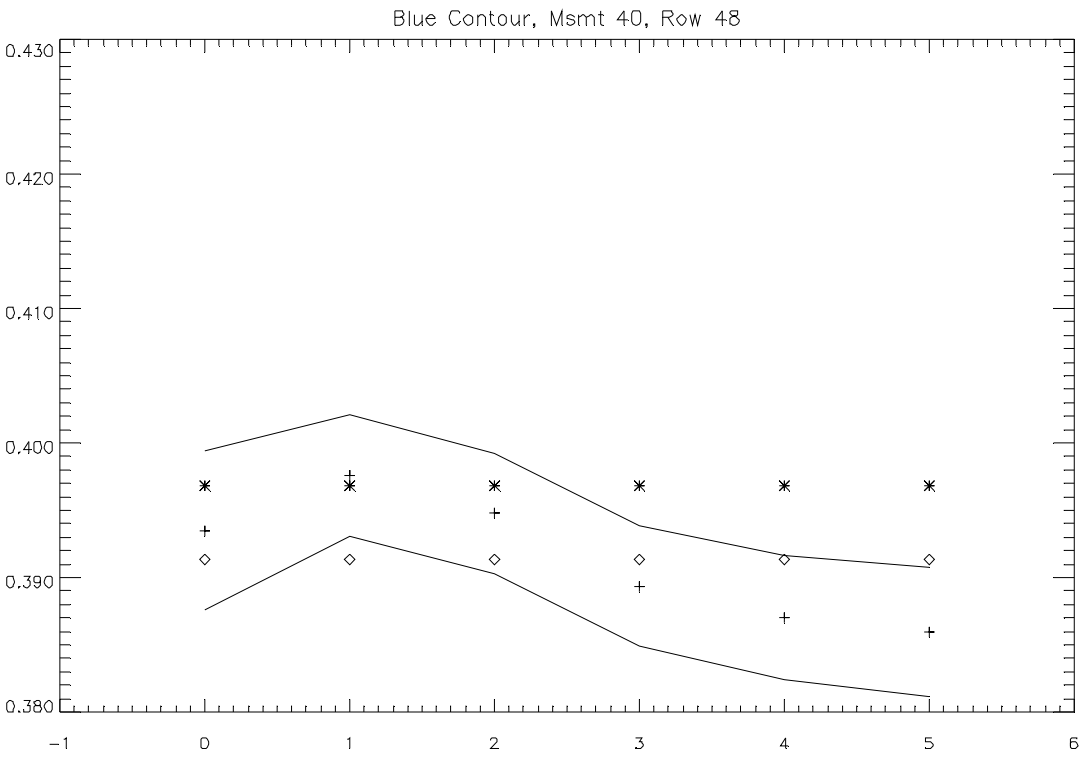
Blue Contour, Msmt 40, Row 48
0.430
0.420
0.410
0.400
0.390
0.380
−1
0
1
2
3
4
5
6

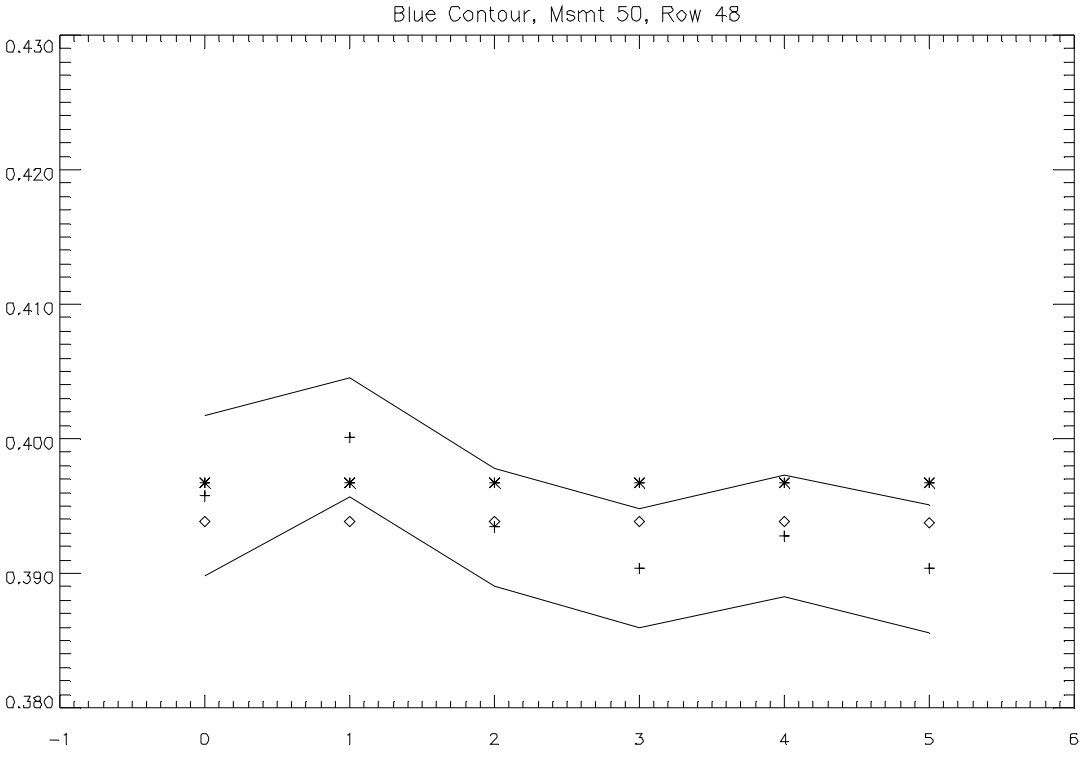
Blue Contour, Msmt 50, Row 48
0.430
0.420
0.410
0.400
0.390
0.380
−1
0
1
2
3
4
5
6

13.1.5.2 Red Un-Summed Data

Now we turn to the red channels, and we consider the same 10 plots as for the blue. Again, there can be vastly different shapes measured across the row, but the variations are under 1% in the central column, and there are no systematic variations. The extreme row shows 1% relative accuracy most of the time, but in some cases it decreases to 2% accuracy.

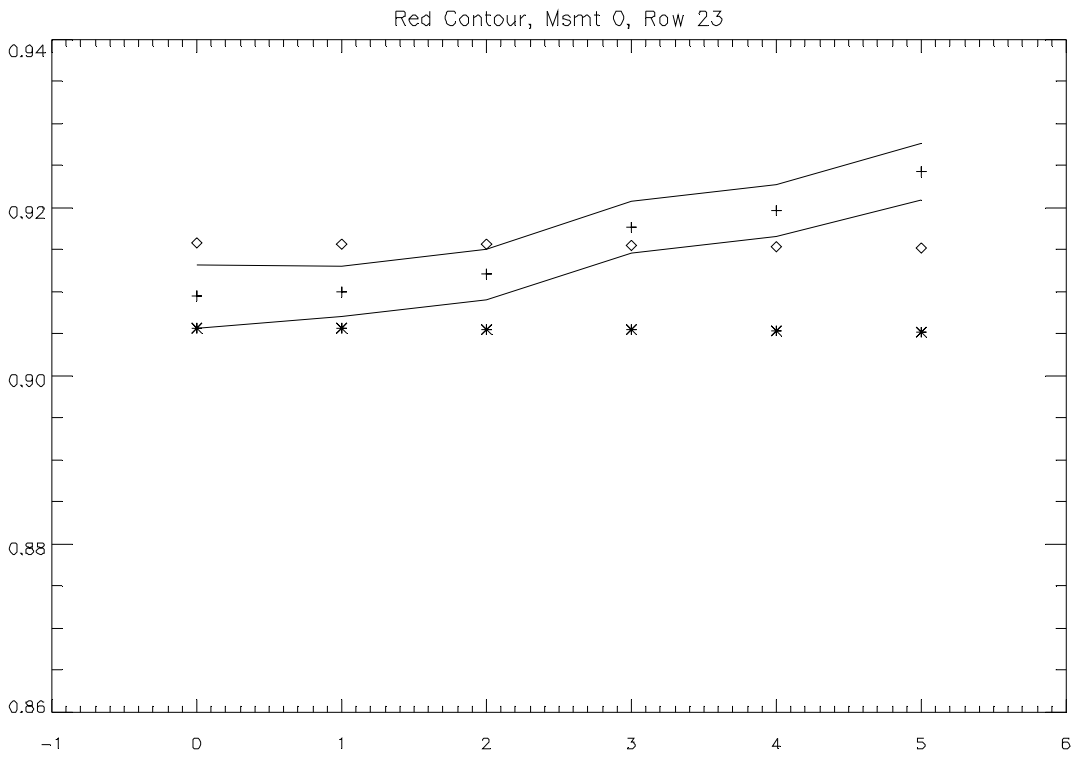
Red Contour, Msmt 0, Row 23
0.94
0.92
0.90
0.88
0.86
−1
0
1
2
3
4
5
6

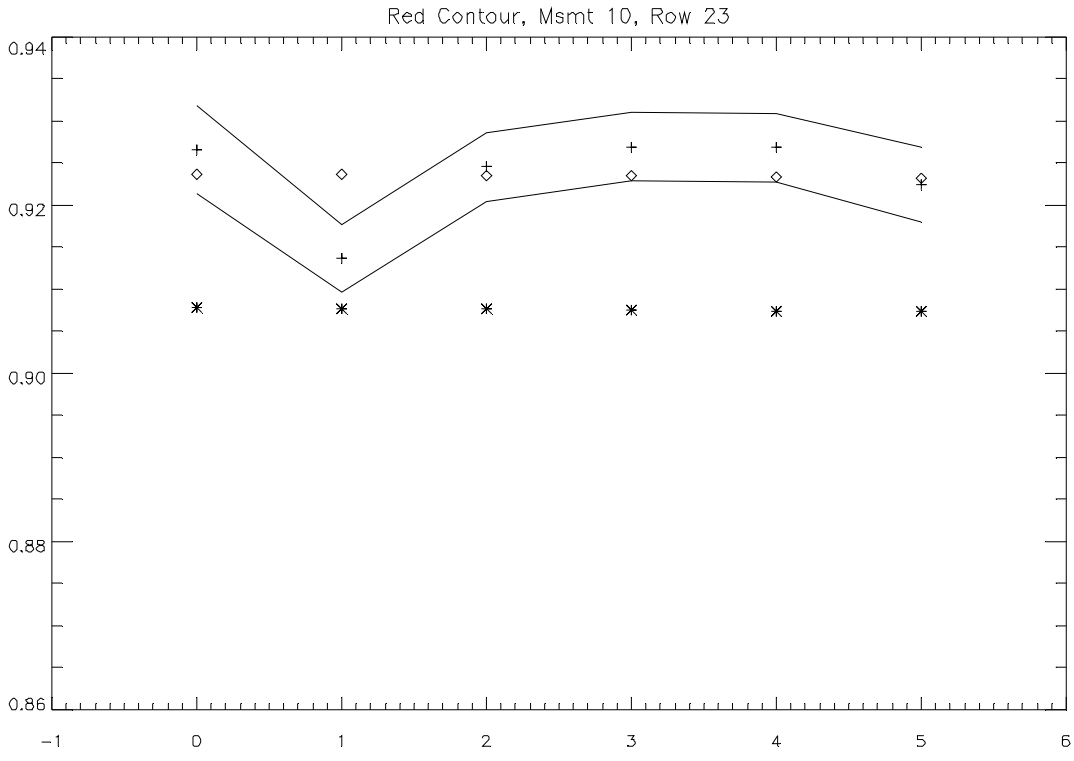
Red Contour, Msmt 10, Row 23
0.94
0.92
0.90
0.88
0.86
−1
0
1
2
3
4
5
6

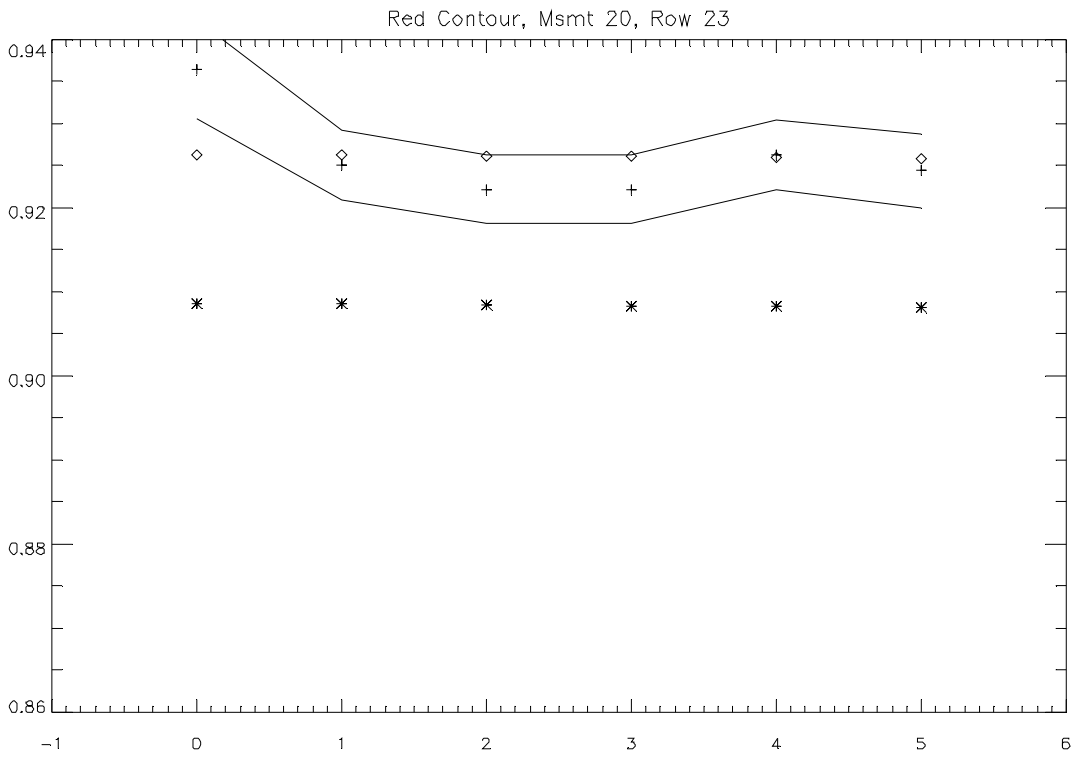
Red Contour, Msmt 20, Row 23
0.94
0.92
0.90
0.88
0.86
−1
0
1
2
3
4
5
6

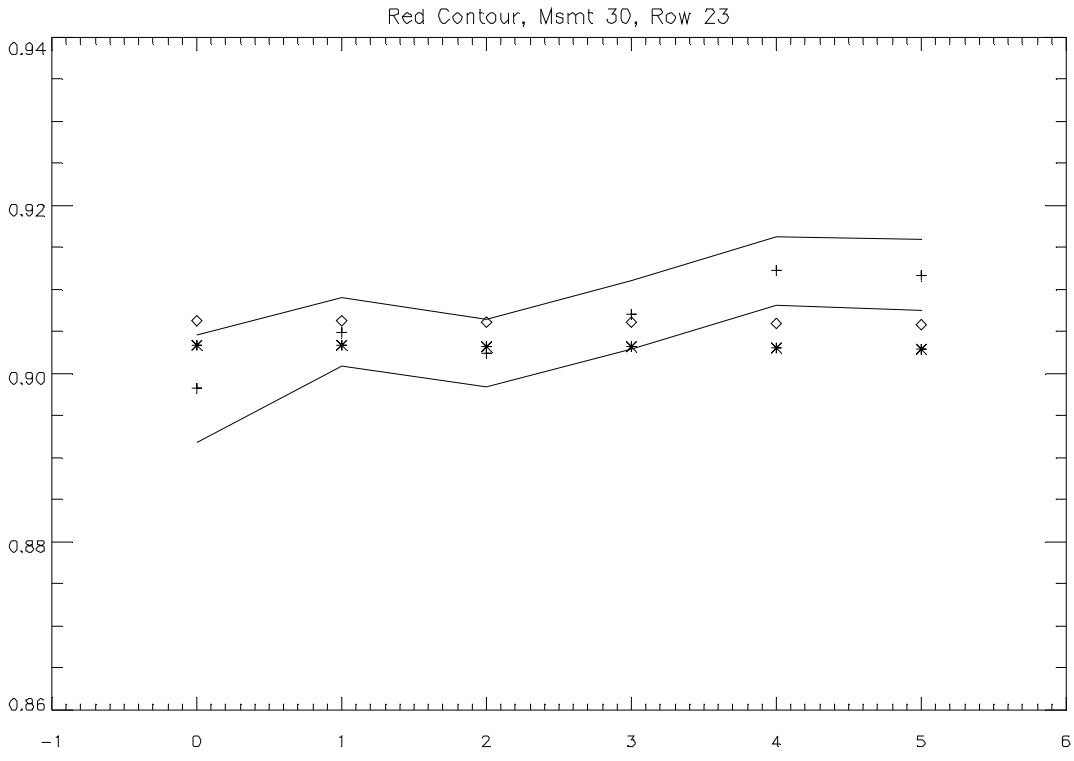
Red Contour, Msmt 30, Row 23
0.94
0.92
0.90
0.88
0.86
−1
0
1
2
3
4
5
6

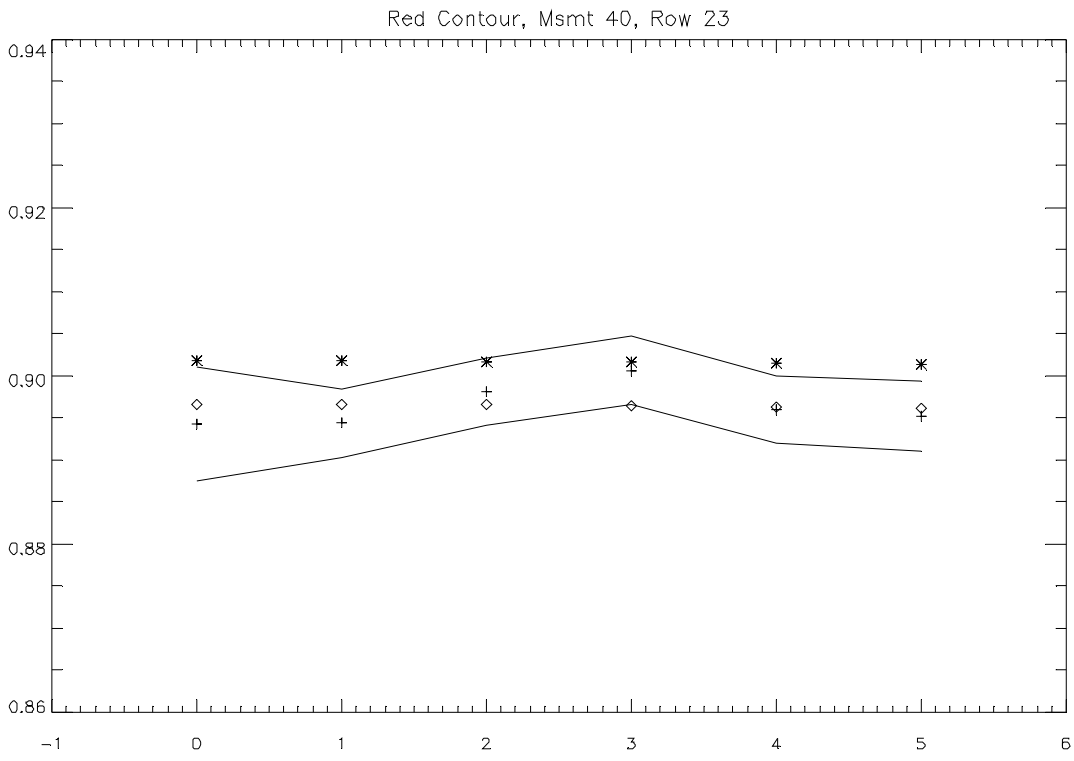
Red Contour, Msmt 40, Row 23
0.94
0.92
0.90
0.88
0.86
−1
0
1
2
3
4
5
6

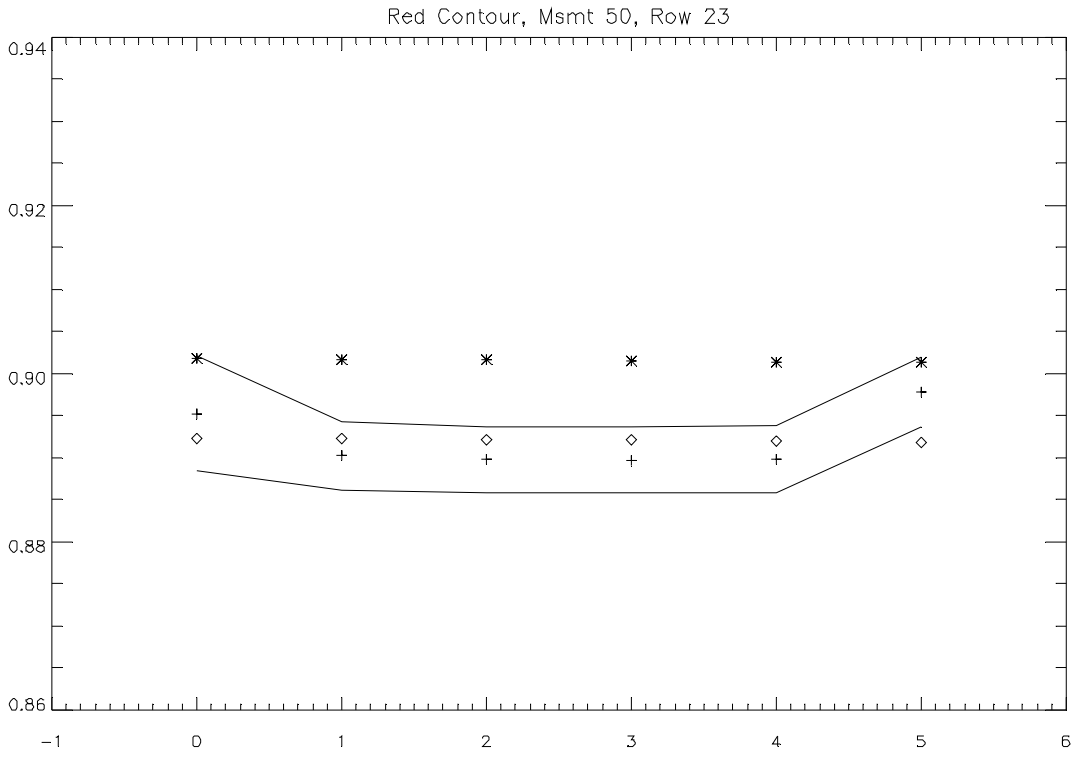
Red Contour, Msmt 50, Row 23
0.94
0.92
0.90
0.88
0.86
−1
0
1
2
3
4
5
6

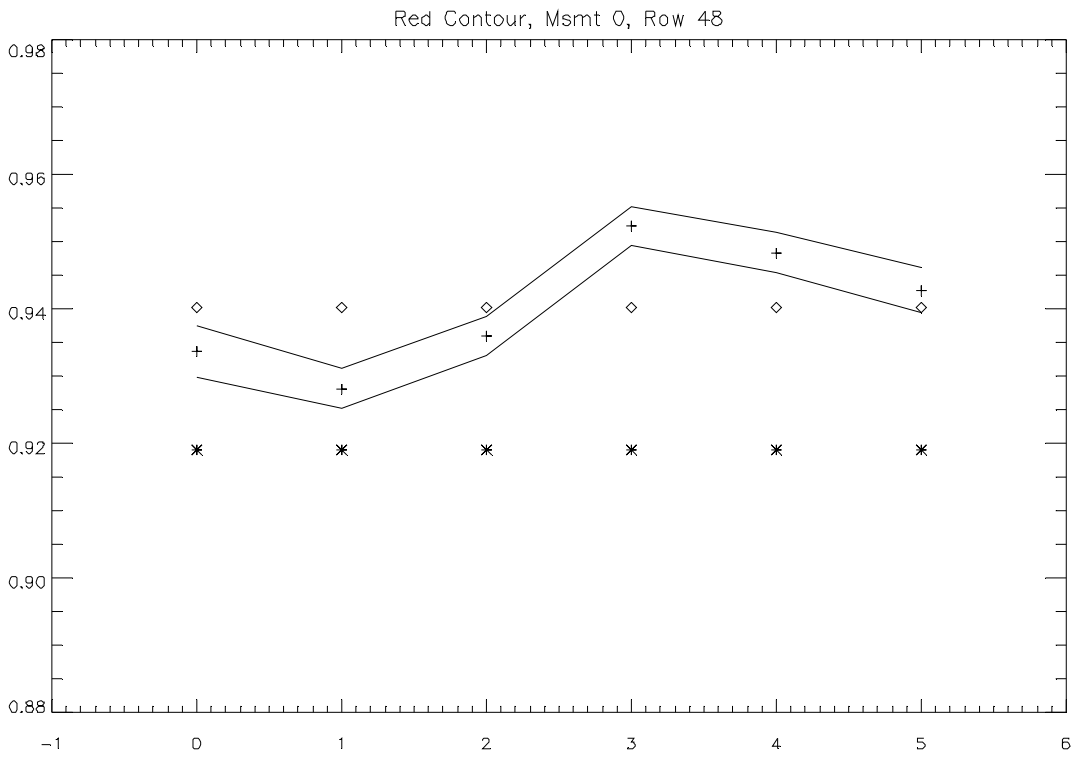
Red Contour, Msmt 0, Row 48
0.98
0.96
0.94
0.92
0.90
0.88
-1
0
1
2
3
4
5
6

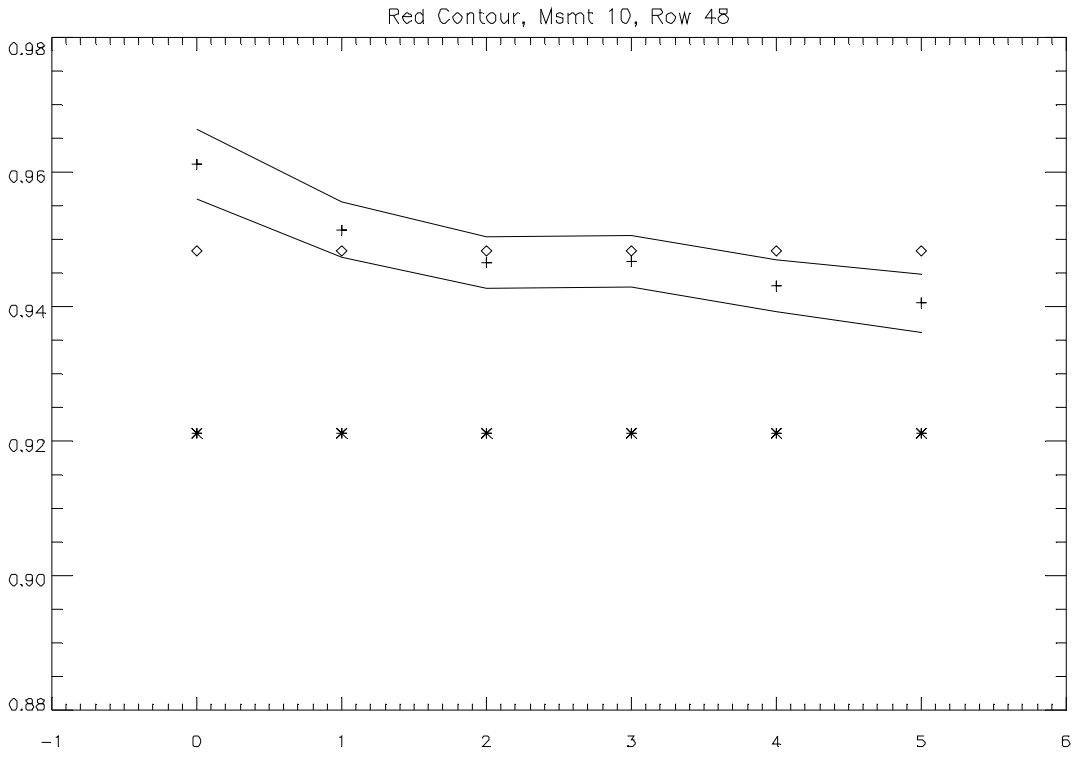
Red Contour, Msmt 10, Row 48
0.98
0.96
0.94
0.92
0.90
0.88
-1
0
1
2
3
4
5
6

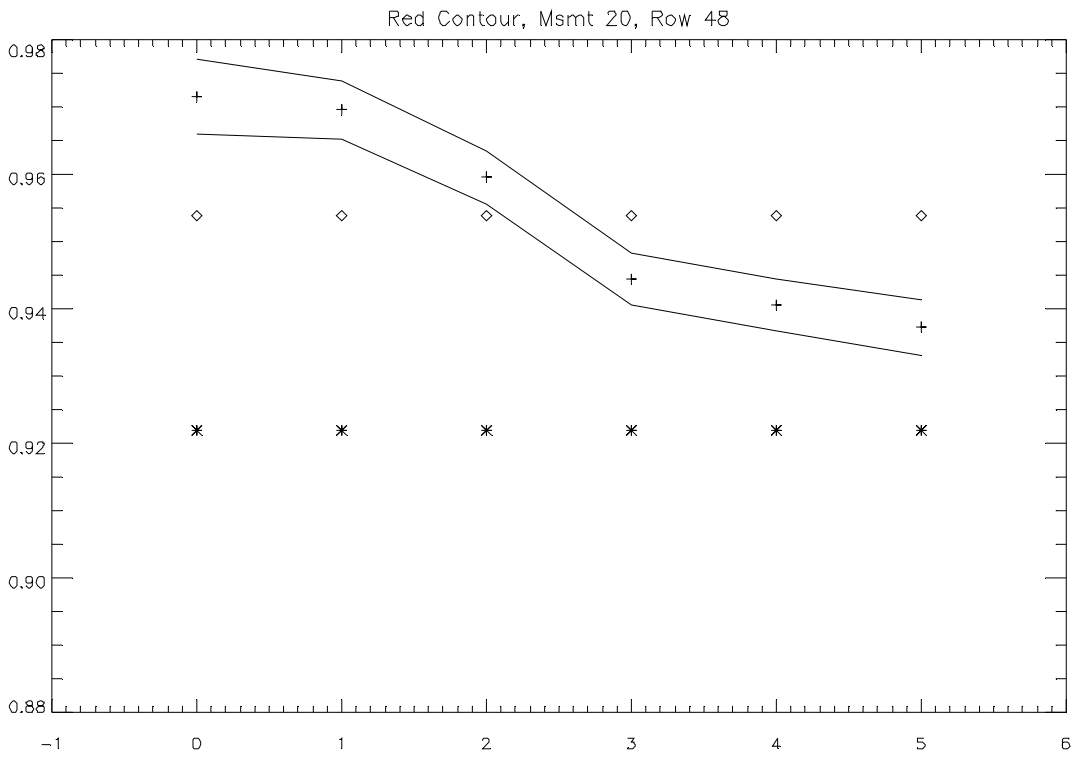
Red Contour, Msmt 20, Row 48
0.98
0.96
0.94
0.92
0.90
0.88
−1
0
1
2
3
4
5
6

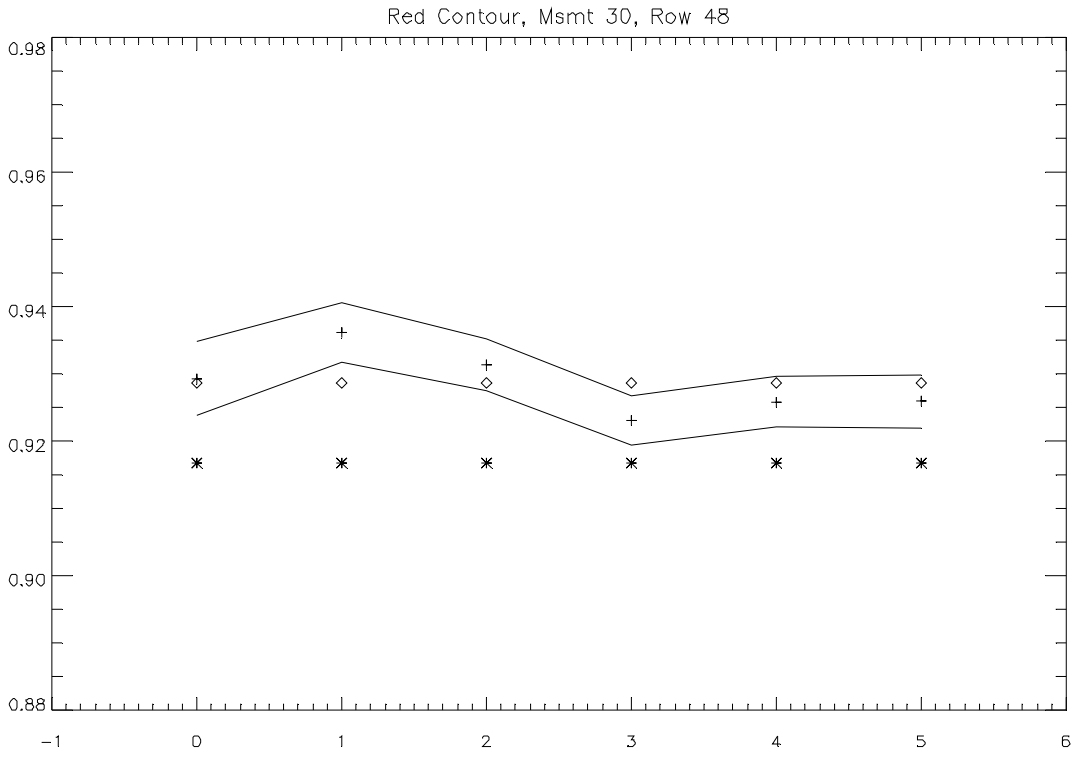
Red Contour, Msmt 30, Row 48
0.98
0.96
0.94
0.92
0.90
0.88
−1
0
1
2
3
4
5
6

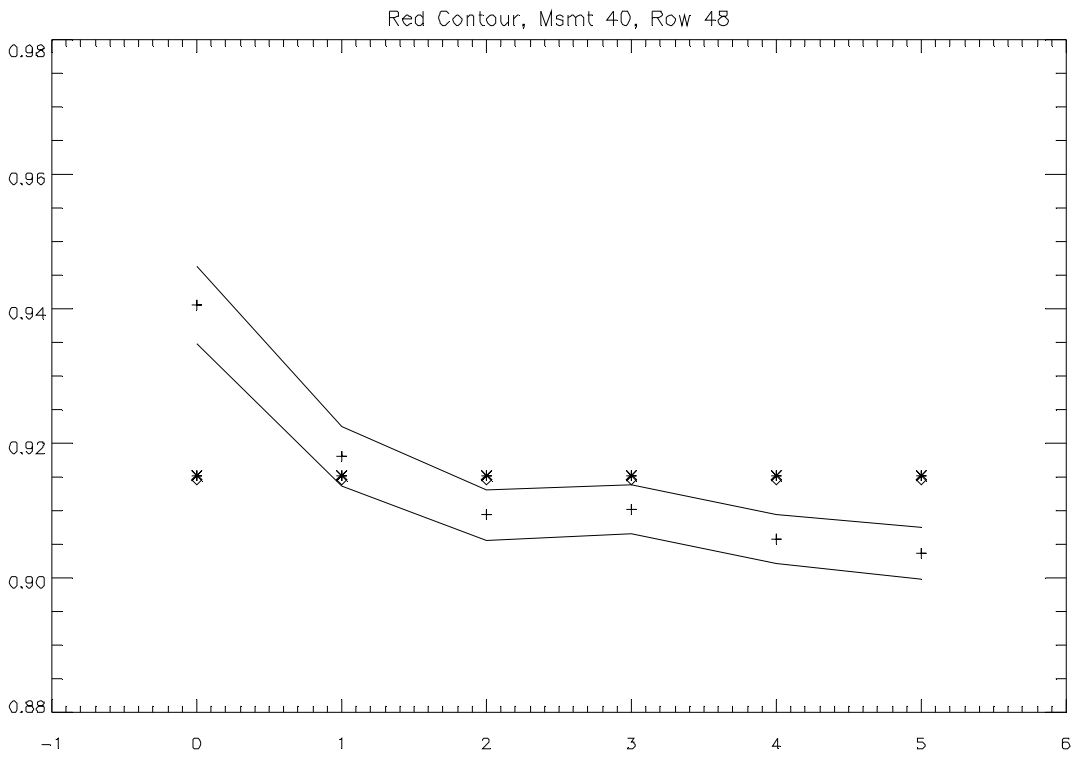
Red Contour, Msmt 40, Row 48
0.98
0.96
0.94
0.92
0.90
0.88
−1
0
1
2
3
4
5
6

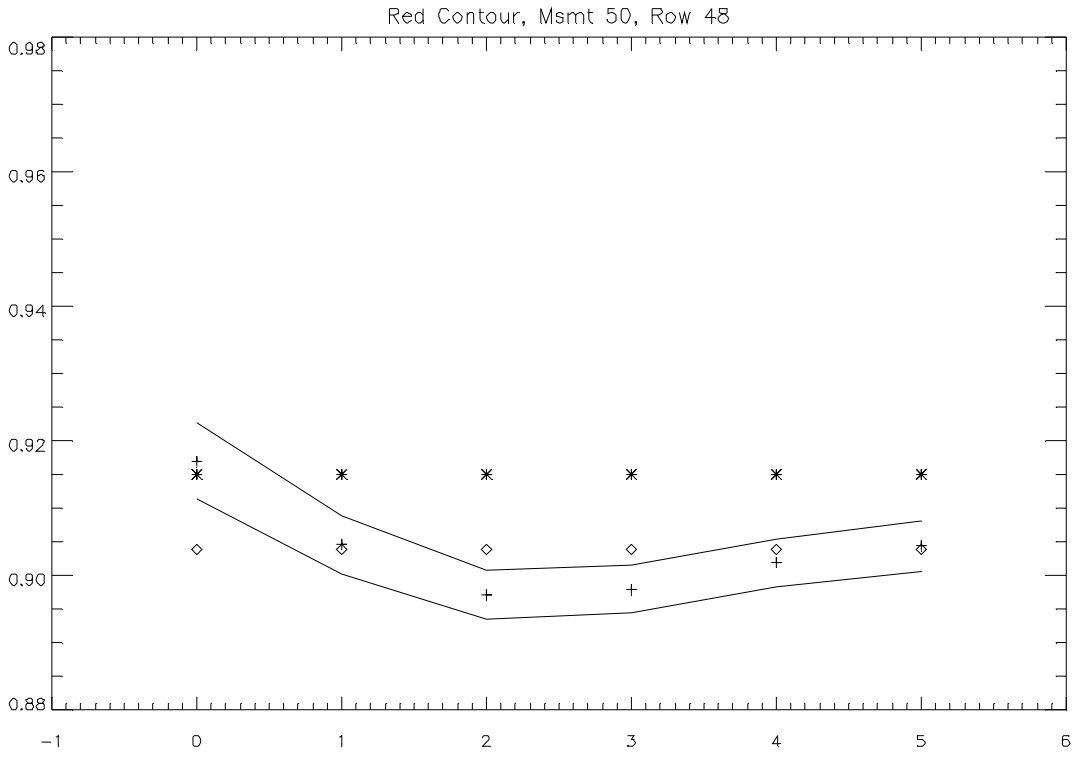
Red Contour, Msmt 50, Row 48
0.98
0.96
0.94
0.92
0.90
0.88
−1
0
1
2
3
4
5
6

13.1.6 Definition of SNR

Because the SNR bands are given on all these plots and are used as a figure of merit, the method of computing the SNR is described below. Note that for all the data returned from the descent_analysis code, the perpendicular and parallel channels are already registered in angle and summed.

For the unsummed data, the SNR is defined as follows. The signal electrons are computed as the data numbers from the SA minus the dark plus bias model, times the electrons per data number:

$$signal\_electrons = (data\_numbers\text{-}dark\_plus\_bias)*e\_per\_dn \qquad 1.$$

This is computed for each pixel in each channel. The noise electrons are computed as the root-sum-square of the shot noise and the read noise, all in electrons:

$$noise\_electrons = \sqrt{signal\_electrons + (dark\_plus\_bias\text{-}bias)*e\_per\_dn + read\_noise^2} \qquad 2.$$

This is also computed for each pixel in each channel. Finally, the total SNR is computed for the sum of the perpendicular and parallel channels on a pixel by pixel basis as:

$$SNR = \frac{signal\_electrons\_perp + signal\_electrons\_para}{\sqrt{noise\_electrons\_perp^2 + noise\_electrons\_para^2}} \qquad 3.$$

For the summed data, the SNR is defined as follows. First, the dark plus bias model must be summed across columns.

$$dark\_plus\_bias\_sum = \sum_{col} dark\_plus\_bias(row, col) \qquad 4.$$

Then, the signal electrons are computed:

$$signal\_electrons = (data\_numbers\text{-}dark\_plus\_bias\_sum)*e\_per\_dn \qquad 5.$$

Next, the noise electrons are computed, dividing by the square root of 6 because of the summing of 6 columns:

$$noise\_electrons = \frac{\sqrt{signal\_electrons + (dark\_plus\_bias\_sum\text{-}6*bias)*e\_per\_dn + read\_noise^2}}{\sqrt{6}} \qquad 6.$$

Finally, the SNR is computed in two steps. The data sets which are returned as sums have SNR computed using equation 3, with signal and noise electrons as computed in equations 5 and 6. The data sets which are given in full format have the following equation, with the signal and noise electron definitions given in equations 1 and 2 above.

$$SNR = \frac{\sum_{col} signal\_electrons\_perp + \sum_{col} signal\_electrons\_para}{\sqrt{\sum_{col} noise\_electrons\_perp^2 + \sum_{col} noise\_electrons\_para^2}} \quad 7.$$

13.1.7 Conclusion – Relative Calibration

The relative calibration of the Solar Aureole appears in many cases to be good to 1%. However, in some cases it decreases to 2% or even 3%.

Because of the many ways to consider relative calibration, the results are given in a summary table below.

Type of Data	Relative Calibration Along:	Accuracy
Summed Blue	Column	1%
Summed Red	Column	1%
Un-summed Blue	Column 2	Within noise
Un-summed Red	Column 2	Much within noise, some within 1%, all within 2%
Un-summed Red	Column 0	Within 3%
Un-summed Blue	Row 23	Most within 1%, some within 2%
Un-summed Blue	Row 48	Most within 1%, some within 2%
Un-summed Red	Row 23	1%
Un-summed Red	Row 48	2%

The signal shape versus column number is reasonably well represented in all cases, but there appears to be a small systematic increase in intensity for high row numbers in the red.

The derived signal shape versus row number can vary significantly from the true shape, even though each data point may be close to the noise band. This is largely due to the small number of data points over which to make a "shape". However, the variations are only on the order of 1% to 2%. The central rows of the red are within 1%, but the outer rows do not match the true shape as well, with accuracy of 2%.

One reason the relative calibration could be not as good across rows as across columns is that the relative spectral response model and the absolute response model are created for given columns. Therefore, there is more analytic independence between columns than between rows.

13.1.8 Overall Conclusion

The overall conclusion of this analysis is that the absolute calibration models for the Solar Aureole instrument are good to roughly 2%. The relative calibration can be much better, but not in every case. Overall, the relative calibration accuracy is within the 2% region in almost all cases.

13.2 Several Operational Points of Note

13.2.1 Software

With the exception of the timing considerations discussed below, the collection of data from the Solar Aureole system is routine relative to other DISR sub-instruments. Data from the DISR instrument is collected in different types of data cycles, limited in time to about three minutes. These cycles vary throughout the descent and attempt to optimize the mix of vertical and azimuthal resolution in the measurements. However, the Solar Aureole measurements are taken the same way in each standard cycle through the descent, one near the sun and one away from the sun as described in the overview section.

13.2.2 Timing

The timing of the Solar Aureole measurement taken near the sun is especially critical. It is desirable to collect a measurement as near to the sun as possible to determine the aureole characteristics of Titan as a function of altitude. However, the direct solar beam must be kept from the field.

As shown in the drawings and discussion in the overview section, a Shadow Bar shields the SA field from the direct solar beam. In fact, this Shadow Bar defines the SA field of view in that direction. The near sun measurement must be made beginning at a probe azimuth of 2.5 degrees to get as close to the sun as possible with the direct beam out of the field. If the measurement starts at an azimuth less than 2.5 degrees, the direct beam will enter the field. The probe can spin at a rate up to 15 RPM. Therefore, the timing of this measurement collection is critical.

Azimuthal knowledge is provided real time during the descent by data collected from the DISR Sun Sensor. For highest accuracy, the most recent Sun Sensor pulse is used to schedule the SA measurement near the sun. In the case of 15 RPM spin rate, a Sun Sensor central pulse could occur within 28 milliseconds of the time the SA measurement should begin. Therefore, the software allows for scheduling the SA measurement near the sun before the third pulse of a valid Sun Sensor triplet is received. The geometric field of view of the Solar Aureole is mapped in calibration relative to the Sun Sensor central slit to accommodate this measurement. The Shadow Bar knife edge is adjusted during calibration to form the SA field of view.

In short, the mechanical and software links between the Sun Sensor, the Shadow Bar, and Solar Aureole are tight to allow for this near sun measurement for mapping the aureole at Titan.

13.2.3 Electronic Shutter Effect

The electronic shutter effect is caused by the lack of a mechanical shutter in any of the optical systems that use the CCD detector. Rapid shifts of the charge from the imaging half of the chip to the memory half of the chip serve to begin and end the integration. This shift is rapid, but not instantaneous, so a small accumulation of charge occurs during the shift which must be removed from short integrations.

The Solar Aureole data is shifted through the Visible Spectrometer focal plane on its way to the memory zone. This effect was studied and found to be negligible for the Solar Aureole because of the relative brightness of the SA signal compared to the dim visible spectra.

13.2.4 Lossless Compression

The SA data is compressed in a way that produces no loss in information. The compression technique is completely invertible; i.e., an inverse algorithm applied to the compressed data will exactly reproduce the original data. The algorithms designated Psi–14 and Psi–f are used; these algorithms also use Psi–0 and Psi–1 and optionally Psi–2. DISR uses the 8–option Psi–14 noiseless data compressor with lambda equal to 0; hence, DISR does not use Psi–2. These compression schemes will reduce the volume of data to near the intrinsic entropy level of the data in the range of 0 to 5 bits per sample. These schemes are described in the Practical Universal Noiseless Coding paper by Rice.

13.2.5 Auto Exposure Control

Each Solar Aureole measurement, after the first cycle is complete, has an exposure time determined from previous measurements and the probe spin rate. There are two streams of exposure time computation, one for the measurements near the sun, and one for the measurements away from the sun. The first cycle initializes the automatic exposure algorithms for both streams. Note that there is a single exposure time for all four SA channels, so while the exposure time may be optimal for one channel, the other three may be underexposed.

The exposure times are limited so that the probe rotates no more than 3.5 degrees for near the sun measurements and no more than 20 degrees for away from the sun measurements. However, the exposures are also limited by the full well of the CCD detector. The auto exposure algorithm attempts to have a signal at half the full well without saturating the field. It does this as follows:

$$e\_opt=e\_old*(R*F)/X$$

where:
F is the full scale data value (4095)
R is the target full well scale factor (50%)
X is the pixel value at the Nth percentile desired (97%)
E_old is the exposure time for the data used in the statistics
E_opt is the calculated optimum exposure time.

The CCD minimum and maximum exposure times are 0 and 32 seconds with a resolution of 0.5 milliseconds. Additionally, conditions exist in the exposure time algorithm for hard over- or under-saturation cases.

13.2.6 Noise Model

The sources of noise in the Solar Aureole include the read noise, the quantization noise, and the shot noise. The variance in the measured quantity is the sum of the variances of each of these three quantities. Of course, the dark current must be subtracted from the measurements made in the atmosphere, and any uncertainty in the dark values is also included in the

uncertainty of the measured intensities. The noise model is dominated by the signal shot noise for all but the lowest signal levels.

The read noise has been determined from prelaunch and inflight tests to be about 17 electrons. The quantization scale is 30 electrons/data number (DN). The read noise is thus about 0.57 DN. The quantization noise is 1/sqrt(12), or 0.289 DN. The shot noise, be it from dark current or signal, in measuring N electrons is sqrt(N) in electrons, or sqrt (DN*30)/30 DN.

13.2.7 Linearity

The DISR Solar Aureole system has linear response over its entire range from 0 to 4095 data numbers. This section of the report is added solely for clarification. There were some tests performed (June 26, 1996) on different cabling configurations before delivery of DISR to ESA. Some configurations had non-linear response. The non-linear response resulted in SA pixels never achieving the full 4095 scale because they would saturate at lower values. The cabling used in the mission did not have this problem, and over 96% of the SA pixels hit 4095 at some point in the Titan descent (due to lack of real time azimuthal knowledge).

13.2.8 Self Bleedthrough

On 2 August 1996, a test was performed to measure the bleedthrough from one Solar Aureole color to the other. The test was performed in the integrating sphere. First, a red filter was introduced after the light source so that the red channels would be bright, but the blue channels dark. Brights and darks were taken at 4 exposure times. The same series was repeated with a blue filter in the source.

The measurement specifics are in the table below.

Table 13-1 Self Bleedthrough Measurement Details

Measurement #	Shutter State	Exposure Time (ms)	Filter	Saturation Notes
0	Open (bright)	0	Red	
1	Open	65	Red	
2	Open	650	Red	Red Saturated
3	Open	1300	Red	Red Saturated
4	Closed (dark)	0	Red	
5	Closed	65	Red	
6	Closed	650	Red	
7	Closed	1300	Red	
8	Open	0	Blue	
9	Open	170	Blue	
10	Open	1740	Blue	Blue Saturated
11	Open	3480	Blue	Blue Saturated
12	Closed	0	Blue	
13	Closed	170	Blue	
14	Closed	1740	Blue	
15	Closed	3480	Blue	

The method of analysis is to compute the count rates by subtracting bright from dark and removing the electronic shutter effect using the 0 msec exposures.

$$Rate = \frac{(bright - dark) - (bright(0ms) - dark(0ms))}{Integration\_Time}$$

A base count rate in the bright channels was generated to compare with the bleedthrough count rates. This base count rate was derived using the vertical channels (the central two on the CCD). The count rates using measurements 1 and 9 are used since the others are saturated or 0ms exposures. For the bleedthrough into the blue channels from the red, the base count rate is the rate derived using the above equation for measurement 1, averaged over columns 12 through 17. For the bleedthrough into the red channels from the blue, the base count rate is the rate for measurement 9, averaged over columns 6 through 11.

The percent bleedthrough then is the ratio of the count rate in the dark channels to the base count rate in the nearest bright channel. The following is a plot of this bleedthrough for all three integration times for row 23. The +'s are for measurement 1 (with poor SNR); the *'s are for measurement 2; the diamonds are for measurement 3.

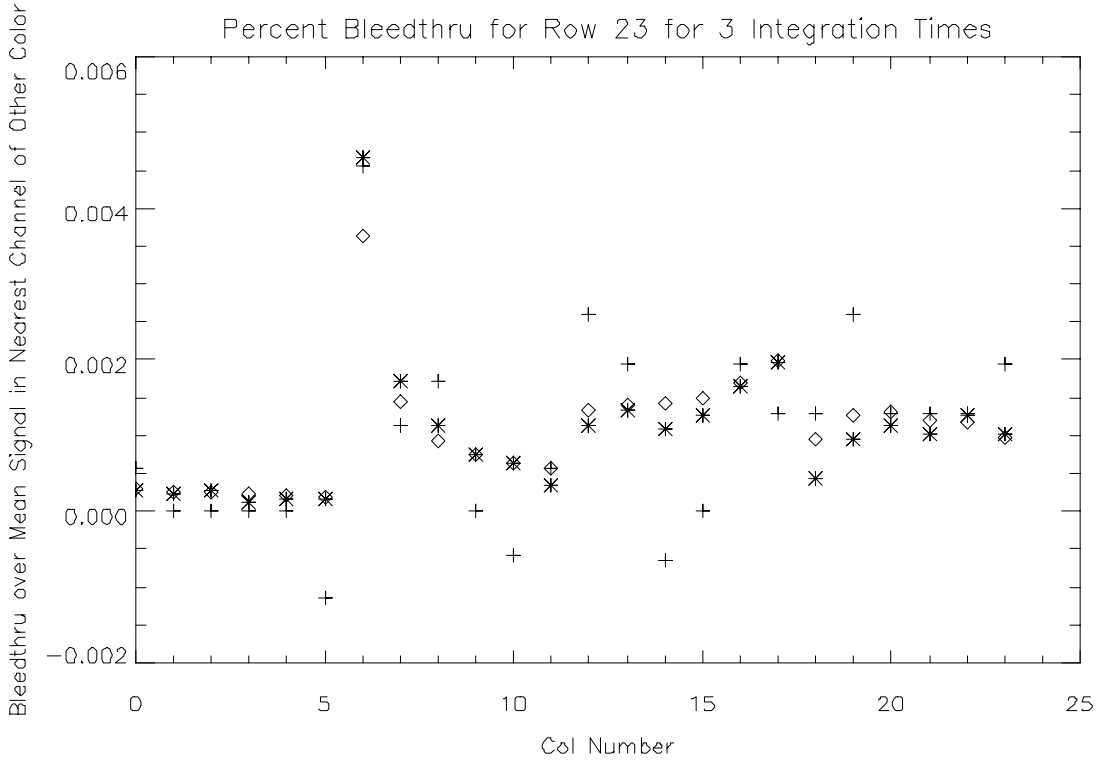

Over all rows and columns, the largest percent bleedthrough is 3.1%. There are 13 occurrences out of 3*24*50=3600 which have percent bleedthrough between 1 and 1.5%. One occurrence is 2.3%, and one is 3.1%. The remaining bleedthrough percentages are under 1%. The larger bleedthroughs occur in the blue vertical column 0 (column 6 in the plots) and the bottom rows of both red channels.

The mean percent bleedthrough was computed as well. This figure of merit is the percent bleedthrough averaged over the rows. It is plotted below with the same legend as the previous plot.

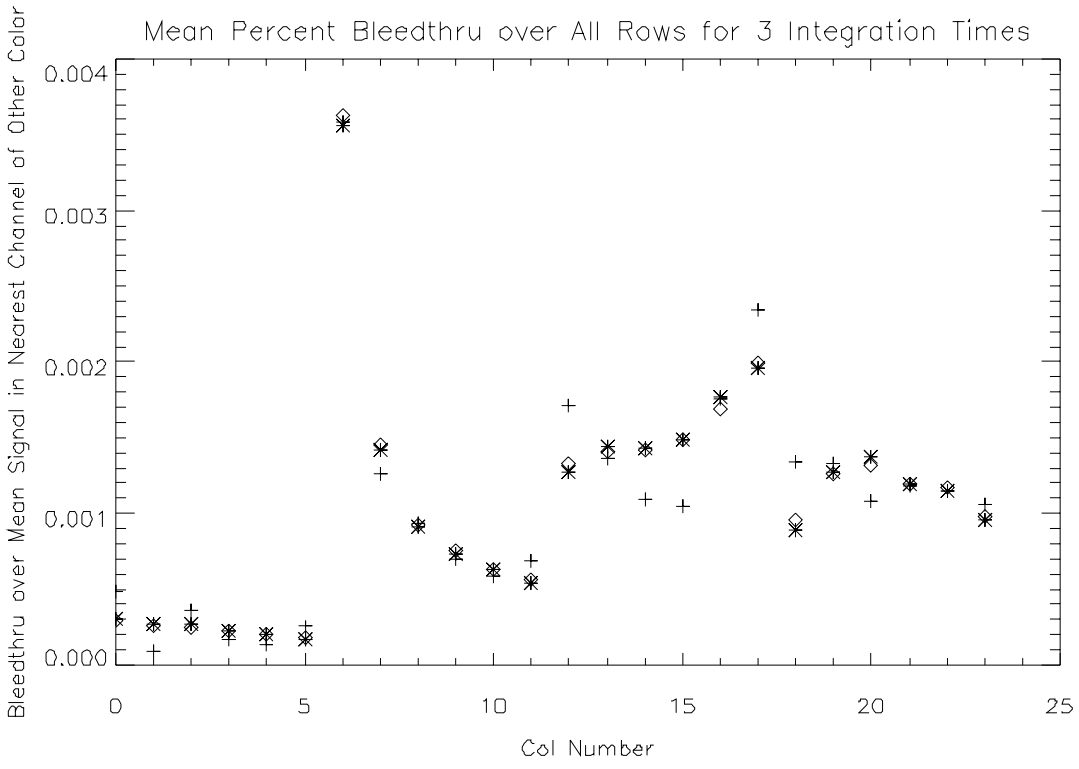

One can see that there is a systematic bleedthrough effect. The structure of this effect is not indicative of the clearing of the serial register, and it appears optical in nature. However, the largest mean bleedthrough is well under 0.5% and can be excluded from any further analysis.

13.3 Geometry and Field of View Derivations

13.3.1 Conversion between Row, Column and DISR Zenith, Azimuth

The zenith and azimuth angles on the sky for each pixel in the 24-column by 50-row array of the Solar Aureole camera was determined by mounting the sensor head on the altitude-azimuth mount in the calibration lab with the system illuminated by light from the collimator. The collimation of the input beam was significantly better than the 1-degree spacing of the pixels of the Solar Aureole array. The sensor head was rotated through various azimuth and zenith angles, and data was recorded that showed the point of light from the collimator in each of the four channels of the Solar Aureole system. We determined the transformation from row and column to zenith and azimuth for each channel of the Solar Aureole system by comparing the centroid of light in row and column on the detector array with the azimuth and zenith at which the sensor head was pointed

Most of the transformation from row and column to zenith and azimuth can be determined by adjusting the constants in the pointing of the Solar Aureole system relative to the coordinate system of the sensor head. The field of view of the Solar Aureole camera is centered at a zenith angle of about 50 degrees. The center of the field of view at this zenith angle is tipped by six degrees toward increasing azimuth, as seen from the drawings for the fiber optic conduit housing shown in Figure 13-2 . In the DISR imaging systems, where the angular

resolution is up to a factor 15 higher than in the Solar Aureole system, distortions in the fiber optic conduit caused negligible distortions in the images. Thus, there is hope that a simple transformation from row and column to zenith and angle can be found by simply adjusting the pointing angles of the Solar Aureole system relative to the basic coordinate system of the sensor head. It is also possible that an additional factor will be necessary to account for the distortion of the field of view of the Solar Aureole optical system, especially in its long direction, where it extends some 50 degrees.

We begin by considering the pointing of the Solar Aureole system as resulting from three separate rotations of coordinates from the basic coordinate system of the sensor head. Let us consider the basic right-handed coordinate system as one in which the z axis points up from the base of the instrument with the y axis pointing toward the direction of zero azimuth. (This system is fixed relative to the DISR sensor head. We will later consider the problem of accommodating situations where the Huygens probe is tipped or tilted relative to the local level.) In this DISR-fixed system, a vector pointing toward a particular zenith angle and azimuth angle will have x, y, z components given by

$$x = -\sin(\text{Zenith angle})\sin(\text{Azimuth angle})$$
$$y = \sin(\text{Zenith angle})\cos(\text{Azimuth angle}) \qquad 15.$$
$$z = \cos(\text{Zenith angle})$$

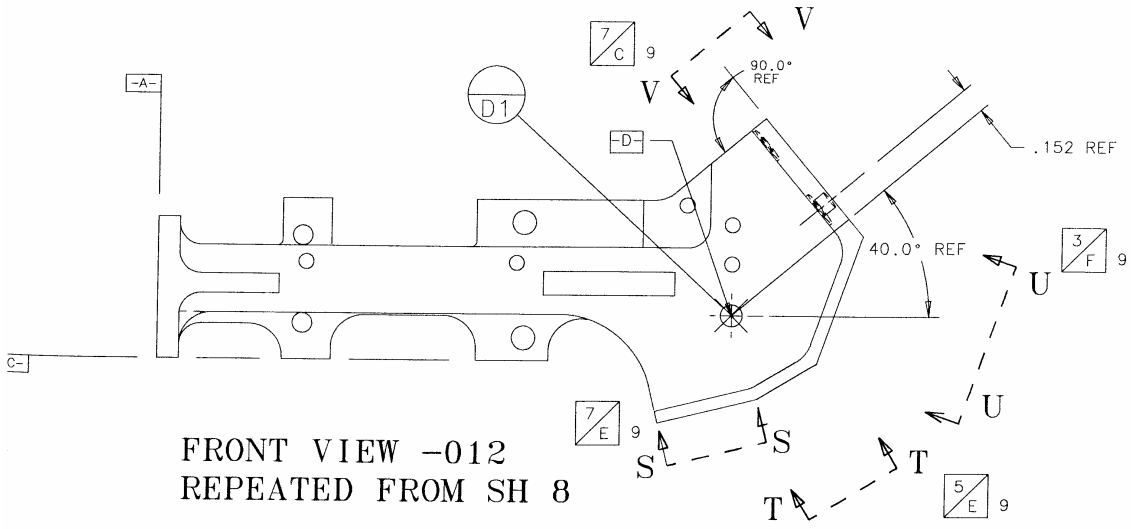

Figure 13-1 Drawing of the fiber optic conduit showing that the face of the surface to which the Solar Aureole optical input optics are attached is tipped up by 40 degrees from horizontal, 50 degrees from vertical.

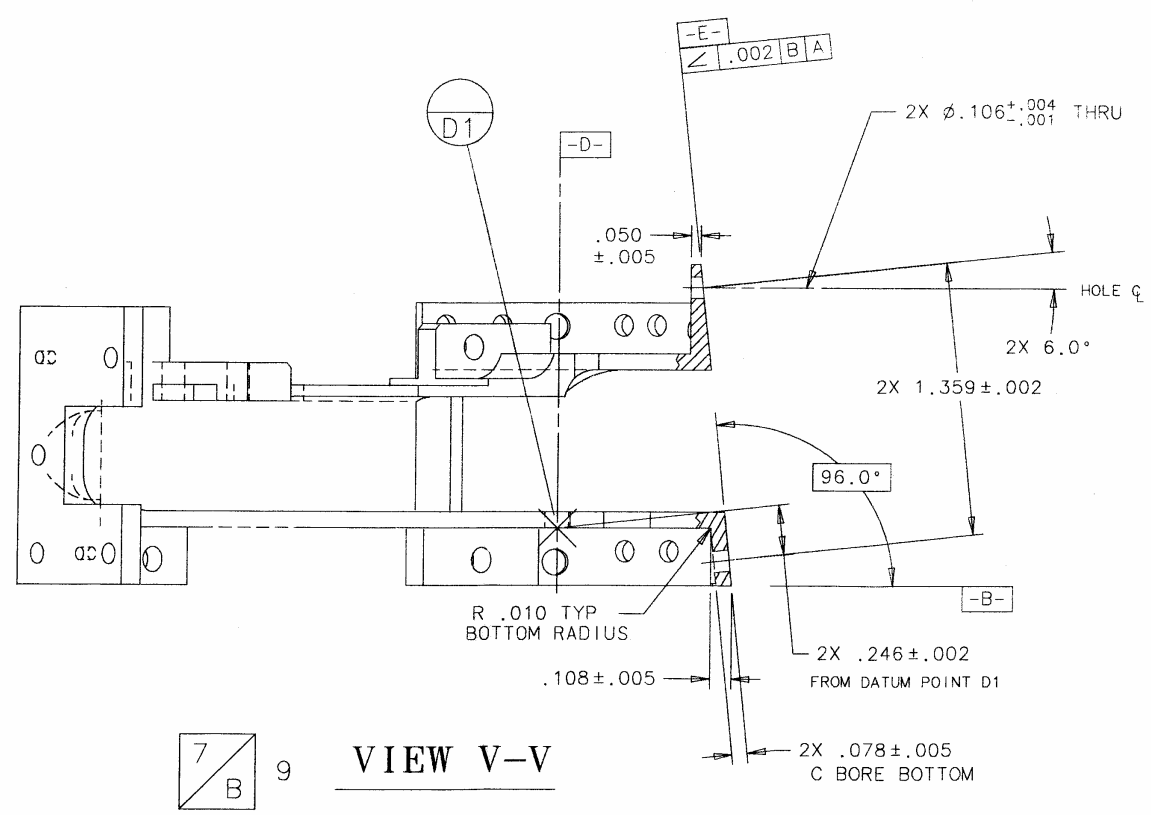

Figure 13-2 Drawing along section V-V shown in Figure 5-1 that shows that the surface to which the input optics of the Solar Aureole system is fastened is tipped by 6 degrees in the direction of increasing azimuth.

The first rotation (to the x', y', z' system) is shown in Figure 13-3 where the tilt of the axis of the Solar Aureole system is centered at 50 degrees zenith angle. In this system, x', y', and z' can be determined from x, y, and z by

$$x' = x,$$
$$y' = \sin(\alpha_0)\, y + \cos(\alpha_0)\, z, \qquad 16.$$
$$z' = -\cos(\alpha_0)\, y + \sin(\alpha_0)\, z,$$

where $\alpha_0 = 50$ degrees is the zenith angle of the center of the Solar Aureole array.

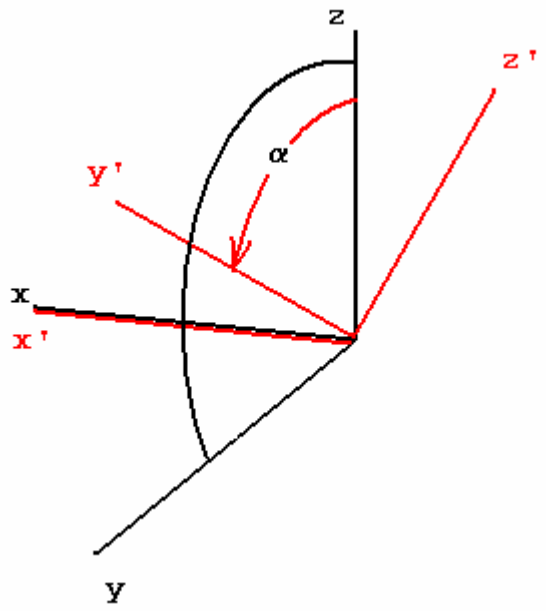

Figure 13-3 This figure shows the relationship of the x, y, z coordinate system of the sensor head to the x', y', z' system in which the y' axis is pointed at the zenith angle of the center of the array (50 degrees).

Next we must account for the rotation by 6 degrees of the center of the Solar Aureole array toward the direction of increasing azimuth angle. The relationship of the rotated x", y", z" system after this rotation is performed to the x', y', z' system is shown in Figure 13-4 . The coordinates of a point in the x", y", z" system is given by

$$x'' = x' \cos(\beta_0) + y' \sin(\beta_0)$$
$$y'' = -x' \sin(\beta_0) + y' \cos(\beta_0) \qquad 17.$$
$$z'' = z'$$

where β_0 is the angle (6 degrees) of rotation toward the direction of increasing azimuth angle.

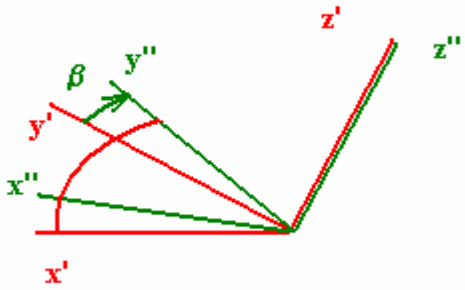

Figure 13-4 This figure shows the relationship of the x", y", z" system after rotation by 6 degrees in the direction if increasing azimuth to the x', y', z' system.

Finally, the optical assembly including the lenses, filters, and polarizers of the Solar Aureole system are bolted to the surface that has been tipped by angles α_0 ,β_0 from the sensor head coordinates system. When this assembly is bolted onto this surface, there is a possibility that the optical assembly will be rotated by a small amount about a line perpendicular to this surface. To account for this possibility, we permit a rotation about the y" axis by a small angle γ. The relationship of this coordinate system x"', y"', z"' to the x", y", z" system is shown in Figure 13-5 . The transformation from the double primed system to the triple primed system is given by

$$x''' = x'' \cos(\gamma) - z'' \sin(\gamma)$$
$$y'''' = y'' \qquad 18.$$
$$z'''' = x'' \sin(\gamma) + z'' \cos(\gamma)$$

Here γ is positive for a counterclockwise rotation looking at the instrument along the y" axis.

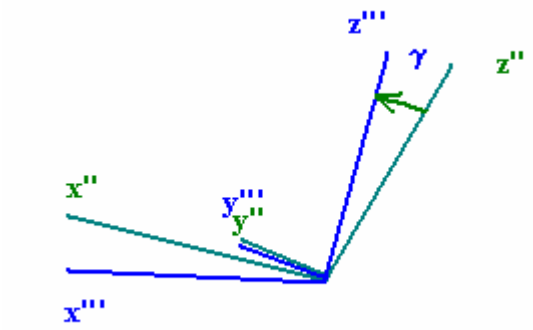

Figure 13-5 The relationship of the x"', y"', z"' system to the x", y", z" system is shown in this figure. The transformation consists of a small rotation about the y" axis as shown.

In the new triple-primed system, the center of the solar array field of view is on the equator of a sphere defined by the x"'-y"' plane. Different columns in the array are identified with different longitudes on this sphere. Different rows are identified with different latitudes on this sphere, with the pole of the sphere pointing in the z"' direction.

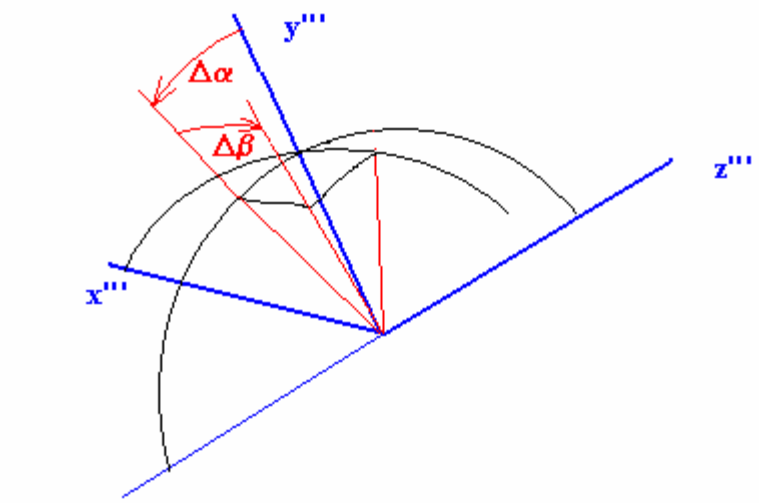

Figure 13-6 The coordinates Δα and Δβ form a latitude-longitude grid in the x"", y"', z"' system, where the pole of the system is the +z"' axis, the Δα represents increasing southern latitude, and Δβ represents the direction of increasing longitude.

Before we convert the angles Δα and Δβ to row and column, we permit a stretch of the angular distance from the center of the array by an amount proportional to the cube of the angular distance from the center of the array. That is, we assume that the center of the array is at the location given by angles $\Delta\alpha_c$ and $\Delta\beta_c$. The vector in this direction thus has components

$$x'''_c = -\cos(\Delta\alpha_c)\sin(\Delta\beta_c)$$
$$y'''_c = \cos(\Delta\alpha_c)\cos(\Delta\beta_c) \qquad 19.$$
$$z'''_c = -\sin(\Delta\alpha_c)$$

The angular distance, δ, of a point given by x"', y"', z"" from the center of the array is

$$\delta = \text{acos}(x''' x'''_c + y''' y'''_c + z''' z'''_c) \qquad 20.$$

This angular distance needs to be increased by an amount proportional to the cube of δ. The direction of the increase is along the great circle from the center of the array to the point x"', y"', z"'. A vector perpendicular to this direction can be formed by computing the cross product of the vector to the center of the array and the x"', y"', z"' vector. This vector Vnx, Vny, Vnz is given by

$$Vnx = (y'''_c\ z''' - z'''_c\ y''')$$
$$Vny = (-x'''_c\ z''' + z'''_c\ x''') \qquad 21.$$
$$Vnz = (x'''_c\ y''' - y'''_c\ x''')$$

This vector needs to be normalized to unit length by setting

$$Wnx = Vnx/ (Vnx^2+Vny^2+Vnz^2)$$
$$Wny = Vny/(Vnx^2+Vny^2+Vnz^2) \qquad 22.$$
$$Wnz = Vnz/(Vnx^2+Vny^2+Vnz^2)$$

The vector in the direction of the increase is given by the cross product of the vector Wn with the vector x''', y''', z''' or

$$\text{Delta } x = Wy\ z''' - Wz\ y'''$$
$$\text{Delta } y = -Wx\ z''' + Wz\ x''' \qquad 23.$$
$$\text{Delta } z = Wx\ y''' - Wy\ x'''$$

Thus the stretched vector xs''', ys''', zs''' is given by adding the vector Delta times the cubic coefficient times the angular distance δ^3 to the vector x''', y''', z'''. This gives

$$xs''' = x''' + \tan[(\delta/20)^3\ CC]\ \text{Delta } x$$
$$ys''' = y''' + \tan[(\delta/20)^3\ CC]\ \text{Delta } y \qquad 24.$$
$$s''' = z''' + \tan[(\delta/20)^3\ CC]\ \text{Delta } z$$

The value CC is the size of the cubic coefficient per 20 degrees of distance off axis. This vector xs''', ys''', zs''' must be normalized to make it a unit vector by dividing each component by the magnitude of the vector to make components xsn''', ysn''', and zsn'''.

Finally, the vector xsn''', ysn''', zsn''' can be projected onto a plane tangent to the sphere perpendicular to the y''' axis. We first evaluate the stretched values of α and β by

$$\alpha s = -\ \text{arc sin}(zs''') \qquad 25.$$

$$\beta s = \text{atan2}(ys''', -xs''') \qquad 26.$$

This projection requires the scale factor of the optical system on axis, sc pixels/degree as well as the value of the central column, cc, and central row, cr. The final column and row numbers are given by

$$\text{Column} = cc + \tan(\beta s)/\tan(1/sc) \qquad 27.$$

$$\text{Row} = cr + \tan(\alpha s)/\tan(1/sc) \qquad 28.$$

The same process can be reversed to transform from given column and row number to the zenith angle and azimuth angle of a particular pixel. The parameters required are collected into the table below.

Table 13-2 Parameters of geometrical transformation of SA observations

Color		Blue	Blue	Red	Red
Direction of E vector		Horizontal	Vertical	Vertical	Horizontal
Columns in SA read		0-5	6-11	12-17	18-23
Columns in full frame		40-45	31-36	23-28	14-19
Definition	Parameter				
Central row	cr	23.432	25.063	25.862	23.943
Central column	cc	3.331	8.343	14.996	21.472
Scale factor in pixels/deg	sc	0.999	1.009	1.028	1.030
Rotation angle	γ	0.69	-0.90	-1.52	1.65
Cubic coefficient per 20 degs.	CC	-0.0196	-0.022	-0.019	-0.020
Center of cubic coeff in α	α_c	-0.10	-0.60	-0.05	-1.00
Center of cubic coeff. in β	β_c	0.0	0.0	0.0	0.0
rms dev. in cols		0.069	0.120	0.082	0.087
rms dev in rows		0.110	0.145	0.075	0.090

To make the computations in the reverse direction, from row and column to azimuth and zenith angle, we begin by finding the stretched values αs and βs from the observed row and column by

$$\beta s = \text{atan}[(\text{column} - cc)*\tan(1/sc)] \quad 29.$$

$$\alpha s = \text{atan}[(\text{row}-cr)*\tan(1/sc)] \quad 30.$$

The stretched vector to the point in the triple primed system is then

$$xs''' = -\cos(\alpha s)\sin(\beta s)$$
$$ys''' = \cos(\alpha s)\cos(\beta s) \quad 31.$$
$$zs''' = \sin(\alpha s)$$

We next must find the vector in the triple-primed system without the cubic stretch. To do this, we must find the components of the unit vector along which the change in position will be applied. This direction is given by a vector along the great circle connecting the center of the aberrations and the stretched vector. This direction is given by taking the cross product of the stretched vector with the vector in the direction of the center of the aberrations,

normalizing it, and taking the cross product of this vector with the stretched vector. The first cross product vector is given by

$$\begin{aligned} Vxn &= (ys''' \; zc''' - zs''' \; yc''') \\ Vyn &= (-xs''' \; zc''' + zs''' \; zc''') \\ Vzn &= (xs''' \; yc''' - ys''' \; xc''') \end{aligned} \qquad 32.$$

This vector can be normalized to give

$$\begin{aligned} Wxn &= Vxn/(Vxn^2 + Vyn^2 + Vzn^2) \\ Wyn &= Vyn/(Vxn^2 + Vyn^2 + Vzn^2) \\ Wzn &= Vzn/(Vxn^2 + Vyn^2 + Vzn^2) \end{aligned} \qquad 33.$$

The vector along the direction of the change to the stretched vector is given by the cross product of this vector with the stretched vector, or

$$\begin{aligned} Delta\ x^* &= Wyn\ zs''' - Wzn\ y''' \\ Delta\ y^* &= -Wxn\ zs''' + Wzn\ x''' \\ Delta\ z^* &= Wxn\ ys''' - Wyn\ xs''' \end{aligned} \qquad 34.$$

The magnitude of the change is related to the angular distance between the stretched vector and the center of the field of aberrations given by equation 19. This angular distance is given by

$$\delta^* = acos(xs''' \; x'''_c + ys''' \; y''''_c + zs''' \; z'''_c) \qquad 35.$$

The cubic coefficient must be applied to the angular distance between the center of the array and the unstretched vector (δ in equation 20.), not the angular distance between the center of the array and the stretched vector (δ^* in equation 35.). The relation between these two angles is given by the cubic expression

$$\delta^* = \delta - atan((\delta/20)^3 * CC) \qquad 36.$$

In order to proceed in the reverse direction, we need an approximation for the difference between the unstretched and the stretched angular distances. The zero-level approximation is to take the unstretched distance as the stretched distance in the expression for the difference between these angular distances, or

$$(\delta - \delta^*)_0 = atan((\delta^*/20)^3 * CC) \qquad 37.$$

The higher-level approximations are given by

$$(\delta - \delta^*)_n = atan[\{\delta^* + (\delta - \delta^*)_{n-1}\}/20)^3 * CC] \qquad 38.$$

We continue to the third-order approximation, where the error is less than 0.01 degrees.

The unstretched vector in the triple primed system is then

$$\begin{aligned} x''' &= xs''' + \tan[(\{\delta^{*}+(\delta-\delta^{*})_3\}/20)^3\ CC]\ \text{Delta } x^{*} \\ y''' &= ys''' + \tan[(\{\delta^{*}+(\delta-\delta^{*})_3\}/20)^3\ CC]\ \text{Delta } y^{*} \\ z''' &= zs''' + \tan[(\{\delta^{*}+(\delta-\delta^{*})_3\}/20)^3\ CC]\ \text{Delta } z^{*} \end{aligned} \qquad 39.$$

This vector must be normalized to unit length to give the vector xn''', yn''', zn''' to the point in the triple primed system.

Now this vector can be rotated from the triple primed system to the double primed system according to

$$\begin{aligned} x'' &= xn''' \cos(\gamma) - zn''' \sin(\gamma) \\ y'' &= yn''' \\ z'' &= xn'''\sin(\gamma) + zn'''\cos(\gamma) \end{aligned} \qquad 40.$$

The vector can next be rotated from the double primed system to the primed system, and then to the unprimed system as follows.

$$\begin{aligned} x' &= x'' \cos(\beta_0) - y'' \sin(\beta_0) \\ y' &= x'' \sin(\beta_0) + y'' \cos(\beta_0) \\ z' &= z'' \end{aligned} \qquad 41.$$

and

$$\begin{aligned} x &= x' \\ y &= y'\sin(\alpha_0) - z' \cos(\alpha_0) \\ z &= y' \cos(\alpha_0) + z' \sin(\alpha_0) \end{aligned} \qquad 42.$$

Finally, the azimuth and zenith angle of the point can be obtained from

$$\text{Zenith} = \text{acos}(z) \qquad 43.$$

$$\text{Azimuth} = \text{atan2}(y, -x) \qquad 44.$$

In order to determine the constants required, we mounted the sensor head on the altitude-azimuth mount, illuminated the sensor head with collimated light, and recorded images in the Solar Aureole system for a range of zenith and azimuth angles of the incoming beam relative to the basic coordinate system of the sensor head. We then subtracted the dark current from each image and divided the net counts by the integration time and the pattern of absolute responsivity of each pixel in the Solar Aureole array obtained from the reduction of the absolute responsivity data shown in a section below.

We next found the centroid of light in row and column for each azimuth and zenith angle at which the sensor head was illuminated. The data for each of the four SA channels is given in

Table 13-3 through Table 13-6 . We next adjusted the pointing parameters to minimize the residuals between the observed location of the centroids of light from each measurement with the row and column number computed by the model equations describing the geometry above. Note that each of the parameters has a unique effect on the residuals. If the central row or column number is incorrect, the entire pattern of residuals is shifted up or down from zero. When the rotation angle γ is changed, the pattern of column residuals rotates away from a horizontal line in the residual plot, either sloping up with column number or down with column number rather than remaining horizontal. When the scale factor is changed, the pattern of residuals in a plot of row residual plotted versus row is not flat near the central row, but slopes either upward or downward with row. When the cubic parameter for optical aberrations is changed, the row residuals at very small and very large row numbers move upward or downward by large amounts. Finally, the center of the aberrations in $\Delta\alpha$ increases the residual at one end of the array while decreasing the residual at the other end. The value of the cubic coefficient and the direction of the center of the aberrations must both be adjusted together to minimize the residuals at both the low row and high row number ends of the array. When all six parameters are optimally adjusted, the root mean square residuals in both row and column can be decreased to about 0.1 pixel. This is about the accuracy to which the centroid algorithm gives the location of the center of light from the original data.

Table 13-3 Observed Centroids in Column and Row when the Solar Aureole was Stimulated by a Point Source at Various Azimuth and Zenith angles

Azimuth	Zenith	Observed Column	Observed Row	Model Column	Model Row	Column Error	Row Error
3.00	70.00	0.71	42.95	0.752	42.946	0.042	-0.004
4.00	70.00	1.76	42.91	1.687	42.912	-0.073	0.002
5.00	70.00	2.61	42.83	2.622	42.861	0.012	0.031
6.00	70.00	3.47	42.77	3.557	42.794	0.087	0.024
7.00	70.00	4.40	42.71	4.491	42.712	0.091	0.002
6.00	71.00	3.54	43.95	3.639	43.714	0.099	-0.236
6.00	71.50	3.76	44.09	3.681	44.170	-0.079	0.080
6.00	72.00	3.67	44.74	3.722	44.623	0.052	-0.117
6.00	72.50	3.85	45.01	3.762	45.073	-0.088	0.063
6.00	73.00	3.81	45.47	3.803	45.520	-0.007	0.050
6.00	73.50	3.90	45.98	3.844	45.964	-0.056	-0.016
6.00	74.00	3.90	46.23	3.885	46.404	-0.015	0.174
6.00	74.50	3.94	46.92	3.925	46.842	-0.015	-0.078
6.00	75.00	3.96	47.14	3.966	47.275	0.006	0.135
6.00	75.50	3.97	47.94	4.006	47.705	0.036	-0.235
6.00	76.00	3.98	48.09	4.046	48.131	0.066	0.041
10.00	27.00	2.04	0.77	2.073	0.873	0.033	0.103
10.00	27.50	2.06	1.22	2.135	1.317	0.075	0.097
10.00	28.00	2.13	1.84	2.197	1.763	0.067	-0.077
10.00	28.50	2.15	2.03	2.259	2.213	0.109	0.183
10.00	29.00	2.23	2.59	2.322	2.666	0.092	0.076
10.00	29.50	2.30	3.01	2.384	3.121	0.084	0.111
10.00	30.00	2.43	3.33	2.447	3.579	0.017	0.249
10.00	30.50	2.56	4.01	2.510	4.039	-0.050	0.029
4.00	60.00	0.98	33.38	1.005	33.318	0.025	-0.062
5.00	60.00	1.93	33.37	1.868	33.269	-0.062	-0.101
6.00	60.00	2.74	33.22	2.731	33.207	-0.009	-0.013
7.00	60.00	3.55	33.10	3.593	33.134	0.043	0.034
8.00	60.00	4.41	33.04	4.455	33.050	0.045	0.010
5.00	50.00	1.02	23.36		23.351		-0.009
6.00	50.00	1.99	23.35	1.924	23.295	-0.066	-0.055
7.00	50.00	2.80	23.18	2.686	23.230	-0.114	0.050
8.00	50.00	3.34	23.16	3.448	23.156	0.108	-0.004
9.00	50.00	4.16	23.05	4.209	23.074	0.049	0.024
5.00	40.00	0.60	13.40	0.515	13.435	-0.085	0.035
6.00	40.00	1.04	13.37	1.156	13.383	0.116	0.013
7.00	40.00	1.85	13.34	1.797	13.325	-0.053	-0.015
8.00	40.00	2.53	13.23	2.437	13.261	-0.093	0.031
9.00	40.00	3.02	13.24	3.076	13.191	0.056	-0.049
10.00	40.00	3.84	13.03	3.714	13.115	-0.126	0.085
11.00	40.00	4.34	12.99	4.351	13.033	0.011	0.043
7.00	30.00	1.01	3.91	0.957	3.753	-0.053	-0.157

8.00	30.00	1.52	3.92	1.454	3.699	-0.066	-0.221
9.00	30.00	2.00	3.85	1.951	3.641	-0.049	-0.209
10.00	30.00	2.57	3.81	2.447	3.579	-0.123	-0.231
11.00	30.00	3.00	3.66	2.942	3.513	-0.058	-0.147
12.00	30.00	3.49	3.45	3.436	3.443	-0.054	-0.007
13.00	30.00	4.00	3.24	3.929	3.370	-0.071	0.130
14.00	30.00	4.37	3.17	4.420	3.293	0.050	0.123

Note: Model and residual values are omitted for pixels near the edge of the array.

Table 13-4 Observed Centroids in Column and Row when the Solar Aureole was Stimulated by a Point Source at Various Azimuth and Zenith angles

Azimuth	Zenith	Observed Column	Observed Row	Model Column	Model Row	Column Error	Row Error
5.00	70.00	7.02	44.18	7.097	44.394	0.077	0.214
6.00	70.00	8.00	44.16	8.032	44.358	0.032	0.198
7.00	70.00	8.99	44.13	8.967	44.306	-0.023	0.176
8.00	70.00	9.99	44.06	9.901	44.237	-0.089	0.177
6.00	71.00	8.03	45.14	8.089	45.251	0.059	0.111
6.00	71.50	8.04	45.84	8.118	45.692	0.078	-0.148
6.00	72.00	8.08	46.05	8.146	46.130	0.066	0.080
6.00	72.50	8.07	46.86	8.174	46.563	0.104	-0.297
6.00	73.00	8.11	47.02	8.203	46.993	0.093	-0.027
6.00	73.50	8.14	47.48	8.231	47.418	0.091	-0.062
6.00	74.00	8.22	47.98	8.259	47.839	0.039	-0.141
6.00	74.50	8.25	48.23	8.288	48.255	0.038	0.025
10.00	25.50	7.43	0.67	7.562	1.057	0.132	0.387
10.00	26.00	7.57	1.21	7.611	1.485	0.041	0.275
10.00	26.50	7.69	1.95	7.660	1.917	-0.030	-0.033
10.00	27.00	7.75	2.22	7.710	2.353	-0.040	0.133
10.00	27.50	7.88	2.97	7.759	2.793	-0.121	-0.177
10.00	28.00	7.89	3.11	7.808	3.236	-0.082	0.126
10.00	28.50	7.91	3.86	7.858	3.684	-0.052	-0.176
10.00	29.00	7.97	4.01	7.908	4.134	-0.062	0.124
10.00	29.50	7.96	4.55	7.958	4.589	-0.002	0.039
10.00	30.00	7.99	5.00	8.008	5.046	0.018	0.046
10.00	30.50	7.99	5.54	8.058	5.506	0.068	-0.034
5.00	60.00	6.88	34.97	6.596	34.908	-0.284	-0.062
6.00	60.00	7.81	34.97	7.466	34.872	-0.344	-0.098
7.00	60.00	8.45	34.88	8.336	34.824	-0.114	-0.056
8.00	60.00	9.07	34.60	9.205	34.764	0.135	0.164
9.00	60.00	10.01	34.55	10.074	34.691	0.064	0.141
6.00	50.00	6.97	24.84	6.926	24.885	-0.044	0.045
7.00	50.00	7.93	24.80	7.698	24.841	-0.232	0.041
8.00	50.00	8.73	24.85	8.469	24.788	-0.261	-0.062
9.00	50.00	9.10	24.73	9.239	24.727	0.139	-0.003
10.00	50.00	10.00	24.71	10.008	24.657	0.008	-0.053

7.00	40.00	7.01	14.92	7.077	14.809	0.067	-0.111
8.00	40.00	7.96	14.96	7.725	14.763	-0.235	-0.197
9.00	40.00	8.11	14.94	8.372	14.711	0.262	-0.229
10.00	40.00	9.00	14.88	9.018	14.653	0.018	-0.227
11.00	40.00	9.69	14.62	9.664	14.589	-0.026	-0.031
12.00	40.00	10.15	14.30	10.308	14.519	0.158	0.219
8.00	30.00	6.94	5.14	7.007	5.135	0.067	-0.005
9.00	30.00	7.51	5.15	7.508	5.092	-0.002	-0.058
10.00	30.00	7.98	5.08	8.008	5.046	0.028	-0.034
11.00	30.00	8.44	5.05	8.508	4.995	0.068	-0.055
12.00	30.00	8.99	5.00	9.006	4.942	0.016	-0.058
13.00	30.00	9.43	4.99	9.503	4.884	0.073	-0.106
14.00	30.00	9.98	4.99	9.999	4.823	0.019	-0.167

Table 13-5Observed Centroids in Column and Row when the Solar Aureole was Stimulated by a Point Source at Various Azimuth and Zenith angles

Azimuth	Zenith	Observed Column	Observed Row	Model Column	Model Row	Column Error	Row Error
5.00	70.00	13.53	45.78	13.492	45.856	-0.038	0.076
6.00	70.00	14.47	45.85	14.459	45.828	-0.011	-0.022
7.00	70.00	15.29	45.78	15.425	45.784	0.135	0.004
8.00	70.00	16.45	45.59	16.390	45.723	-0.060	0.133
6.00	71.00	14.48	46.75	14.507	46.785	0.027	0.035
6.00	71.50	14.53	47.27	14.531	47.259	0.001	-0.011
6.00	72.00	14.50	47.62	14.555	47.731	0.055	0.111
6.00	72.50	14.54	48.15	14.579	48.200	0.039	0.050
10.00	25.50	14.52	1.09	14.459	1.191	-0.061	0.101
10.00	26.00	14.57	1.45	14.505	1.644	-0.065	0.194
10.00	26.50	14.57	2.10	14.551	2.100	-0.019	0.000
10.00	27.00	14.59	2.51	14.597	2.560	0.007	0.050
10.00	27.50	14.64	2.97	14.643	3.023	0.003	0.053
10.00	28.00	14.64	3.48	14.689	3.488	0.049	0.008
10.00	28.50	14.75	3.94	14.735	3.957	-0.015	0.017
10.00	29.00	14.71	4.45	14.782	4.428	0.072	-0.022
10.00	29.50	14.82	4.82	14.828	4.902	0.008	0.082
10.00	30.00	14.78	5.38	14.874	5.379	0.094	-0.001
10.00	30.50	14.91	5.82	14.921	5.858	0.011	0.038
5.00	60.00	13.16	36.05	13.100	35.924	-0.060	-0.126
6.00	60.00	13.98	36.03	13.991	35.896	0.011	-0.134
7.00	60.00	14.81	35.93	14.881	35.856	0.071	-0.074
6.00	50.00	13.53	25.62	13.554	25.665	0.024	0.045
7.00	50.00	14.42	25.61	14.341	25.628	-0.079	0.018
8.00	50.00	15.30	25.64	15.127	25.583	-0.173	-0.057
9.00	50.00	16.05	25.59	15.912	25.529	-0.138	-0.061
6.00	40.00	13.20	15.42	13.158	15.438	-0.042	0.018
7.00	40.00	13.67	15.44	13.819	15.404	0.149	-0.036

8.00	40.00	14.48	15.44	14.480	15.365	0.000	-0.075
9.00	40.00	15.27	15.27		15.365		0.095
10.00	40.00	15.74	15.32	15.799	15.267	0.059	-0.053
7.00	30.00	13.38	5.52	13.333	5.493	-0.047	-0.027
8.00	30.00	13.66	5.53	13.847	5.459	0.187	-0.071
9.00	30.00	14.51	5.50	14.361	5.421	-0.149	-0.079
10.00	30.00	14.80	5.43	14.874	5.379	0.074	-0.051
11.00	30.00	15.56	5.44	15.387	5.333	-0.173	-0.107
12.00	30.00	15.84	5.40	15.898	5.283	0.058	-0.117

Note: The entry in red is believed to be in error, and has not been used in computing the residual in column.

Table 13-6 Observed Centroids in Column and Row when the Solar Aureole was Stimulated by a Point Source at Various Azimuth and Zenith angles

Azimuth	Zenith	Observed Column	Observed Row	Model Column	Model Row	Column Error	Row Error
3.00	70.00	18.90	43.93	19.169	43.893	0.269	-0.037
4.00	70.00	20.05	43.90	20.124	43.842	0.074	-0.058
5.00	70.00	21.05	43.83	21.080	43.774	0.030	-0.056
6.00	70.00	22.01	43.79	22.035	43.690	0.025	-0.100
7.00	70.00	22.96	43.49		43.588		0.098
6.00	71.00	22.23	44.72	22.135	44.611	-0.095	-0.109
6.00	71.50	22.22	45.15	22.185	45.067	-0.035	-0.083
6.00	72.00	22.29	45.55	22.234	45.520	-0.056	-0.030
6.00	72.50	22.32	46.07	22.284	45.969	-0.036	-0.101
6.00	73.00	22.37	46.44	22.333	46.414	-0.037	-0.026
6.00	73.50	22.42	46.91	22.382	46.856	-0.038	-0.054
6.00	74.00	22.45	47.35	22.431	47.294	-0.019	-0.056
6.00	74.50	22.48	47.84	22.479	47.728	-0.001	-0.112
10.00	28.00	19.86	1.34	19.921	1.450	0.061	0.110
10.00	28.50	19.94	1.89	19.993	1.920	0.053	0.030
10.00	29.00	20.04	2.30	20.066	2.393	0.026	0.093
10.00	29.50	20.12	2.83	20.139	2.869	0.019	0.039
10.00	30.00	20.08	3.36	20.212	3.347	0.132	-0.013
10.00	30.50	20.31	3.83	20.285	3.828	-0.025	-0.002
5.00	60.00	20.03	33.99	20.138	34.061	0.108	0.071
6.00	60.00	21.03	33.92	21.024	33.984	-0.006	0.064
7.00	60.00	21.99	33.82	21.909	33.894	-0.081	0.074
8.00	60.00	22.59	33.73		33.792		0.062
9.00	60.00	22.97	33.52		33.678		0.158
6.00	50.00	19.92	23.77	20.019	23.825	0.099	0.055
7.00	50.00	20.86	23.70	20.804	23.745	-0.056	0.045
8.00	50.00	21.62	23.67	21.588	23.657	-0.032	-0.013
9.00	50.00	22.35	23.58	22.370	23.559	0.020	-0.021
10.00	50.00	22.71	23.41		23.453		0.043
11.00	50.00	22.99	23.36		23.338		-0.022

7.00	40.00	19.67	13.43	19.712	13.516	0.042	0.086
8.00	40.00	20.36	13.37	20.372	13.438	0.012	0.068
9.00	40.00	21.13	13.28	21.031	13.354	-0.099	0.074
10.00	40.00	21.88	13.18	21.689	13.264	-0.191	0.084
11.00	40.00	22.56	13.06	22.346	13.168	-0.214	0.108
12.00	40.00	22.81	12.82		13.065		0.245
8.00	30.00	19.12	3.65	19.186	3.492	0.066	-0.158
9.00	30.00	19.71	3.53	19.699	3.422	-0.011	-0.108
10.00	30.00	20.10	3.45	20.212	3.347	0.112	-0.103
11.00	30.00	20.66	3.37	20.723	3.269	0.063	-0.101
12.00	30.00	21.30	3.24	21.234	3.186	-0.066	-0.054
13.00	30.00	21.76	3.18	21.743	3.099	-0.017	-0.081
14.00	30.00	22.33	3.09	22.250	3.009	-0.080	-0.081
15.00	30.00	22.66	2.89		2.914		0.024
16.00	30.00	22.89	2.69		2.816		0.126
17.00	30.00	22.99	2.91		2.714		-0.196

Note: Model and residual values are omitted for pixels near the edge of the array.

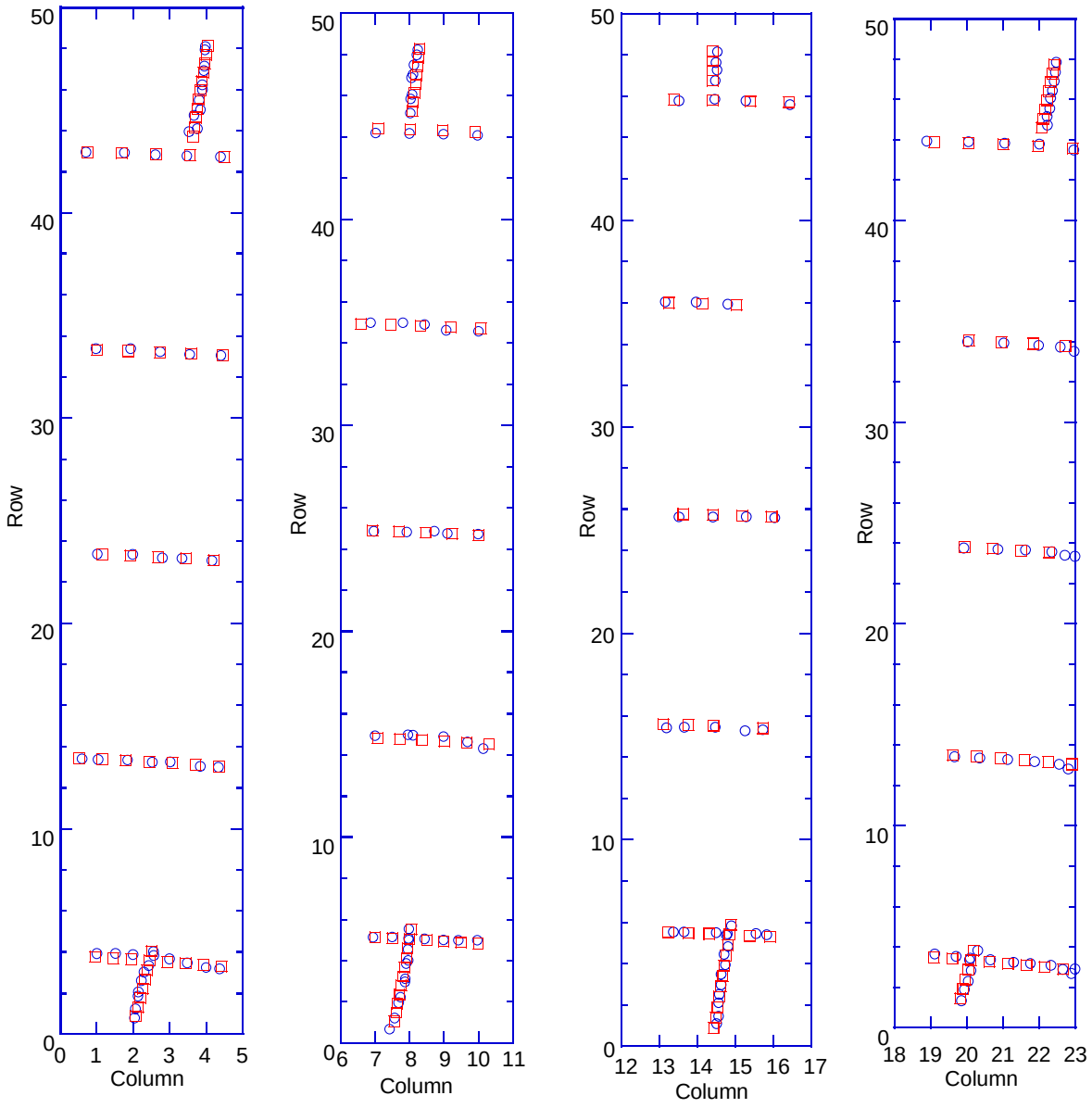

Figure 13-7 The observed centroid in row and column is plotted by blue circles, while the model location of each point is plotted by red squares for each of the points observed in the four channels of the Solar Aureole system.

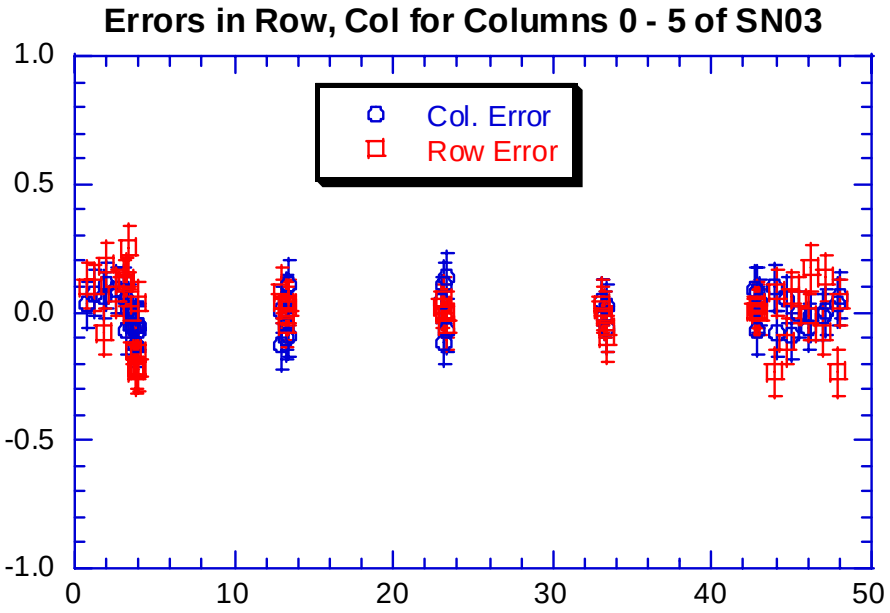

Figure 13-8 The pattern of residuals in row (red squares) and column (blue circles) is plotted versus observed row for the model to the Solar Aureole geometry for columns 0 to 5. The rms residual is about 0.07 in columns and 0.11 in row.

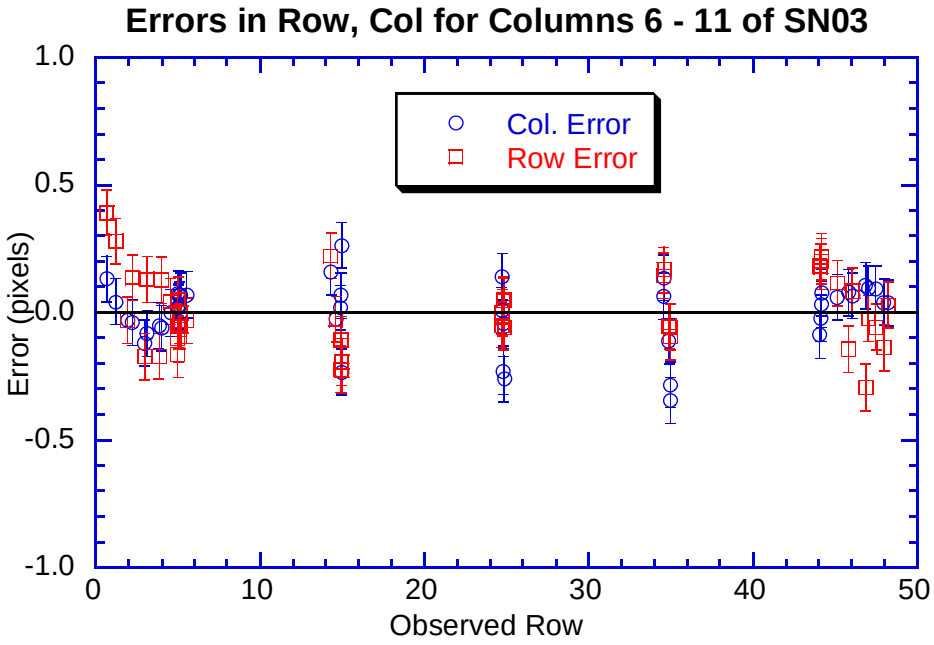

Figure 13-9 The pattern of residuals in row (red squares) and column (blue circles) is plotted versus observed row for the model to the Solar Aureole geometry for columns 6 to 11. The rms residual is about 0.12 in columns and 0.15 in row.

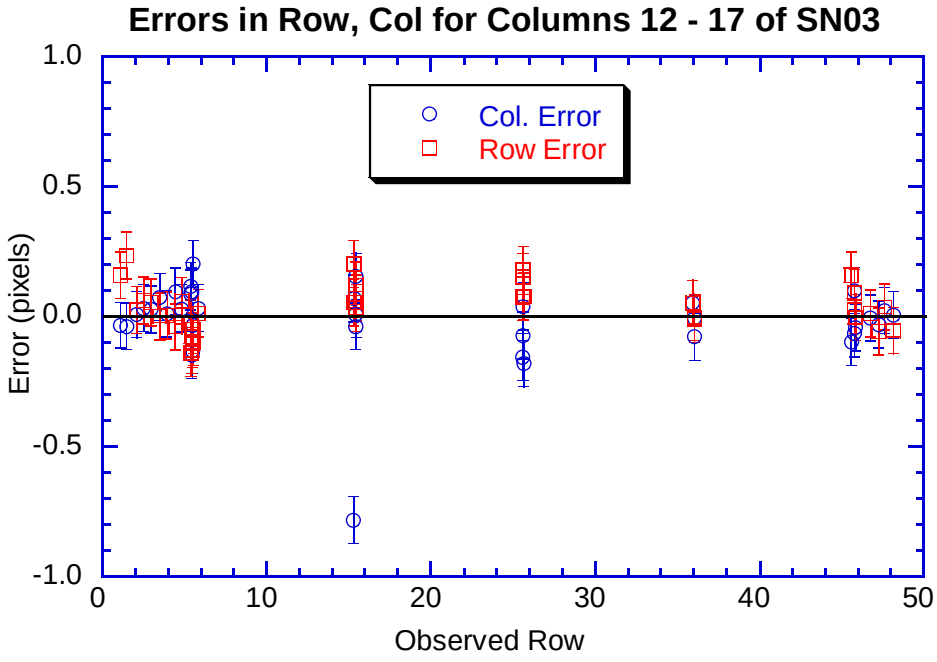

Figure 13-10 The pattern of residuals in row (red squares) and column (blue circles) is plotted versus observed row for the model to the Solar Aureole geometry for columns 12 to 17. The rms residual is about 0.08 in columns and 0.08 in row.

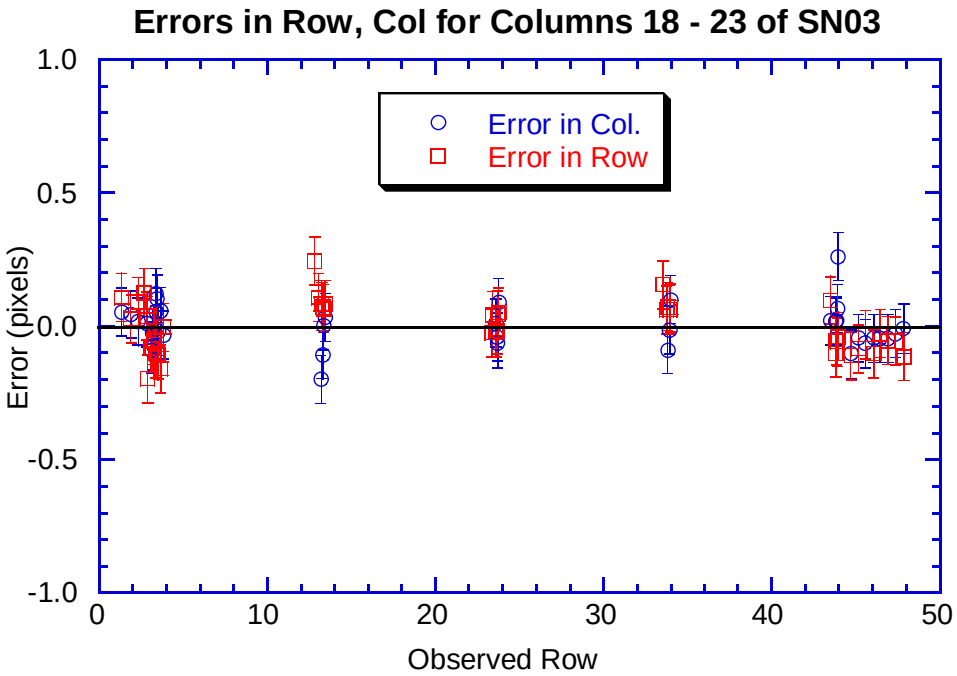

Figure 13-11 The pattern of residuals in row (red squares) and column (blue circles) is plotted versus observed row for the model to the Solar Aureole geometry for columns 18 to 23. The rms residual is about 0.09 in columns and 0.09 in row.

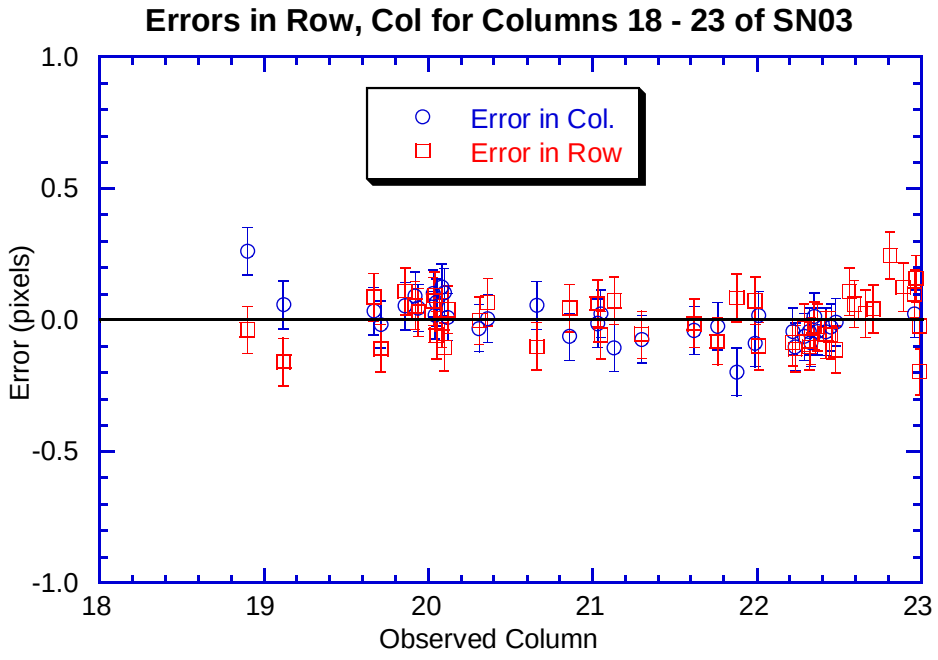

Figure 13-12 The pattern of residuals in row (red squares) and column (blue circles) is plotted versus observed column for the model to the Solar Aureole geometry for columns 18 to 23. The rms residual is about 0.08 in columns and 0.09 in row. Note that the points with centroids at observed columns within 0.5 column of the edge of the array have been omitted because of the systematic errors in locating the centroid of points where the peak of light is within 0.5 pixel of the edge of the array.

13.3.2 Conversion between DISR Zenith, Azimuth to True Zenith, Azimuth

In the DISR x, y, z coordinate system, z points upward from the baseplate of the instrument, and the sun is in the y-z plane. The DISR instrument (and the entire probe) is constrained by the parachute harness to rotate about the DISR z axis. The DISR measures the solar zenith angle of the sun from the DISR z axis, SZA_{DISR}, on every rotation of the probe. The vector to the sun in the x, y, z system is given by

$$x_{sun} = 0$$
$$y_{sun} = \sin(SZA_{DISR}) \qquad 45.$$
$$_{sun} = \cos(SZA_{DISR})$$

Now suppose that the DISR z axis does not point vertically upward, but that the probe is tilted. Let the vector pointing vertically upward be at an angle θ_1 in the y-z plane (positive measured from the DISR z axis away from the vector to the sun), and at an angle θ_2 perpendicular to the plane containing the z axis and the vector to the sun. Let θ_2 be positive in the direction of decreasing azimuth. Now the vector to the vertical in the x, y, z system is given by

$$x_v = -\sin(\theta_2)$$
$$y_v = -\cos(\theta_2)\sin(\theta_1) \qquad 46.$$
$$z_v = \cos(\theta_2)\cos(\theta_1)$$

We now define a new coordinate system x*, y*, z* where z* points vertically upward and the vector to the sun lies in the y*-z* plane. In this system, a unit vector i* in the direction x* is given by the (normalized) cross product of the vector to the sun and the vector to the vertical. The unit vector k* along the z* direction is given by the vertical vector. That is,

$$\begin{aligned} i^* = &(y_{sun}\, x_v - z_{sun}\, y_v)/\sin(SZA_{DISR})\ \ i \\ &+(-x_{sun}\, z_v + z_{sun}\, x_v)/\sin(SZA_{DISR})\ \ j \\ &+(x_{sun}\, y_v - y_{sun}\, x_v)/\sin(SZA_{DISR})\ \ k \end{aligned} \qquad 47.$$

where i, j, k are unit vectors along the directions of the x, y, and z axes. Similarly, a unit vector j* along the y* axis is given by the cross product of the vertical vector crossed with i*. That is

$$\begin{aligned} j^* = &(y_v\, i^*_x - z_v\, i^*_y)\ \ i \\ &+ (-x_v\, i^*_z + z_v\, i^*_x)\ \ j \\ &+ (x_v\, i^*_y - y_v\, i^*_x)\ \ k \end{aligned} \qquad 48.$$

Finally, the unit vector k* along the direction z* is given by the vertical vector,

$$k^* = x_v\, i + y_v\, j + z_v\, k \qquad 49.$$

Now any vector x i +y j +z k can be converted to the vector in the x*, y*, z* system by the use of equations 47. through 49., or

$$\begin{aligned} x^* = &(y_{sun}\, x_v - z_{sun}\, y_v)\, x \\ &+(-x_{sun}\, z_v + z_{sun}\, x_v)\, y \\ &+(x_{sun}\, y_v - y_{sun}\, x_v)\, z \\ y^* = &\ (y_v\, i^*_x - z_v\, i^*_y)\, x \\ &+ (-x_v\, i^*_z + z_v\, i^*_x)\, y \\ &+ (x_v\, i^*_y - y_v\, i^*_x)\, z \\ z^* = &\ x_v\, x + y_v\, y + z_v\, z \end{aligned} \qquad 50.$$

The true zenith and azimuth angles to the point at coordinates x, y, z can now be evaluated as

$$\text{Zenith Angle}_{true} = \text{acos}(z^*) \qquad 51.$$
$$\text{Azimuth Angle}_{true} = \text{atan2}(y^*, -x^*) \qquad 52.$$

The reverse transformation from the true zenith and angles on the sky to the x, y, z coordinates in the tipped DISR coordinate system is also possible given the relations above.

Here we begin by determining the x*, y*, z* coordinates of the point at true zenith and true azimuth angle. We have

$$x^* = -\sin(\text{Zenith Angle}_{true})\sin(\text{Azimuth Angle}_{true})$$
$$y^* = \sin(\text{Zenith Angle}_{true})\cos(\text{Azimuth Angle}_{true}) \quad 53.$$
$$z^* = \cos(\text{Zenith Angle}_{true})$$

These coordinates can be transformed to the x, y, z system by collecting the components from the relations in equations 47. through 49.. We have

$$x = x^*(y_{sun}\,x_v - z_{sun}\,y_v)/\sin(SZA_{DISR}) + y^*(y_v\,i^*_x - z_v\,i^*_y) + z^*x_v \quad 54.$$

$$y = x^*(-x_{sun}\,z_v + z_{sun}\,x_v)/\sin(SZA_{DISR}) + y^*(-x_v\,i^*_z + z_v\,i^*_x) + z^*y_v \quad 55.$$

$$z = x^*(x_{sun}\,y_v - y_{sun}\,x_v)/\sin(SZA_{DISR}) + y^*(-x_v\,i^*_z + z_v\,i^*_x) + z^*z_v \quad 56.$$

Now the zenith angle and the azimuth angle in the DISR coordinates are given by

$$\text{Zenith Angle}_{DISR} = \text{acos}(z) \quad 57.$$
$$\text{Azimuth Angle}_{DISR} = \text{atan2}(y, -x) \quad 58.$$

13.4 Relative Spectral Response

13.4.1 Transmission of Filters as Functions of Temperature

The Solar Aureole system includes interference filters to limit the passband of the red and blue channels. The interference filters are at the very front of the optical system, close to the front windows of the sensor head. In this location, they will get very cold during the descent into the atmosphere of Titan. In our laboratory measurements of the relative spectral response of the entire Solar Aureole instrument on the flight model we were able to vary the temperature of the focal plane over the complete range of temperatures expected during the Titan entry, but we were not able to independently collect data with the filters near the front windows at the temperatures they will have during entry.

Therefore, we arranged a special test after launch in which the transmissions of filters from the flight lot were measured over a wide range of temperature. Co-Investigator Bernard Schmitt made these measurements in his laboratory in Grenoble, France. A beam of about f/3 rather than collimated light was used to measure the transmission. The measurements of the red Solar Aureole filter are contained in Table 13-7 below at temperatures of 70 K, 180 K, and 301 K. The measured transmissions of the filter at the three temperatures are plotted in Figure 13-13 below. Fortunately, the plot shows that very little shift in the response of the

filter occurs over this range of temperatures. Figure 13-14 shows the deviations in the transmissions at each temperature from the average of the transmission measurements at the three temperatures. We see that the deviations at any temperature are less than 1% of the peak transmission of the filter at all wavelengths, and are much less than this at most wavelengths. Hence, in considering the variations in the relative spectral response of the Solar Aureole instrument, the variation in response of the CCD detector will provide the major effect, and this effect was well measured in our laboratory before delivery.

Table 13-7 Transmission of the Red Solar Aureole Filter at Three Temperatures

Wavelength (nm)	70 K	180 K	301 K	Average	sigma average
850	0.00064	0.00076	0.00050	0.00063	0.00008
852	0.00096	0.00084	0.00063	0.00081	0.00010
854	0.00080	0.00101	0.00098	0.00093	0.00007
856	0.00115	0.00103	0.00100	0.00106	0.00004
858	0.00135	0.00115	0.00099	0.00117	0.00010
860	0.00155	0.00144	0.00114	0.00138	0.00012
862	0.00148	0.00173	0.00160	0.00160	0.00007
864	0.00181	0.00185	0.00161	0.00176	0.00007
866	0.00210	0.00197	0.00188	0.00198	0.00006
868	0.00251	0.00258	0.00230	0.00246	0.00008
870	0.00298	0.00300	0.00273	0.00290	0.00009
872	0.00363	0.00370	0.00330	0.00354	0.00012
874	0.00447	0.00454	0.00437	0.00446	0.00005
876	0.00598	0.00577	0.00553	0.00576	0.00013
878	0.00774	0.00744	0.00726	0.00748	0.00014
880	0.00988	0.00981	0.00948	0.00973	0.00012
882	0.01341	0.01304	0.01268	0.01305	0.00021
884	0.01813	0.01787	0.01762	0.01787	0.00015
886	0.02532	0.02502	0.02431	0.02488	0.00030
888	0.03566	0.03540	0.03463	0.03523	0.00031
890	0.05141	0.05105	0.05047	0.05098	0.00027
892	0.07503	0.07483	0.07399	0.07462	0.00032
894	0.11012	0.11085	0.10969	0.11022	0.00034
896	0.16176	0.16400	0.16279	0.16285	0.00065
898	0.23398	0.23925	0.23772	0.23698	0.00157
900	0.32830	0.33779	0.33646	0.33418	0.00297
902	0.43780	0.45136	0.45055	0.44657	0.00439
904	0.54775	0.56382	0.56363	0.55840	0.00533
906	0.64093	0.65583	0.65606	0.65094	0.00501
908	0.70772	0.71921	0.71958	0.71550	0.00389
910	0.74889	0.75639	0.75647	0.75392	0.00251
912	0.77096	0.77510	0.77504	0.77370	0.00137
914	0.78152	0.78319	0.78313	0.78261	0.00055
916	0.78594	0.78640	0.78633	0.78622	0.00014
918	0.78686	0.78695	0.78695	0.78692	0.00003
920	0.78651	0.78645	0.78663	0.78653	0.00005
922	0.78564	0.78537	0.78568	0.78556	0.00010
924	0.78439	0.78434	0.78476	0.78450	0.00013
926	0.78266	0.78288	0.78343	0.78299	0.00023
928	0.78076	0.78110	0.78188	0.78125	0.00033
930	0.77845	0.77921	0.78020	0.77929	0.00051

932	0.77540	0.77649	0.77760	0.77650	0.00064
934	0.77315	0.77478	0.77619	0.77471	0.00088
936	0.76964	0.77181	0.77345	0.77163	0.00110
938	0.76730	0.76969	0.77149	0.76949	0.00121
940	0.76507	0.76763	0.76964	0.76745	0.00132
942	0.76251	0.76460	0.76661	0.76457	0.00118
944	0.75998	0.76146	0.76351	0.76165	0.00102
946	0.75845	0.75901	0.76101	0.75949	0.00078
948	0.75732	0.75711	0.75893	0.75779	0.00057
950	0.75639	0.75499	0.75670	0.75603	0.00053
952	0.75547	0.75321	0.75493	0.75454	0.00068
954	0.75524	0.75227	0.75405	0.75385	0.00086
956	0.75437	0.75076	0.75267	0.75260	0.00104
958	0.75321	0.74928	0.75123	0.75124	0.00113
960	0.75129	0.74716	0.74921	0.74922	0.00119
962	0.74796	0.74386	0.74623	0.74602	0.00119
964	0.74253	0.73825	0.74066	0.74048	0.00124
966	0.73332	0.72875	0.73138	0.73115	0.00132
968	0.71740	0.71273	0.71567	0.71527	0.00136
970	0.68997	0.68518	0.68823	0.68779	0.00140
972	0.64661	0.64208	0.64549	0.64473	0.00136
974	0.58361	0.57985	0.58360	0.58235	0.00125
976	0.50244	0.50000	0.50388	0.50211	0.00113
978	0.41074	0.40956	0.41323	0.41118	0.00108
980	0.32006	0.31969	0.32284	0.32086	0.00099
982	0.23988	0.23983	0.24230	0.24067	0.00082
984	0.17533	0.17542	0.17717	0.17597	0.00060
986	0.12650	0.12659	0.12761	0.12690	0.00036
988	0.09108	0.09111	0.09171	0.09130	0.00020
990	0.06581	0.06571	0.06609	0.06587	0.00011
992	0.04791	0.04793	0.04812	0.04799	0.00007
994	0.03532	0.03538	0.03535	0.03535	0.00002
996	0.02636	0.02631	0.02627	0.02632	0.00003
998	0.01990	0.01991	0.01987	0.01990	0.00001
1000	0.01521	0.01528	0.01507	0.01519	0.00006
1002	0.01171	0.01198	0.01168	0.01179	0.00010
1004	0.00917	0.00937	0.00917	0.00923	0.00007
1006	0.00731	0.00747	0.00731	0.00736	0.00005
1008	0.00589	0.00613	0.00585	0.00595	0.00009
1010	0.00481	0.00497	0.00480	0.00486	0.00005
1012	0.00393	0.00423	0.00398	0.00405	0.00009
1014	0.00328	0.00360	0.00329	0.00339	0.00010
1016	0.00280	0.00295	0.00275	0.00283	0.00006
1018	0.00237	0.00260	0.00234	0.00244	0.00008
1020	0.00196	0.00224	0.00209	0.00210	0.00008
1022	0.00173	0.00193	0.00185	0.00184	0.00006
1024	0.00151	0.00172	0.00160	0.00161	0.00006
1026	0.00142	0.00156	0.00142	0.00147	0.00005
1028	0.00122	0.00140	0.00127	0.00130	0.00005
1030	0.00115	0.00132	0.00106	0.00118	0.00008
1032	0.00100	0.00112	0.00109	0.00107	0.00004
1034	0.00092	0.00108	0.00094	0.00098	0.00005
1036	0.00082	0.00102	0.00092	0.00092	0.00006
1038	0.00074	0.00080	0.00095	0.00083	0.00006

1040	0.00072	0.00071	0.00080	0.00075	0.00003
1042	0.00066	0.00081	0.00070	0.00072	0.00005
1044	0.00068	0.00073	0.00070	0.00070	0.00001
1046	0.00063	0.00067	0.00061	0.00064	0.00002
1048	0.00056	0.00068	0.00069	0.00064	0.00004
1050	0.00069	0.00066	0.00055	0.00063	0.00004

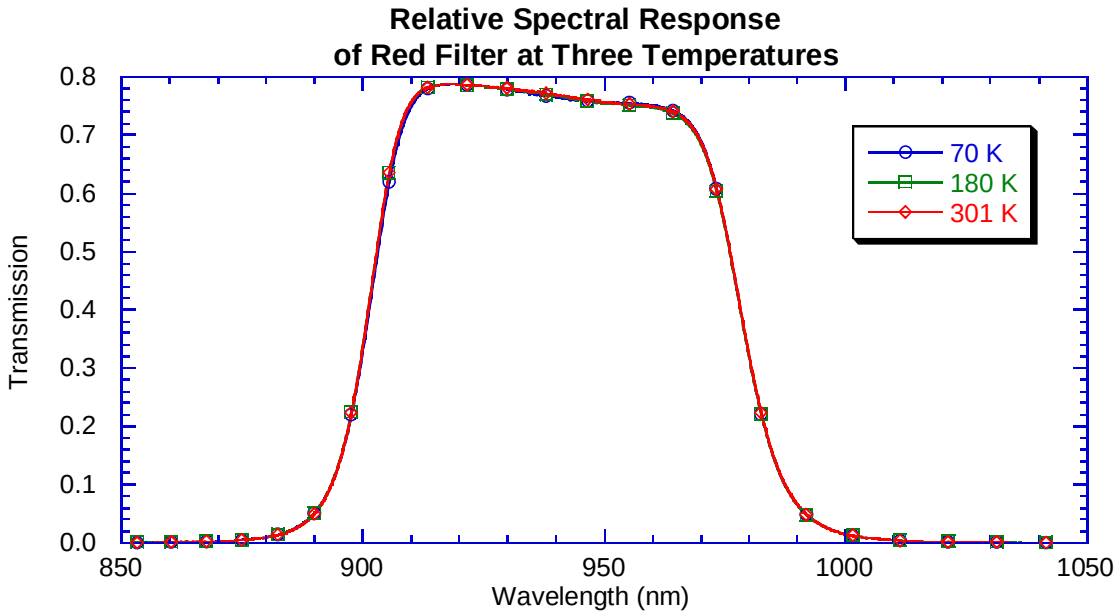

Figure 13-13 The transmission of the red Solar Aureole filter as a function of wavelength as measured by Bernard Schmitt at three different temperatures. The three measurements show rather little dependence on temperature.

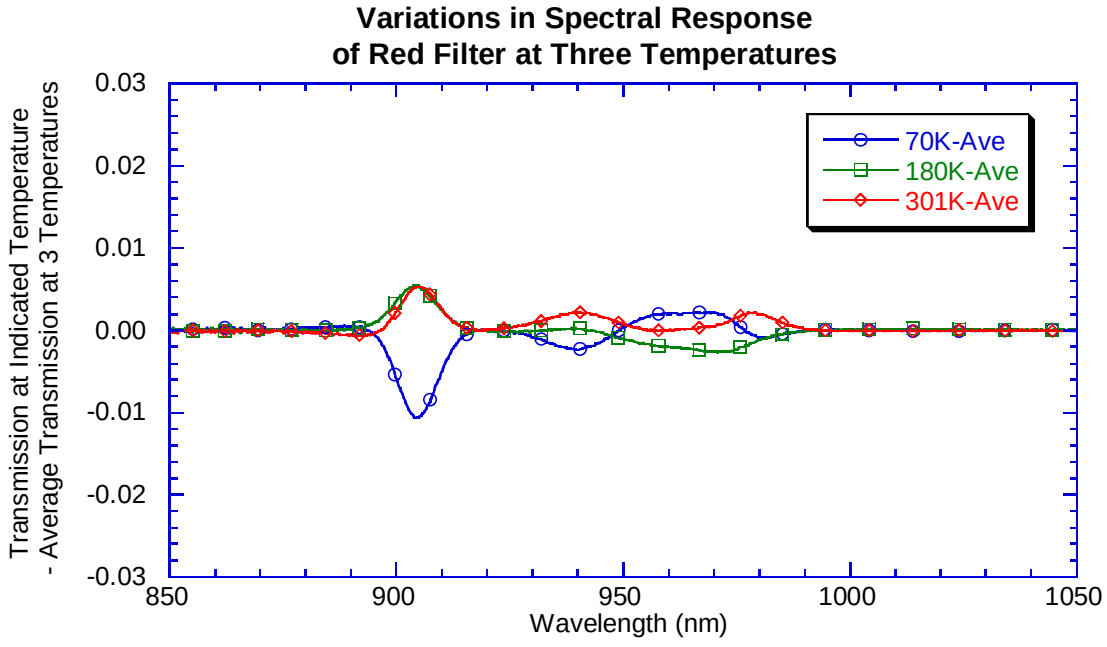

Figure 13-14 The difference in the measured transmission of the red filter from the average of the measurements at three temperatures from the data of Table 13-7. Note that the difference of a

measurement at any of the three temperatures from the average is less than 1% at all wavelengths, and usually less than a few tenths of a percent.

Table 13-8 shows the measurements of the blue Solar Aureole filter from the flight lot at four temperatures. Figure 13-15 shows the transmission of the filter at each temperature as a function of wavelength. Figure 13-16 shows the deviation at each temperature from the average of the measurements at the four temperatures. We note that the curves of the deviations do not change monotonically with temperature, but the curves often cross over each other. The deviations are not more than about 2% from the mean at any temperature. We conclude that the transmission of the blue filter does not change significantly with temperature even over the rather large temperature range of the measurements.

Table 13-8 Transmission of the Blue Solar Aureole Filter at Four Temperatures

Wavelength (nm)	70 K	150 K	220 K	300 K	Average	sigma average
450	0.0026	0.0051	0.0031	0.0008	0.0029	0.0009
451	0.0022	0.0029	0.0033	0.0012	0.0024	0.0005
452	0.0047	0.0040	0.0059	-0.0003	0.0035	0.0013
453	0.0038	0.0024	0.0031	0.0022	0.0029	0.0004
454	0.0030	0.0042	0.0040	0.0019	0.0033	0.0005
455	0.0036	0.0042	0.0032	0.0026	0.0034	0.0003
456	0.0042	0.0036	0.0037	0.0023	0.0035	0.0004
457	0.0046	0.0047	0.0053	0.0032	0.0044	0.0004
458	0.0056	0.0057	0.0063	0.0048	0.0056	0.0003
459	0.0069	0.0053	0.0067	0.0056	0.0061	0.0004
460	0.0077	0.0071	0.0059	0.0055	0.0065	0.0005
461	0.0091	0.0096	0.0094	0.0080	0.0091	0.0003
462	0.0119	0.0097	0.0108	0.0100	0.0106	0.0005
463	0.0142	0.0126	0.0124	0.0121	0.0128	0.0005
464	0.0176	0.0172	0.0154	0.0144	0.0161	0.0008
465	0.0236	0.0225	0.0205	0.0185	0.0213	0.0011
466	0.0293	0.0293	0.0272	0.0259	0.0279	0.0008
467	0.0416	0.0392	0.0371	0.0333	0.0378	0.0018
468	0.0613	0.0582	0.0528	0.0474	0.0549	0.0031
469	0.0893	0.0860	0.0782	0.0701	0.0809	0.0043
470	0.1331	0.1258	0.1174	0.1047	0.1202	0.0061
471	0.1938	0.1855	0.1701	0.1553	0.1762	0.0085
472	0.2648	0.2600	0.2414	0.2187	0.2462	0.0105
473	0.3386	0.3387	0.3217	0.2958	0.3237	0.0101
474	0.4062	0.4077	0.3929	0.3713	0.3945	0.0084
475	0.4547	0.4606	0.4458	0.4274	0.4471	0.0072
476	0.4841	0.4952	0.4817	0.4653	0.4816	0.0062
477	0.5056	0.5188	0.5063	0.4893	0.5050	0.0061
478	0.5213	0.5392	0.5267	0.5072	0.5236	0.0066
479	0.5399	0.5571	0.5476	0.5275	0.5430	0.0063
480	0.5628	0.5784	0.5676	0.5501	0.5647	0.0059
481	0.5868	0.6033	0.5899	0.5702	0.5875	0.0068

482	0.6096	0.6289	0.6142	0.5915	0.6111	0.0077
483	0.6309	0.6522	0.6378	0.6137	0.6336	0.0080
484	0.6492	0.6707	0.6575	0.6347	0.6530	0.0075
485	0.6641	0.6874	0.6729	0.6499	0.6686	0.0079
486	0.6748	0.6985	0.6852	0.6620	0.6801	0.0077
487	0.6809	0.7058	0.6927	0.6699	0.6873	0.0077
488	0.6839	0.7089	0.6972	0.6740	0.6910	0.0076
489	0.6831	0.7083	0.6966	0.6753	0.6908	0.0073
490	0.6798	0.7043	0.6934	0.6726	0.6875	0.0071
491	0.6736	0.6978	0.6875	0.6671	0.6815	0.0069
492	0.6658	0.6887	0.6780	0.6587	0.6728	0.0066
493	0.6557	0.6779	0.6668	0.6478	0.6620	0.0066
494	0.6426	0.6661	0.6549	0.6353	0.6497	0.0068
495	0.6299	0.6516	0.6426	0.6245	0.6371	0.0061
496	0.6179	0.6373	0.6287	0.6133	0.6243	0.0054
497	0.6082	0.6252	0.6156	0.6018	0.6127	0.0050
498	0.5983	0.6156	0.6048	0.5905	0.6023	0.0053
499	0.5901	0.6076	0.5971	0.5829	0.5944	0.0053
500	0.5846	0.6013	0.5916	0.5776	0.5888	0.0051
501	0.5816	0.5971	0.5876	0.5744	0.5852	0.0048
502	0.5812	0.5955	0.5862	0.5733	0.5840	0.0046
503	0.5831	0.5963	0.5862	0.5738	0.5848	0.0046
504	0.5862	0.5993	0.5876	0.5750	0.5870	0.0050
505	0.5907	0.6042	0.5920	0.5778	0.5912	0.0054
506	0.5942	0.6088	0.5978	0.5821	0.5957	0.0055
507	0.5992	0.6130	0.6025	0.5882	0.6007	0.0051
508	0.6056	0.6173	0.6060	0.5929	0.6055	0.0050
509	0.6109	0.6232	0.6095	0.5953	0.6097	0.0057
510	0.6129	0.6281	0.6141	0.5975	0.6131	0.0063
511	0.6138	0.6297	0.6181	0.6017	0.6158	0.0058
512	0.6160	0.6296	0.6187	0.6057	0.6175	0.0049
513	0.6174	0.6295	0.6166	0.6053	0.6172	0.0050
514	0.6157	0.6293	0.6152	0.6019	0.6155	0.0056
515	0.6096	0.6266	0.6132	0.5990	0.6121	0.0057
516	0.5998	0.6174	0.6078	0.5958	0.6052	0.0048
517	0.5883	0.6029	0.5954	0.5879	0.5936	0.0035
518	0.5718	0.5847	0.5754	0.5708	0.5757	0.0032
519	0.5449	0.5604	0.5502	0.5445	0.5500	0.0037
520	0.5058	0.5260	0.5192	0.5132	0.5160	0.0043
521	0.4580	0.4779	0.4770	0.4750	0.4720	0.0047
522	0.4057	0.4206	0.4226	0.4261	0.4187	0.0045
523	0.3496	0.3617	0.3622	0.3680	0.3604	0.0039
524	0.2913	0.3038	0.3034	0.3064	0.3012	0.0034
525	0.2349	0.2480	0.2492	0.2511	0.2458	0.0037
526	0.1859	0.1965	0.1994	0.2025	0.1961	0.0036

527	0.1459	0.1532	0.1565	0.1602	0.1539	0.0030
528	0.1145	0.1189	0.1205	0.1243	0.1195	0.0020
529	0.0894	0.0931	0.0936	0.0957	0.0930	0.0013
530	0.0695	0.0730	0.0733	0.0741	0.0725	0.0010
531	0.0541	0.0572	0.0575	0.0581	0.0567	0.0009
532	0.0431	0.0452	0.0456	0.0458	0.0449	0.0006
533	0.0345	0.0360	0.0361	0.0365	0.0358	0.0004
534	0.0283	0.0291	0.0289	0.0295	0.0290	0.0003
535	0.0231	0.0237	0.0236	0.0236	0.0235	0.0001
536	0.0190	0.0198	0.0195	0.0193	0.0194	0.0002
537	0.0159	0.0164	0.0162	0.0159	0.0161	0.0001
538	0.0132	0.0140	0.0134	0.0135	0.0135	0.0002
539	0.0111	0.0118	0.0118	0.0114	0.0115	0.0002
540	0.0098	0.0102	0.0101	0.0094	0.0099	0.0002
541	0.0085	0.0085	0.0084	0.0081	0.0084	0.0001
542	0.0072	0.0076	0.0073	0.0070	0.0073	0.0001
543	0.0065	0.0068	0.0064	0.0062	0.0065	0.0001
544	0.0053	0.0056	0.0057	0.0051	0.0054	0.0001
545	0.0047	0.0050	0.0048	0.0050	0.0049	0.0001
546	0.0044	0.0044	0.0043	0.0038	0.0042	0.0001
547	0.0039	0.0036	0.0035	0.0035	0.0036	0.0001
548	0.0034	0.0033	0.0031	0.0032	0.0032	0.0001
549	0.0032	0.0029	0.0031	0.0030	0.0030	0.0001
550	0.0027	0.0030	0.0026	0.0021	0.0026	0.0002

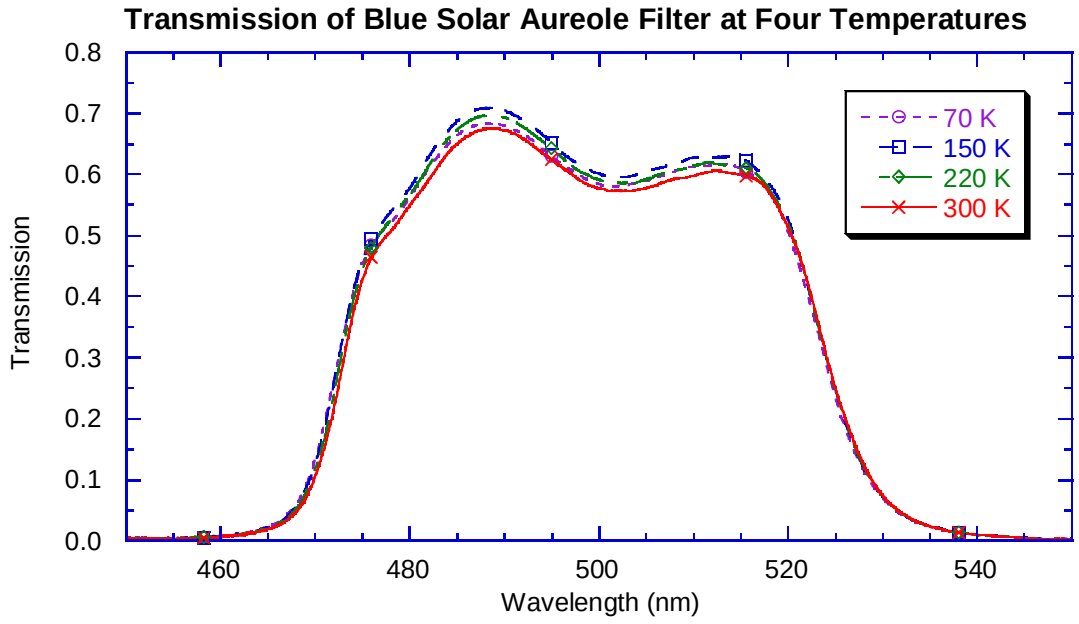

Figure 13-15 Measured transmission of blue Solar Aureole filter at four temperatures, as labeled.

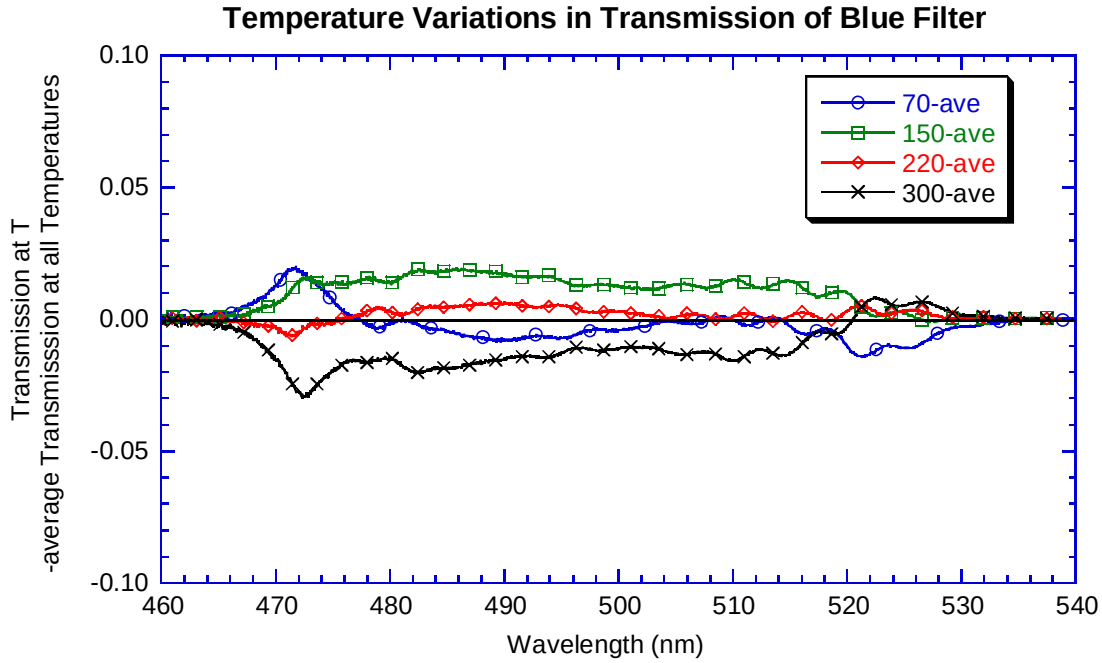

Figure 13-16 The difference in the transmission measurements at each of the four temperatures from the average of the measurements at all four temperatures is shown as a function of wavelength. Note that the differences do not vary monotonically with temperature, and that the differences are within about 2% of the mean value at all wavelengths. We conclude that the transmission of the blue filter has little real variation in transmission with temperature even over the large range from 70 K to 300 K.

13.4.2 Transmission of Filters as Functions of Angle of Incidence.

While the Solar Aureole filters have essentially the same spectral transmission independent of temperature, we know that the transmission of the filter does depend significantly on the angle of incidence of the light beam. This effect is responsible for changing the relative spectral response of the Solar Aureole system as a function of row number (elevation) on the detector array. In fact the relative spectral response of the Solar Aureole system is a complex function of row number, column number, wavelength, and detector temperature.

It was thought that we could separate the complex relative spectral response function into two parts by first characterizing the variation in filter spectral transmission with angle of incidence and then deriving the detector response as a function of wavelength and temperature. This, however, did not yield adequate results, so a different approach was pursued as discussed in the following section. However, the spectral transmission of a set of filters from the flight lot was characterized versus angle of incidence. The results of this test and analysis are included here.

We measured the transmission of the red and blue Solar Aureole filters from the flight lot as a function of the angle of incidence of a collimated beam to the normal of the filter at the University of Arizona's Lunar and Planetary Lab clean room (room 222c) between the February 13 and March 13, 2001. Both the 'Red' (936 nm) and 'Blue' (500 nm) filters were measured.

We used the high intensity light source to illuminate the input to the monochrometer. The output from the monochrometer was directed through the filter, to the Standard Silicon Detector. The reflex telescope was attached to the output of the monochrometer to collimate the monochromatic beam. The filter was attached to a holder that also served as a baffle. A baffle was also placed in front of the detector to reduce the stray light contamination.

The filter holder was mounted to a rotary table to allow for accurate angular positioning of the sample relative to the collimated beam. An index datum was placed on the monochrometer directly below its output port so that the retro reflection from the filter holder could be used to determine the orthogonal orientation of the beam.

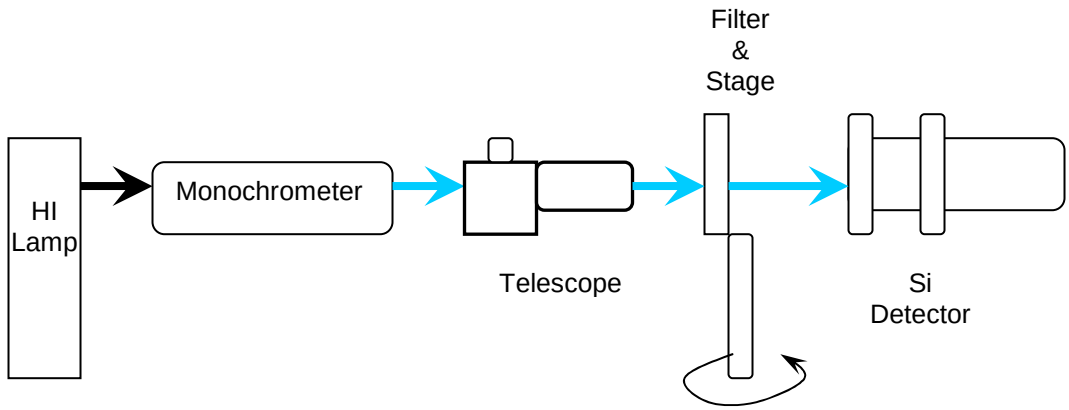

Figure 13-17 Test setup schematic for measuring the filter transmission as a function of angle of incidence.

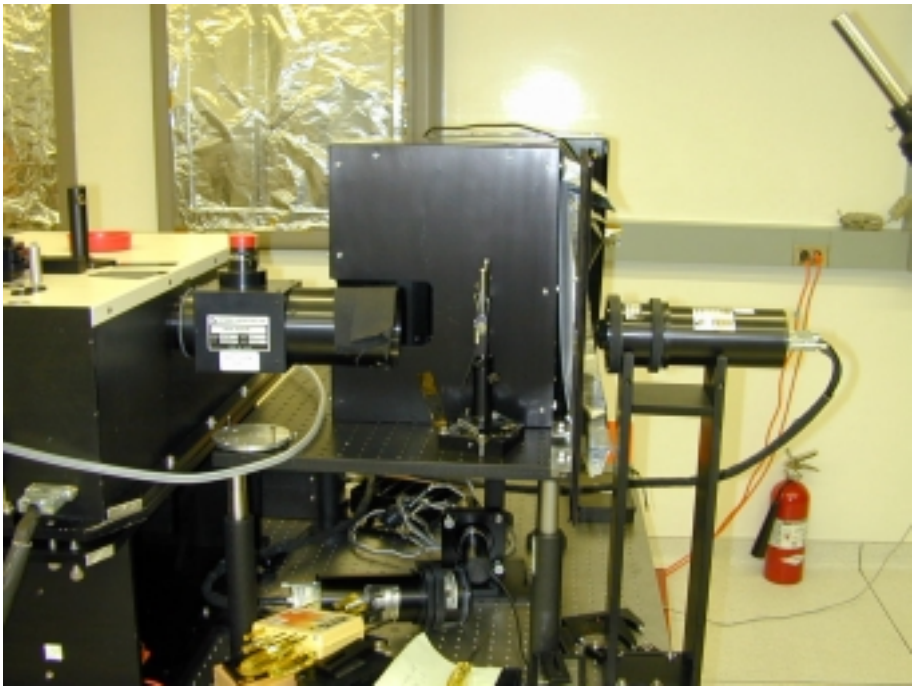

Figure 13-18 A view of the laboratory setup used to measure the transmission of the Solar Aureole filters as a function of the angle of incidence of the collimated beam. The monochrometer and the collimating

reflex telescope are visible at the left in the image. The filter holder mounted on a calibrated angle stage is visible at center. The standard silicon detector is visible at the right.

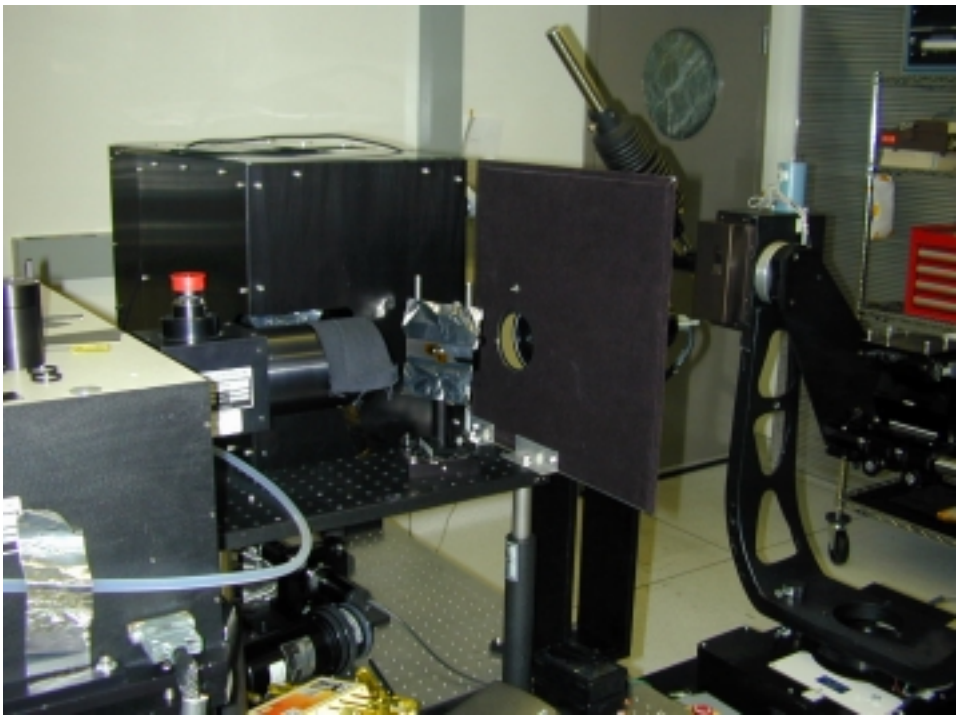

Figure 13-19 Like Figure 13-18 but showing the baffle between the filter holder and the standard silicon detector.

For the measurements of the blue filter we covered the range from 420 to 570 nm in 5 nm steps. For the red measurements, we covered the range from 830 to 1020 nm in 5 nm steps. The scans were performed at incidence angles of 90, 85, 75, 65, 55, 100, 110, & 120 degrees relative to the plane of the filter in the direction of its long axis.

The measurements were taken in three steps. First the beam was scanned over its entire wavelength range with the filter and holder removed. Second, the beam was again scanned over its wavelength range with the filter holder in place but with no filter installed. This scan was repeated at each incidence angle. Third, the beam was scanned over its wavelength range with the filter and holder installed, and this scan was repeated at each incidence angle.

We calculated the transmission of the filter for each incidence angle by taking the ratio of the detector readings with the filter in place to the detector readings with only the filter holder in place and normalizing by the intensity of the beam during each measurement.

$$Transmission = \frac{S\_filter}{S\_holder} * \frac{I\_holder}{I\_filter}$$

or,

$$Transmission = \frac{S\_filter / I\_filter}{S\_holder / I\_holder} \qquad 59.$$

where:

S_filter = Spectrum with the filter and holder in place

S_holder = Spectrum with only the filter holder in place

I_filter = Intensity of the source with no holder or filter, taken during filter measurements

I_holder = Intensity of the source taken during the holder-only measurements

The results, presented in terms of degrees from the normal to the filter, are shown in Table 13-9 and Table 13-10.

Table 13-9 Spectral Transmission of Blue Filter for Various Angles of Incidence

Wavelength (nm)	0 deg	5 deg	10 deg	15 deg	20 deg	25 deg	30 deg	35 deg
420	0.0000	0.0001	0.0000	0.0001	0.0000	0.0002	0.0000	0.0003
425	0.0000	0.0001	0.0000	0.0001	0.0000	0.0002	0.0001	0.0006
430	0.0000	0.0001	0.0000	0.0001	0.0000	0.0002	0.0004	0.0012
435	0.0000	0.0001	0.0000	0.0001	0.0001	0.0004	0.0010	0.0029
440	0.0000	0.0001	0.0001	0.0002	0.0003	0.0009	0.0028	0.0097
445	0.0001	0.0002	0.0002	0.0005	0.0010	0.0026	0.0109	0.0426
450	0.0005	0.0006	0.0008	0.0015	0.0034	0.0096	0.0512	0.1559
455	0.0016	0.0019	0.0026	0.0048	0.0143	0.0475	0.1836	0.3460
460	0.0059	0.0069	0.0107	0.0225	0.0752	0.1906	0.3994	0.4791
465	0.0319	0.0383	0.0628	0.1256	0.2646	0.4214	0.5471	0.5217
470	0.1710	0.1934	0.2514	0.3592	0.4900	0.5648	0.5872	0.5305
475	0.4086	0.4303	0.4753	0.5447	0.6069	0.6013	0.5858	0.5268
480	0.5614	0.5751	0.6027	0.6366	0.6399	0.5931	0.5752	0.5325
485	0.6480	0.6563	0.6614	0.6566	0.6222	0.5680	0.5778	0.5226
490	0.6696	0.6684	0.6538	0.6265	0.5937	0.5646	0.5784	0.5125
495	0.6340	0.6301	0.6133	0.5929	0.5909	0.5742	0.5760	0.4912
500	0.5954	0.5944	0.5913	0.5920	0.6027	0.5770	0.5460	0.3413
505	0.5911	0.5945	0.6000	0.6059	0.6052	0.5497	0.3871	0.1392
510	0.6044	0.6076	0.6090	0.6020	0.5512	0.3886	0.1683	0.0406
515	0.5912	0.5886	0.5677	0.5100	0.3590	0.1589	0.0500	0.0135
520	0.4749	0.4576	0.3997	0.2833	0.1417	0.0457	0.0156	0.0061
525	0.2521	0.2293	0.1764	0.0962	0.0416	0.0145	0.0064	0.0035
530	0.0857	0.0745	0.0539	0.0278	0.0133	0.0061	0.0033	0.0023
535	0.0254	0.0223	0.0166	0.0098	0.0055	0.0032	0.0020	0.0018
540	0.0094	0.0085	0.0067	0.0045	0.0028	0.0020	0.0015	0.0016

545	0.0042	0.0040	0.0032	0.0025	0.0017	0.0014	0.0012	0.0014
550	0.0022	0.0022	0.0018	0.0016	0.0012	0.0011	0.0010	0.0013
555	0.0014	0.0014	0.0012	0.0011	0.0009	0.0010	0.0009	0.0012
560	0.0009	0.0010	0.0009	0.0009	0.0008	0.0009	0.0008	0.0010
565	0.0007	0.0008	0.0007	0.0008	0.0007	0.0008	0.0007	0.0010
570	0.0006	0.0007	0.0006	0.0007	0.0006	0.0007	0.0006	0.0008

Table 13-10 Spectral Transmission of Red Filter for Various Angles of Incidence

Wavelength(nm)	0 deg	5 deg	10 deg	15 deg	20 deg	25 deg	30 deg
830	0.0002	0.0003	0.0002	0.0003	0.0007	0.0022	0.0026
835	0.0002	0.0004	0.0003	0.0006	0.0011	0.0029	0.0038
840	0.0003	0.0006	0.0005	0.0010	0.0015	0.0036	0.0063
845	0.0006	0.0009	0.0009	0.0015	0.0019	0.0049	0.0116
850	0.0009	0.0013	0.0013	0.0019	0.0027	0.0073	0.0235
855	0.0012	0.0017	0.0016	0.0024	0.0043	0.0121	0.0535
860	0.0016	0.0021	0.0022	0.0034	0.0076	0.0236	0.1292
865	0.0033	0.0041	0.0044	0.0069	0.0163	0.0474	0.2112
870	0.0057	0.0068	0.0084	0.0141	0.0410	0.1221	0.4053
875	0.0111	0.0130	0.0183	0.0329	0.1064	0.2743	0.6216
880	0.0243	0.0286	0.0437	0.0842	0.2382	0.4979	0.7947
885	0.0596	0.0708	0.1088	0.2020	0.4353	0.7182	0.8959
890	0.1460	0.1707	0.2398	0.3992	0.6503	0.8624	0.9321
895	0.3091	0.3466	0.4362	0.6243	0.8151	0.9220	0.9391
900	0.5286	0.5684	0.6567	0.8109	0.9101	0.9360	0.9424
905	0.7362	0.7666	0.8314	0.9164	0.9472	0.9383	0.9460
910	0.8784	0.8967	0.9312	0.9587	0.9586	0.9404	0.9494
915	0.9491	0.9567	0.9668	0.9713	0.9589	0.9438	0.9485
920	0.9686	0.9723	0.9706	0.9729	0.9538	0.9435	0.9436
925	0.9699	0.9738	0.9648	0.9703	0.9458	0.9402	0.9277
930	0.9665	0.9682	0.9565	0.9607	0.9393	0.9317	0.8733
935	0.9599	0.9593	0.9487	0.9524	0.9356	0.9180	0.7489
940	0.9529	0.9519	0.9454	0.9459	0.9315	0.8760	0.5559
945	0.9473	0.9472	0.9449	0.9436	0.9115	0.7676	0.3495
950	0.9421	0.9439	0.9415	0.9354	0.8428	0.5781	0.1835
955	0.9364	0.9374	0.9264	0.8994	0.7064	0.3601	0.0833
960	0.9215	0.9180	0.8858	0.8042	0.5163	0.1847	0.0350
965	0.8748	0.8607	0.7918	0.6379	0.3178	0.0836	0.0151
970	0.7703	0.7413	0.6327	0.4330	0.1641	0.0370	0.0073
975	0.6045	0.5631	0.4336	0.2468	0.0744	0.0180	0.0039
980	0.4075	0.3625	0.2506	0.1192	0.0330	0.0100	0.0024
985	0.2299	0.1945	0.1237	0.0530	0.0156	0.0064	0.0016
990	0.1133	0.0930	0.0580	0.0248	0.0082	0.0047	0.0012
995	0.0527	0.0434	0.0278	0.0128	0.0047	0.0038	0.0010
1000	0.0255	0.0218	0.0144	0.0074	0.0030	0.0033	0.0008
1005	0.0134	0.0121	0.0081	0.0047	0.0021	0.0030	0.0007
1010	0.0079	0.0075	0.0050	0.0033	0.0016	0.0029	0.0007

1015	0.0050	0.0051	0.0034	0.0025	0.0013	0.0028	0.0007
1020	0.0034	0.0037	0.0025	0.0020	0.0011	0.0027	0.0007

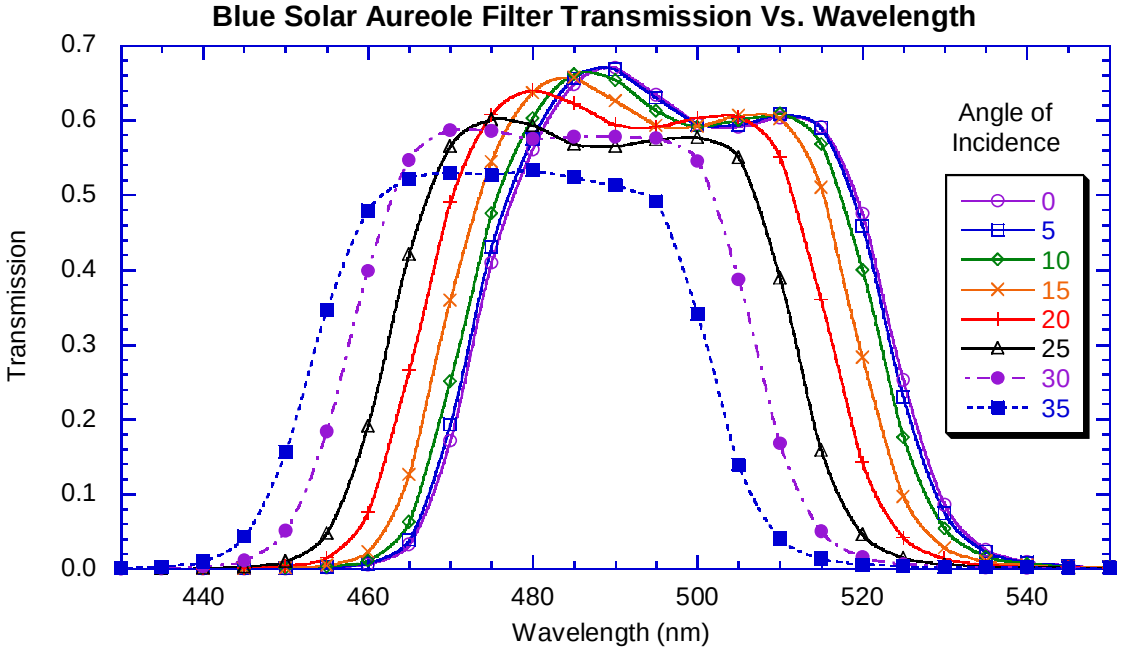

Figure 13-20 Measurements of the transmission of the blue Solar Aureole filter from the flight lot for different angles of incidence of collimated light, as labeled. Note the shift in the transmission of the filter with different incidence angles.

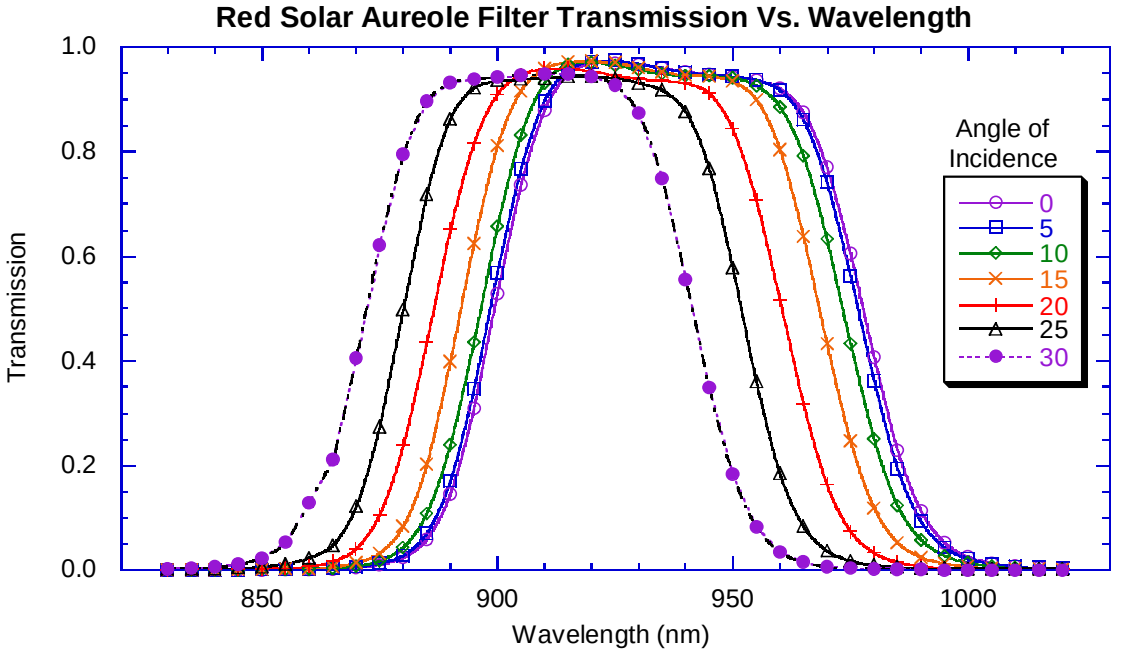

Figure 13-21 Like Figure 13-20 but for the red Solar Aureole filter. Note the shift in the transmission of the filter with different incidence angles.

We note that the bandpass of both the red and blue Solar Aureole filters shift significantly with differing angle of incidence of the beam to the normal of the filter.

13.4.3 Relative Spectral Response of Solar Aureole System versus Temperature

It has been shown above that while the bandpass filters do not show significant variations in their spectral transmissions with temperature, they do change strongly with angle of incidence (zenith angle or row number). The goal of this effort is to decompose the temperature dependent Solar Aureole Relative Spectral Response (SA RSR) into a relatively simple analytic function and table for each of the four channels. The model fit should match the original data with a root-mean-squared deviation over the bandpass of 1% or less for every pixel and every temperature.

Measurements of the relative spectral response of the complete flight Solar Aureole system were made in the integrating sphere in July and August, 1996 at the detector temperatures shown in Table 13-11. The data was reduced by several individuals, and the final RSRs are located in /local/SA/Rel_Spec_Resp/DISR#3/output/save_files/.

Table 13-11 Dates, File Names, and Detector Temperatures of Relative Spectral Response Measurements of the SN03 Solar Aureole System

Date (1996)	File Name	Detector Temperature
July 26	26Jul_2/	293.869 K
July 29	29Jul_1/	168.197 K
July 30	30Jul_1/	267.683 K
July 30	30Jul_2/	184.082 K
July 31	31Jul_1/	237.042 K
August 1	1Aug_1/	200.855 K
August 2	1Aug_2/	224.700 K

13.4.3.1 The Form of Relative Spectral Response Model

The form of the RSR model includes a foundational set of spectrally varying curves, *filter*, whose characteristics are largely due to the interference filters in each channel. The filter curves are functions of the row number (angle of incidence) for each pixel. To result in the RSR model, the filter curves are multiplied by a polynomial function that includes all thermally varying effects and some spatial effects, all of which are presumed to reside in the CCD chip and fiber bundle. This latter function is called the “non-filter model”, or NFM, because it is derived analytically by eliminating the interference filter effects from the measured relative spectral response. It includes some spatial variation on a columnwise basis.

As derived, the relative spectral response for each of the four SA channels can be found by the following equation.

$$SA\_RSR(T,\lambda,c,r) = filter(\lambda,r) * NFM(T,\lambda,c)$$

where:

$filter$ = scaled model of interference filter transmission

NFM = everything in the SA channel contributing to relative spectral response except the interference filter

T = temperature

λ = wavelength

c = column

r = row

60.

The form of the NFM is the following polynomial equation, where the thermal coefficients, a, b, c, and d, are properties of the SA channel, and the column coefficients, M0 through M3, are column dependent for each channel.

$$NFM(T,\lambda,c) = NFM_{ini}(\lambda) * (M0(c) + M1(c)*\lambda + M2(c)*\lambda^2 + M3(c)*\lambda^3) + (293K - T) * (a + b*\lambda + c*\lambda^2 + d*\lambda^3)$$

61.

where :

$NFM_{ini}(\lambda)$ = an initial spectral non filter model

Due to fiber ribbon/CCD misalignments, a few columns do not match their neighbors in RSR shape. These columns are treated in the manner described above, but with their own set of filters and coefficients. Additional localized spatial effects are found throughout the system – the CCD has some pixel to pixel variation and the optical train has obvious illumination variations over the field due to the cameras and fiber ribbon underfilling the CCD – but the number of pixels affected and the degree of modeling error are small.

13.4.3.2 Approach

The following approach can be used to find the set of filter curves and NFMs whose product best matches the original data for each channel over temperature.

13.4.3.3 Step 1-Prepare Derived Data

The previously derived SA RSR data, which is taken to be the "measured data" in this modeling exercise, is given at specific wavelengths. When fitting curves to this data, splining the data to a finer wavelength grid, 0.5 nm, and then normalizing the splined function to 1, improves the fit of the models. The normalization in the blue channels is best performed on the second hump in the response curve.

The approach consists of polynomial fits to variations in the relative spectral response at a reference column and temperature. The reference columns and temperature can be varied to determine sensitivity on the modeling results. The central temperature, 224.7K, yields the best overall results. Little variation in results are indicated when any of the central columns are used. The following columns are used in this derivation.

Table 13-12 Reference Columns Used in Relative Spectral Response Model Derivation

Channel	Reference Column
Blue Horizontal	3
Blue Vertical	2
Red Horizontal	2
Red Vertical	3

13.4.3.4 Step 2-Find the Initial Non-Filter Models

The initial NFM, $NFM_{ini}(\lambda)$, is an underlying spectrally varying function which includes structure in the CCD quantum efficiency. The blue channels have no underlying structure, so NFM_{ini} is defined to be unity. The red channels, on the other hand, do have some structure over the SA bandpass, and this structure can be modeled as follows.

Analysis on the DISR Imager Relative Spectral Response indicates that there is a bump in the CCD spectral response around 854 nm. This can be seen in the following plot of the Side Looking Imager spectral response.

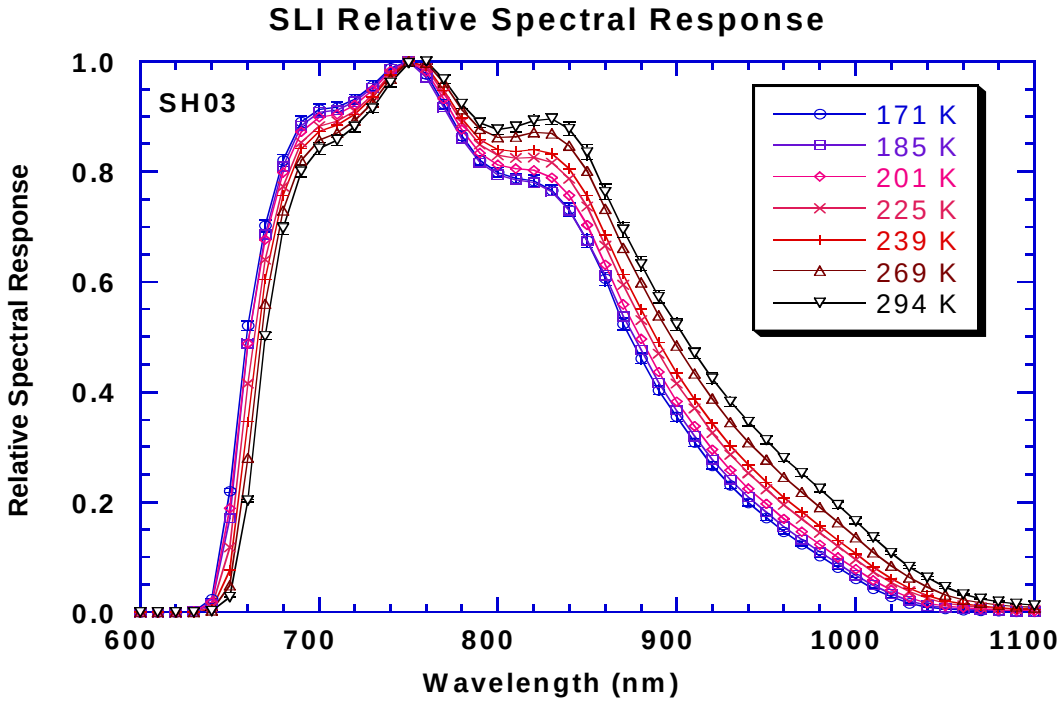

Figure 13-22 Side Looking Imager Spectral Response

This bump can be seen in the SA RSR as well, so it is modeled empirically in the initial NFM as a lorentzian function with a center wavelength of 854 nm, a full-width at half maximum response of 15 nm, and a peak amplitude of 0.4, as follows.

$$Bump(\lambda) = 1 + \frac{0.4}{1 + \left(2 * \frac{(854 - \lambda)}{15}\right)^2} \qquad 62.$$

The quadratic shape of the falloff can also be modeled. We normalize the derived RSR data in the wavelength range from 922 to 938 nm, and then for each wavelength, we form the average for all rows with good response (greater than 50%). This average can then be fit by a quadratic to be used in the initial NFM.

In mathematical terms, the quadratic portion of the initial NFM is as follows.

$$RSR'(T,\lambda,r) = RSR(T,\lambda,c_{ref},r) * \frac{\left\| RSR(T_{ref},\lambda,c_{ref},r)\right|_{922-938nm}\Big|_{row}}{\left|RSR(T,\lambda,c_{ref},r)\right|_{922-938nm}}$$

where:

$$RSR(T,\lambda,c_{ref},r) = \text{Measured RSR at reference column}$$
$$T_{ref} = \text{Reference temperature} \qquad 63.$$
$$c_{ref} = \text{Reference column}$$
$$\left|RSR(T_{ref},\lambda,c_{ref},r)\right|_{922-938nm} = \text{Average of meas'd RSR over } 922-938\text{nm}$$
$$\left\|RSR(T_{ref},\lambda,c_{ref},r)\right|_{922-938nm}\Big|_{row} = \text{Average of } \left|RSR(T_{ref},\lambda,c_{ref},r)\right|_{922-938nm} \text{ over all rows}$$

This new array RSR' at the reference temperature is then averaged over the rows in the wavelength regions with good filter response and fit with a quadratic in wavelength to create the initial NFM. The coefficients of the initial NFM quadratic fit for the red horizontal and vertical channels are as follows.

Table 13-13 Table of NFM_{ini} Quadratic Coefiicients

	Red Horizontal	Red Vertical
nfm0	67.900400	25.311233
nfm1	-0.13372830	-0.043105799
nfm2	6.6157520e-005	1.8006592e-005

Thus, the initial NFM is as follows for the blue or red channels.

$$NFM_{ini}(\lambda) = \left\{ \begin{array}{c} 1.0 \\ or \\ Bump(\lambda) * \left(nfm0 + nfm1 * \lambda + nfm2 * \lambda^2\right) \end{array} \right\} \qquad 64.$$

Following are plots of the RSR' curves and NFM_{ini} for both red channels.

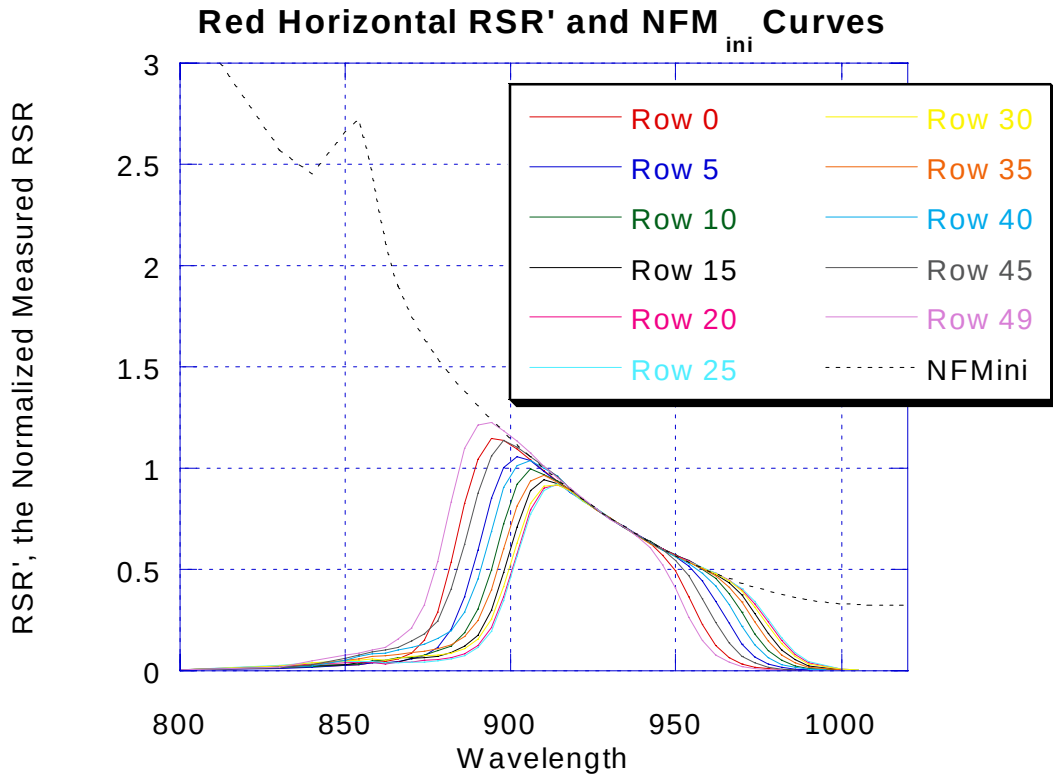

Figure 13-23 Red Horizontal NFM Curves

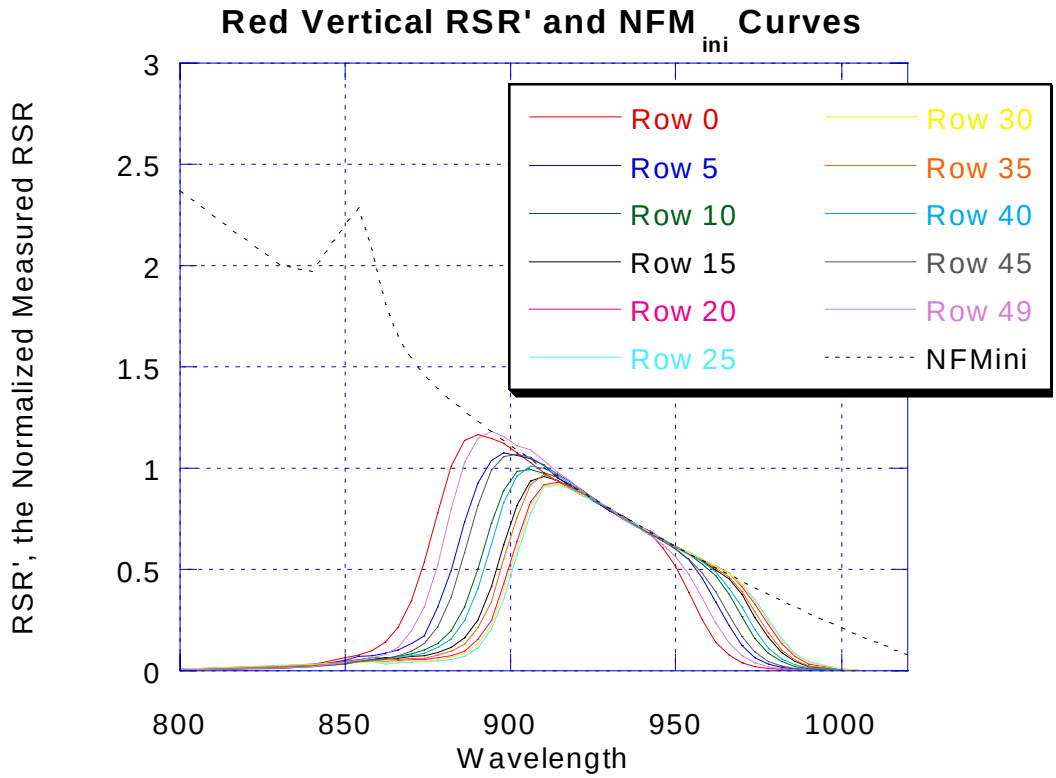

Figure 13-24 Red Vertical NFM Curves

13.4.3.5 Step 3-Find the Filter Curves

After finding the initial NFM, the filter curves can be determined. Because the filter transmission varies with incident angle, the filter shape is strongly dependent on row number. The beamsplitter in the optical train influences the shape as well, so the full field of view must be mapped rather than only half. A set of 12 curves can be chosen, at rows 0.5, 5, 10, 15, 20, 25, 30, 35, 40, 43, 45, and 48.5. These filter curves are defined at the reference temperature and column as the average of three adjacent measured RSRs. The filter curves for the top and bottom rows are defined as the average of the extreme two rows instead of three.

The red channel filters can be derived as above, but using as the foundation the RSR' as defined in equation 63. instead of the measured RSRs. The RSR' can then be divided by NFM_{ini} to result in the filter set.

It was found that the red channels have a few columns with RSR curves that do not match the rest of the channels. This is likely due to the fiber ribbon underfilling the fields of these channels. These columns have their own set of filter curves and coefficients. They are columns 0 and 1 for the red horizontal and column 0 for the red vertical.

Below are plots of the filter curves for all four channels. The filters are plotted in linear and log forms for clarity at extreme wavelengths. Tabular values are given in the body of the text.

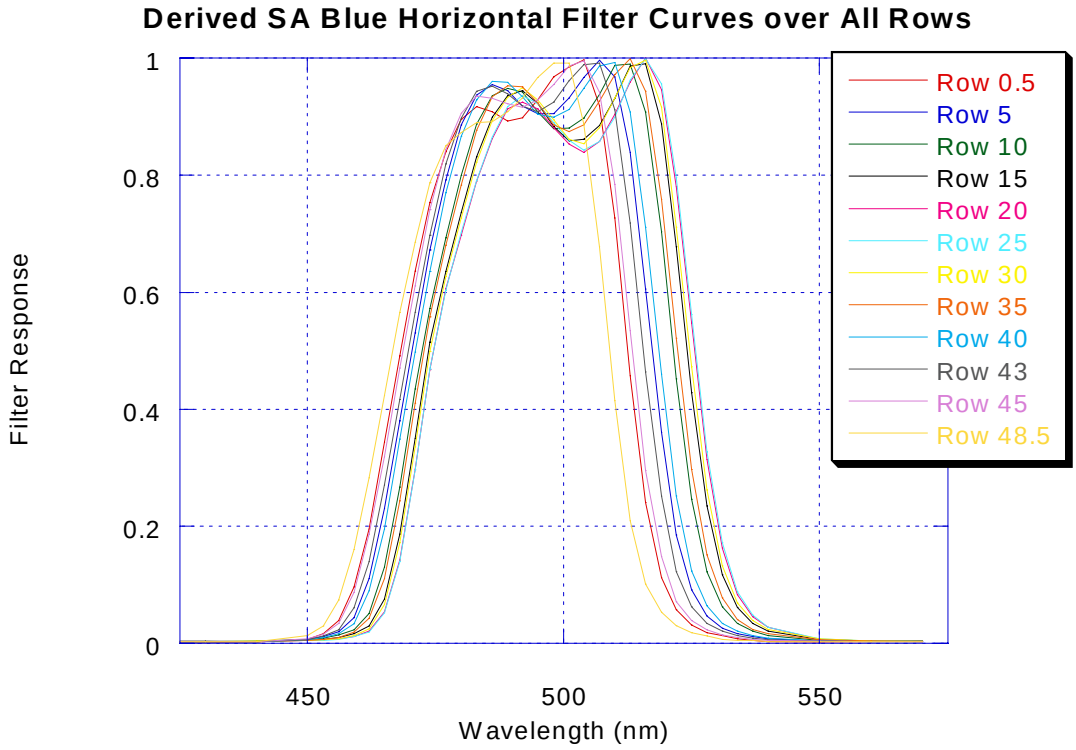

Figure 13-25 Derived Blue Horizontal Filter Curves

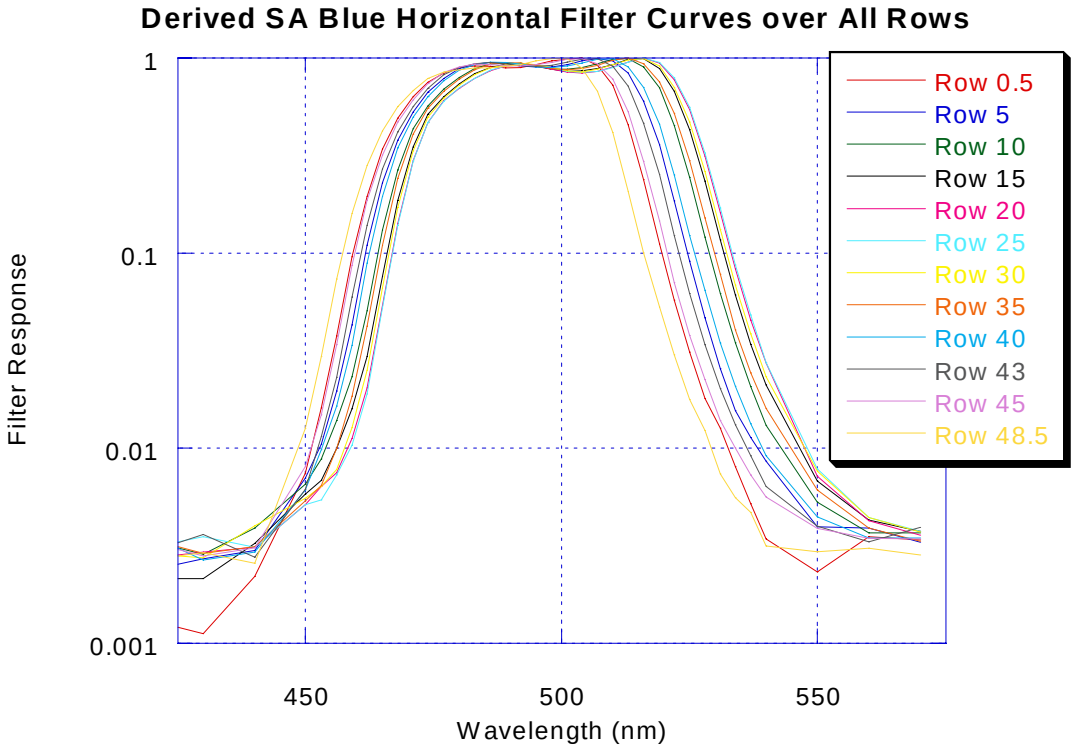

Figure 13-26 Derived Blue Horizontal Filter Curves, Log Scale

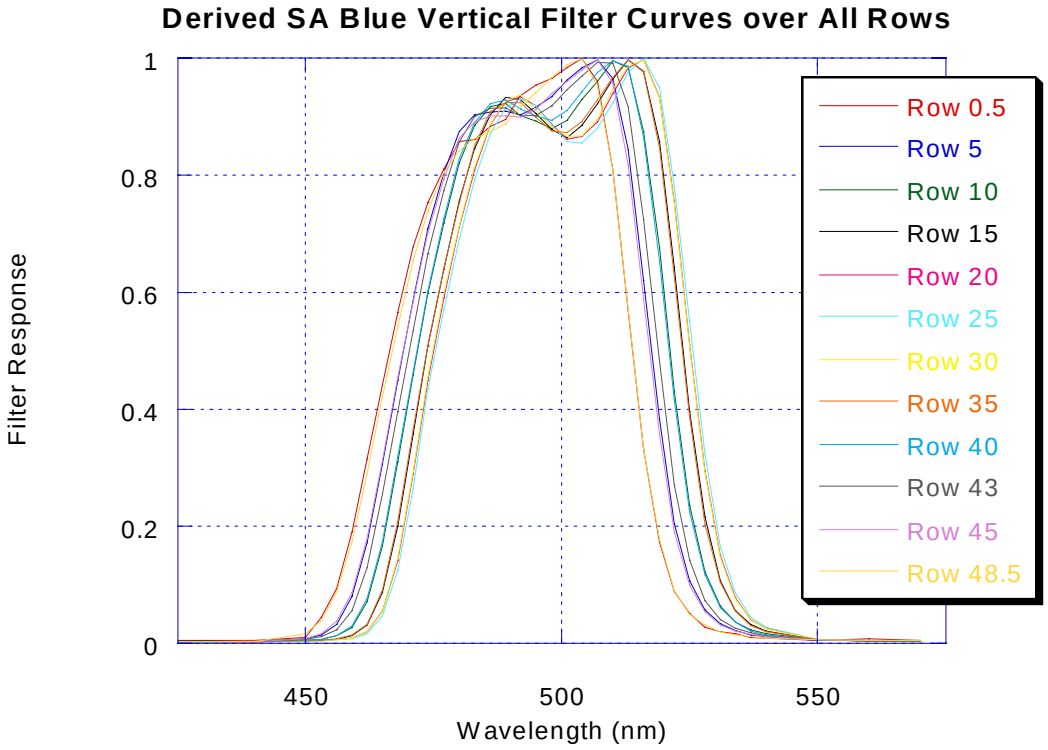

Figure 13-27 Derived Blue Vertical Filter Curves

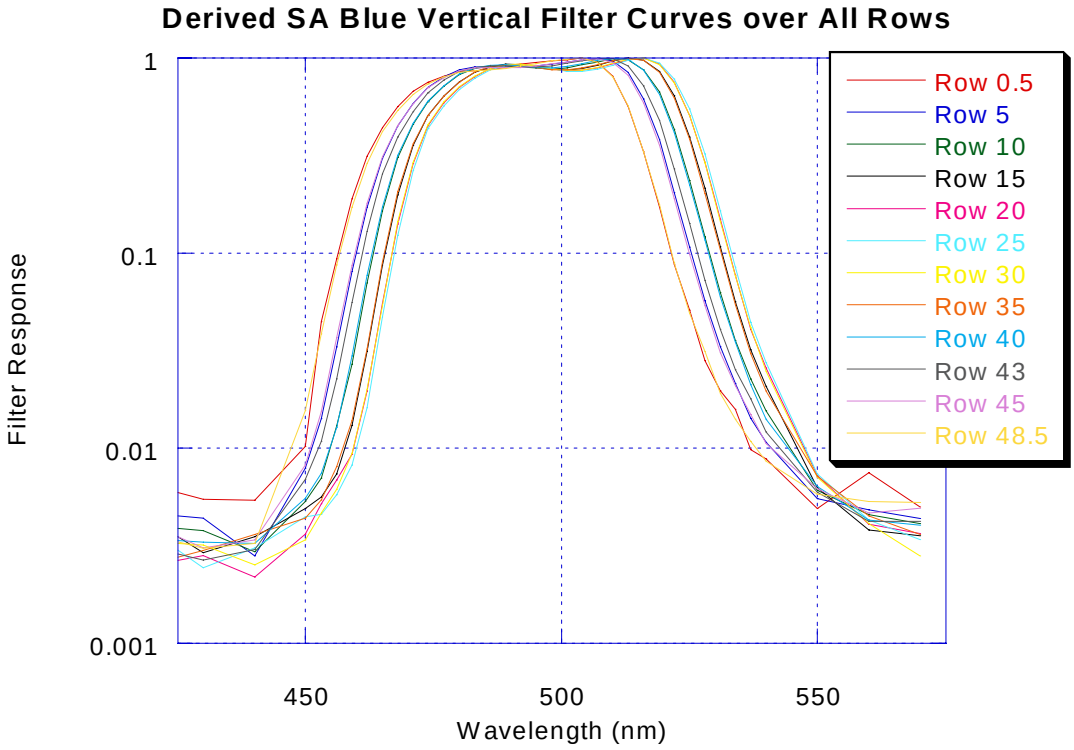

Figure 13-28 Derived Blue Vertical Filter Curves, Log Scale

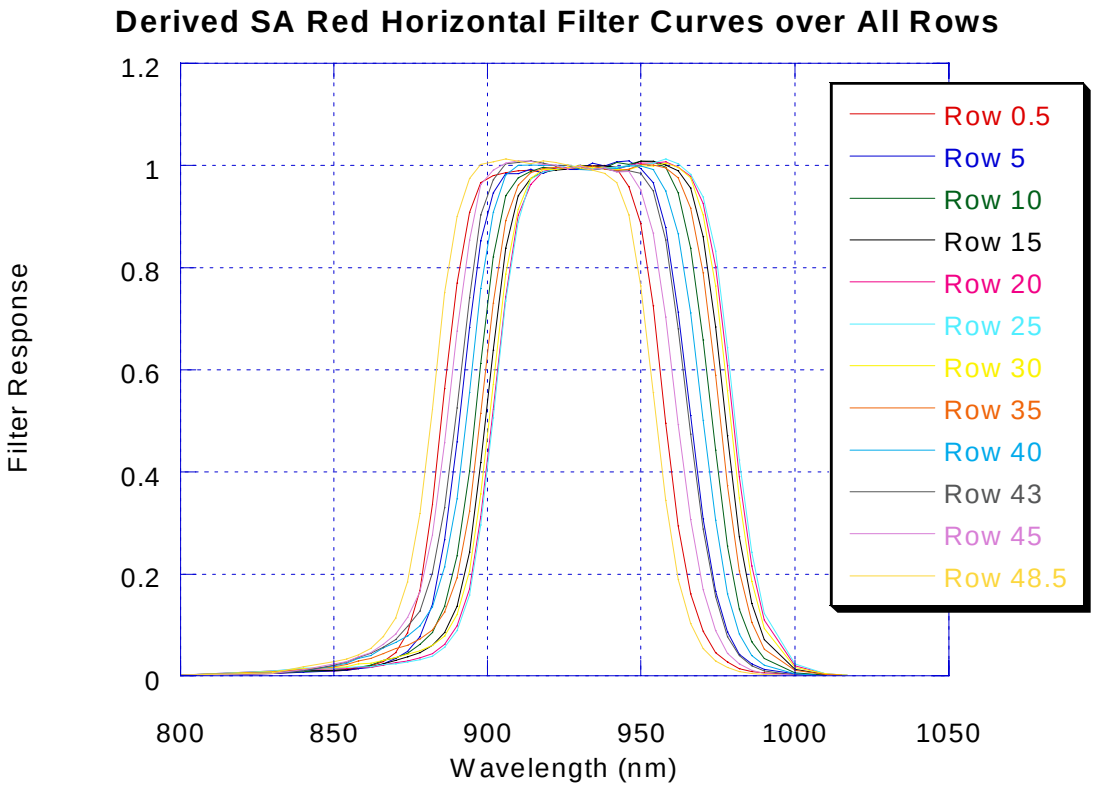

Figure 13-29 Derived Red Horizontal Filter Curves

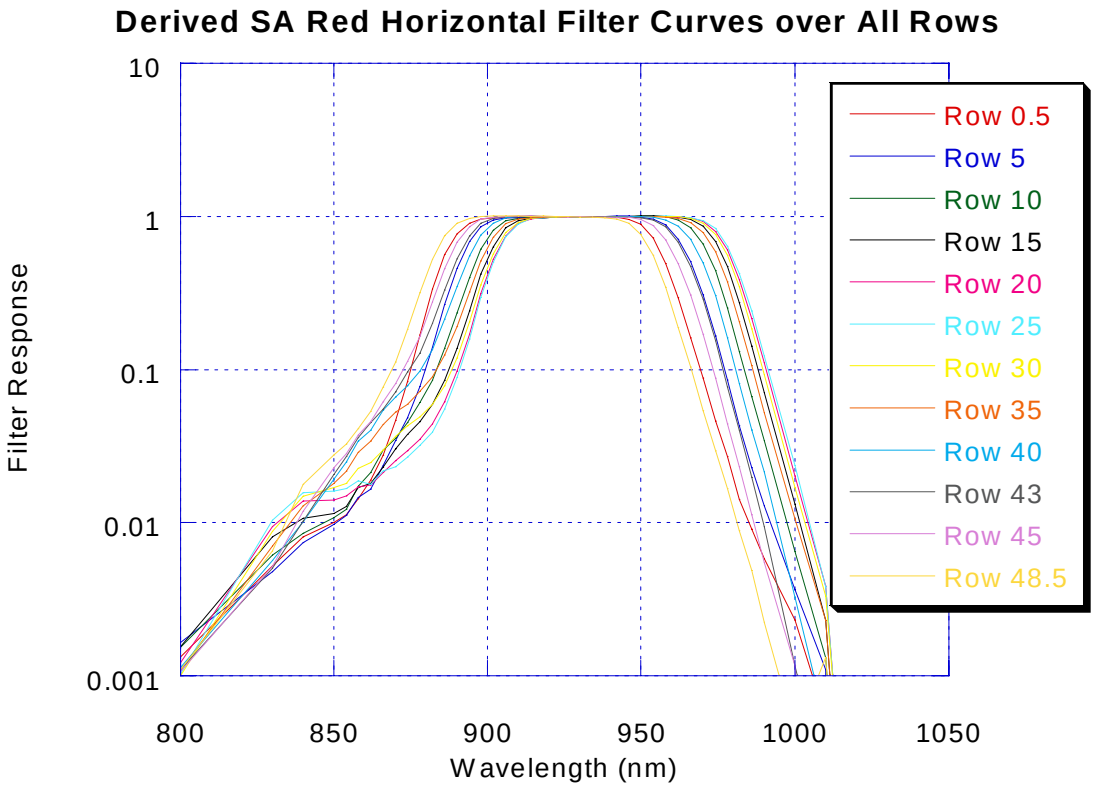

Figure 13-30 Derived Red Horizontal Filter Curves, Log Scale

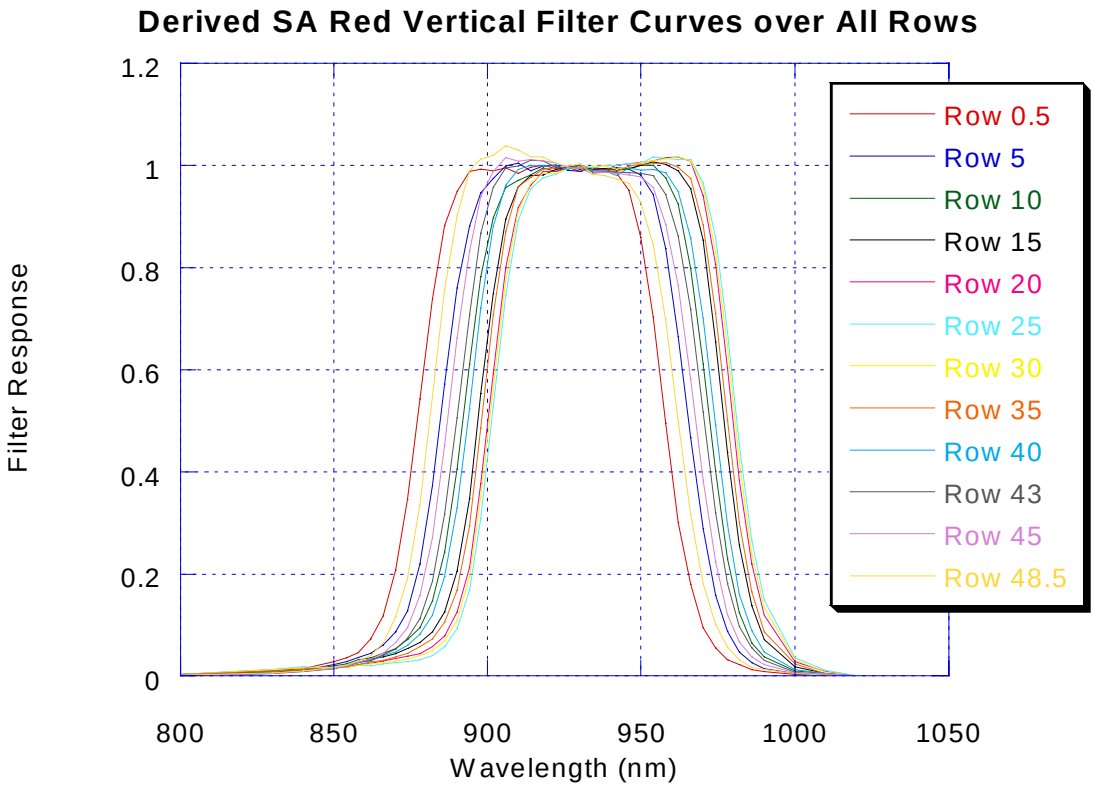

Figure 13-31 Derived Red Vertical Filter Curves

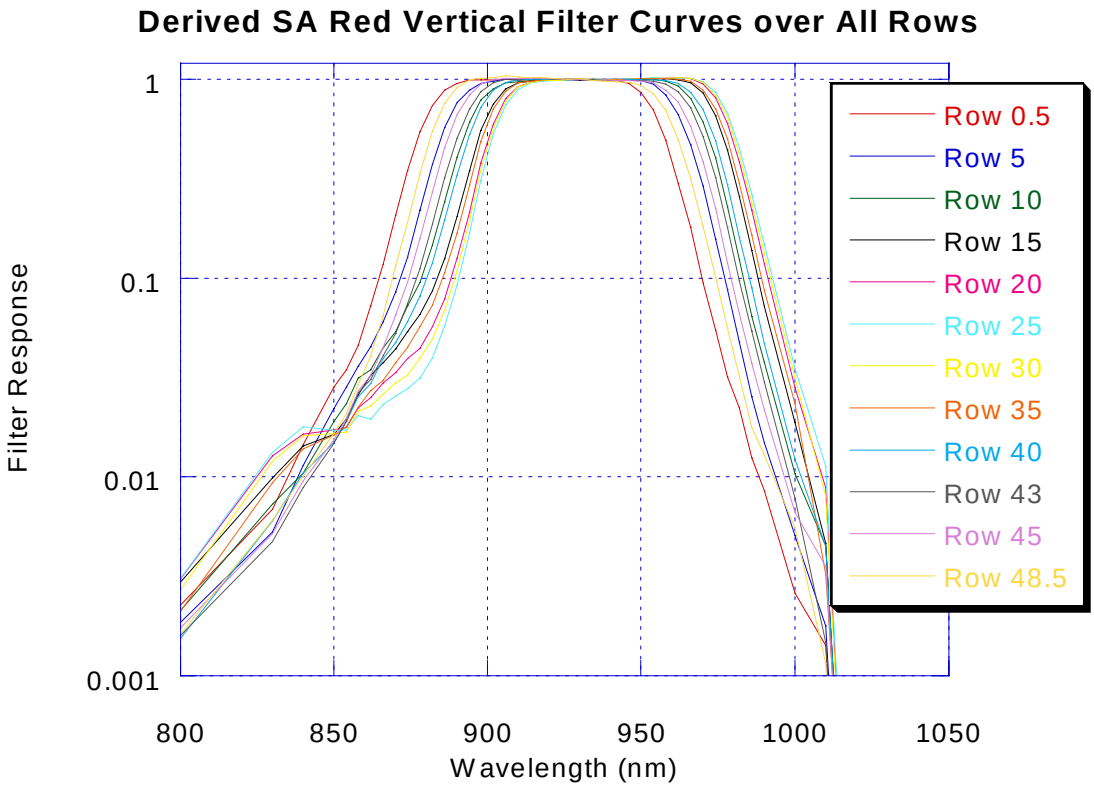

Figure 13-32 Derived Red Vertical Filter Curves, Log Scale

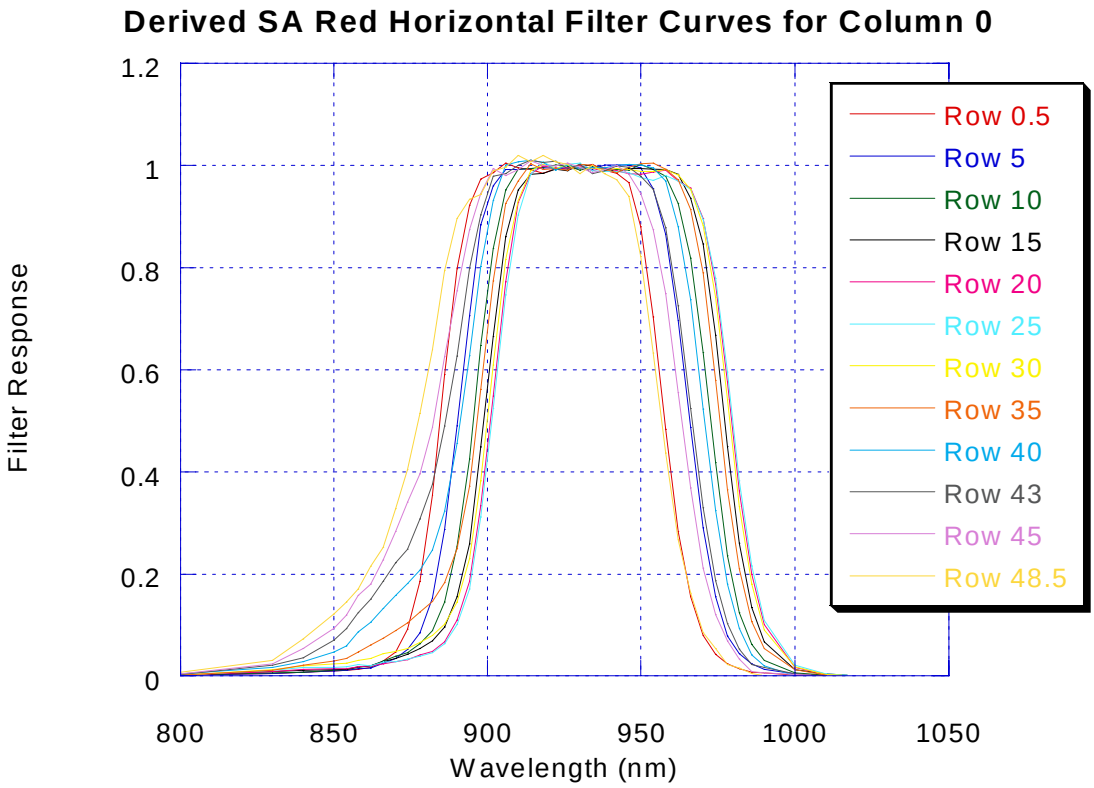

Figure 13-33 Derived Red Horizontal Column 0 Filter Curves

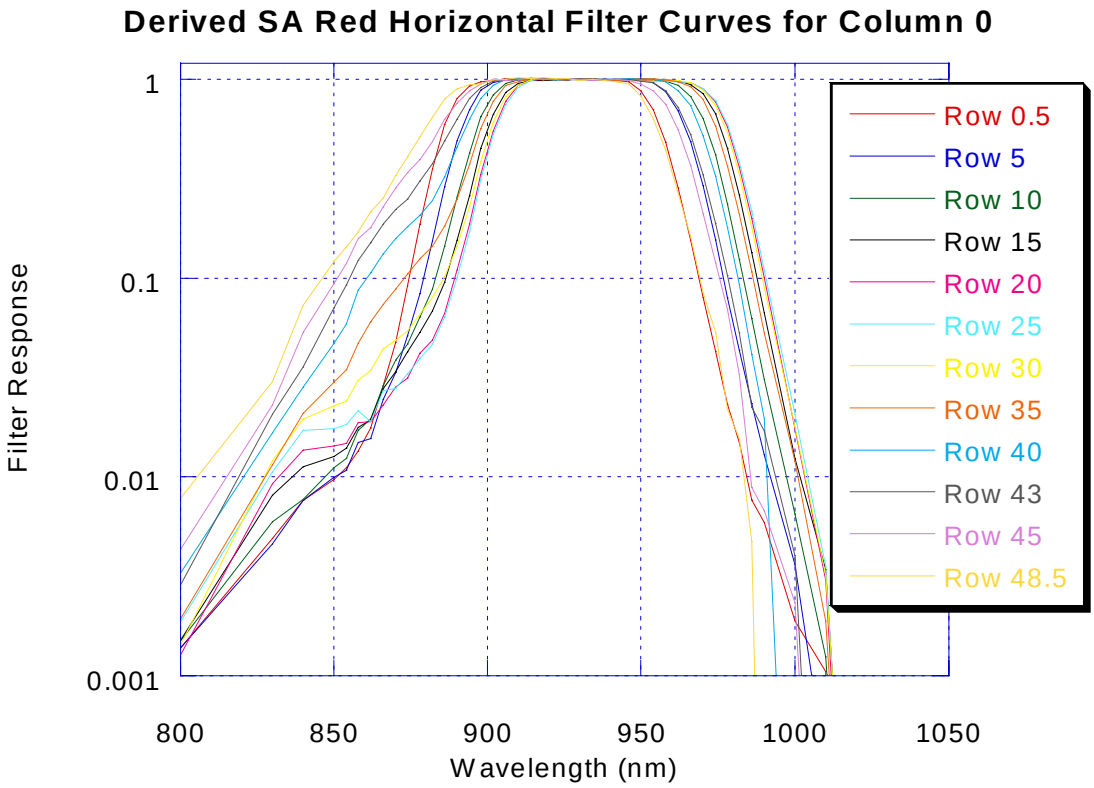

Figure 13-34 Derived Red Horizontal Column 0 Filter Curves, Log Scale

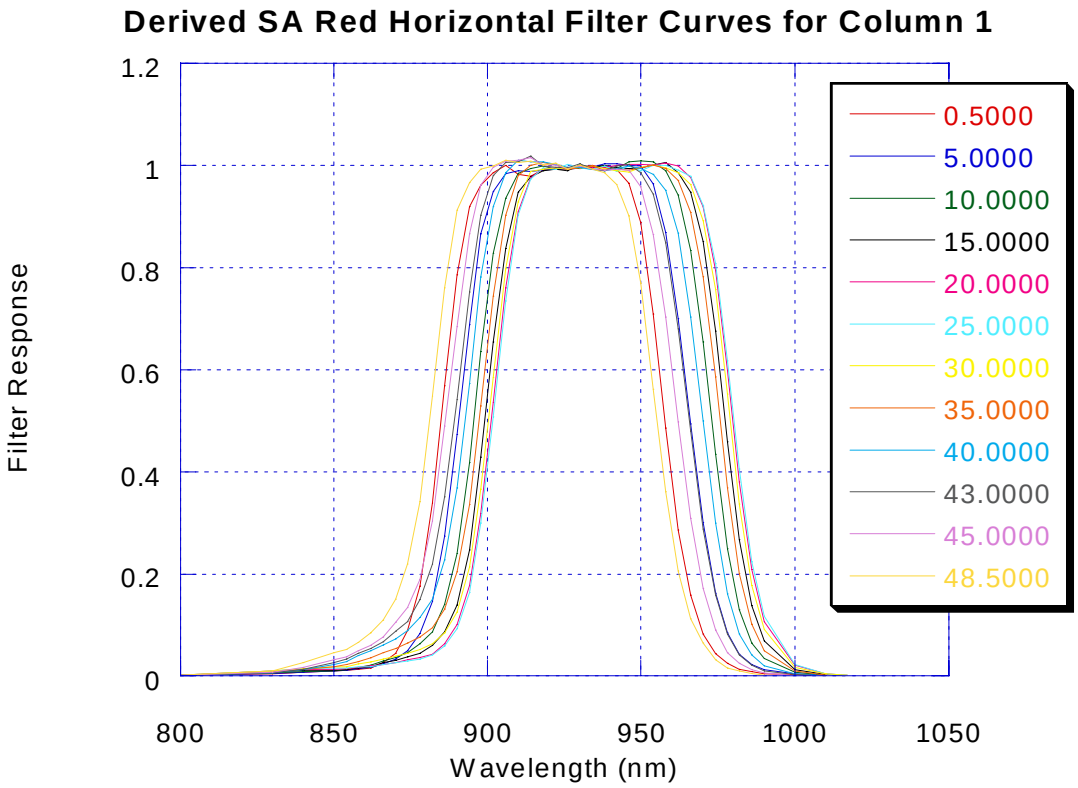

Figure 13-35 Derived Red Horizontal Column 1 Filter Curves

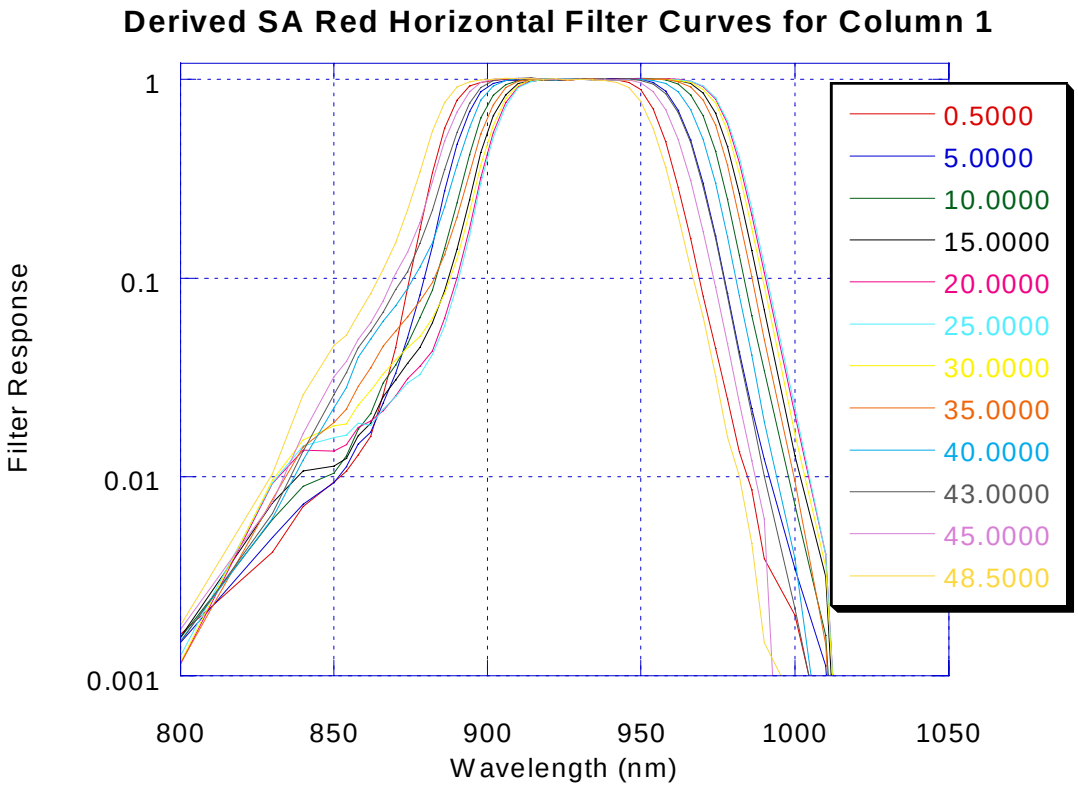

Figure 13-36 Derived Red Horizontal Column 1 Filter Curves, Log Scale

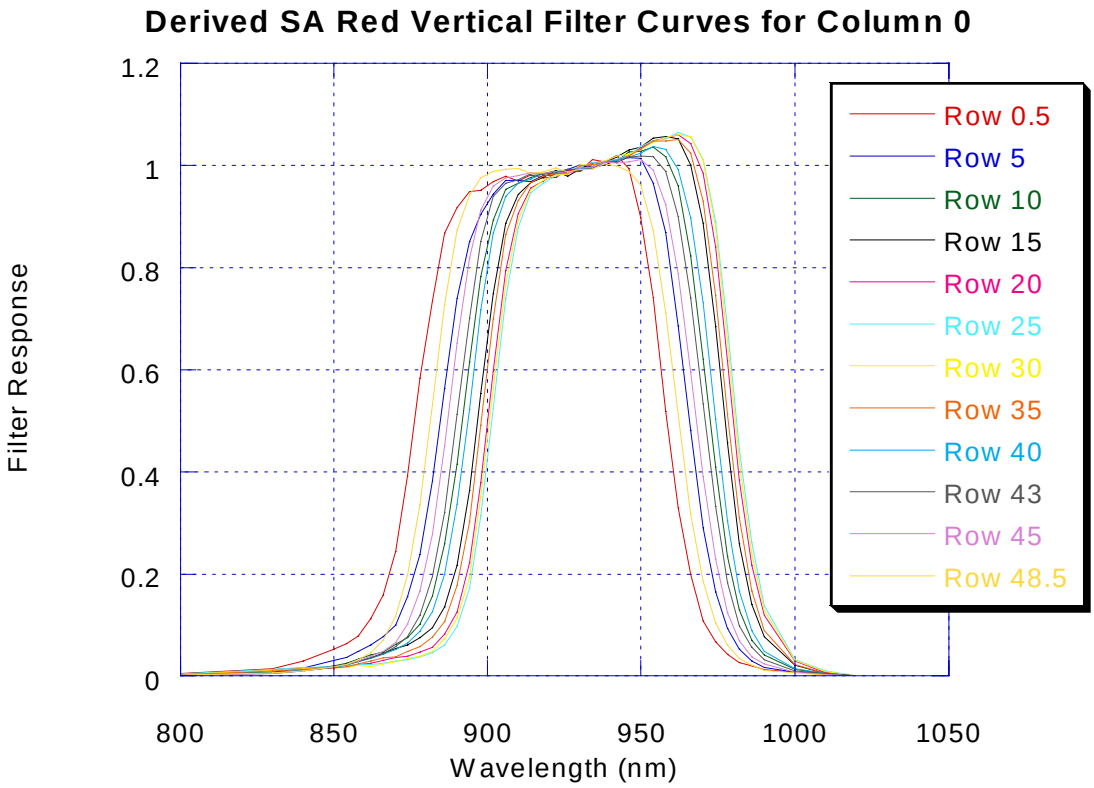

Figure 13-37 Derived Red Vertical Column 0 Filter Curves

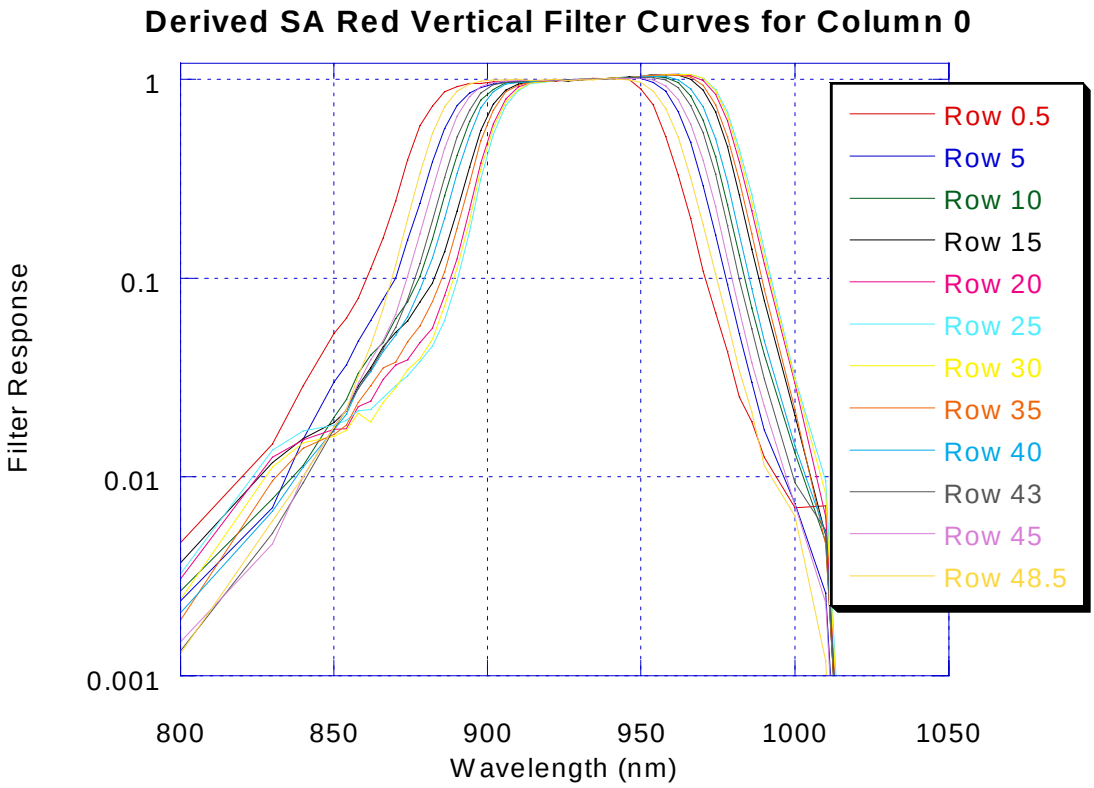

Figure 13-38 Derived Red Vertical Column 0 Filter Curves, Log Scale

13.4.3.6 Step 4-Find the Thermal Variations of the Non-Filter Models

To find the thermal variations in the NFM, we use the filter derived above as a base. Recall that for the blue, the filter is defined by averaging the surrounding rows in the original RSR measurement at a reference temperature and column. This average can be performed at each temperature and then divided by the filter (the result at the reference temperature). The resultant ratio can then be averaged over row in wavelengths with good filter response. In mathematical language, the following can be performed.

$$\begin{aligned} avgd\_RSR(T,\lambda,r) &= \left|RSR(T,\lambda,c_{ref},r)\right|_{\text{avg of r-1,r,r+1}} \\ filter(\lambda,r) &= avgd\_RSR(T_{ref},\lambda,r) \\ NFM\_ratio(T,\lambda,r) &= \frac{avgd\_RSR(T,\lambda,r)}{filter(\lambda,r)} \\ NFM\_ratio\_avg(T,\lambda) &= \left|NFM\_ratio(T,\lambda,r)\right|_{\text{avg over row where filter response} > 50\%} \end{aligned} \qquad 65.$$

Next, we form a ratio of *NFM_ratio_avg* to show the change in NFM per degree. This ratio can be averaged over temperature and then fit with a polynomial in wavelength.

$$ratio(T,\lambda) = \frac{NFM\_ratio\_avg(T,\lambda) - NFM\_ratio\_avg(T_{ref},\lambda)}{T_{ref} - T} \qquad 66.$$

$$avg\_ratio(\lambda) = \left| ratio(T,\lambda) \right|_{\text{avg over T}}$$

For the red, the process is identical, except the definition of NFM_ratio in equation 65. uses the RSR' in the numerator instead of the filter, and the bump is included, as follows.

$$NFM\_ratio(T,\lambda,r) = \frac{RSR'(T,\lambda,r)}{filter(\lambda,r) * Bump(\lambda) * (nfm0 + nfm1 * \lambda * nfm2 * \lambda^2)} \qquad 67.$$

The result is a set of thermal coefficients in wavelength that can be used to find the non-filter model at any temperature. Recall that the reference temperature is 224.7K.

$$NFM(T,\lambda) = NFM_{ini}(\lambda) * \left(1 + \left(T_{ref} - T\right) * \left[a + b\lambda + c\lambda^2 + d\lambda^3\right]\right)$$

$$where: \qquad 68.$$

a, b, c, and d are the thermal coefficients of the SA channel

The coefficients in all cases are in the following table. Red Horizontal columns 0 and 1 require their own set of thermal coefficients. These special coefficients are included here.

Table 13-14 Thermal Coefficients for All SA Channels

Channel	a	b	c	d
Blue Hor	2.0519205	-0.012112786	2.3854392e-005	-1.5672918e-008
Blue Ver	2.6717794	-0.015919638	3.1632590e-005	-2.0960937e-008
Red Hor	4.1627853	-0.013355480	1.4316606e-005	-5.1278929e-009
Red Ver	0.46694120	-0.0014621260	1.5654954e-006	-5.7336477e-010
Red Hor, 0	5.2851043	-0.016804565	1.7844364e-005	-6.3286793e-009
Red Hor, 1	4.9409769	-0.015830010	1.6938123e-005	-6.0531465e-009

Following are plots of the thermal ratios and their polynomial fits for all channels.

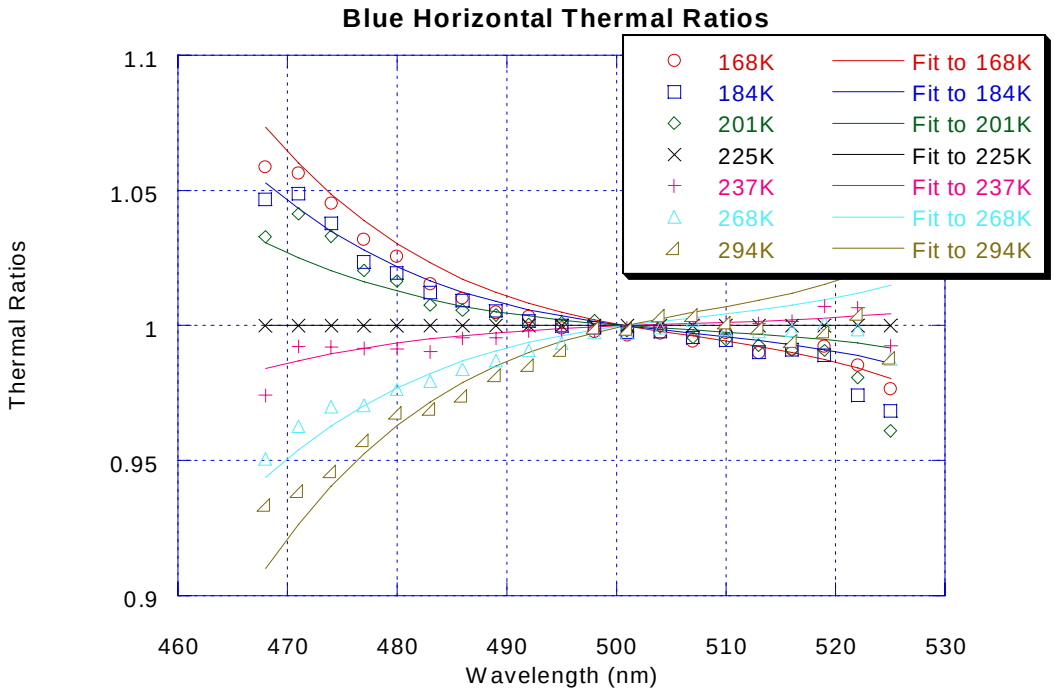

Figure 13-39 Blue Horizontal Non-Filter Model Thermal Performance for Reference Column

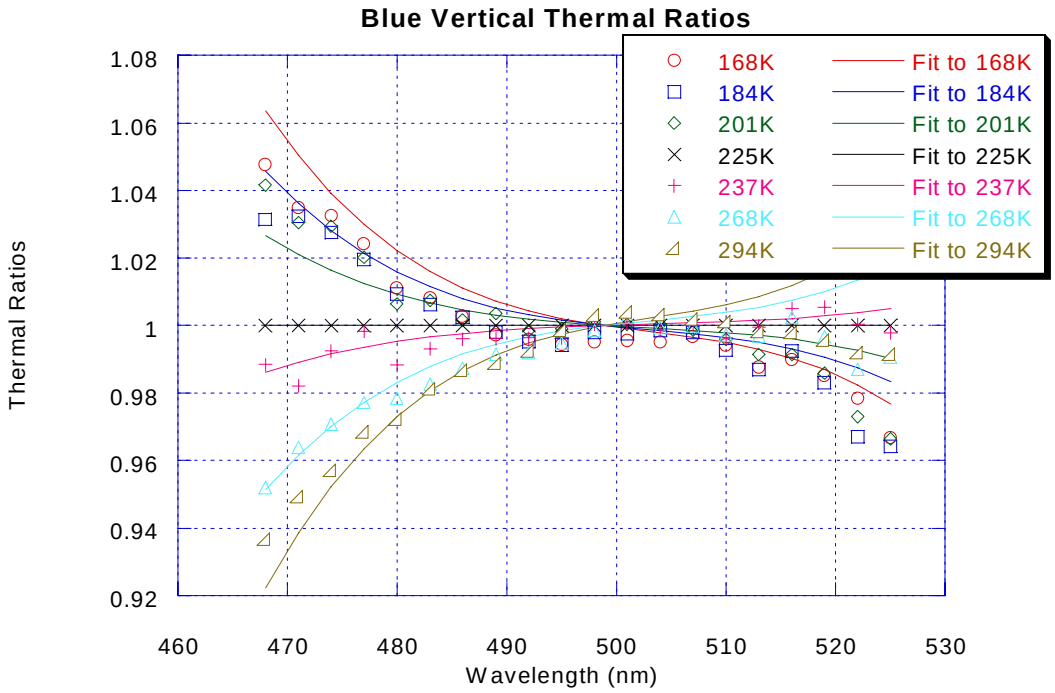

Figure 13-40 Blue Vertical Non-Filter Model Thermal Performance for Reference Column

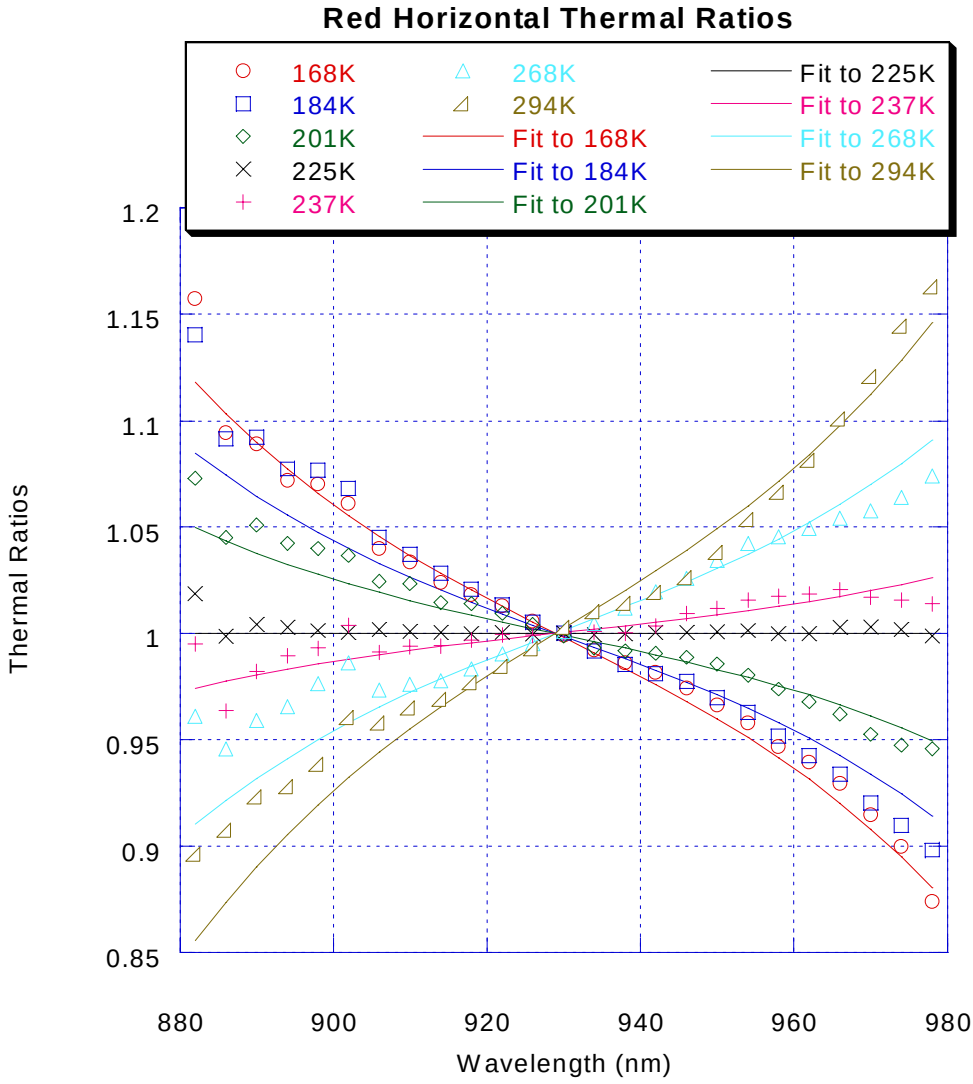

Figure 13-41 Red Horizontal Non-Filter Model Thermal Performance for Reference Column

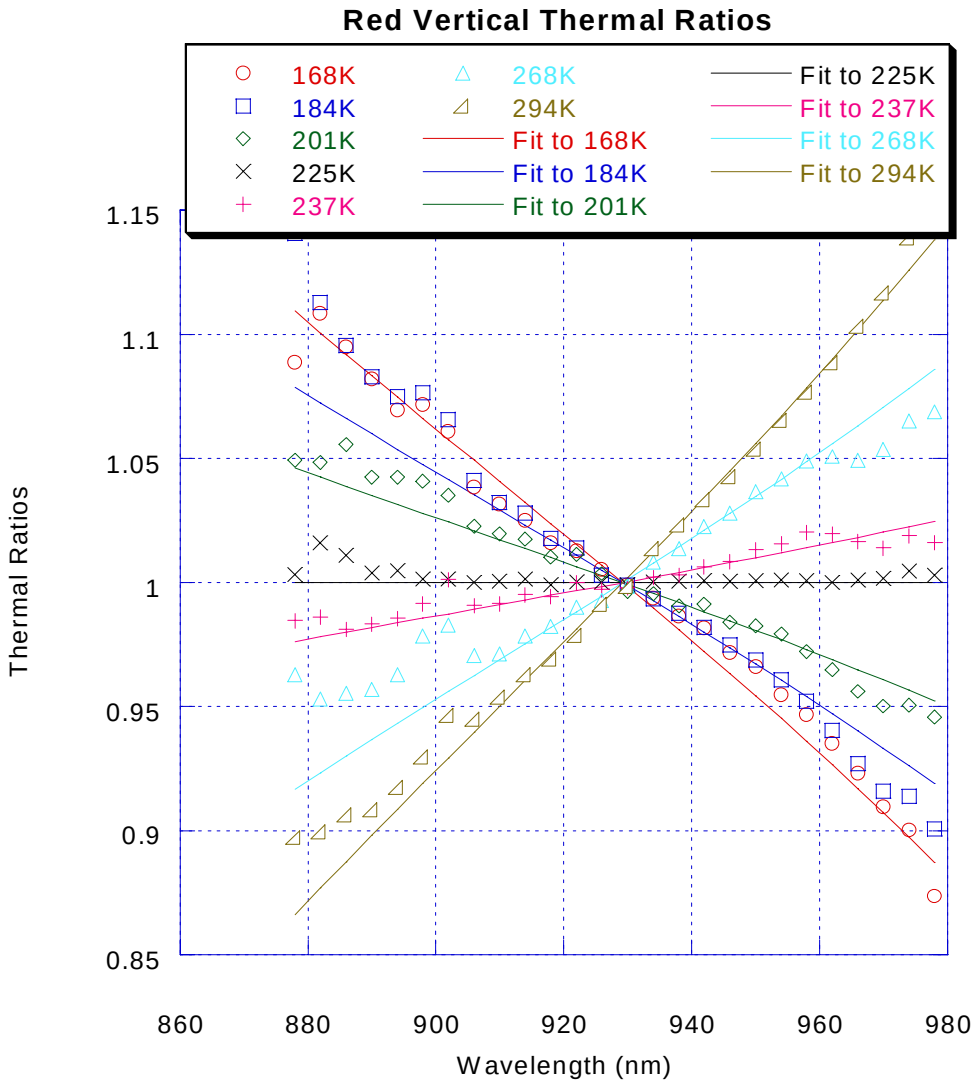

Figure 13-42 Red Vertical Non-Filter Model Thermal Performance for Reference Column

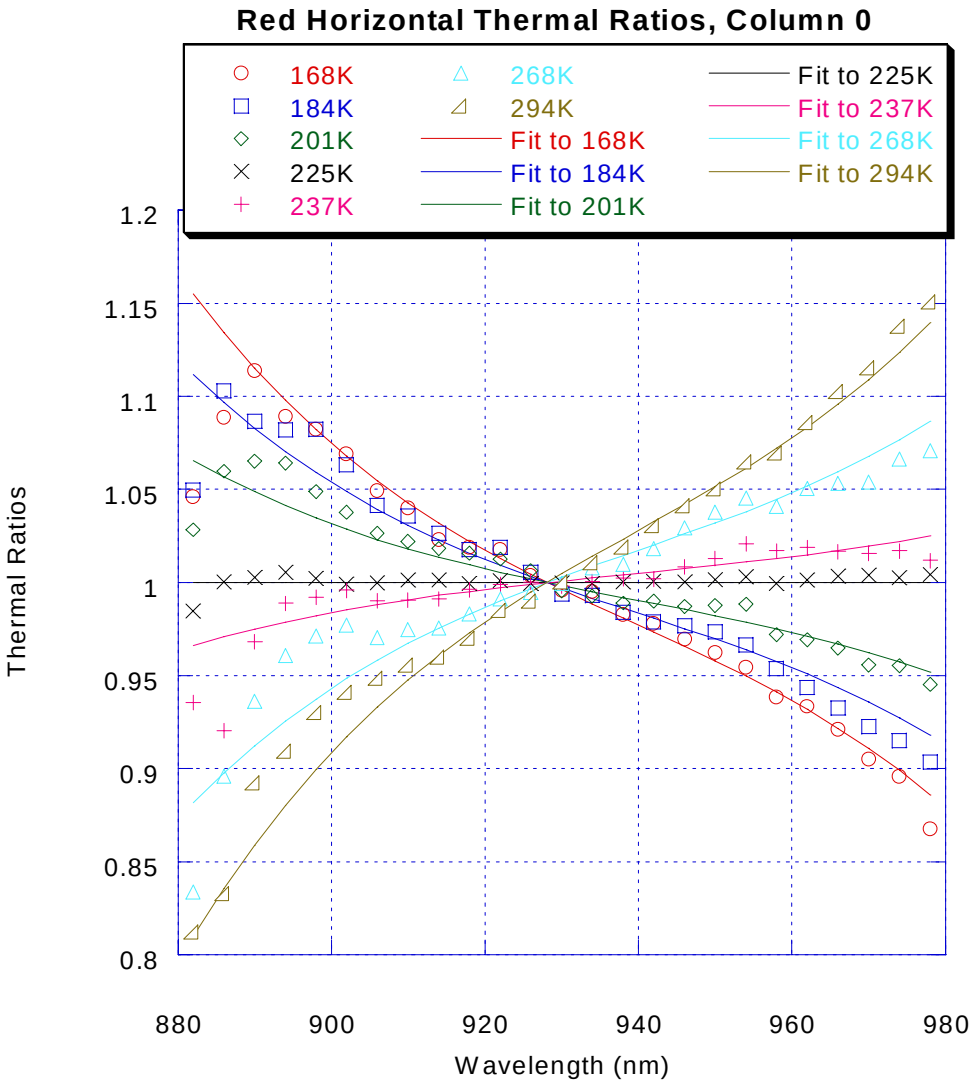

Figure 13-43 Red Horizontal Non-Filter Model Thermal Performance for Column 0

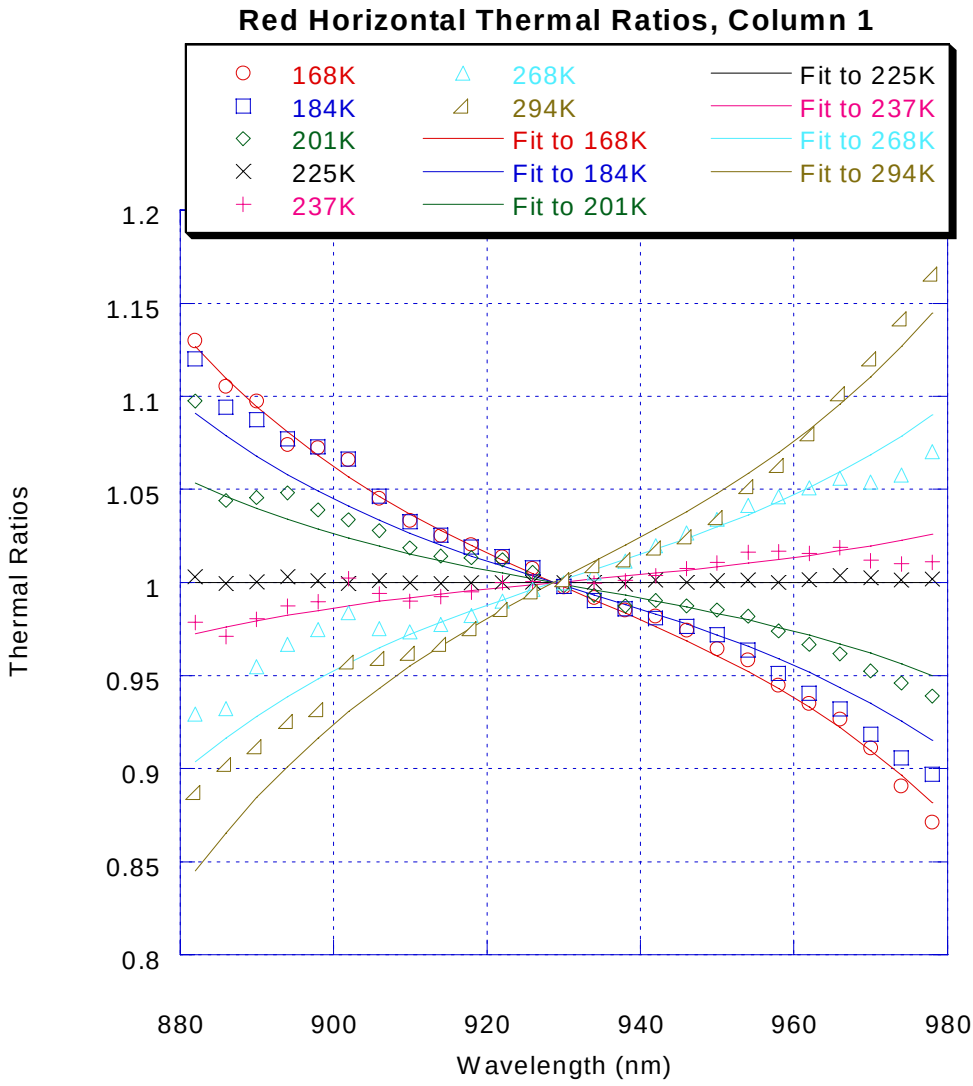

Figure 13-44 Red Horizontal Non-Filter Model Thermal Performance for Column 1

13.4.3.7 Step 5-Find the Column Variations of the Non-Filter Models

At this point in the analysis, the relative spectral response is modeled for the reference column at all temperatures. The other columns can be modeled in a similar way by fitting a polynomial to the variation of the column RSR to the reference column RSR at the reference temperature.

$$NFM\_ratio(\lambda,c,r) = \frac{Measured\_RSR(T_{ref},\lambda,c,r)}{filter(\lambda,r)} \qquad 69.$$

$$NFM\_ratio\_avg(\lambda,c) = \left|NFM\_ratio(\lambda,c,r)\right|_{\text{avg over row where filter response} > 50\%}$$

Now a polynomial can be fit to *NFM_ratio_avg* to result in the column coefficients that are used as M0(c), M1(c), M2(c), and M3(c). The curve fits are shown in the following plots.

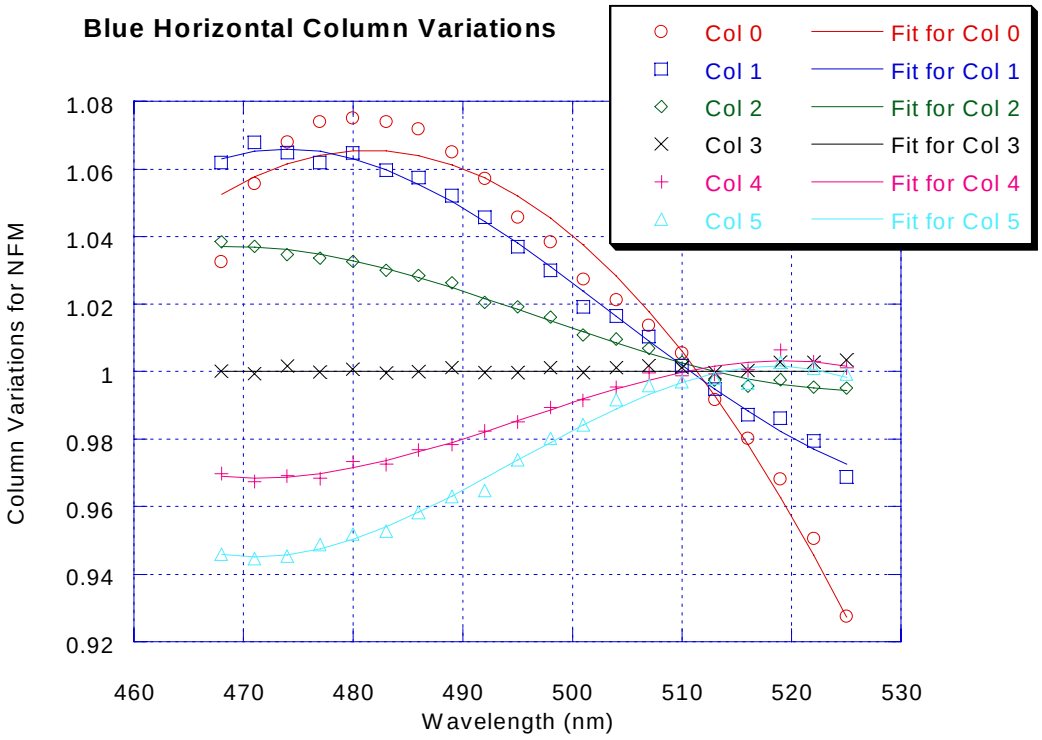

Figure 13-45 Blue Horizontal Non-Filter Model Column Performance

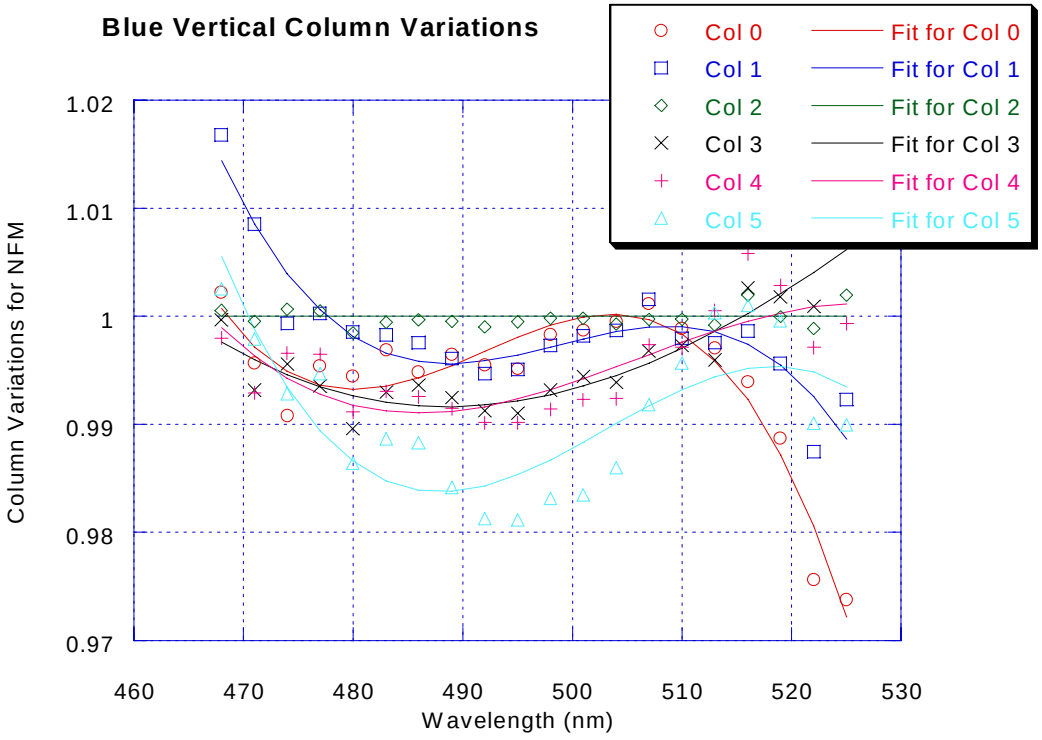

Figure 13-46 Blue Vertical Non-Filter Model Column Performance

The red channels have an additional complexity in their derivation as they did in the thermal fits. Instead of the measured RSR data, a normalized, averaged RSR function is used in the *NFM_ratio* in equation 69.

$$RSR'(\lambda,c,r) = RSR(T_{ref},\lambda,c,r) * \frac{\left\|RSR(T_{ref},\lambda,c_{ref},r)\right|_{922-938nm}\Big|_{row}}{\left|RSR(T_{ref},\lambda,c,r)\right|_{922-938nm}}$$

where:

$RSR(T_{ref},\lambda,c,r)$ = Measured RSR at reference temperature

T_{ref} = Reference temperature

c_{ref} = Refernence column

$\left|RSR(T_{ref},\lambda,c_{ref},r)\right|_{922-938nm}$ = Average of measured RSR over wavelengths from $922-938nm$

$\left\|RSR(T_{ref},\lambda,c_{ref},r)\right|_{922-938nm}\Big|_{row}$ = Average of $\left|RSR(T_{ref},\lambda,c_{ref},r)\right|_{922-938nm}$ overall rows

$$NFM\_ratio(\lambda,c,r) = \frac{RSR'(\lambda,c,r)}{filter(\lambda,r) * Bump(\lambda) * (nfm0 + nfm1 * \lambda + nfm2 * \lambda^2)} \qquad 70.$$

Then the *NFM_ratio* is averaged as in equation 69. and fit with a polynomial. The curve fits are shown in the following plots.

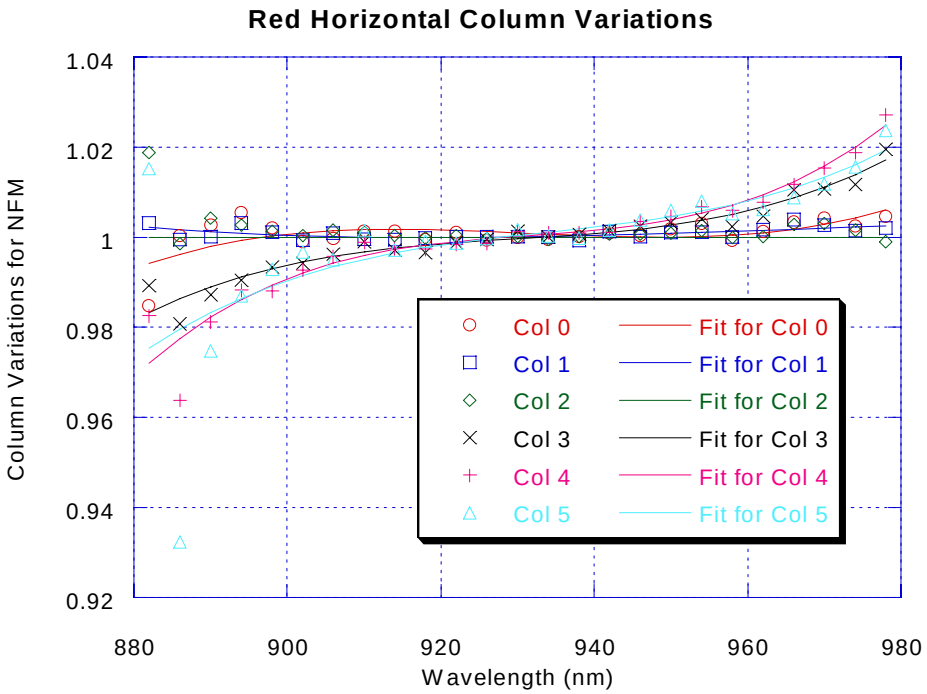

Figure 13-47 Red Horizontal Non-Filter Model Column Performance

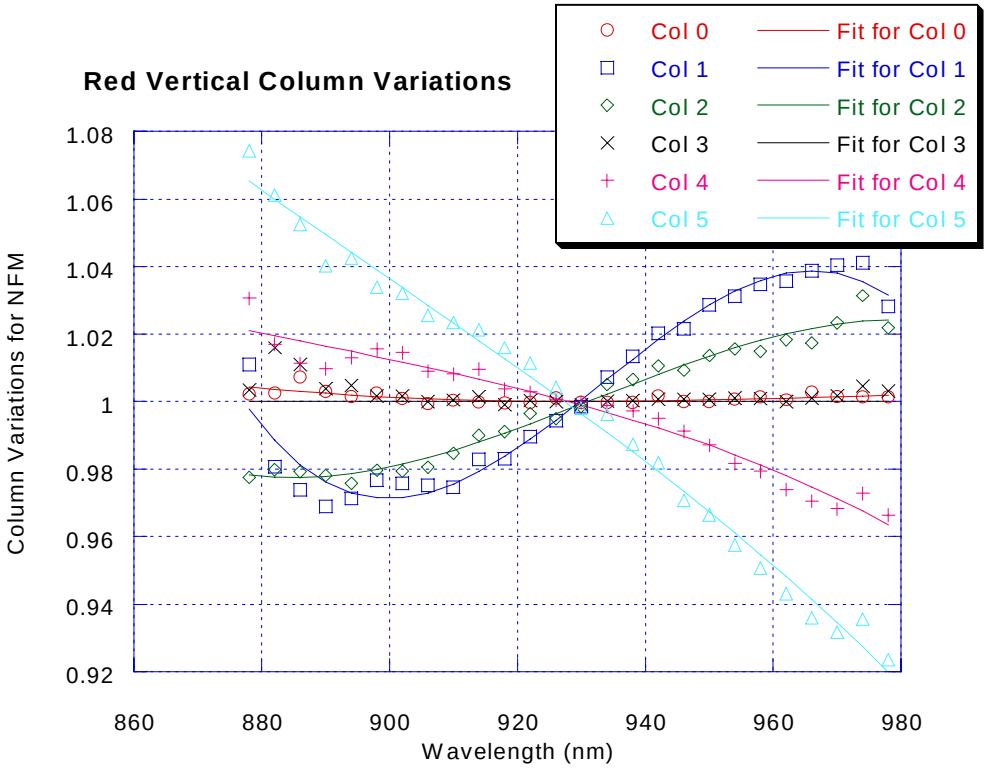

Figure 13-48 Red Vertical Non-Filter Model Column Performance

The column coefficients M0 through M3 for each channel are in the following tables.

Table 13-15 Blue Horizontal Column Coefficients

	M0	M1	M2	M3
Column 0	-1.576161E+01	6.991217E-02	-7.261663E-05	0.000000E+00
Column 1	-1.120476E+02	6.776472E-01	-1.348858E-03	8.917191E-07
Column 2	-5.451464E+01	3.371992E-01	-6.802498E-04	4.559225E-07
Column 3	1.0	0.0	0.0	0.0
Column 4	7.670377E+01	-4.607676E-01	9.324273E-04	-6.274879E-07
Column 5	1.279626E+02	-7.734728E-01	1.566727E-03	-1.055404E-06

Table 13-16 Blue Vertical Column Coefficients

	M0	M1	M2	M3
Column 0	1.287794E+02	-7.803157E-01	1.587449E-03	-1.075872E-06
Column 1	1.076329E+02	-6.419133E-01	1.287519E-03	-8.604670E-07
Column 2	1.0	0.0	0.0	0.0
Column 3	1.033230E+01	-5.103488E-02	9.152373E-05	-5.362022E-08
Column 4	4.158349E+01	-2.413895E-01	4.777937E-04	-3.147463E-07
Column 5	1.067493E+02	-6.317197E-01	1.256640E-03	-8.324925E-07

Table 13-17 Red Horizontal Column Coefficients

	M0	M1	M2	M3
Column 0	-6.951670E+01	2.272747E-01	-2.440805E-04	8.734615E-08
Column 1	9.833868E+00	-2.762700E-02	2.874322E-05	-9.946730E-09
Column 2	1.0	0.0	0.0	0.0
Column 3	-8.488152E+01	2.770449E-01	-2.980202E-04	1.069016E-07
Column 4	-1.488555E+02	4.824542E-01	-5.178775E-04	1.853475E-07
Column 5	-9.319383E+01	3.022677E-01	-3.235209E-04	1.154941E-07

Table 13-18 Red Vertical Column Coefficients

	M0	M1	M2	M3
Column 0	9.037937E+00	-2.485048E-02	2.555993E-05	-8.744530E-09
Column 1	3.750232E+02	-1.205694E+00	1.293924E-03	-4.622855E-07
Column 2	9.085585E+01	-2.906646E-01	3.126092E-04	-1.117840E-07
Column 3	1.0	0.0	0.0	0.0
Column 4	1.899895E+01	-6.003125E-02	6.722727E-05	-2.525717E-08
Column 5	2.436124E+01	-7.513855E-02	8.203623E-05	-3.038352E-08

13.4.3.8 Detailed Results

Thus, the Solar Aureole Relative Spectral Response is modeled. For the blue channels, the final equation is as follows,

$$SA\_RSR(T,\lambda,c,r) = filter(\lambda,r) * \begin{Bmatrix} \left(M0(c) + M1(c)*\lambda + M2(c)*\lambda^2 + M3(c)*\lambda^3\right) + \\ (224.7 - T)*\left(a + b*\lambda + c*\lambda^2 + d*\lambda^3\right) \end{Bmatrix} \quad 71.$$

where the filter and the coefficients M0 through M3 and a through d are in the tables above.

For the red channels, the final equation is as follows,

$$SA\_RSR(T,\lambda,c,r) = filter(\lambda,r) * Bump(\lambda) * \left(nfm0 + nfm1*\lambda + nfm2*\lambda^2\right) * \begin{Bmatrix} \left(M0(c) + M1(c)*\lambda + M2(c)*\lambda^2 + M3(c)*\lambda^3\right) + \\ (224.7 - T)*\left(a + b*\lambda + c*\lambda^2 + d*\lambda^3\right) \end{Bmatrix} \quad 72.$$

where the filter and the coefficients nfm0 through nfm2, M0 through M3 and a through d are in the tables above, and the *Bump* function is in equation 7. Care must be taken to use the correct filters and coefficients for the columns 0 and 1 as appropriate.

A useful figure of merit for the fit of the models is the root-mean-square deviation over wavelength for a pixel at a given temperature. The models were scaled up or down by up to three percent to minimize the root-mean-square deviations over wavelength from the measurements for each pixel and temperature. This scaling will be implicit in the absolute response values.

The following sets of plots show the fidelity of the scaled models to the measured relative spectral responses. In the majority of the cases, the root-mean-square deviations are within 1%. Some pixels at some temperatures, however, have larger deviations. These are addressed in the appendix to this section.

There is a plot set for each SA channel. Within each plot set are five types of plots.

1) The first plot is the bounds of the straight deviation (model minus measured) for all pixels in a column over all temperatures. This gives a feel for the fidelity of the model over wavelength and column.

2) The next plot is the root-mean-square deviation over rows of the root-mean-square deviation over wavelength for all columns and temperatures. This gives a feel for the overall fidelity of the model versus temperature.

3) The next set of two plots is the root-mean-square deviation over wavelength of every pixel for the extremes of the seven temperatures. This plot set shows the fidelity of each pixel's model RSR at these temperatures.

4) The next set of six plots is the measured and modeled RSRs for every pixel in column 4 at 168 K. The choice of this column and temperature was made to show the fidelity of the model prediction in column and temperature. The lines are the model, and the points are the measured points.

5) The final set of nine plots is the straight deviation (model minus measured) versus wavelength with error bars showing the measurement noise. A more detailed discussion of this noise and its impact on the modeling fidelity is in the appendix. The nine plots are for rows 5, 10, 15, 20, 25, 30, 35, 40, and 45 from column 4 at 168 K.

Figure 13-49 Blue Horizontal Relative Spectral Response Modeling Results – Set of Nineteen Plots

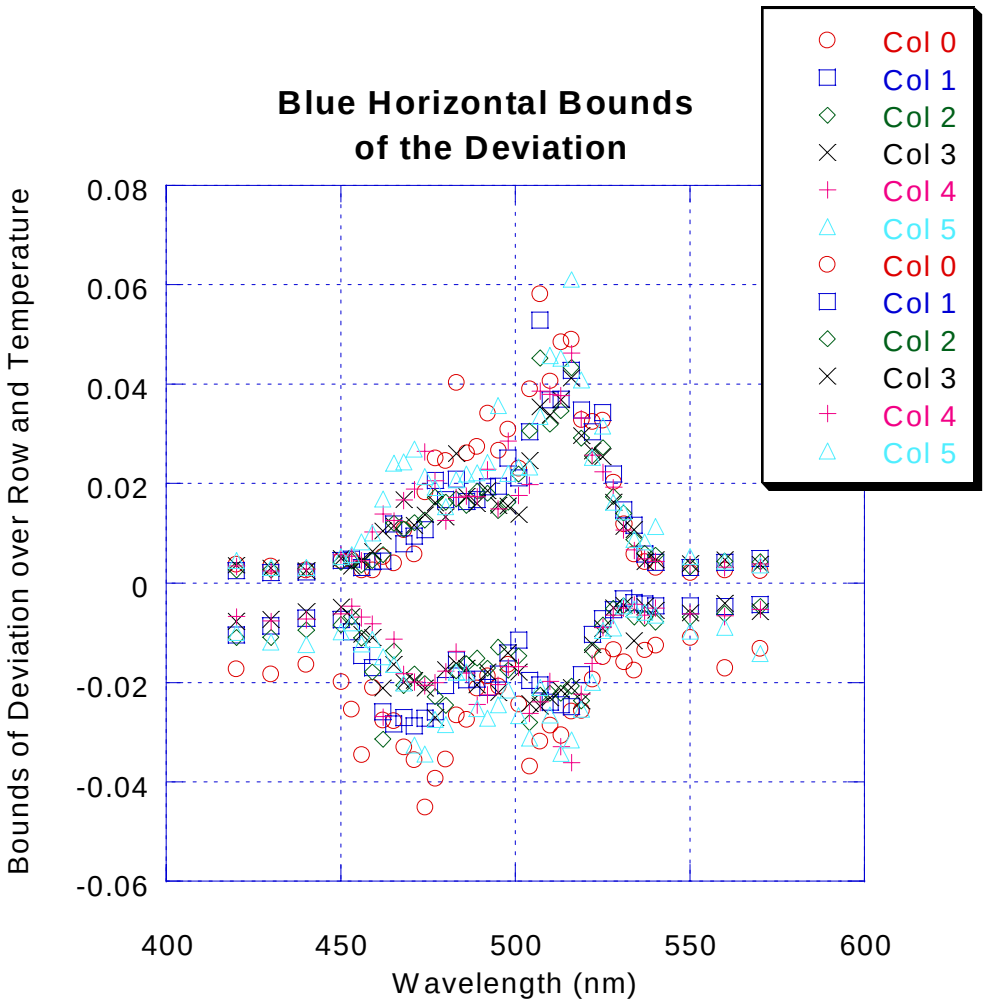

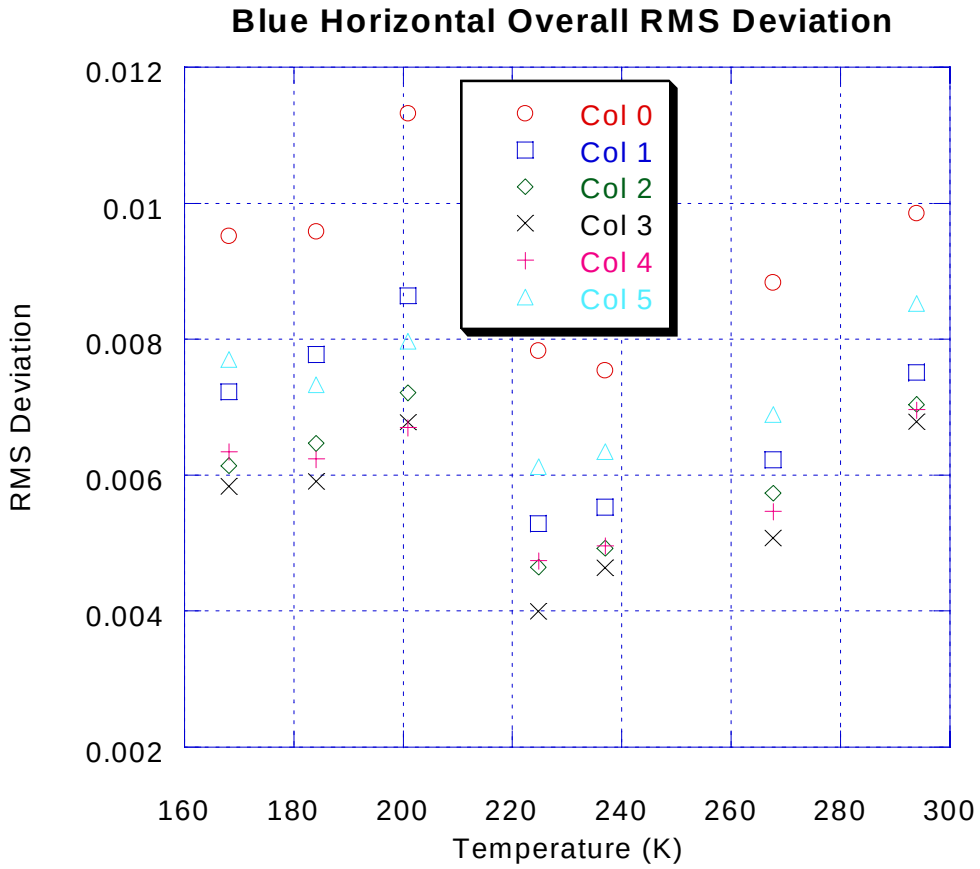
Blue Horizontal Overall RMS Deviation
RMS Deviation
0.012
0.01
0.008
0.006
0.004
0.002
160
180
200
220
240
260
280
300
Temperature (K)
Col 0
Col 1
Col 2
Col 3
Col 4
Col 5

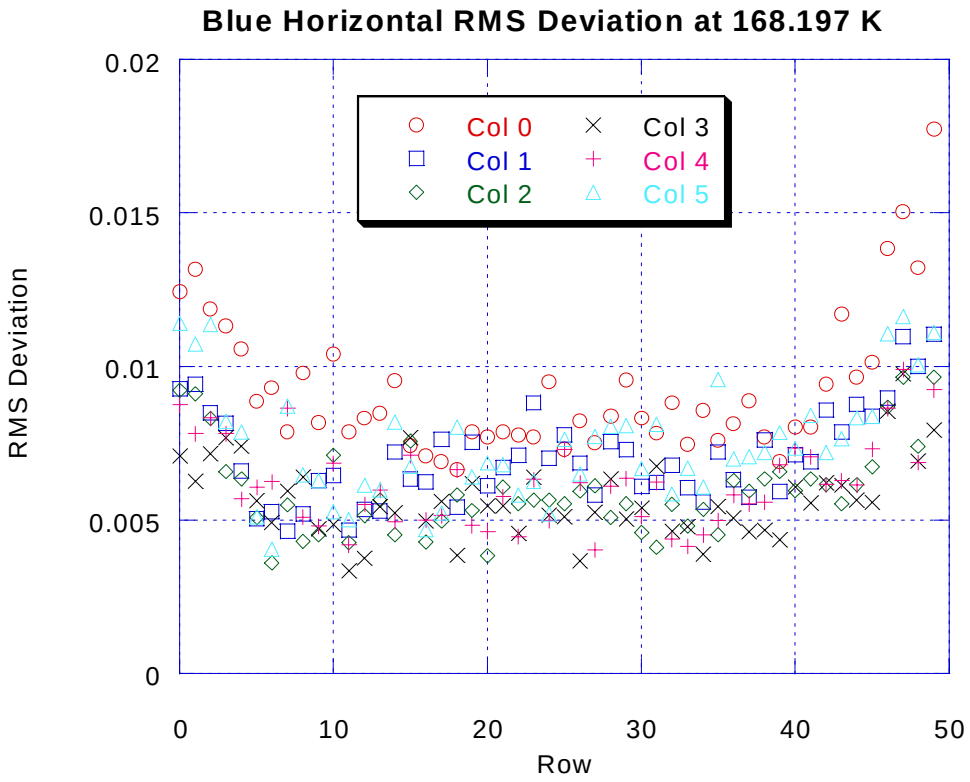
Blue Horizontal RMS Deviation at 168.197 K
RMS Deviation
0.02
0.015
0.01
0.005
0
0
10
20
30
40
50
Row
Col 0
Col 1
Col 2
Col 3
Col 4
Col 5

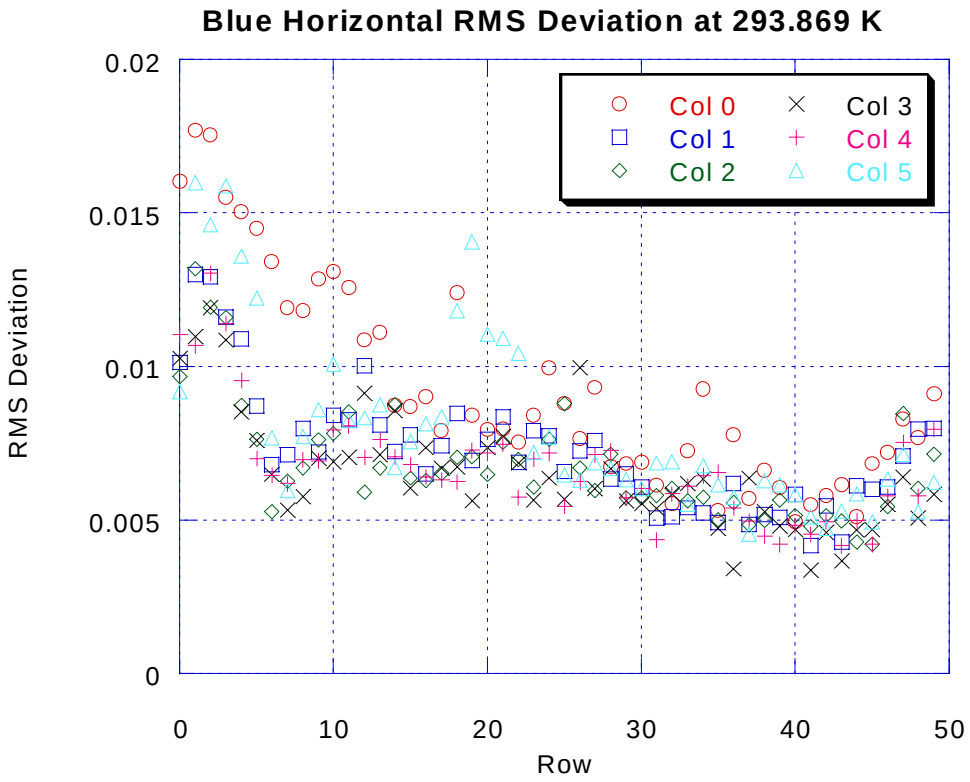
Blue Horizontal RMS Deviation at 293.869 K
RMS Deviation
0.02
0.015
0.01
0.005
0
0
10
20
30
40
50
Row
Col 0
Col 1
Col 2
Col 3
Col 4
Col 5

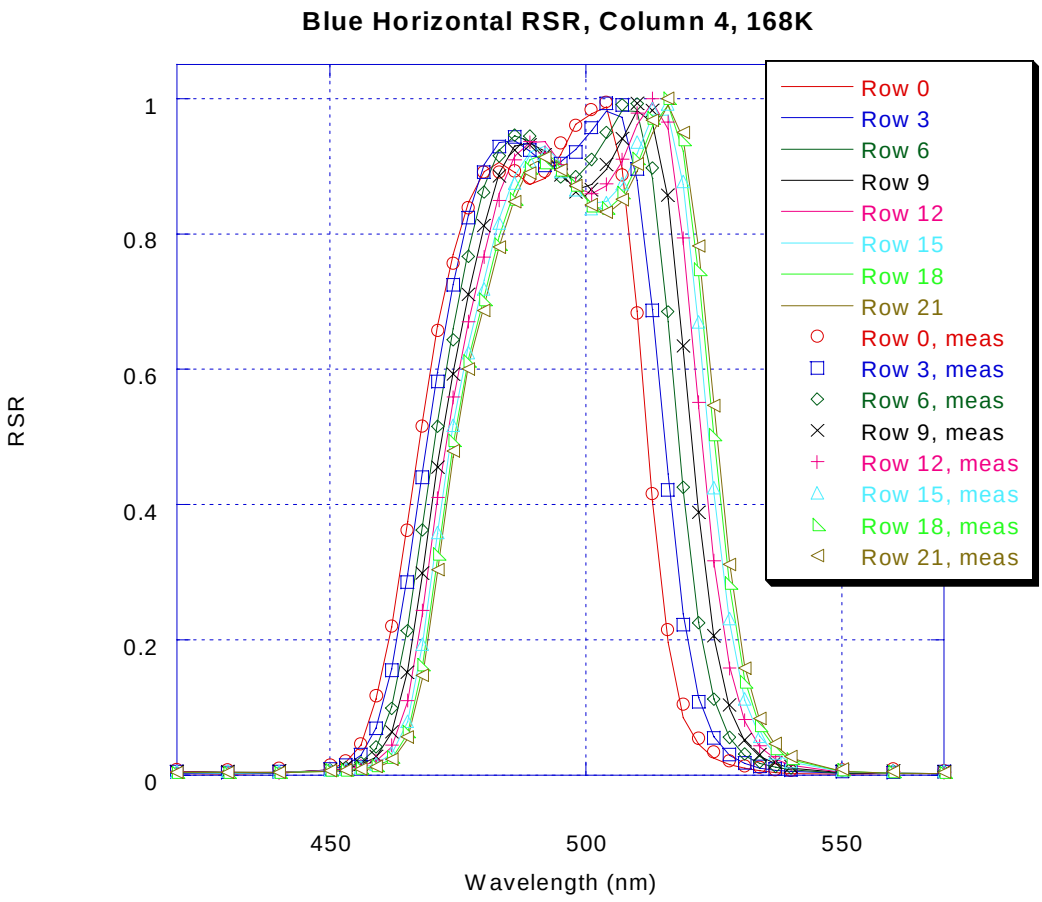
Blue Horizontal RSR, Column 4, 168K
RSR
1
0.8
0.6
0.4
0.2
0
450
500
550
Wavelength (nm)
Row 0
Row 3
Row 6
Row 9
Row 12
Row 15
Row 18
Row 21
Row 0, meas
Row 3, meas
Row 6, meas
Row 9, meas
Row 12, meas
Row 15, meas
Row 18, meas
Row 21, meas

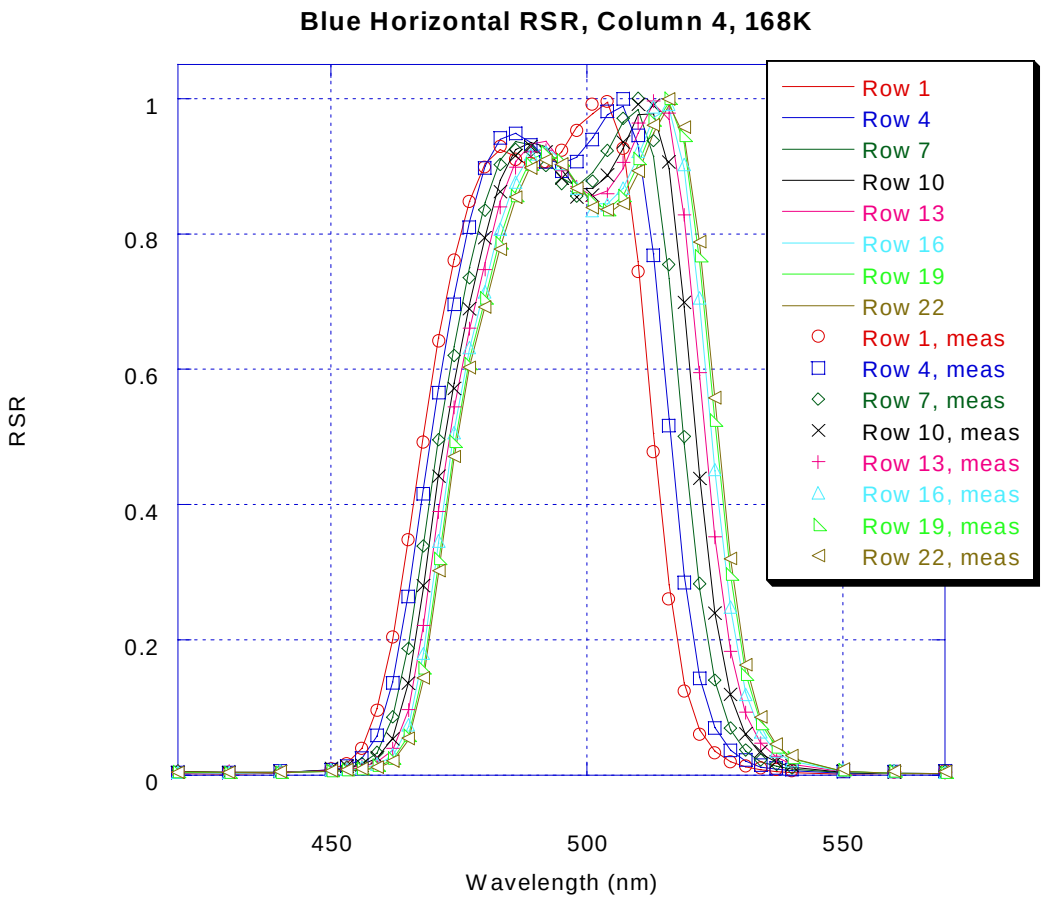
Blue Horizontal RSR, Column 4, 168K
RSR
1
0.8
0.6
0.4
0.2
0
450
500
550
Wavelength (nm)
Row 1
Row 4
Row 7
Row 10
Row 13
Row 16
Row 19
Row 22
Row 1, meas
Row 4, meas
Row 7, meas
Row 10, meas
Row 13, meas
Row 16, meas
Row 19, meas
Row 22, meas

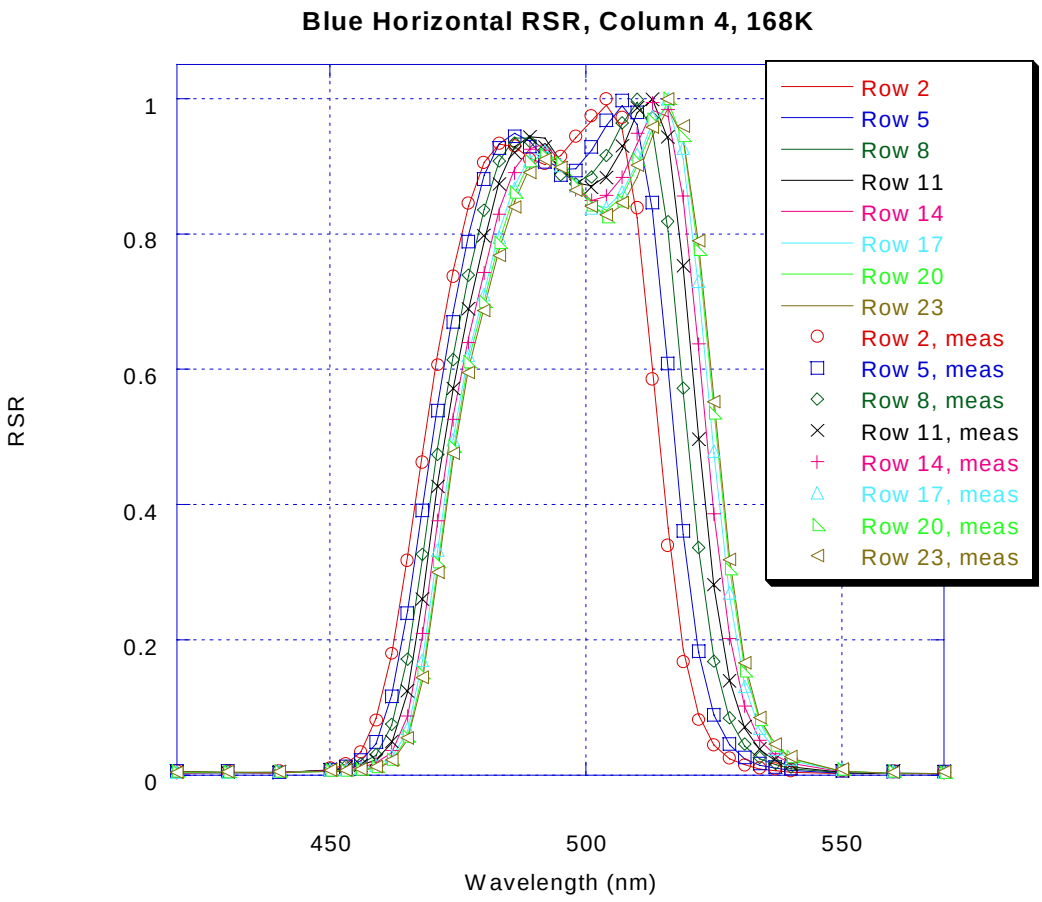
Blue Horizontal RSR, Column 4, 168K
RSR
1
0.8
0.6
0.4
0.2
0
450
500
550
Wavelength (nm)
Row 2
Row 5
Row 8
Row 11
Row 14
Row 17
Row 20
Row 23
Row 2, meas
Row 5, meas
Row 8, meas
Row 11, meas
Row 14, meas
Row 17, meas
Row 20, meas
Row 23, meas

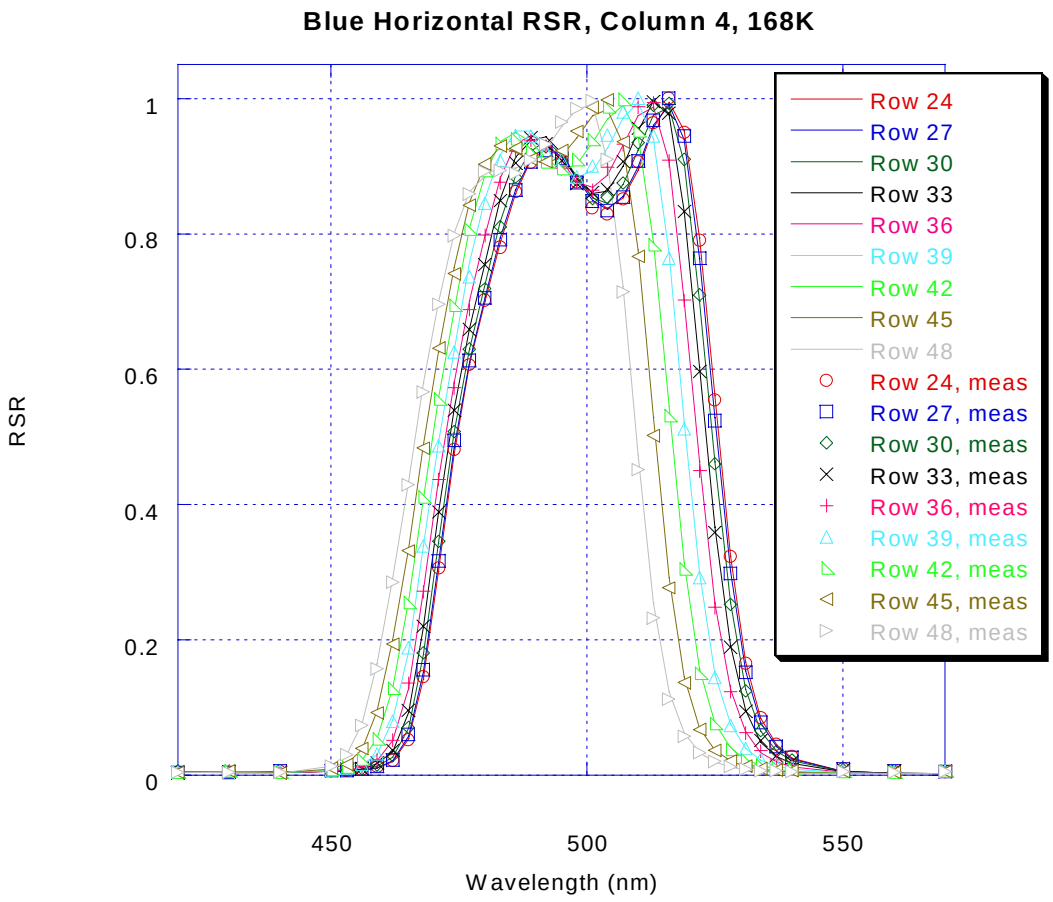
Blue Horizontal RSR, Column 4, 168K
RSR
1
0.8
0.6
0.4
0.2
0
450
500
550
Wavelength (nm)
Row 24
Row 27
Row 30
Row 33
Row 36
Row 39
Row 42
Row 45
Row 48
Row 24, meas
Row 27, meas
Row 30, meas
Row 33, meas
Row 36, meas
Row 39, meas
Row 42, meas
Row 45, meas
Row 48, meas

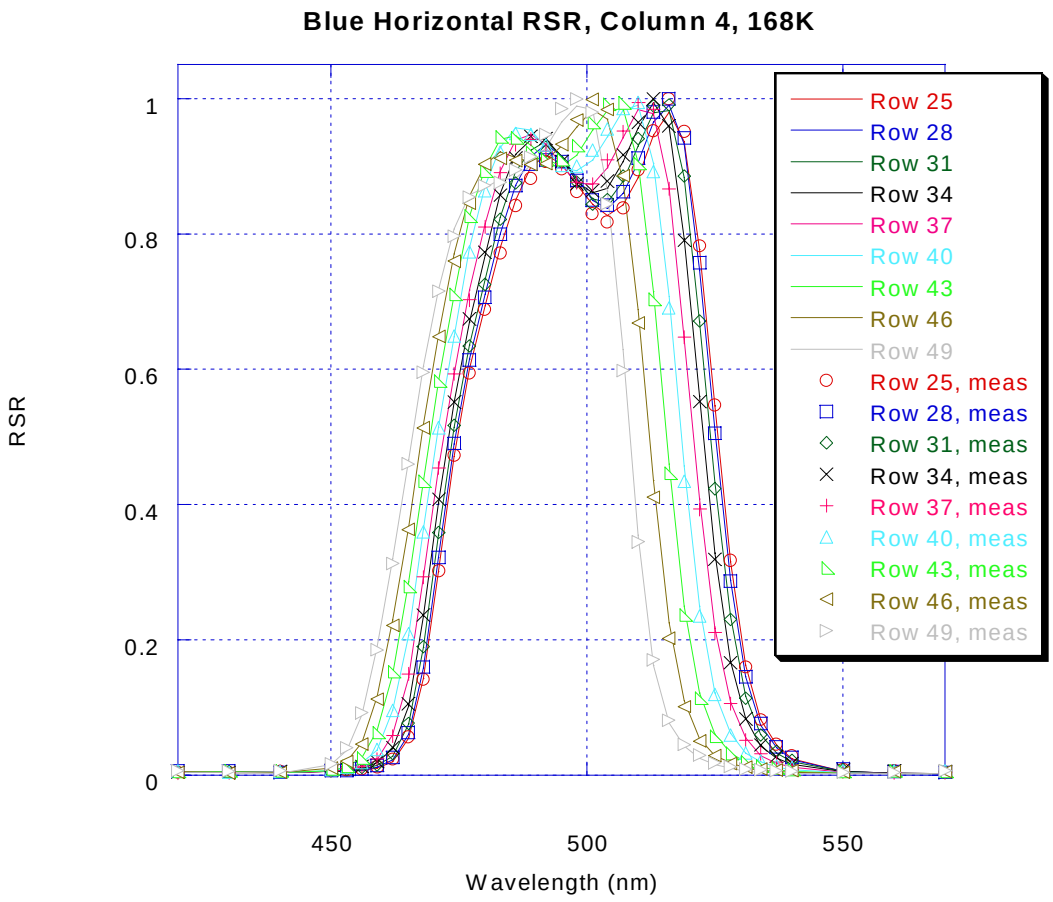
Blue Horizontal RSR, Column 4, 168K
RSR
1
0.8
0.6
0.4
0.2
0
450
500
550
Wavelength (nm)
Row 25
Row 28
Row 31
Row 34
Row 37
Row 40
Row 43
Row 46
Row 49
Row 25, meas
Row 28, meas
Row 31, meas
Row 34, meas
Row 37, meas
Row 40, meas
Row 43, meas
Row 46, meas
Row 49, meas

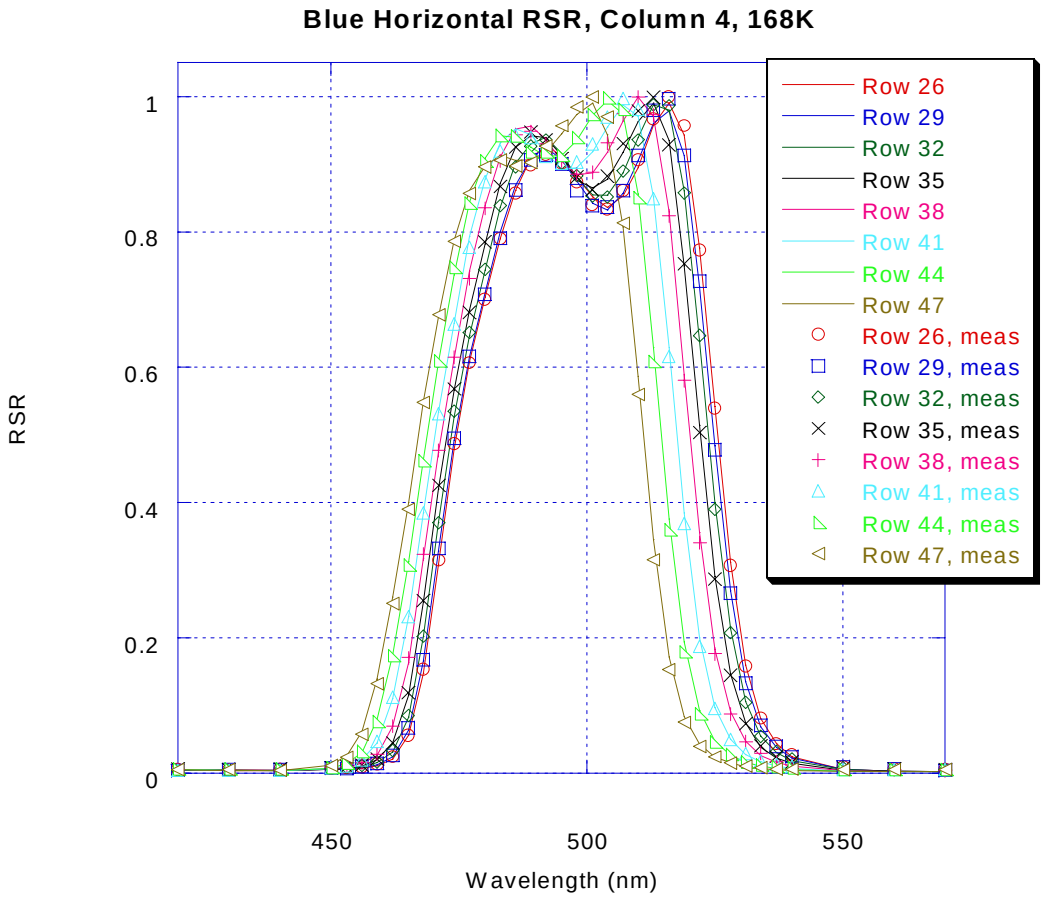
Blue Horizontal RSR, Column 4, 168K
RSR
Wavelength (nm)
Row 26
Row 29
Row 32
Row 35
Row 38
Row 41
Row 44
Row 47
Row 26, meas
Row 29, meas
Row 32, meas
Row 35, meas
Row 38, meas
Row 41, meas
Row 44, meas
Row 47, meas

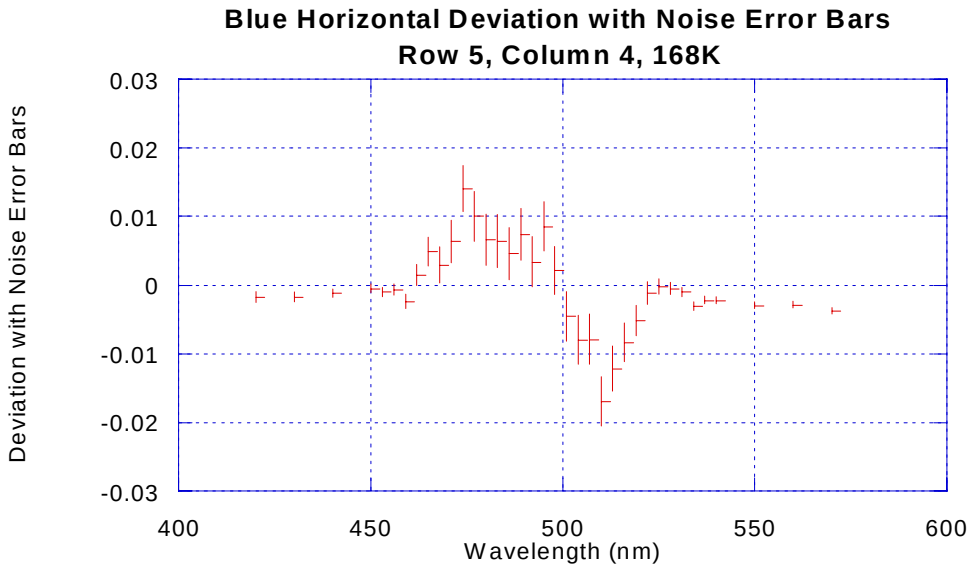
Blue Horizontal Deviation with Noise Error Bars
Row 5, Column 4, 168K
Deviation with Noise Error Bars
Wavelength (nm)

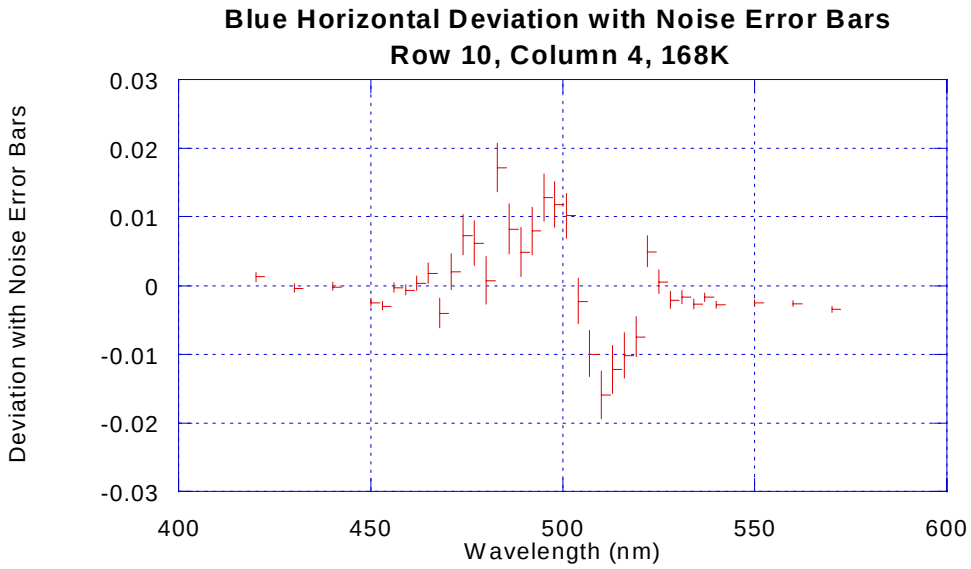
Blue Horizontal Deviation with Noise Error Bars
Row 10, Column 4, 168K
Deviation with Noise Error Bars
0.03
0.02
0.01
0
-0.01
-0.02
-0.03
400
450
500
550
600
Wavelength (nm)

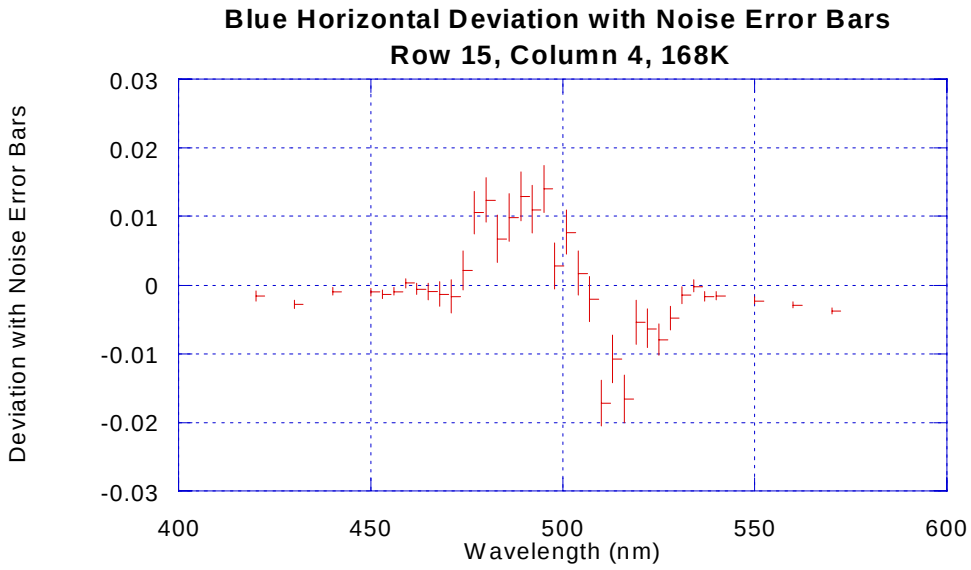
Blue Horizontal Deviation with Noise Error Bars
Row 15, Column 4, 168K
Deviation with Noise Error Bars
0.03
0.02
0.01
0
-0.01
-0.02
-0.03
400
450
500
550
600
Wavelength (nm)

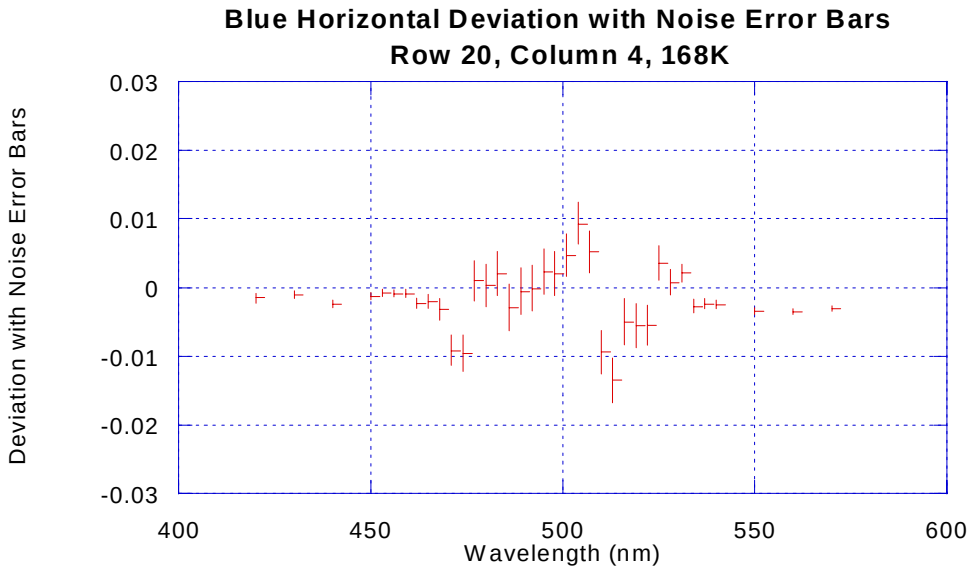
Blue Horizontal Deviation with Noise Error Bars
Row 20, Column 4, 168K
Deviation with Noise Error Bars
0.03
0.02
0.01
0
-0.01
-0.02
-0.03
400
450
500
550
600
Wavelength (nm)

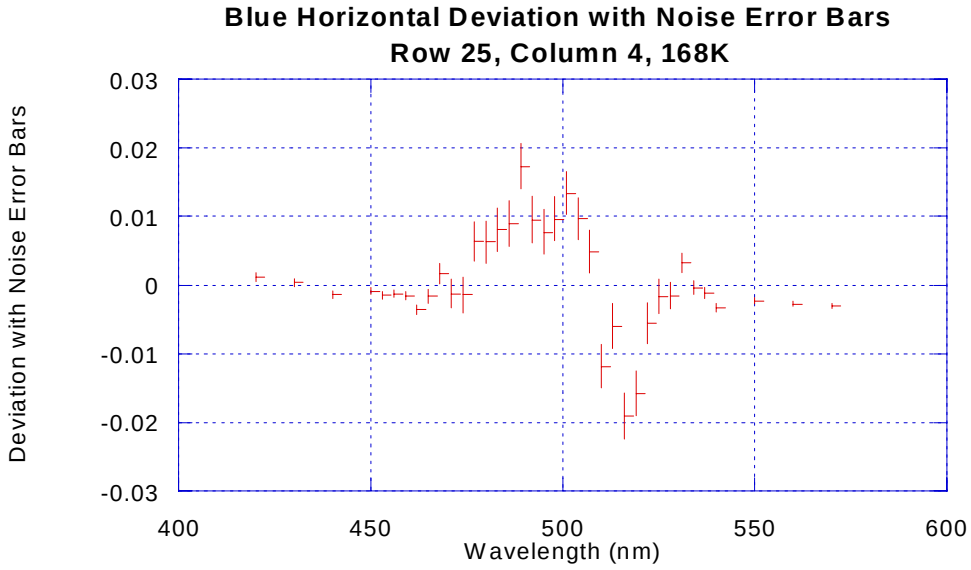
Blue Horizontal Deviation with Noise Error Bars
Row 25, Column 4, 168K
Deviation with Noise Error Bars
0.03
0.02
0.01
0
-0.01
-0.02
-0.03
400
450
500
550
600
Wavelength (nm)

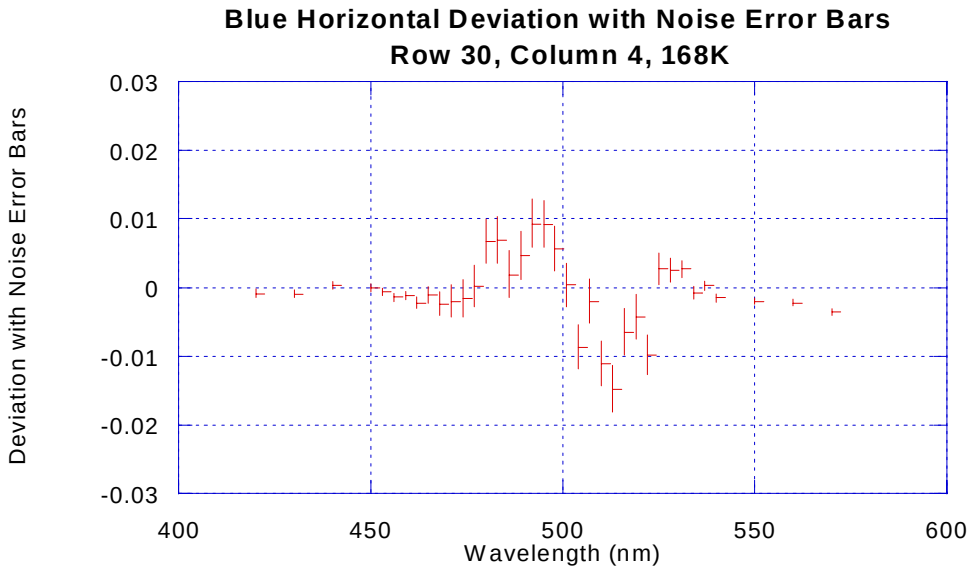
Blue Horizontal Deviation with Noise Error Bars
Row 30, Column 4, 168K
Deviation with Noise Error Bars
0.03
0.02
0.01
0
-0.01
-0.02
-0.03
400
450
500
550
600
Wavelength (nm)

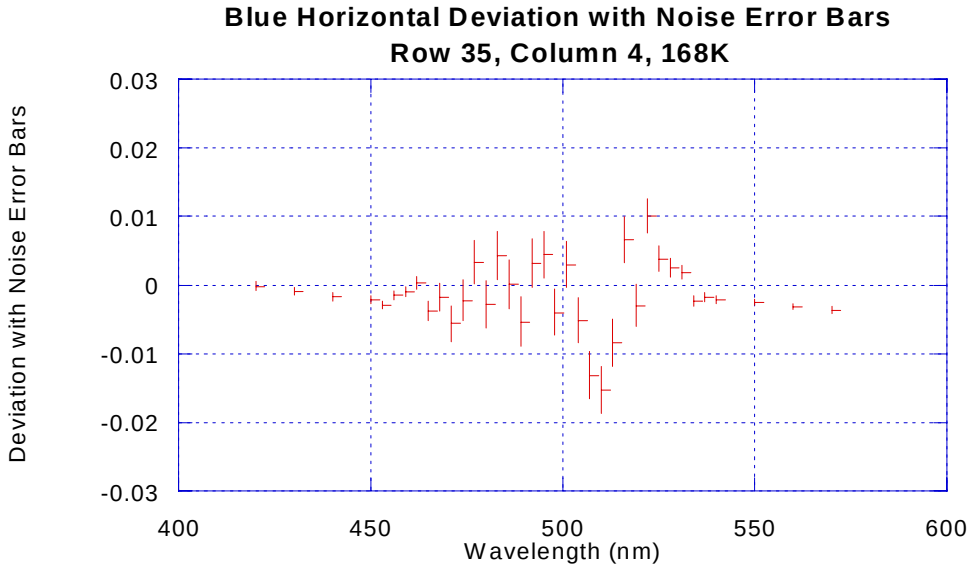
Blue Horizontal Deviation with Noise Error Bars
Row 35, Column 4, 168K
Deviation with Noise Error Bars
0.03
0.02
0.01
0
-0.01
-0.02
-0.03
400
450
500
550
600
Wavelength (nm)

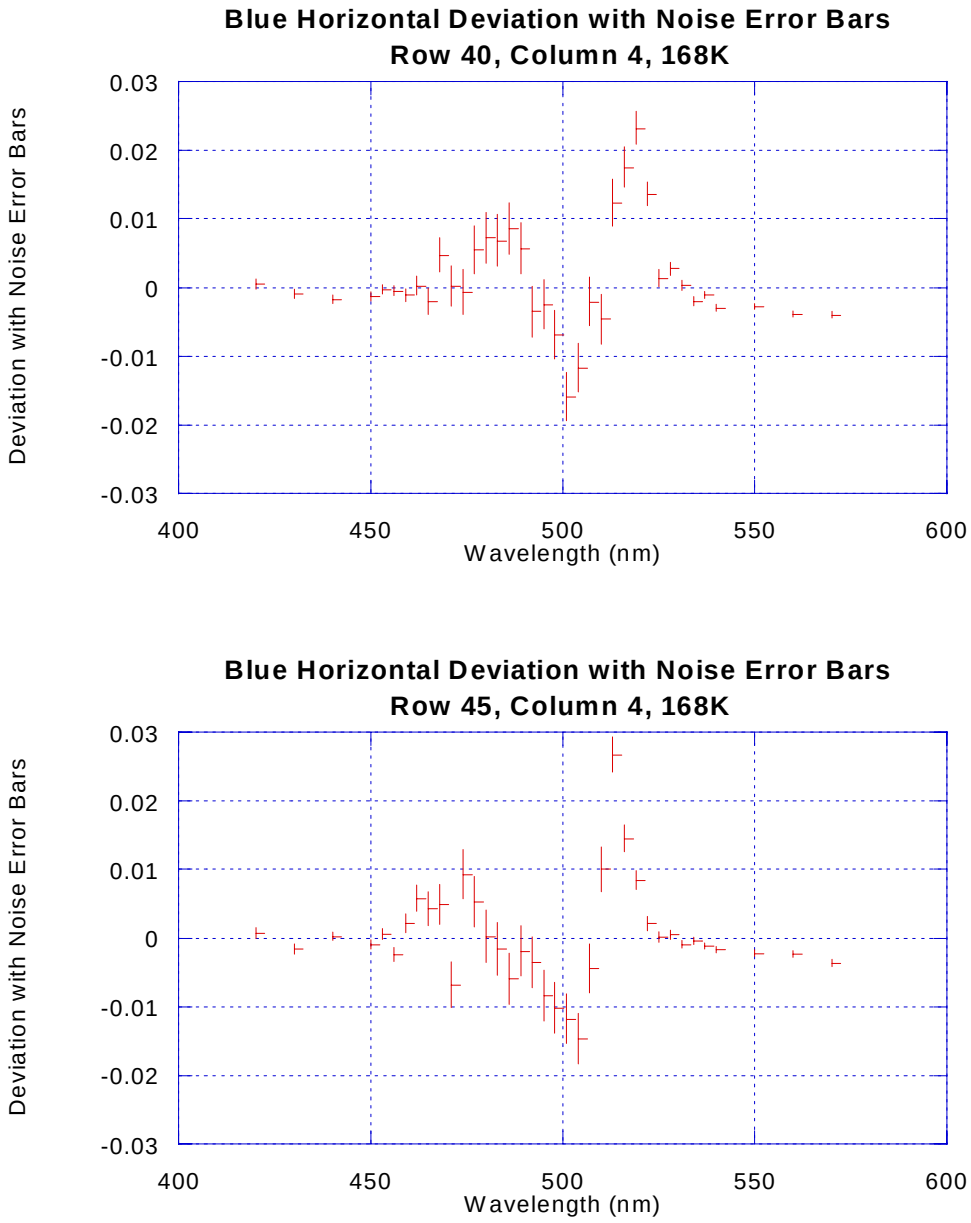

Figure 13-50 Blue Vertical Relative Spectral Response Modeling Results – Set of Nineteen Plots

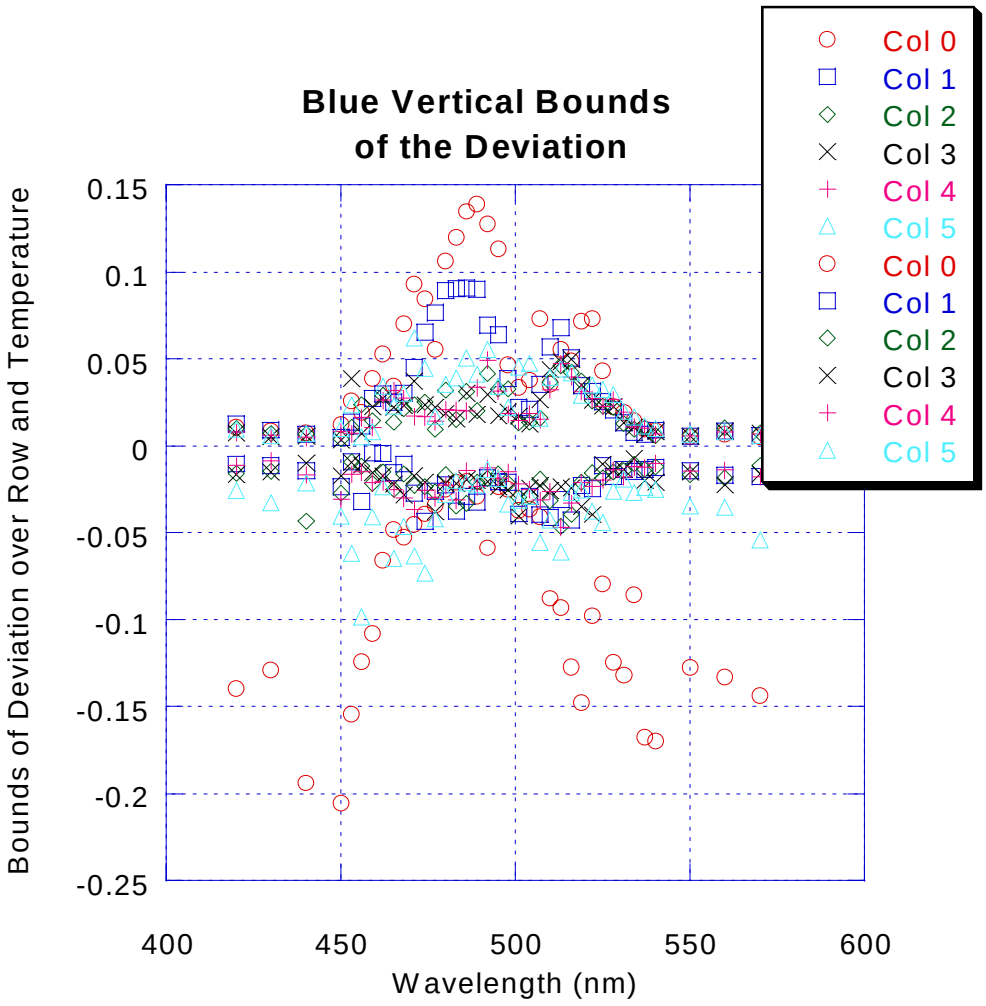
Blue Vertical Bounds
of the Deviation
Bounds of Deviation over Row and Temperature
0.15
0.1
0.05
0
-0.05
-0.1
-0.15
-0.2
-0.25
400
450
500
550
600
Wavelength (nm)
Col 0
Col 1
Col 2
Col 3
Col 4
Col 5
Col 0
Col 1
Col 2
Col 3
Col 4
Col 5

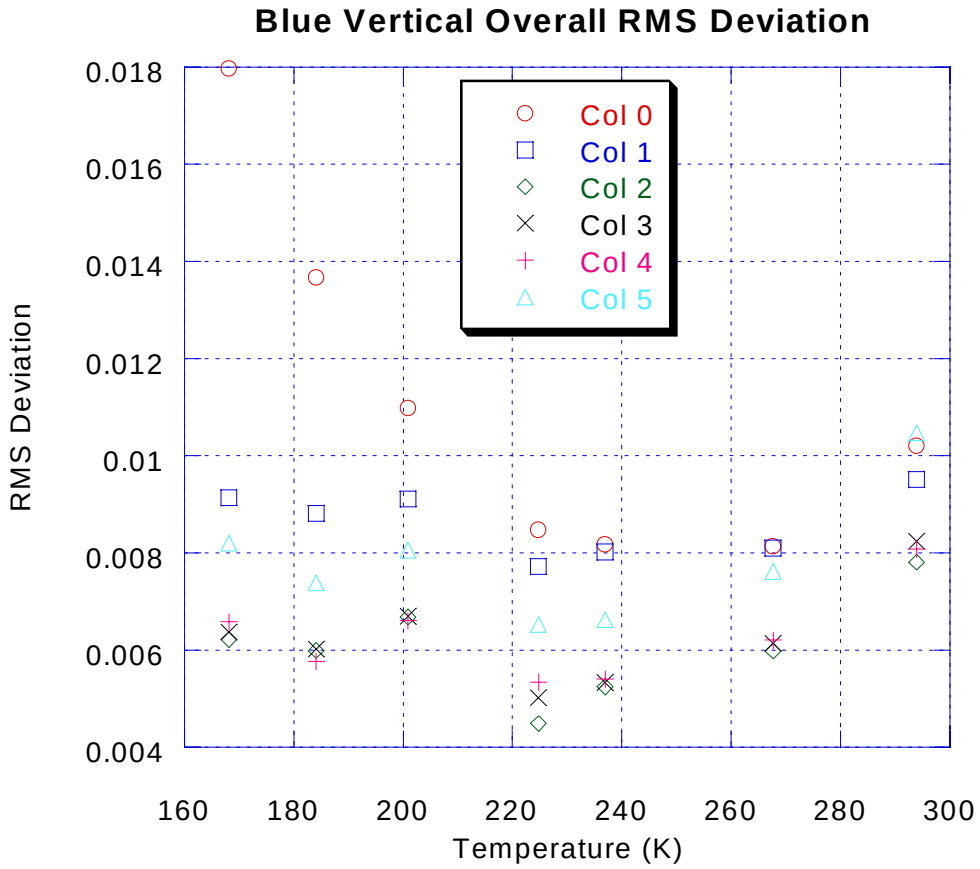
Blue Vertical Overall RMS Deviation
RMS Deviation
0.018
0.016
0.014
0.012
0.01
0.008
0.006
0.004
160
180
200
220
240
260
280
300
Temperature (K)
Col 0
Col 1
Col 2
Col 3
Col 4
Col 5

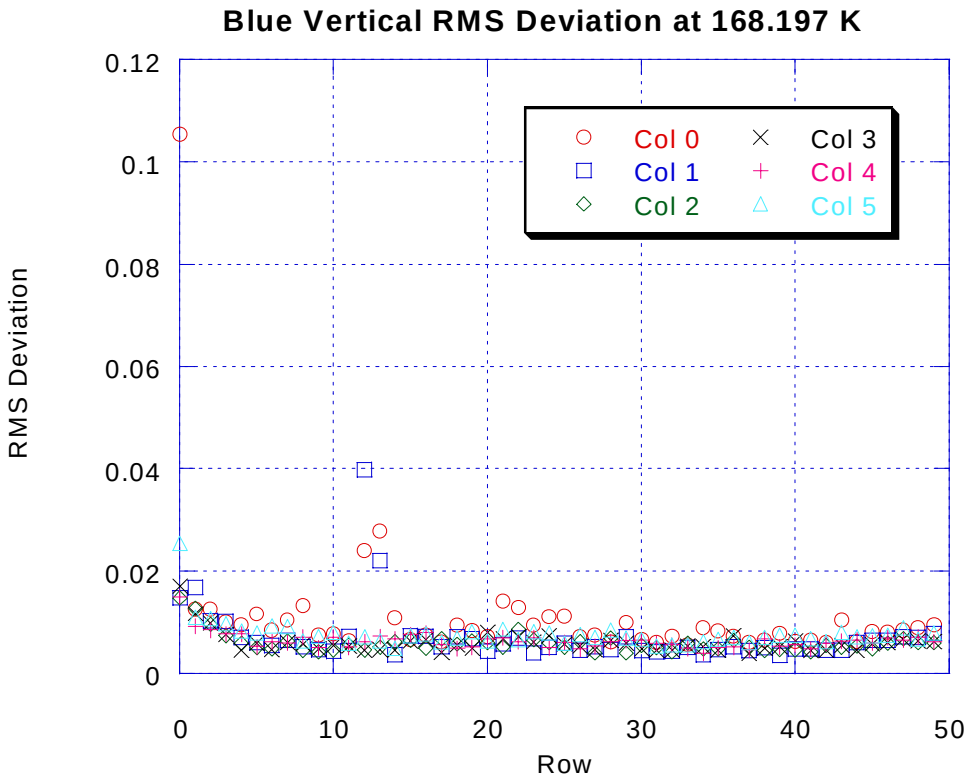
Blue Vertical RMS Deviation at 168.197 K
RMS Deviation
0.12
0.1
0.08
0.06
0.04
0.02
0
0
10
20
30
40
50
Row
Col 0
Col 1
Col 2
Col 3
Col 4
Col 5

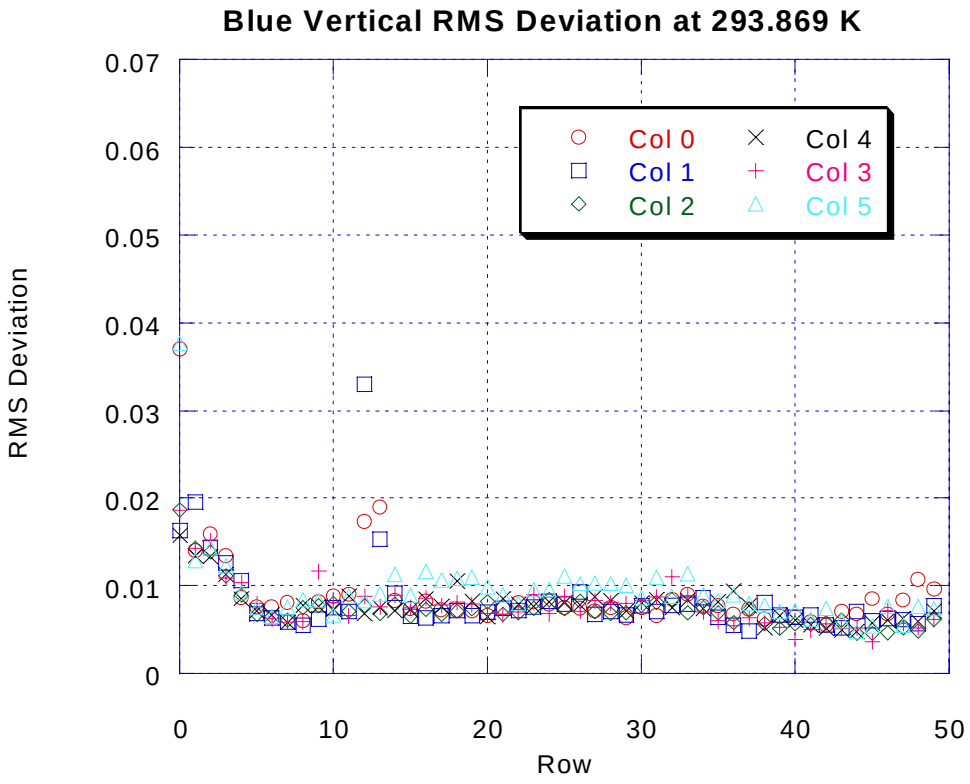
Blue Vertical RMS Deviation at 293.869 K
RMS Deviation
0.07
0.06
0.05
0.04
0.03
0.02
0.01
0
0
10
20
30
40
50
Row
Col 0
Col 1
Col 2
Col 4
Col 3
Col 5

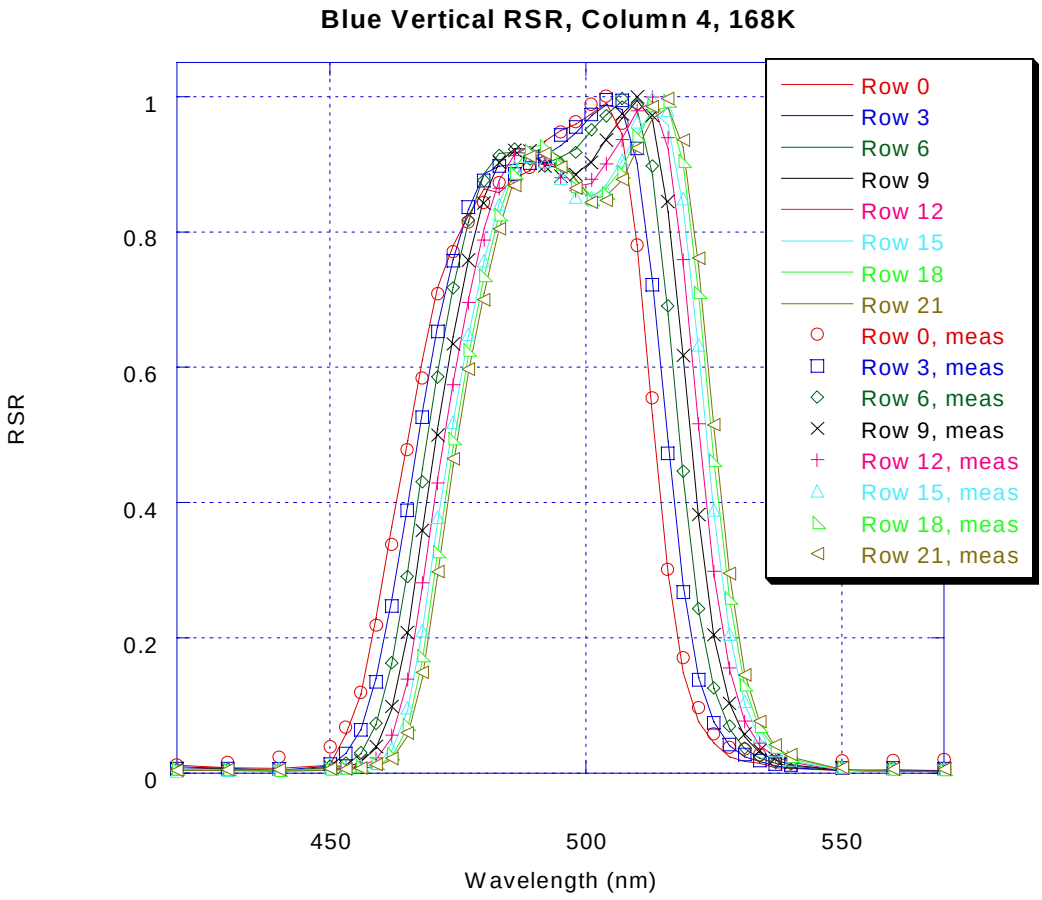
Blue Vertical RSR, Column 4, 168K
RSR
1
0.8
0.6
0.4
0.2
0
450
500
550
Wavelength (nm)
Row 0
Row 3
Row 6
Row 9
Row 12
Row 15
Row 18
Row 21
Row 0, meas
Row 3, meas
Row 6, meas
Row 9, meas
Row 12, meas
Row 15, meas
Row 18, meas
Row 21, meas

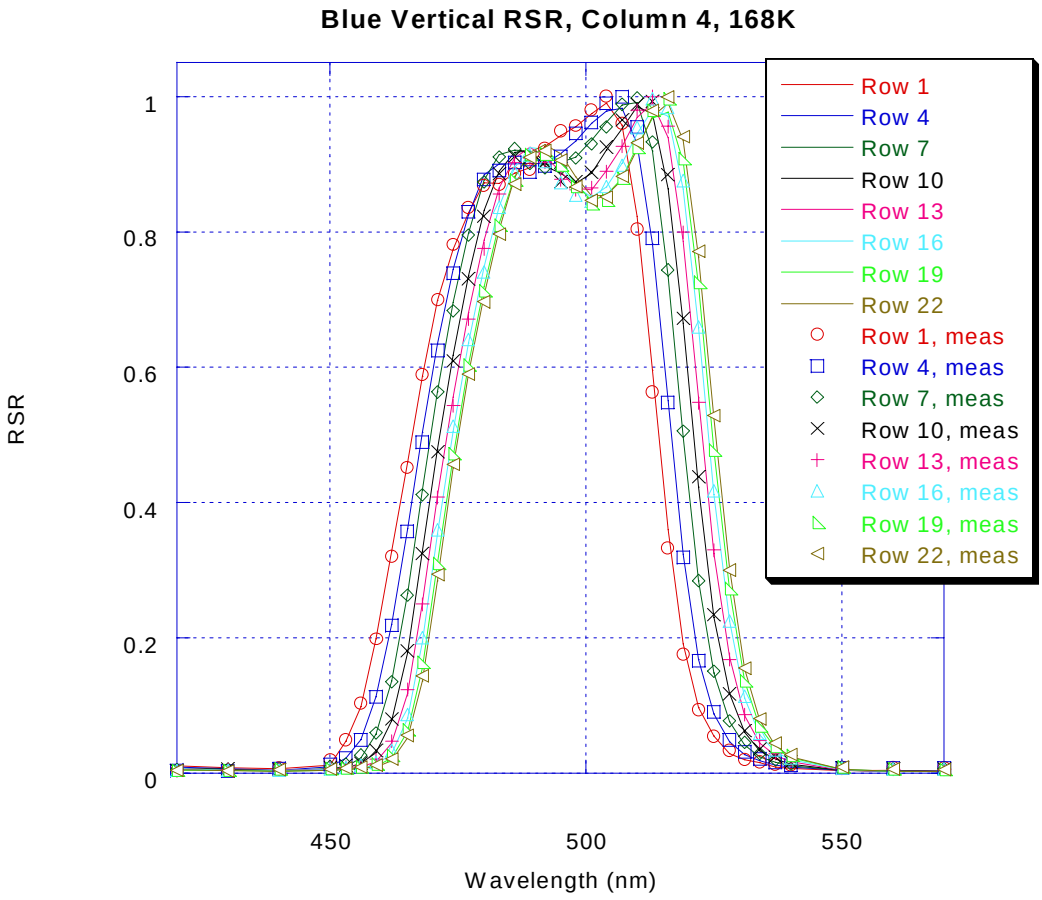
Blue Vertical RSR, Column 4, 168K
RSR
1
0.8
0.6
0.4
0.2
0
450
500
550
Wavelength (nm)
Row 1
Row 4
Row 7
Row 10
Row 13
Row 16
Row 19
Row 22
Row 1, meas
Row 4, meas
Row 7, meas
Row 10, meas
Row 13, meas
Row 16, meas
Row 19, meas
Row 22, meas

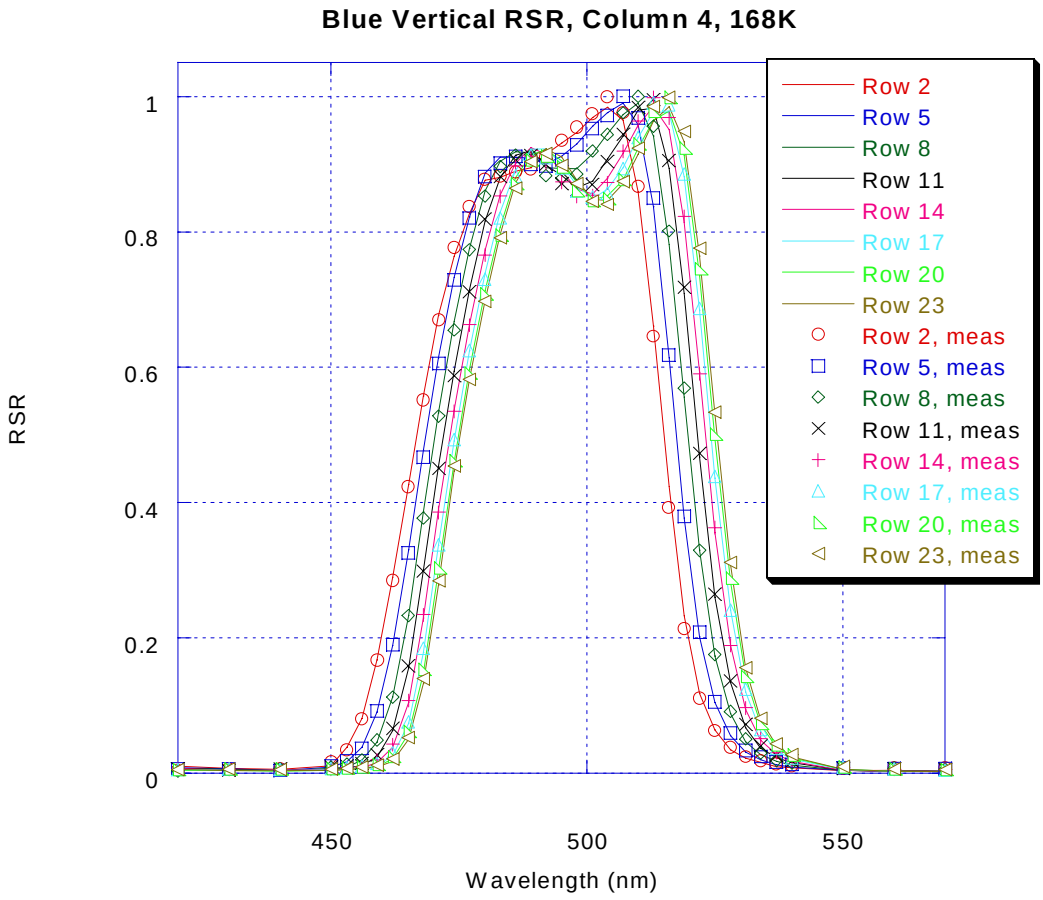
Blue Vertical RSR, Column 4, 168K
RSR
1
0.8
0.6
0.4
0.2
0
450
500
550
Wavelength (nm)
Row 2
Row 5
Row 8
Row 11
Row 14
Row 17
Row 20
Row 23
Row 2, meas
Row 5, meas
Row 8, meas
Row 11, meas
Row 14, meas
Row 17, meas
Row 20, meas
Row 23, meas

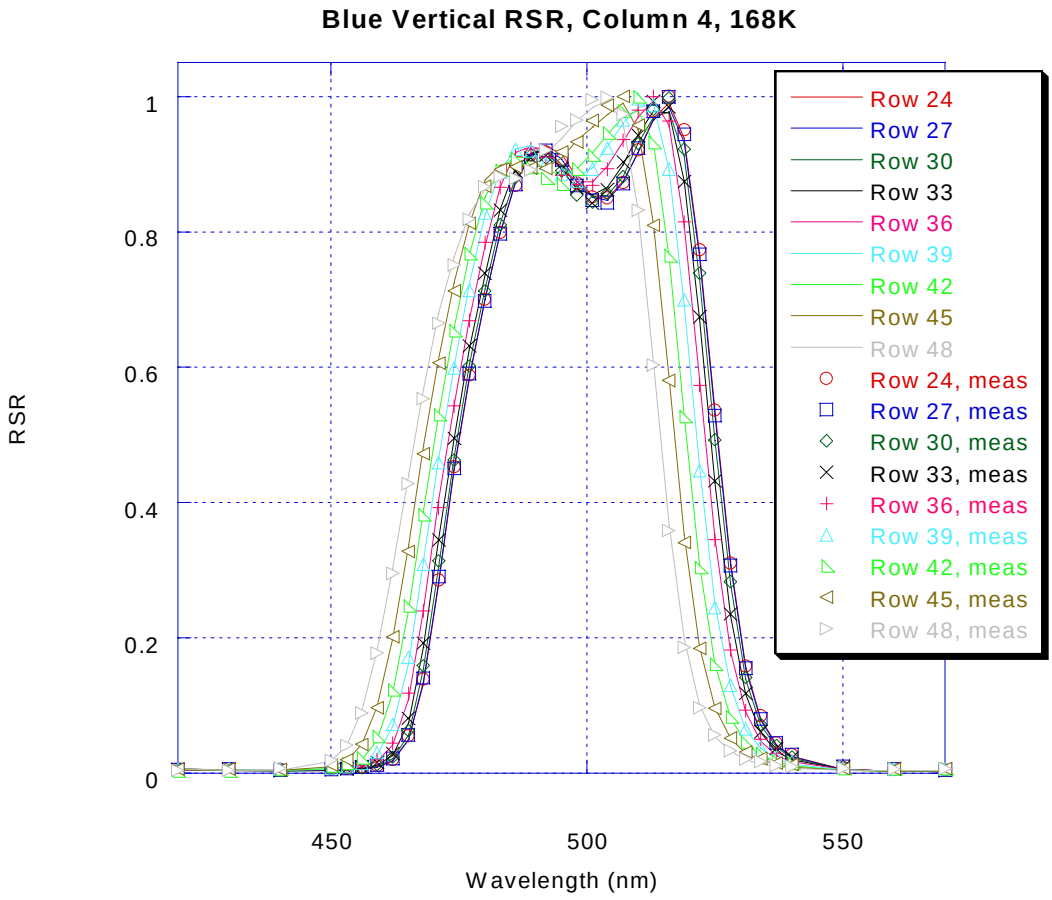
Blue Vertical RSR, Column 4, 168K
RSR
1
0.8
0.6
0.4
0.2
0
450
500
550
Wavelength (nm)
Row 24
Row 27
Row 30
Row 33
Row 36
Row 39
Row 42
Row 45
Row 48
Row 24, meas
Row 27, meas
Row 30, meas
Row 33, meas
Row 36, meas
Row 39, meas
Row 42, meas
Row 45, meas
Row 48, meas

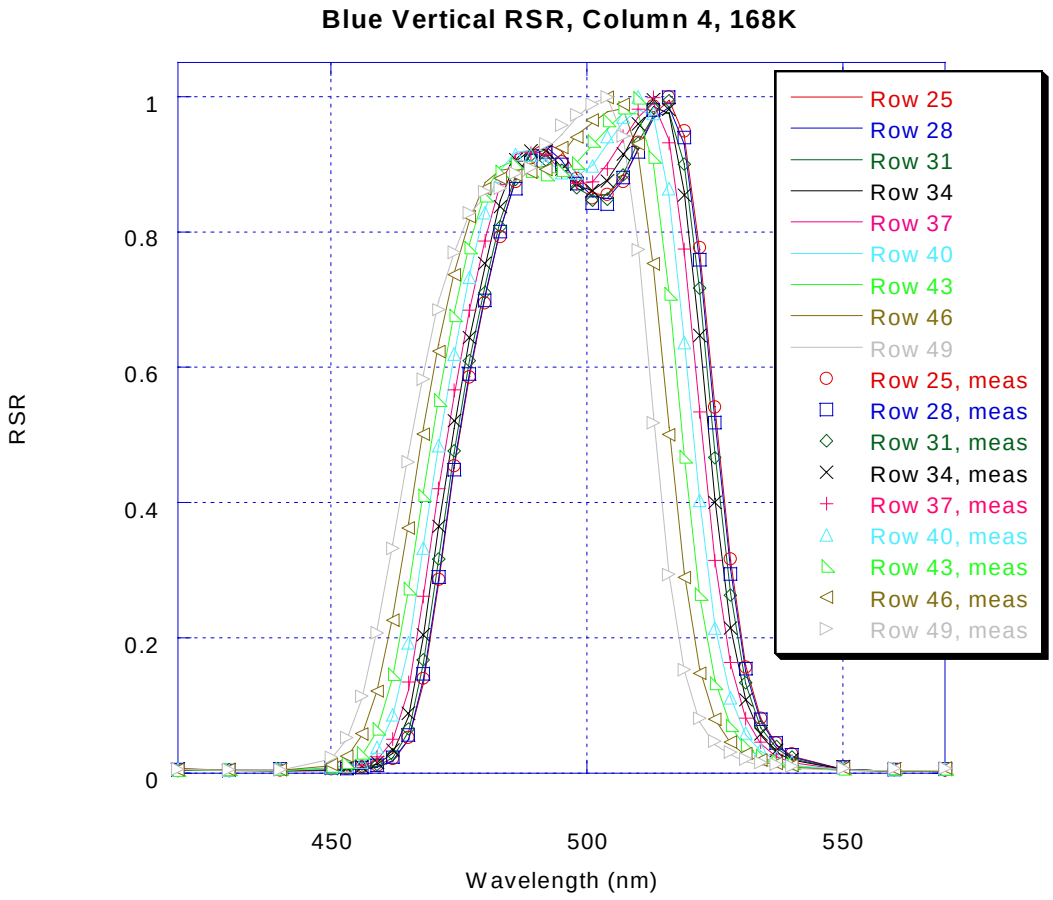
Blue Vertical RSR, Column 4, 168K
RSR
1
0.8
0.6
0.4
0.2
0
450
500
550
Wavelength (nm)
Row 25
Row 28
Row 31
Row 34
Row 37
Row 40
Row 43
Row 46
Row 49
Row 25, meas
Row 28, meas
Row 31, meas
Row 34, meas
Row 37, meas
Row 40, meas
Row 43, meas
Row 46, meas
Row 49, meas

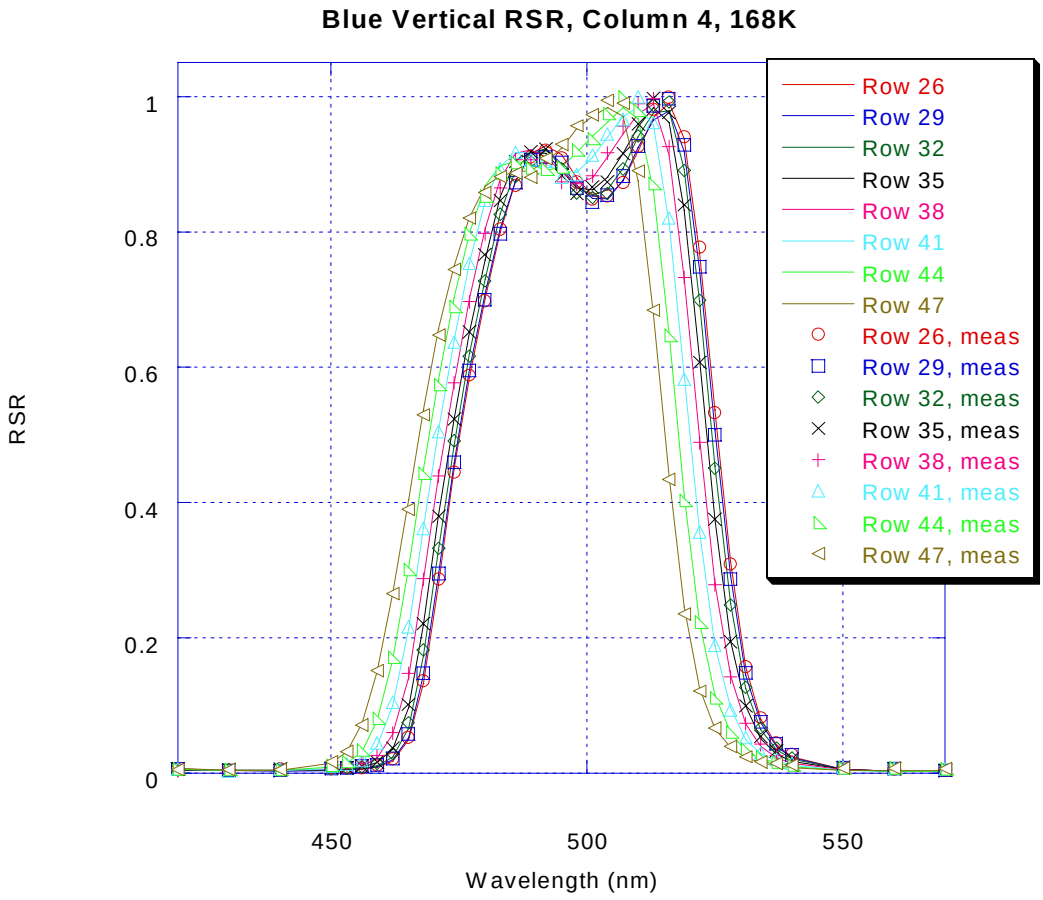
Blue Vertical RSR, Column 4, 168K
RSR
Wavelength (nm)
0
0.2
0.4
0.6
0.8
1
450
500
550
Row 26
Row 29
Row 32
Row 35
Row 38
Row 41
Row 44
Row 47
Row 26, meas
Row 29, meas
Row 32, meas
Row 35, meas
Row 38, meas
Row 41, meas
Row 44, meas
Row 47, meas

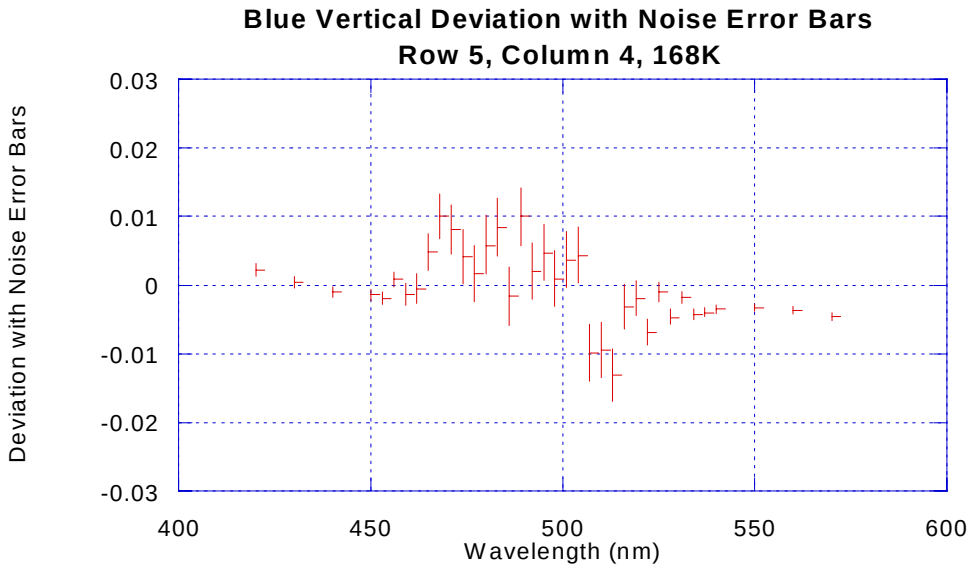
Blue Vertical Deviation with Noise Error Bars
Row 5, Column 4, 168K
Deviation with Noise Error Bars
Wavelength (nm)
0.03
0.02
0.01
0
-0.01
-0.02
-0.03
400
450
500
550
600

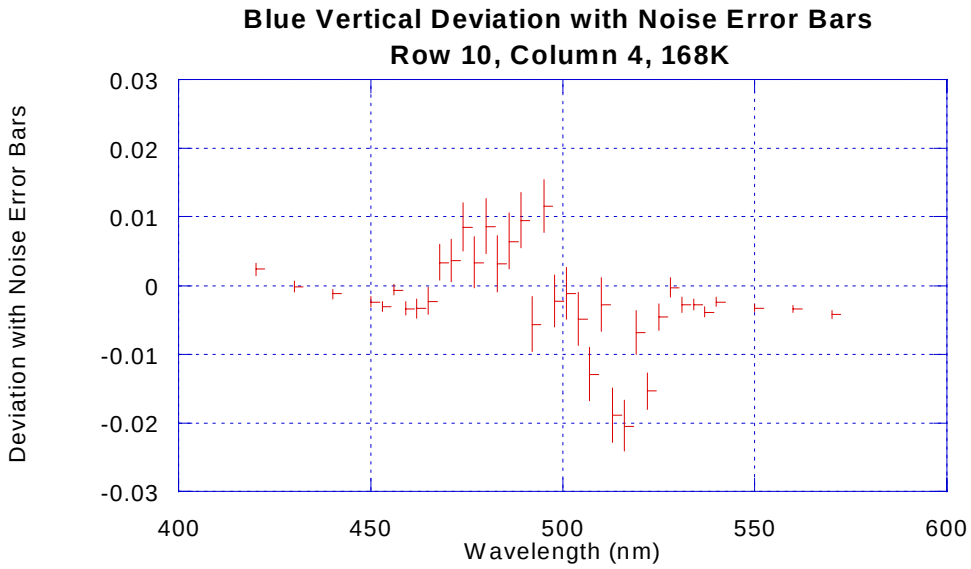
Blue Vertical Deviation with Noise Error Bars
Row 10, Column 4, 168K
Deviation with Noise Error Bars
0.03
0.02
0.01
0
-0.01
-0.02
-0.03
400
450
500
550
600
Wavelength (nm)

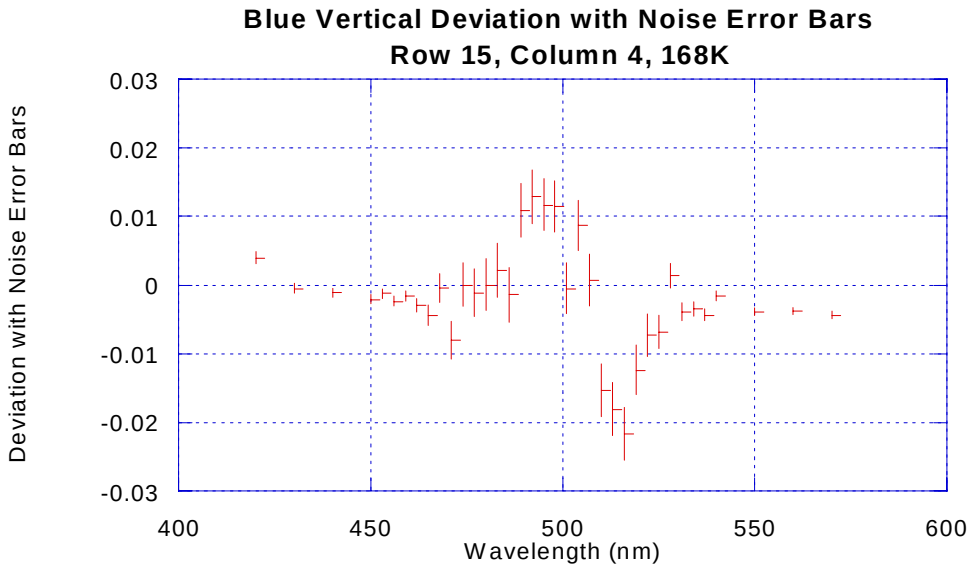
Blue Vertical Deviation with Noise Error Bars
Row 15, Column 4, 168K
Deviation with Noise Error Bars
0.03
0.02
0.01
0
-0.01
-0.02
-0.03
400
450
500
550
600
Wavelength (nm)

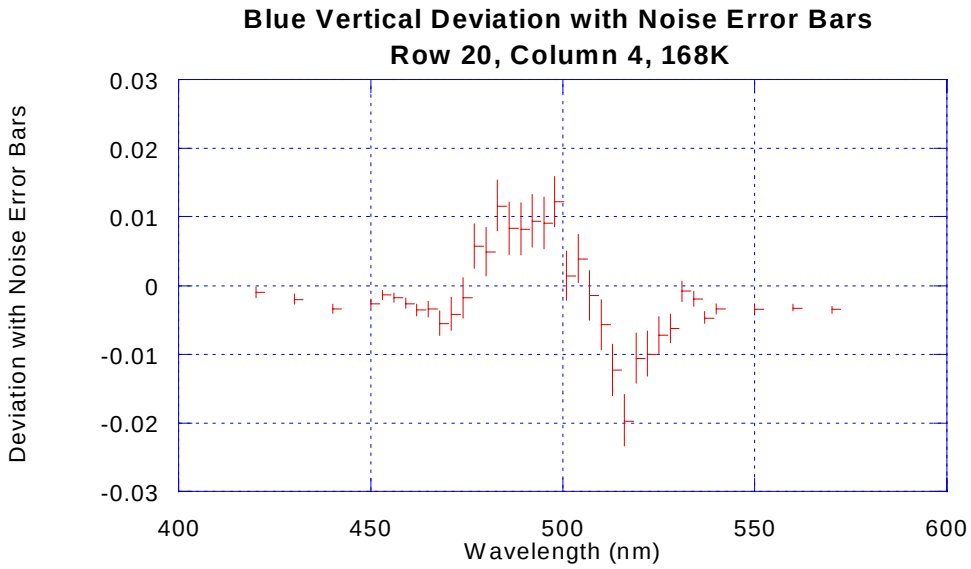
Blue Vertical Deviation with Noise Error Bars
Row 20, Column 4, 168K
Deviation with Noise Error Bars
0.03
0.02
0.01
0
-0.01
-0.02
-0.03
400
450
500
550
600
Wavelength (nm)

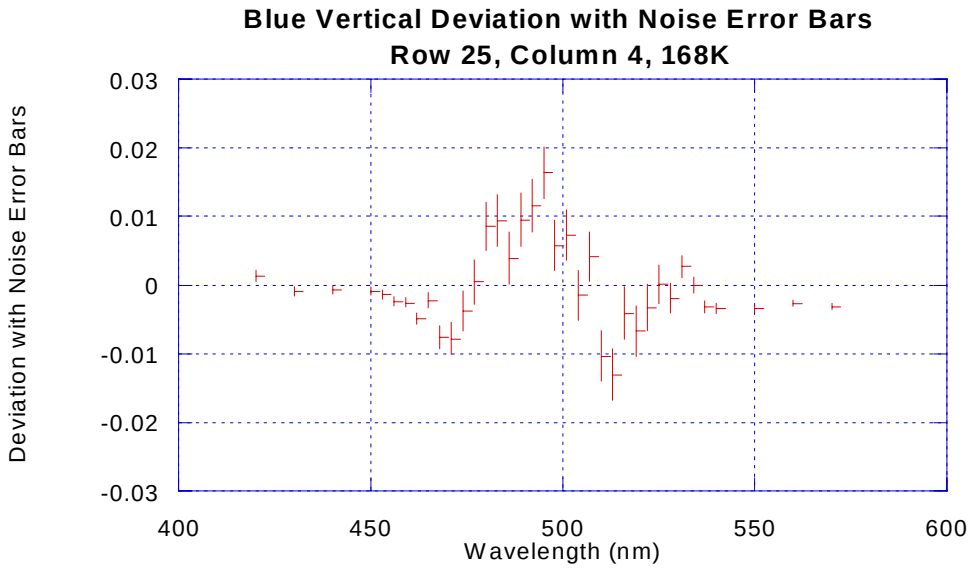
Blue Vertical Deviation with Noise Error Bars
Row 25, Column 4, 168K
Deviation with Noise Error Bars
0.03
0.02
0.01
0
-0.01
-0.02
-0.03
400
450
500
550
600
Wavelength (nm)

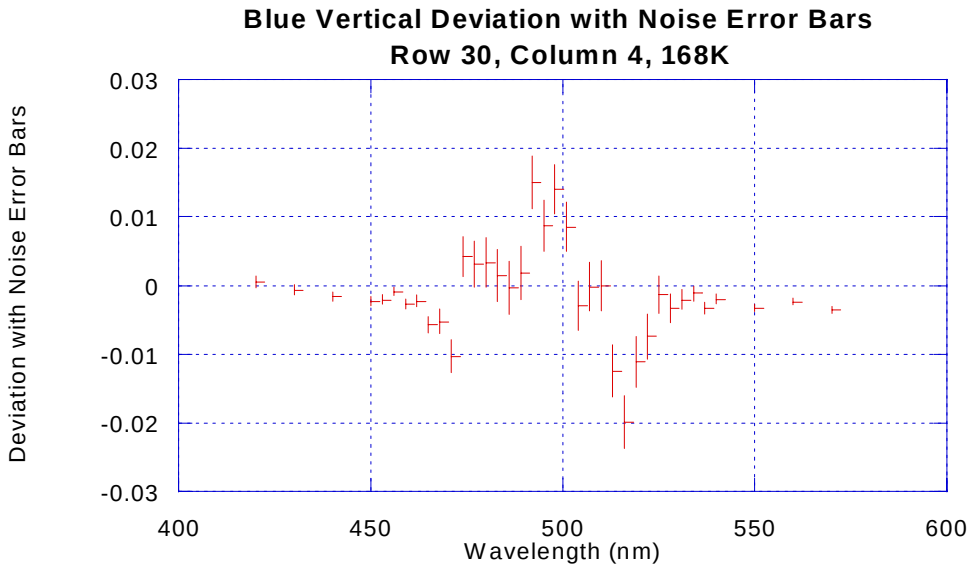
Blue Vertical Deviation with Noise Error Bars
Row 30, Column 4, 168K
Deviation with Noise Error Bars
0.03
0.02
0.01
0
-0.01
-0.02
-0.03
400
450
500
550
600
Wavelength (nm)

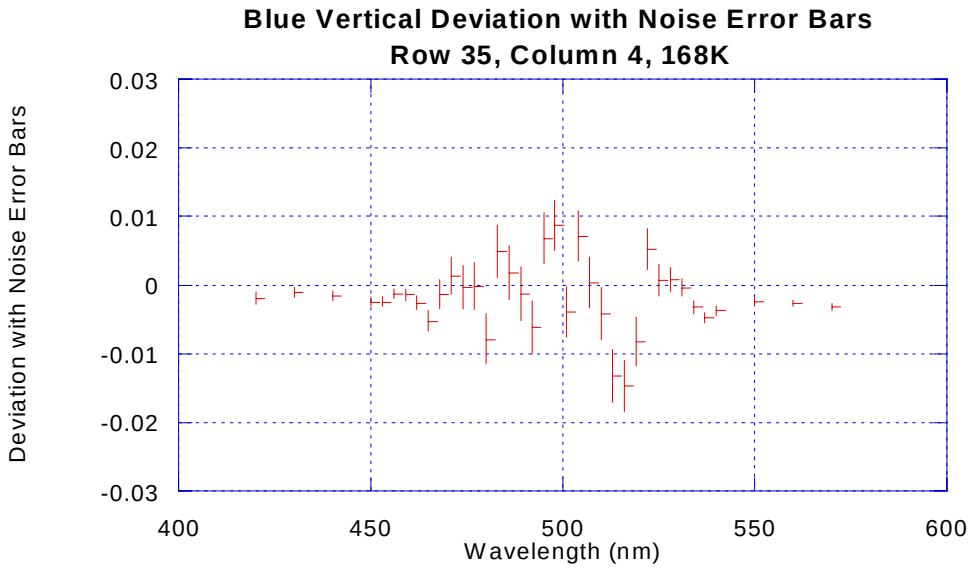
Blue Vertical Deviation with Noise Error Bars
Row 35, Column 4, 168K
Deviation with Noise Error Bars
0.03
0.02
0.01
0
-0.01
-0.02
-0.03
400
450
500
550
600
Wavelength (nm)

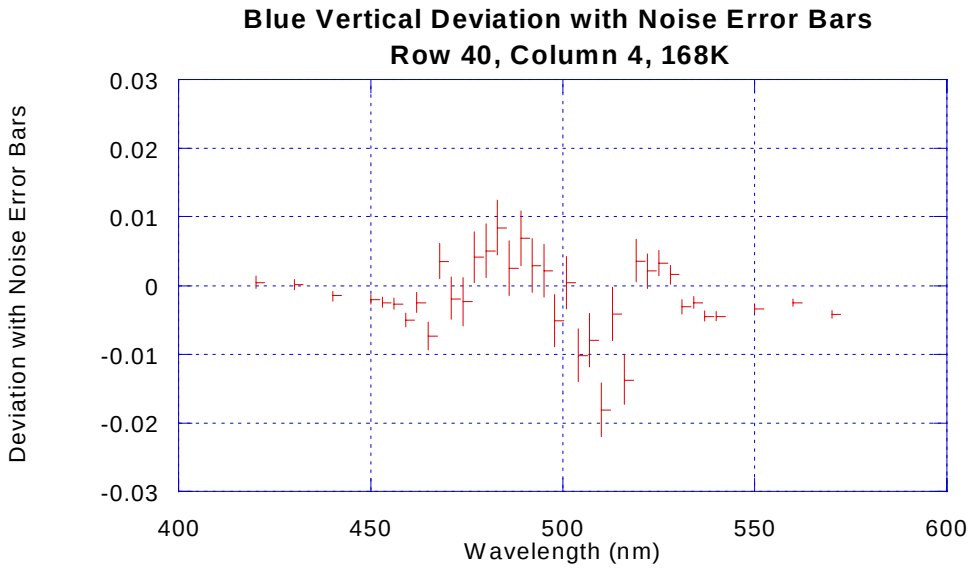
Blue Vertical Deviation with Noise Error Bars
Row 40, Column 4, 168K
Deviation with Noise Error Bars
0.03
0.02
0.01
0
-0.01
-0.02
-0.03
400
450
500
550
600
Wavelength (nm)

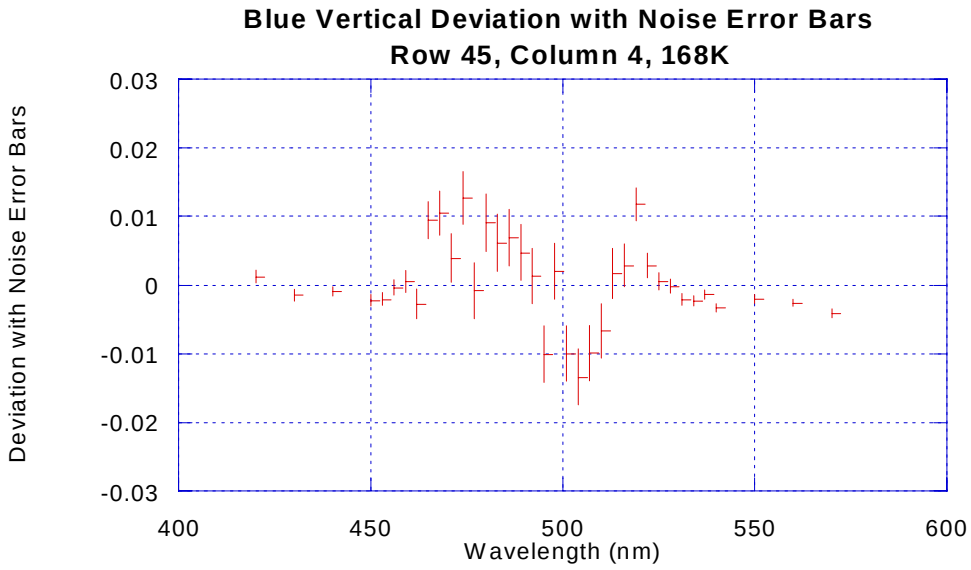
Blue Vertical Deviation with Noise Error Bars
Row 45, Column 4, 168K
Deviation with Noise Error Bars
0.03
0.02
0.01
0
-0.01
-0.02
-0.03
400
450
500
550
600
Wavelength (nm)

Figure 13-51 Red Horizontal Relative Spectral Response Modeling Results – Set of Nineteen Plots

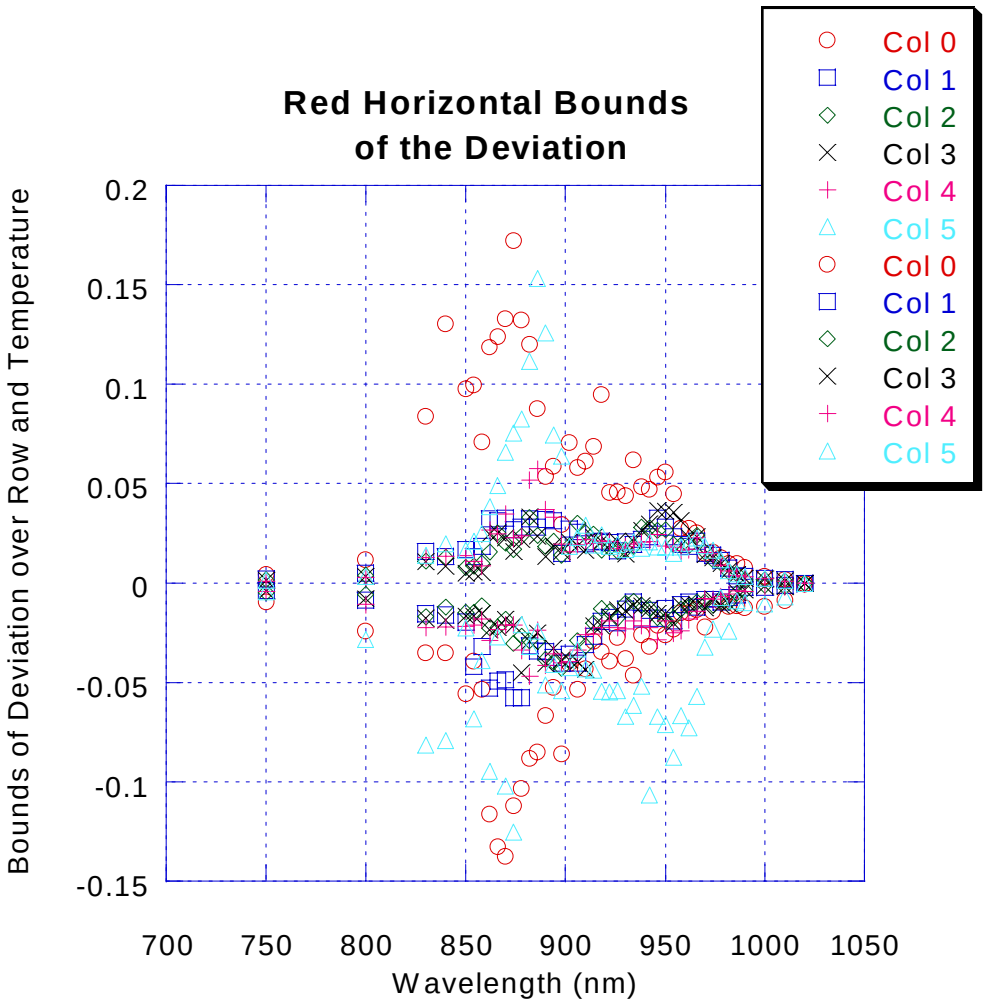

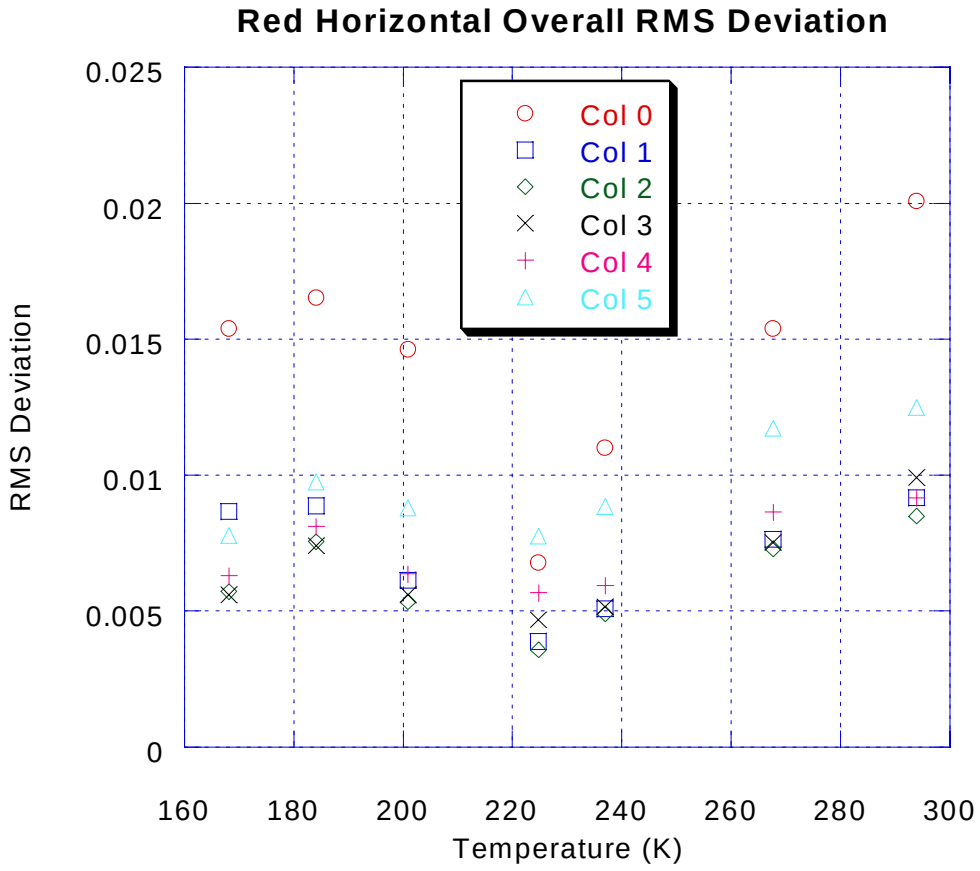
Red Horizontal Overall RMS Deviation
RMS Deviation
0.025
0.02
0.015
0.01
0.005
0
160
180
200
220
240
260
280
300
Temperature (K)
Col 0
Col 1
Col 2
Col 3
Col 4
Col 5

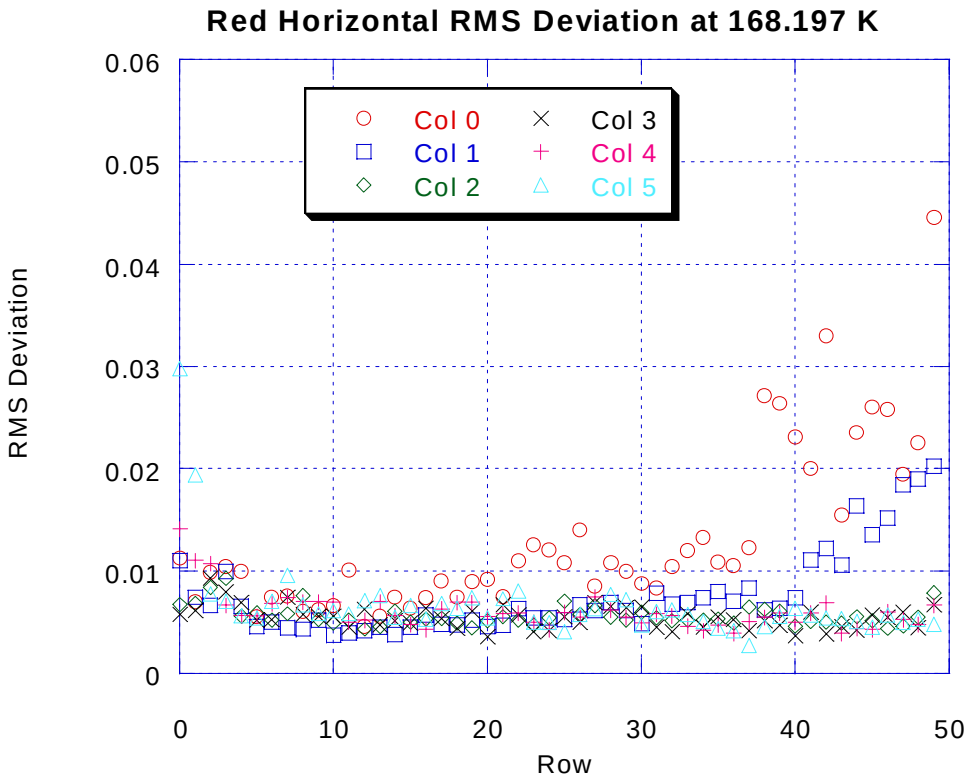
Red Horizontal RMS Deviation at 168.197 K
RMS Deviation
0.06
0.05
0.04
0.03
0.02
0.01
0
Col 0
Col 1
Col 2
Col 3
Col 4
Col 5
0
10
20
30
40
50
Row

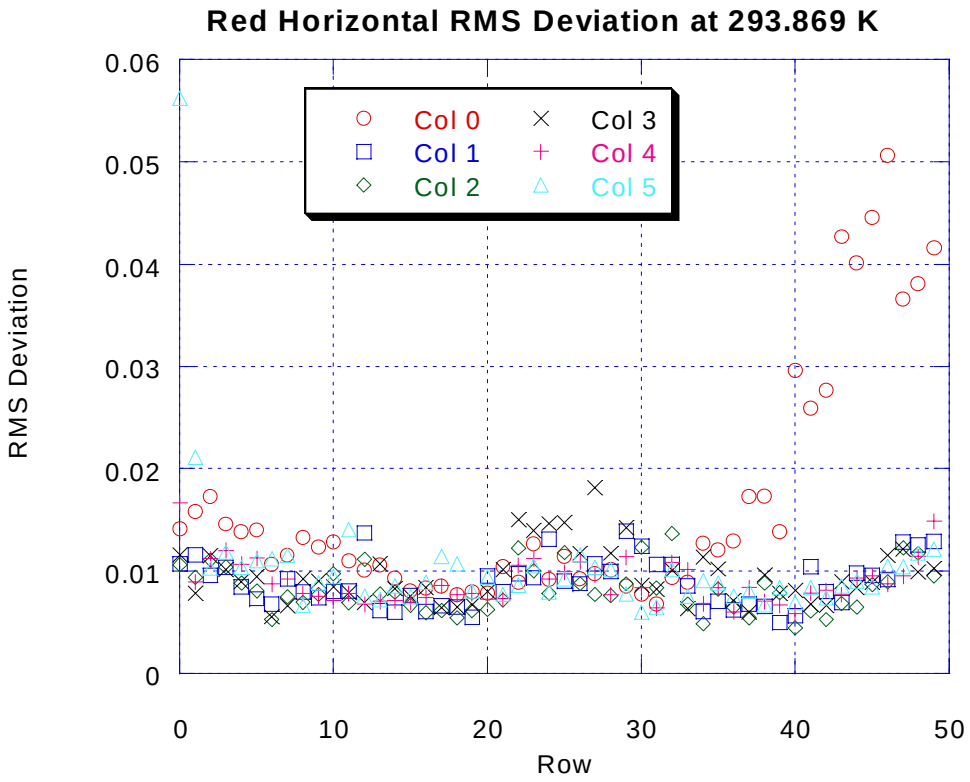
Red Horizontal RMS Deviation at 293.869 K
RMS Deviation
0.06
0.05
0.04
0.03
0.02
0.01
0
0
10
20
30
40
50
Row
Col 0
Col 1
Col 2
Col 3
Col 4
Col 5

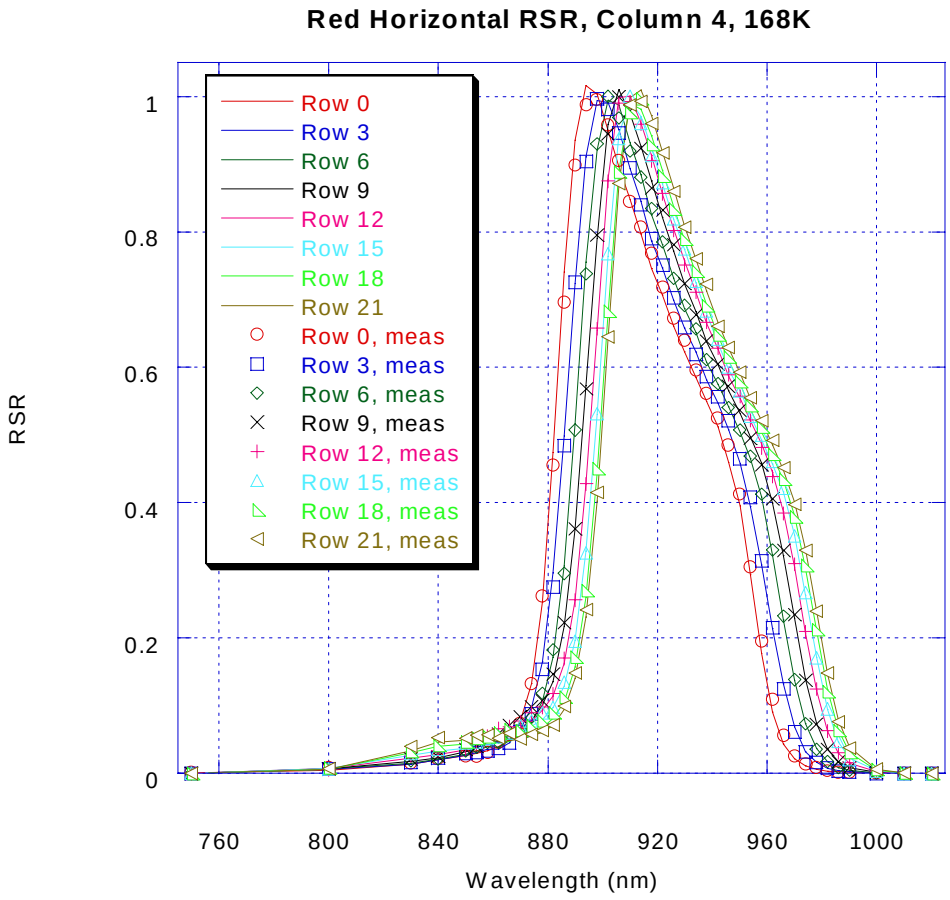
Red Horizontal RSR, Column 4, 168K
RSR
Wavelength (nm)
0
0.2
0.4
0.6
0.8
1
760
800
840
880
920
960
1000
Row 0
Row 3
Row 6
Row 9
Row 12
Row 15
Row 18
Row 21
Row 0, meas
Row 3, meas
Row 6, meas
Row 9, meas
Row 12, meas
Row 15, meas
Row 18, meas
Row 21, meas

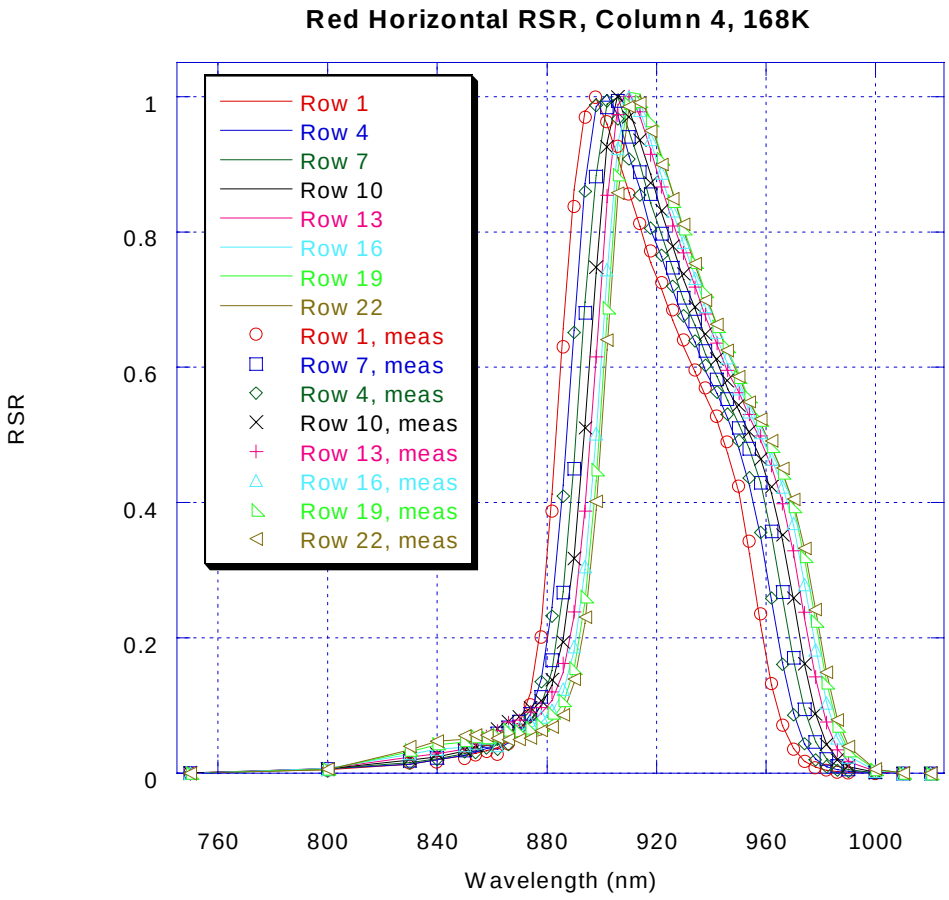
Red Horizontal RSR, Column 4, 168K
RSR
Wavelength (nm)
0
0.2
0.4
0.6
0.8
1
760
800
840
880
920
960
1000
Row 1
Row 4
Row 7
Row 10
Row 13
Row 16
Row 19
Row 22
Row 1, meas
Row 7, meas
Row 4, meas
Row 10, meas
Row 13, meas
Row 16, meas
Row 19, meas
Row 22, meas

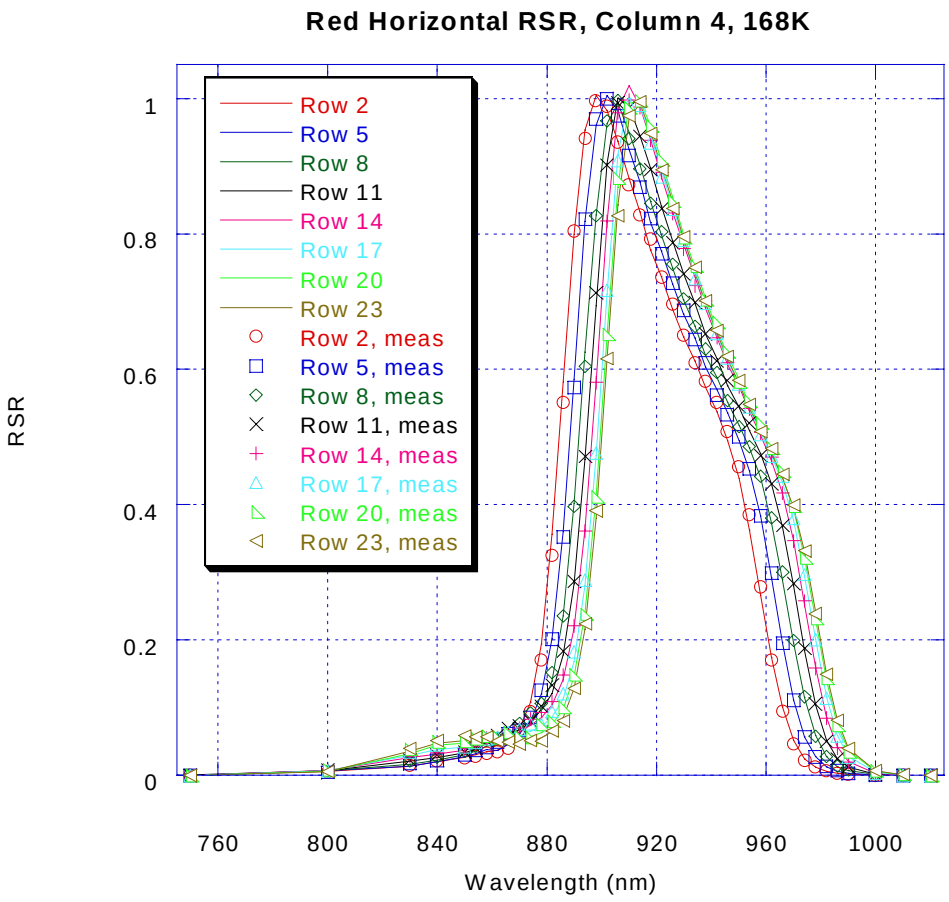
Red Horizontal RSR, Column 4, 168K
RSR
1
0.8
0.6
0.4
0.2
0
760
800
840
880
920
960
1000
Wavelength (nm)
Row 2
Row 5
Row 8
Row 11
Row 14
Row 17
Row 20
Row 23
Row 2, meas
Row 5, meas
Row 8, meas
Row 11, meas
Row 14, meas
Row 17, meas
Row 20, meas
Row 23, meas

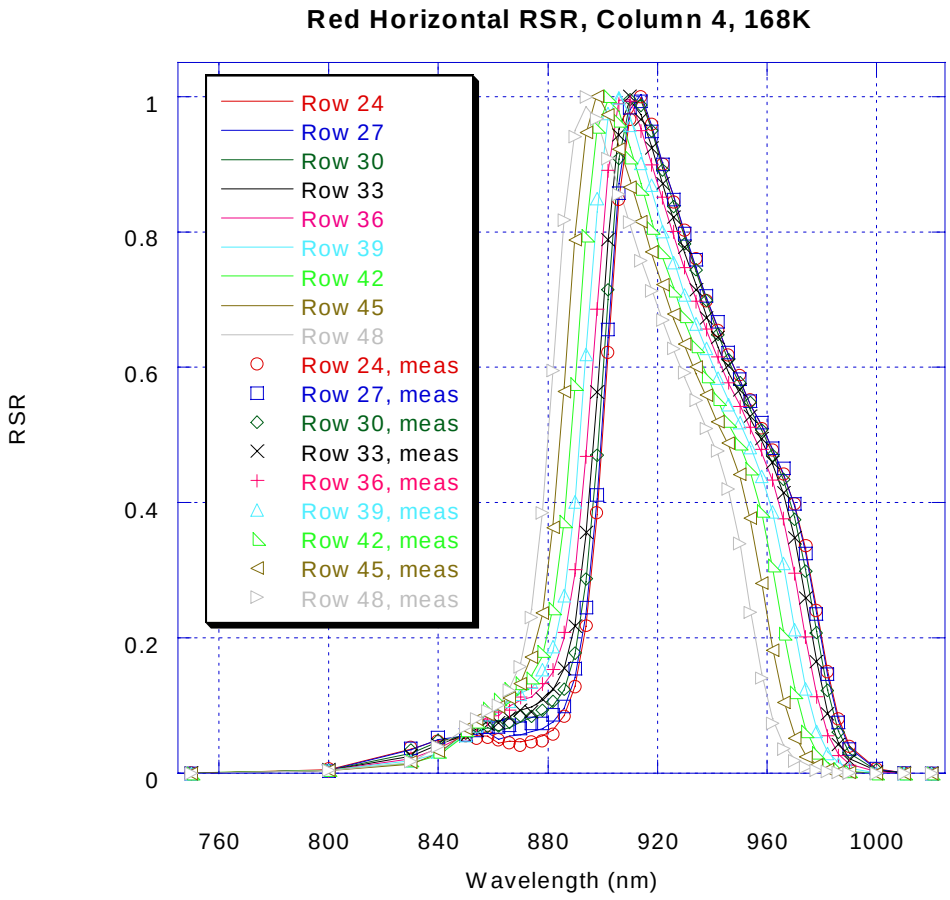
Red Horizontal RSR, Column 4, 168K
RSR
Wavelength (nm)
1
0.8
0.6
0.4
0.2
0
760
800
840
880
920
960
1000
Row 24
Row 27
Row 30
Row 33
Row 36
Row 39
Row 42
Row 45
Row 48
Row 24, meas
Row 27, meas
Row 30, meas
Row 33, meas
Row 36, meas
Row 39, meas
Row 42, meas
Row 45, meas
Row 48, meas

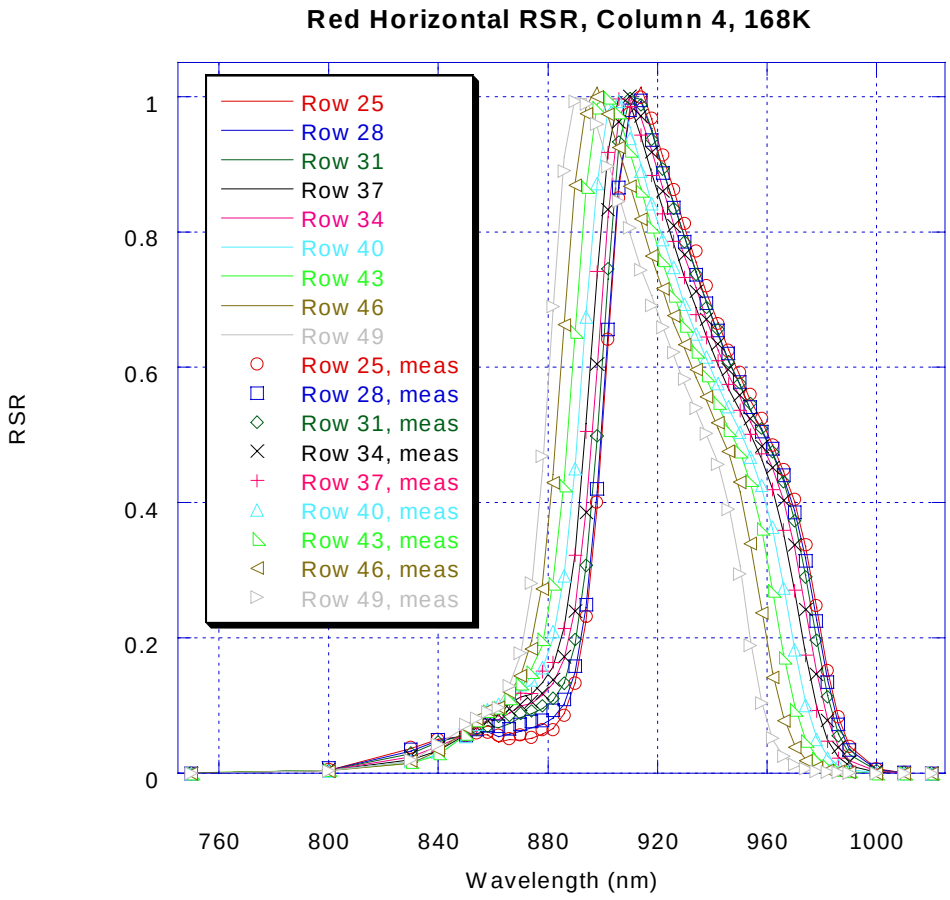
Red Horizontal RSR, Column 4, 168K
RSR
Wavelength (nm)
0
0.2
0.4
0.6
0.8
1
760
800
840
880
920
960
1000
Row 25
Row 28
Row 31
Row 37
Row 34
Row 40
Row 43
Row 46
Row 49
Row 25, meas
Row 28, meas
Row 31, meas
Row 34, meas
Row 37, meas
Row 40, meas
Row 43, meas
Row 46, meas
Row 49, meas

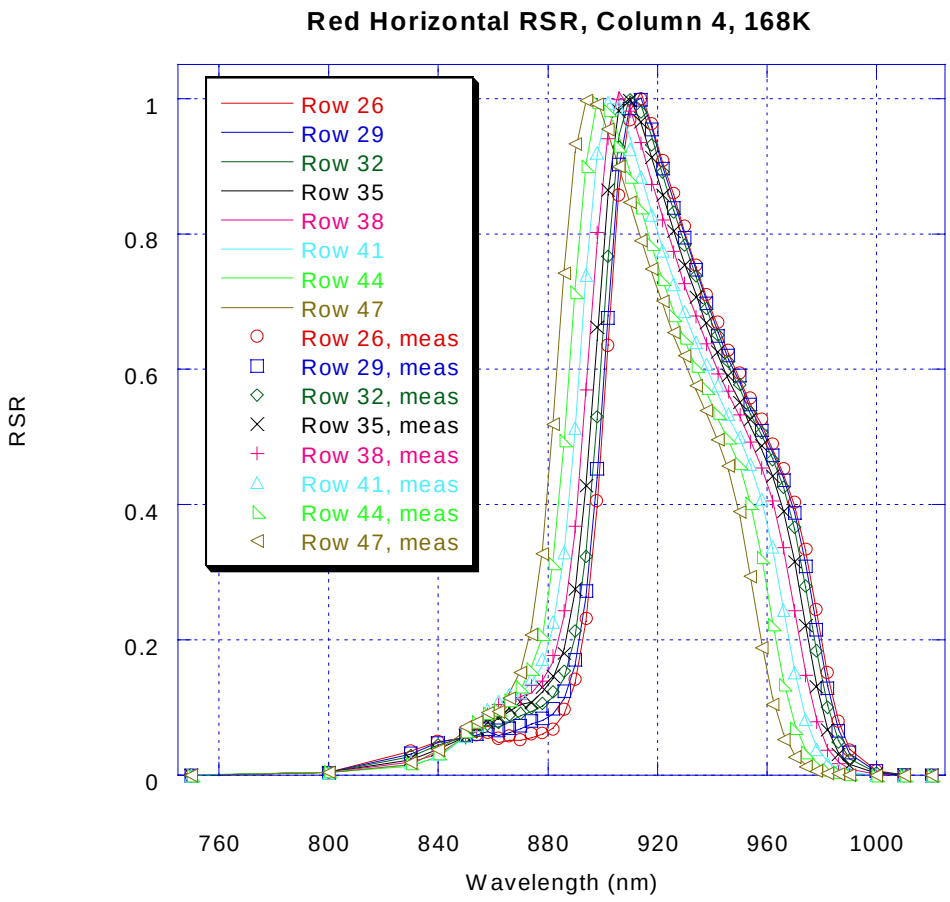
Red Horizontal RSR, Column 4, 168K
RSR
Wavelength (nm)
Row 26
Row 29
Row 32
Row 35
Row 38
Row 41
Row 44
Row 47
Row 26, meas
Row 29, meas
Row 32, meas
Row 35, meas
Row 38, meas
Row 41, meas
Row 44, meas
Row 47, meas
0
0.2
0.4
0.6
0.8
1
760
800
840
880
920
960
1000

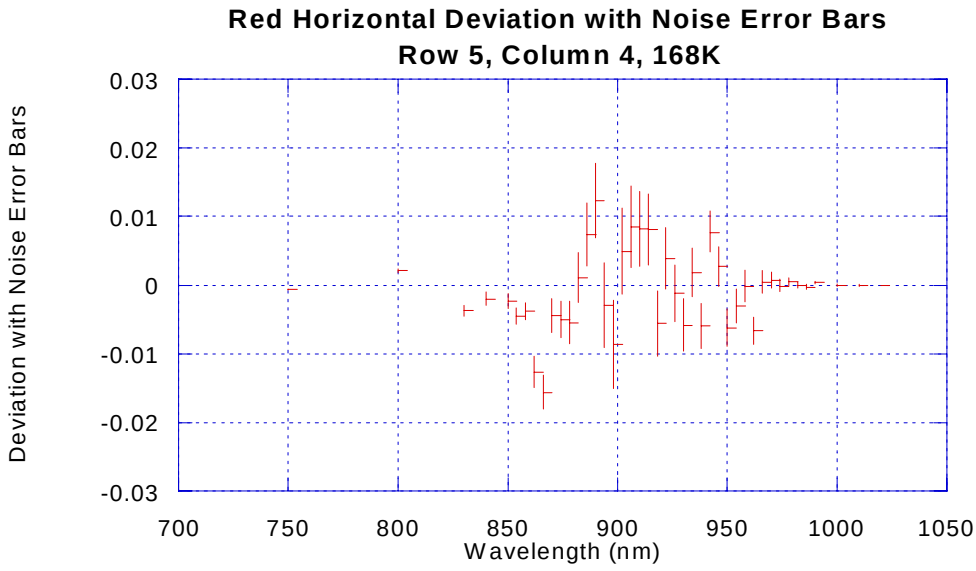
Red Horizontal Deviation with Noise Error Bars
Row 5, Column 4, 168K
Deviation with Noise Error Bars
Wavelength (nm)
0.03
0.02
0.01
0
-0.01
-0.02
-0.03
700
750
800
850
900
950
1000
1050

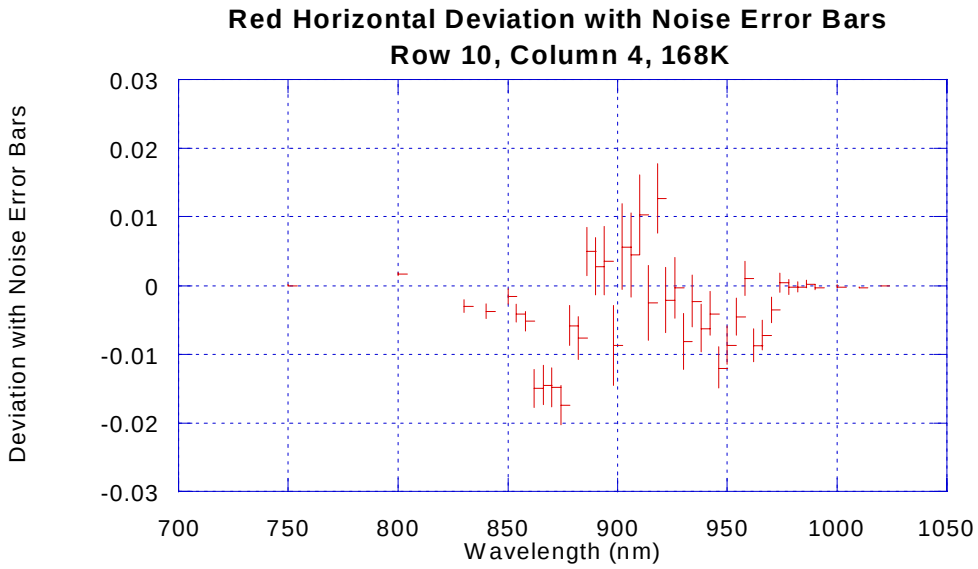
Red Horizontal Deviation with Noise Error Bars
Row 10, Column 4, 168K
Deviation with Noise Error Bars
0.03
0.02
0.01
0
-0.01
-0.02
-0.03
700
750
800
850
900
950
1000
1050
Wavelength (nm)

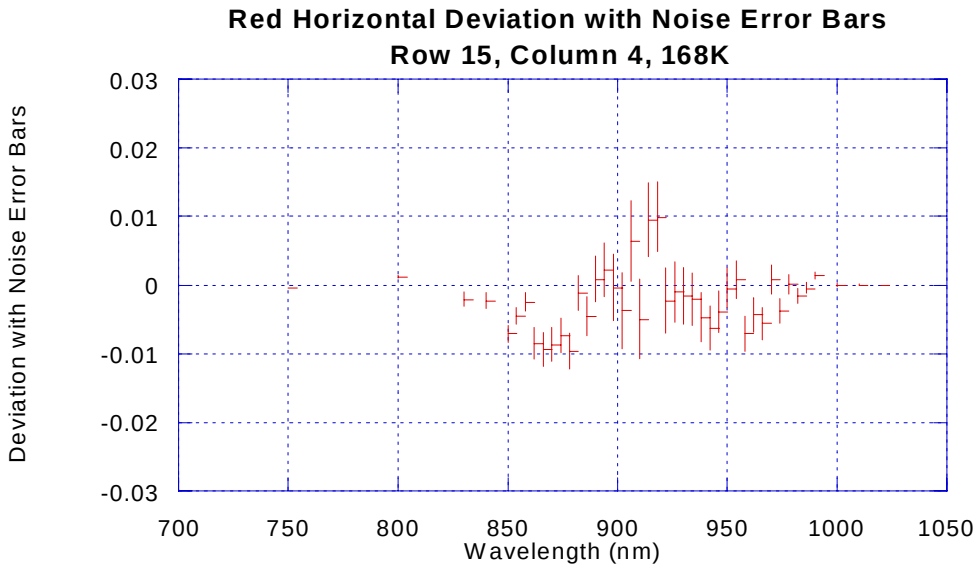
Red Horizontal Deviation with Noise Error Bars
Row 15, Column 4, 168K
Deviation with Noise Error Bars
0.03
0.02
0.01
0
-0.01
-0.02
-0.03
700
750
800
850
900
950
1000
1050
Wavelength (nm)

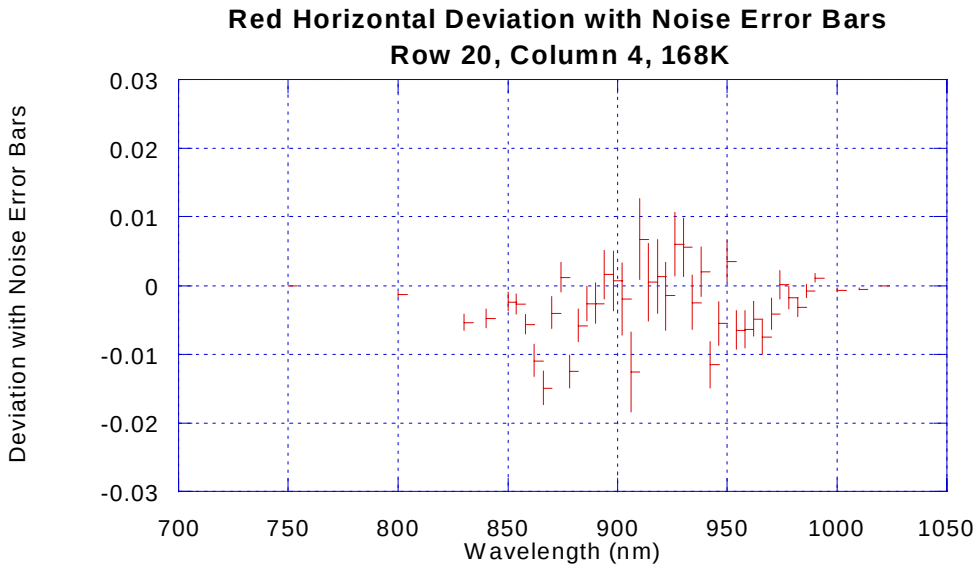
Red Horizontal Deviation with Noise Error Bars
Row 20, Column 4, 168K
Deviation with Noise Error Bars
0.03
0.02
0.01
0
-0.01
-0.02
-0.03
700
750
800
850
900
950
1000
1050
Wavelength (nm)

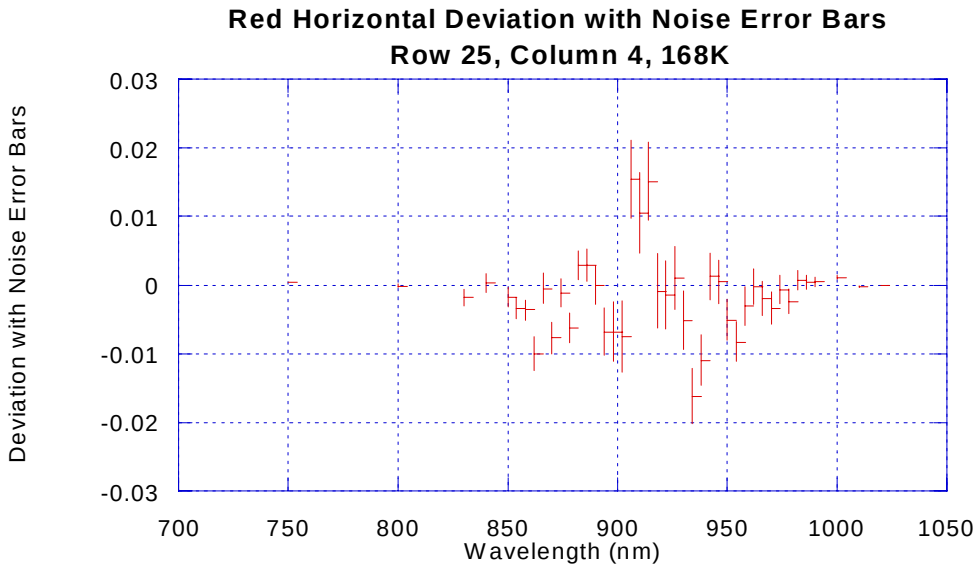
Red Horizontal Deviation with Noise Error Bars
Row 25, Column 4, 168K
Deviation with Noise Error Bars
0.03
0.02
0.01
0
-0.01
-0.02
-0.03
700
750
800
850
900
950
1000
1050
Wavelength (nm)

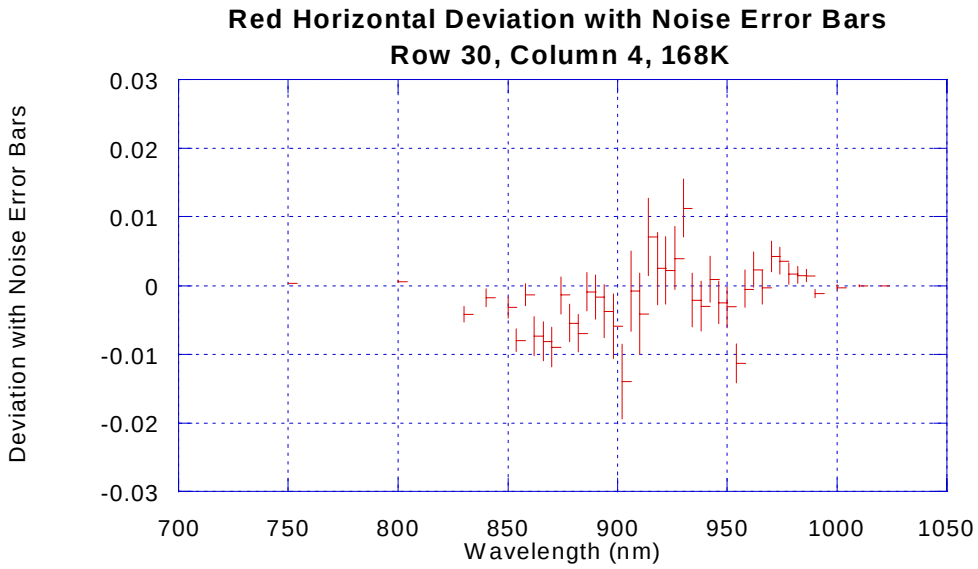
Red Horizontal Deviation with Noise Error Bars
Row 30, Column 4, 168K
Deviation with Noise Error Bars
0.03
0.02
0.01
0
-0.01
-0.02
-0.03
700
750
800
850
900
950
1000
1050
Wavelength (nm)

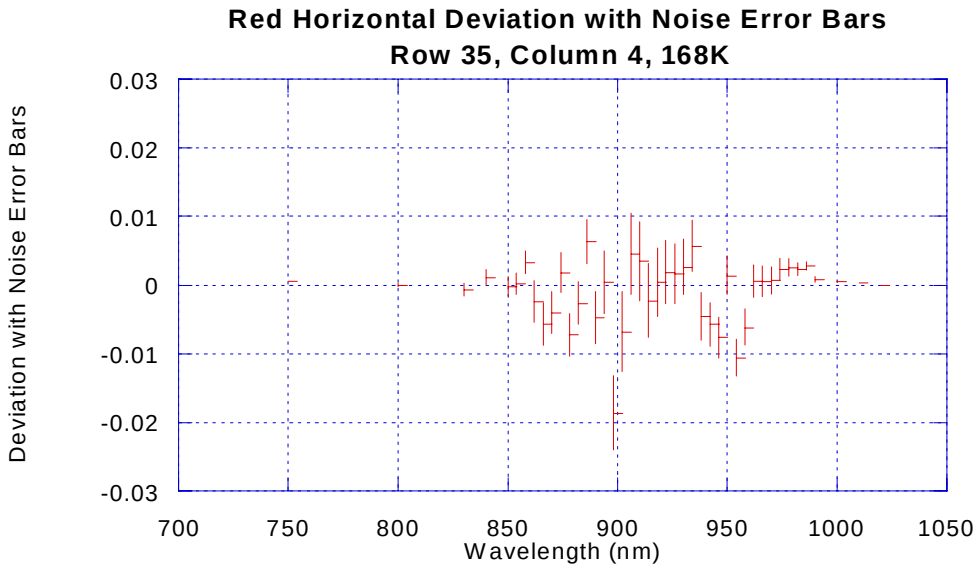
Red Horizontal Deviation with Noise Error Bars
Row 35, Column 4, 168K
Deviation with Noise Error Bars
0.03
0.02
0.01
0
-0.01
-0.02
-0.03
700
750
800
850
900
950
1000
1050
Wavelength (nm)

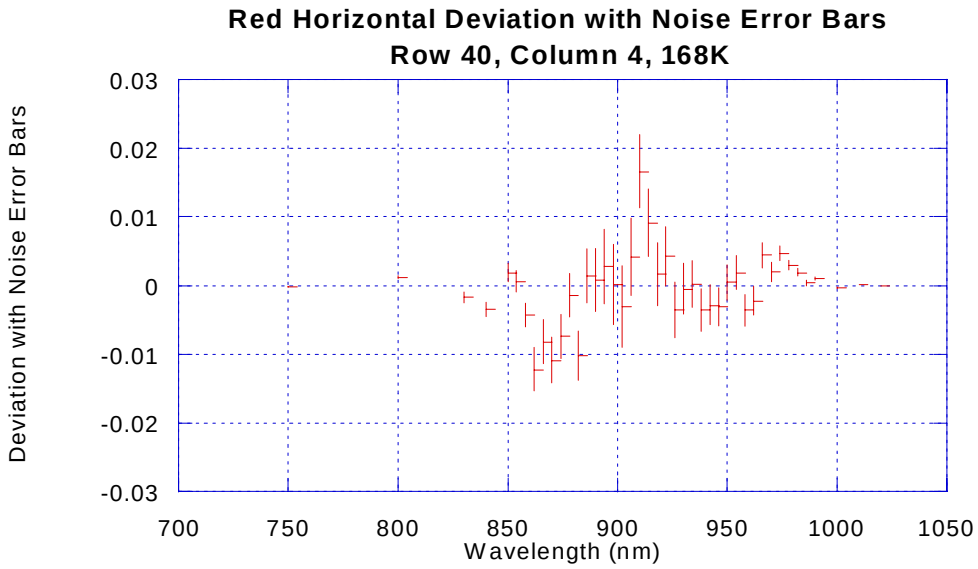
Red Horizontal Deviation with Noise Error Bars
Row 40, Column 4, 168K
Deviation with Noise Error Bars
0.03
0.02
0.01
0
-0.01
-0.02
-0.03
700
750
800
850
900
950
1000
1050
Wavelength (nm)

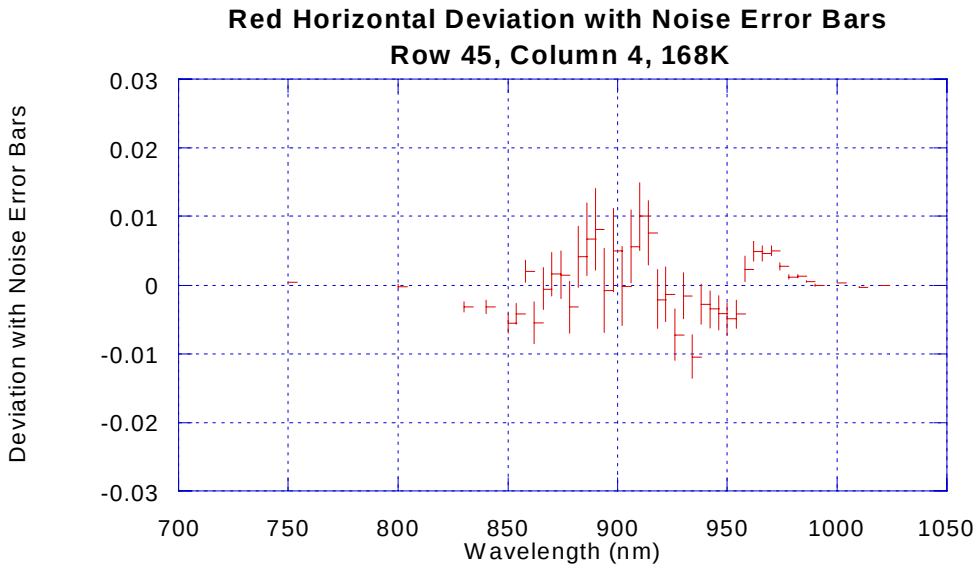
Red Horizontal Deviation with Noise Error Bars
Row 45, Column 4, 168K
Deviation with Noise Error Bars
0.03
0.02
0.01
0
-0.01
-0.02
-0.03
700
750
800
850
900
950
1000
1050
Wavelength (nm)

Figure 13-52 Red Vertical Relative Spectral Response Modeling Results – Set of Nineteen Plots

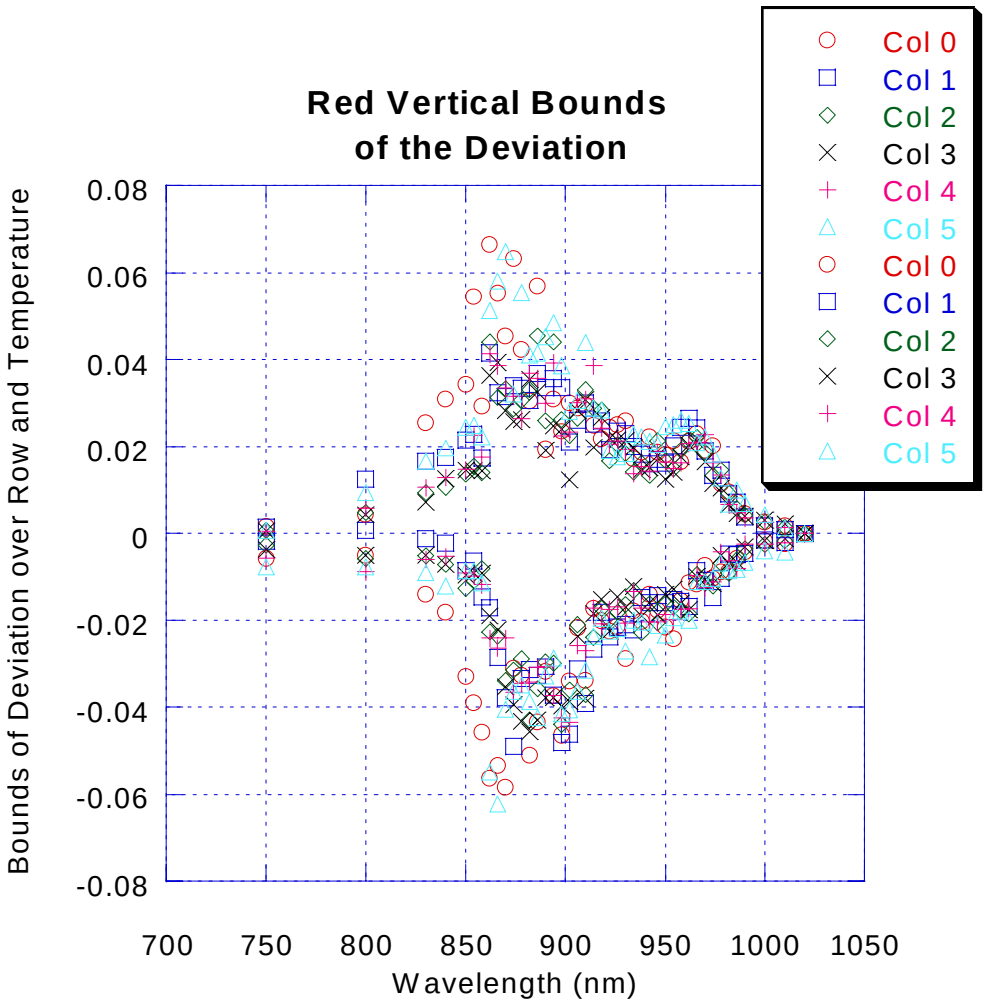

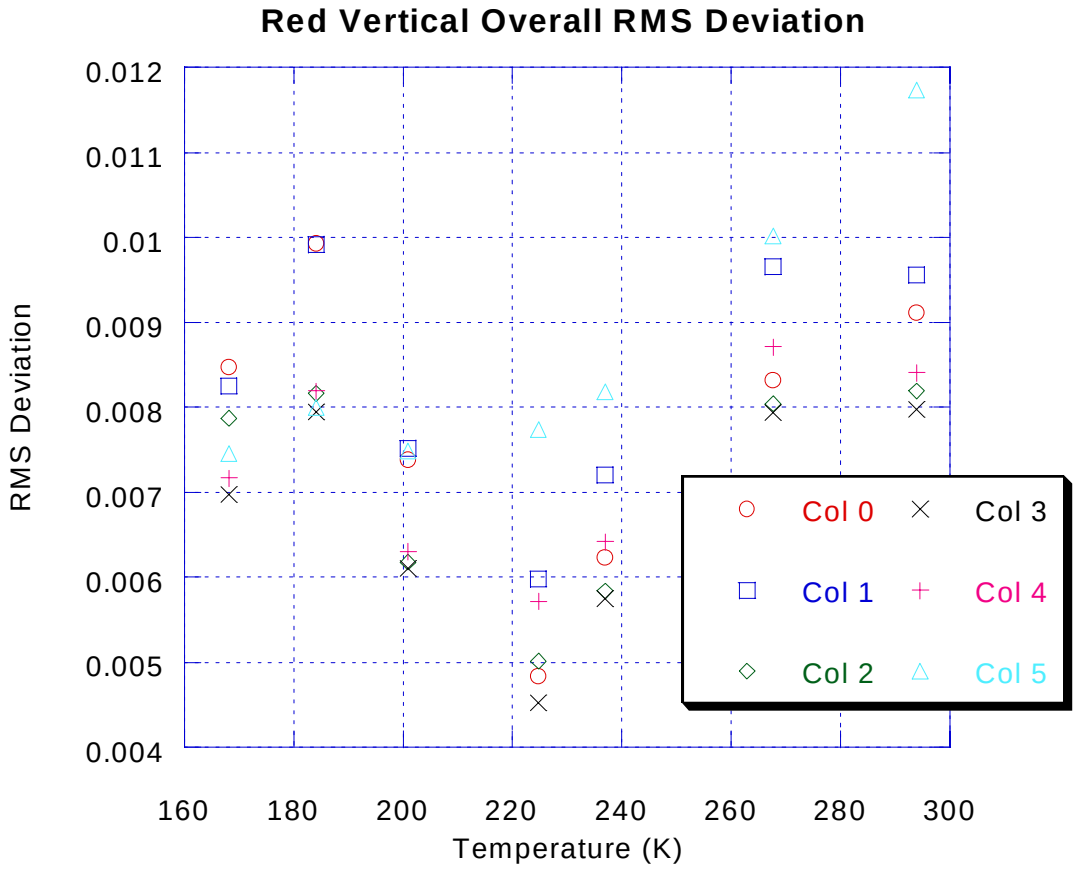
Red Vertical Overall RMS Deviation
RMS Deviation
0.012
0.011
0.01
0.009
0.008
0.007
0.006
0.005
0.004
160
180
200
220
240
260
280
300
Temperature (K)
Col 0
Col 1
Col 2
Col 3
Col 4
Col 5

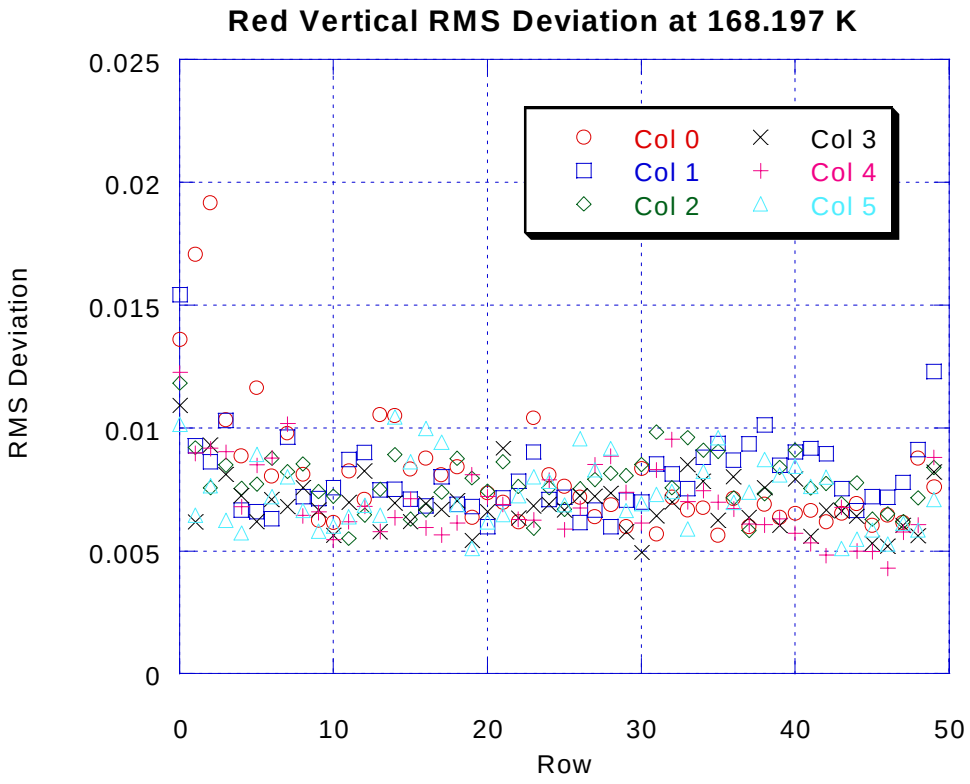
Red Vertical RMS Deviation at 168.197 K
RMS Deviation
0.025
0.02
0.015
0.01
0.005
0
0
10
20
30
40
50
Row
Col 0
Col 1
Col 2
Col 3
Col 4
Col 5

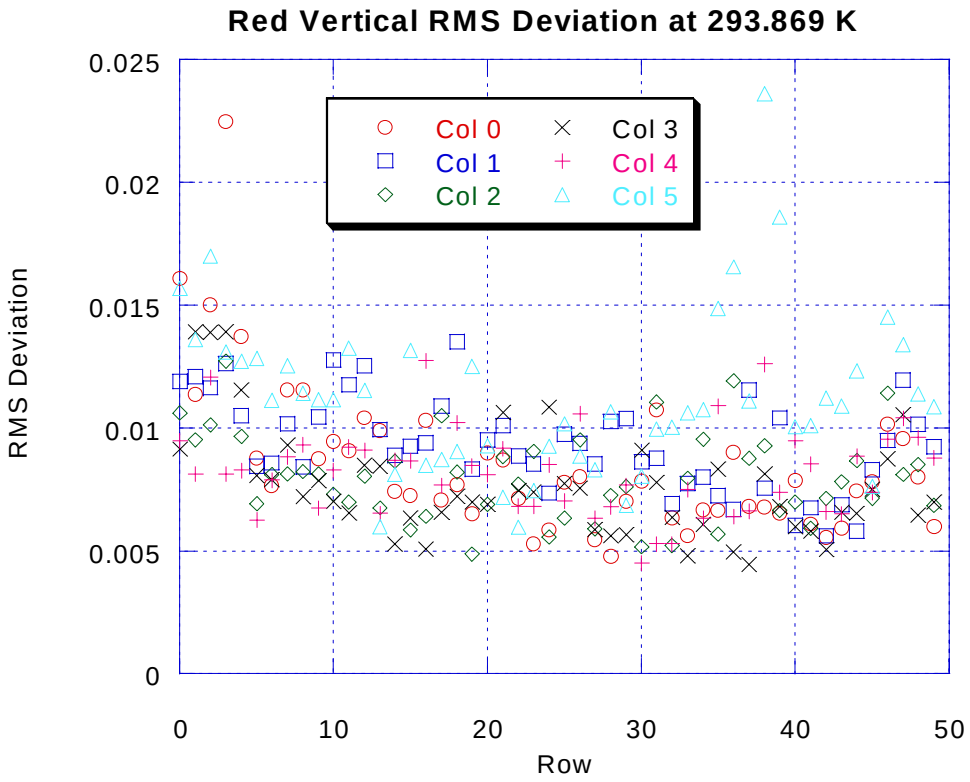
Red Vertical RMS Deviation at 293.869 K
RMS Deviation
0.025
0.02
0.015
0.01
0.005
0
0
10
20
30
40
50
Row
Col 0
Col 1
Col 2
Col 3
Col 4
Col 5

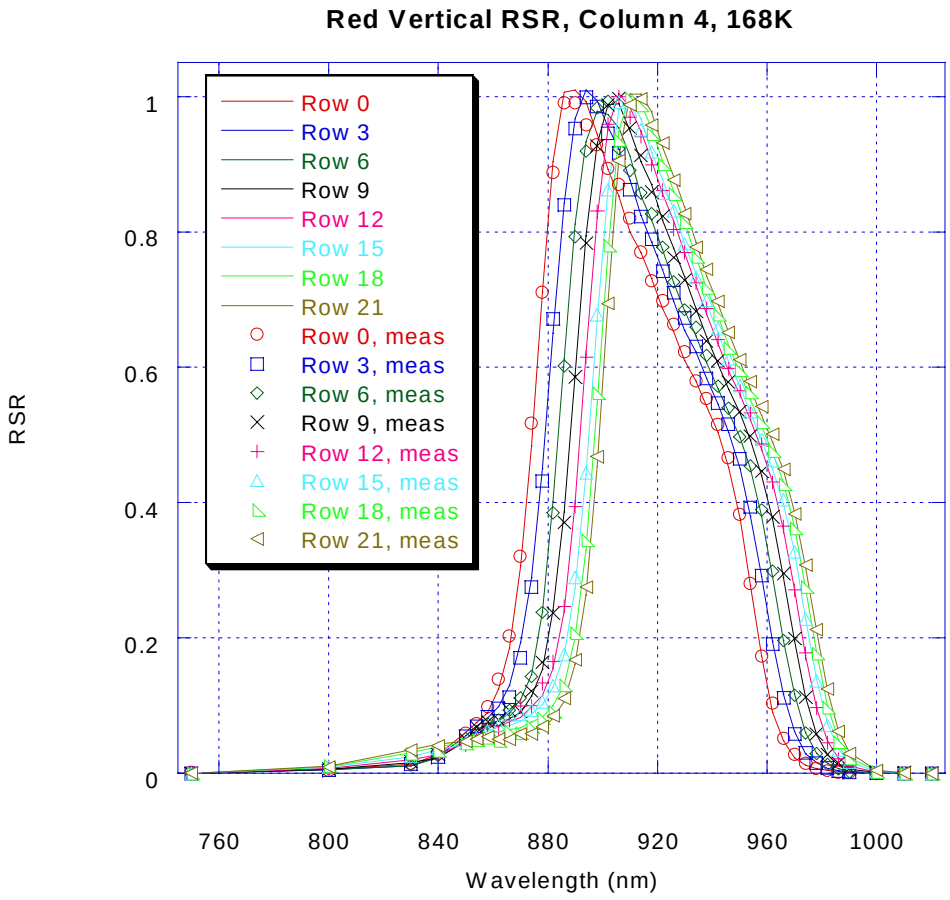
Red Vertical RSR, Column 4, 168K
RSR
Wavelength (nm)
0
0.2
0.4
0.6
0.8
1
760
800
840
880
920
960
1000
Row 0
Row 3
Row 6
Row 9
Row 12
Row 15
Row 18
Row 21
Row 0, meas
Row 3, meas
Row 6, meas
Row 9, meas
Row 12, meas
Row 15, meas
Row 18, meas
Row 21, meas

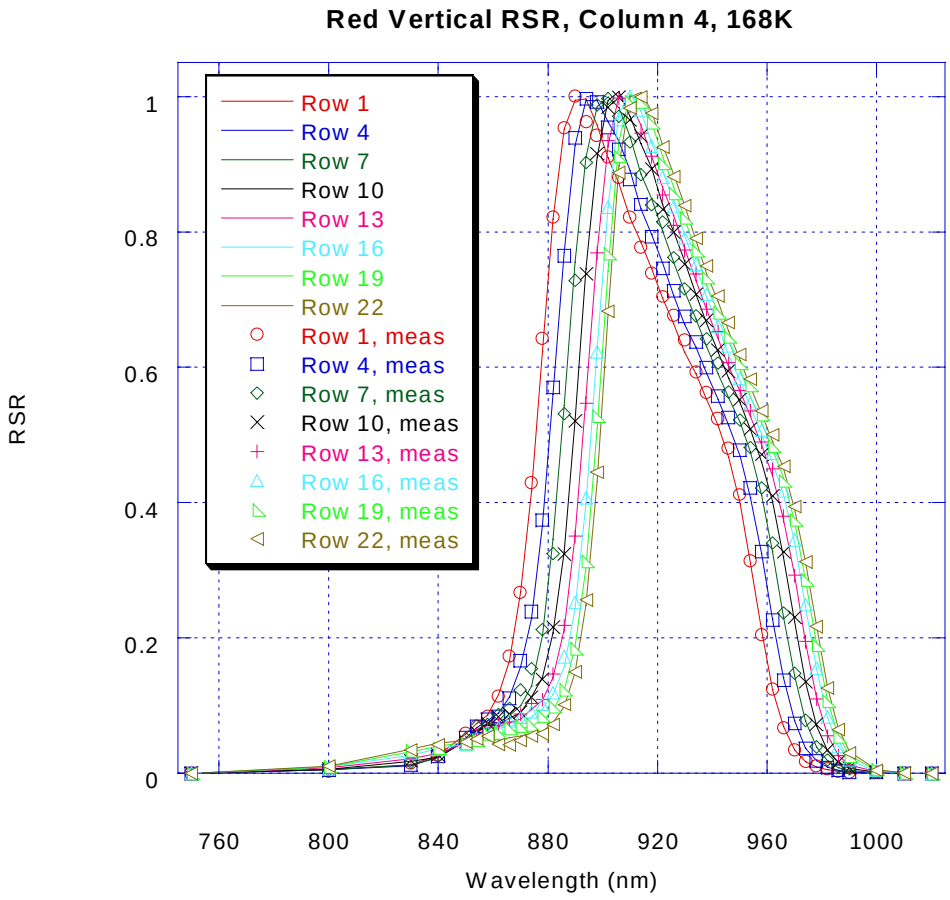
Red Vertical RSR, Column 4, 168K
RSR
Wavelength (nm)
0
0.2
0.4
0.6
0.8
1
760
800
840
880
920
960
1000
Row 1
Row 4
Row 7
Row 10
Row 13
Row 16
Row 19
Row 22
Row 1, meas
Row 4, meas
Row 7, meas
Row 10, meas
Row 13, meas
Row 16, meas
Row 19, meas
Row 22, meas

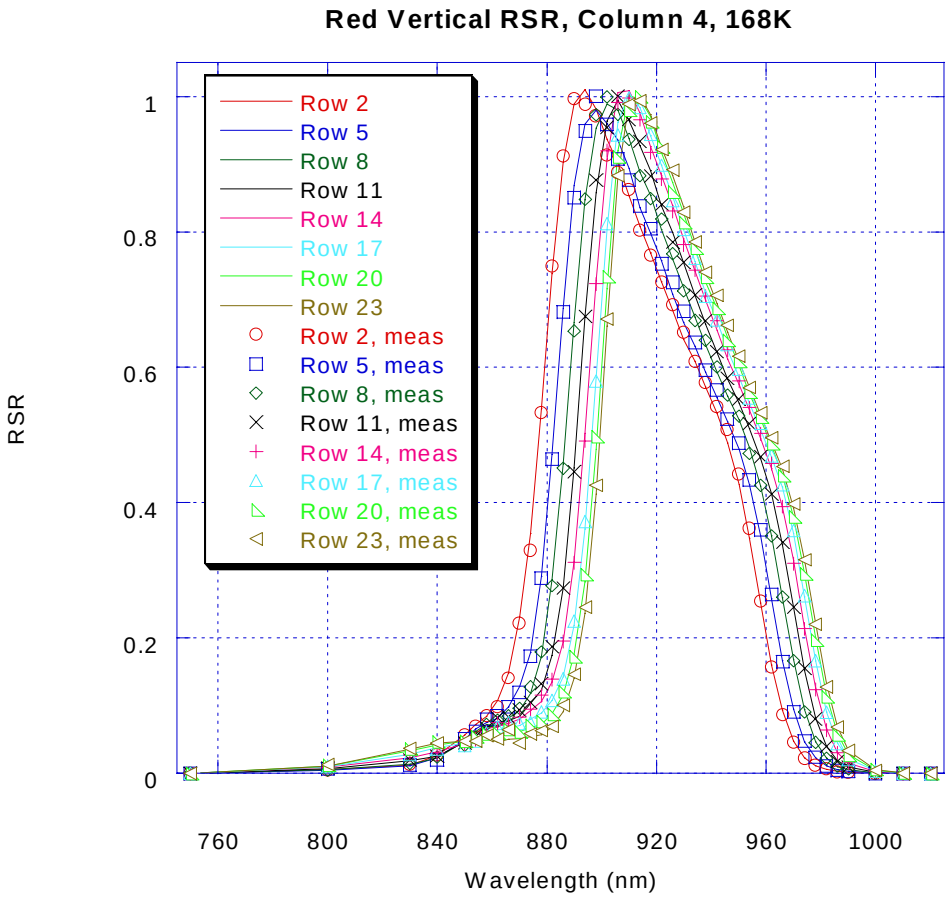
Red Vertical RSR, Column 4, 168K
RSR
Wavelength (nm)
0
0.2
0.4
0.6
0.8
1
760
800
840
880
920
960
1000
Row 2
Row 5
Row 8
Row 11
Row 14
Row 17
Row 20
Row 23
Row 2, meas
Row 5, meas
Row 8, meas
Row 11, meas
Row 14, meas
Row 17, meas
Row 20, meas
Row 23, meas

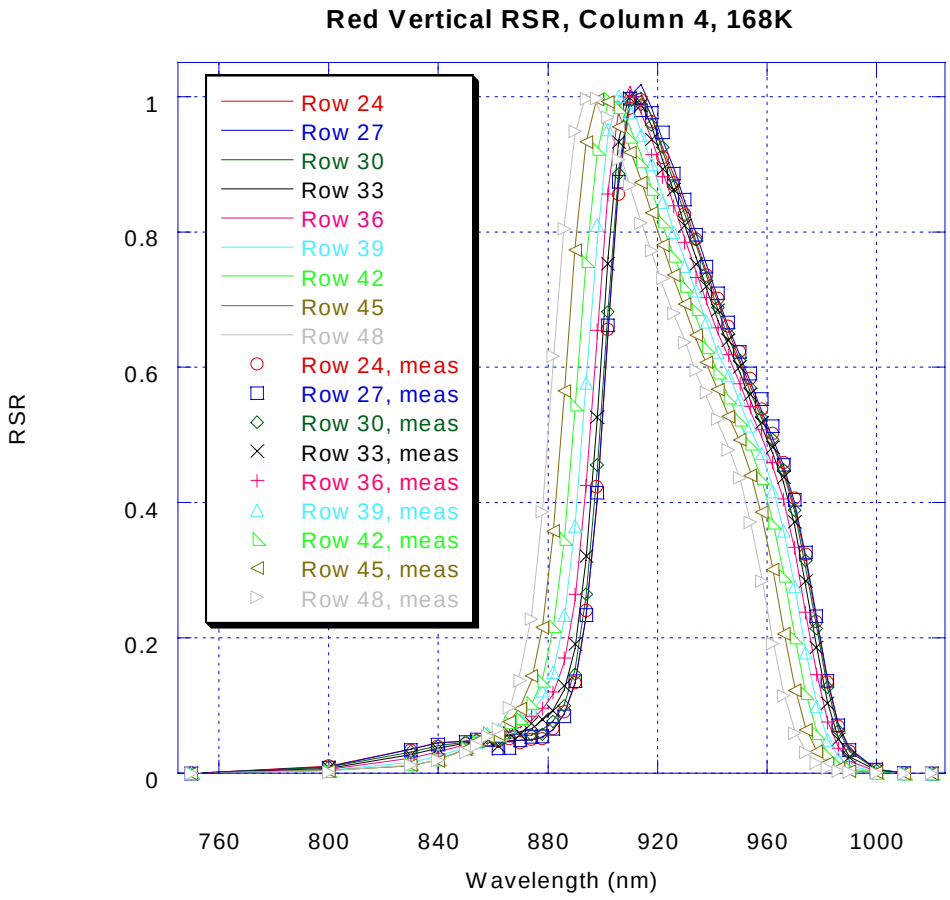
Red Vertical RSR, Column 4, 168K
RSR
Wavelength (nm)
0
0.2
0.4
0.6
0.8
1
760
800
840
880
920
960
1000
Row 24
Row 27
Row 30
Row 33
Row 36
Row 39
Row 42
Row 45
Row 48
Row 24, meas
Row 27, meas
Row 30, meas
Row 33, meas
Row 36, meas
Row 39, meas
Row 42, meas
Row 45, meas
Row 48, meas

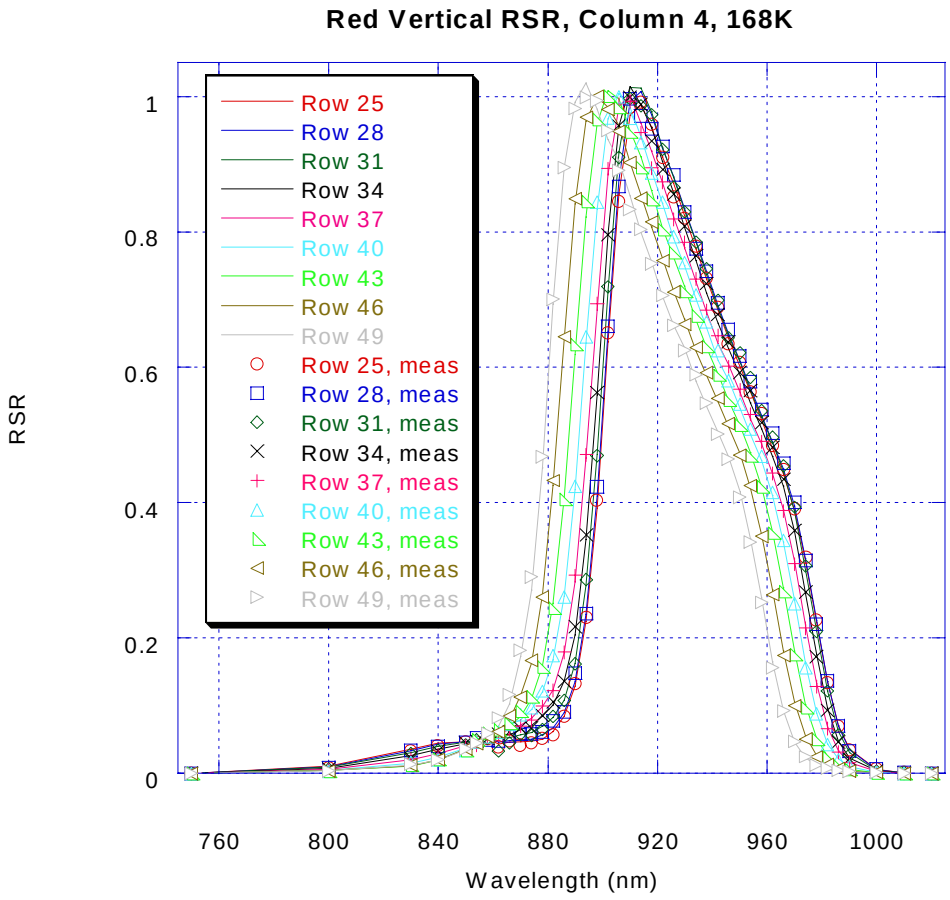
Red Vertical RSR, Column 4, 168K
RSR
1
0.8
0.6
0.4
0.2
0
760
800
840
880
920
960
1000
Wavelength (nm)
Row 25
Row 28
Row 31
Row 34
Row 37
Row 40
Row 43
Row 46
Row 49
Row 25, meas
Row 28, meas
Row 31, meas
Row 34, meas
Row 37, meas
Row 40, meas
Row 43, meas
Row 46, meas
Row 49, meas

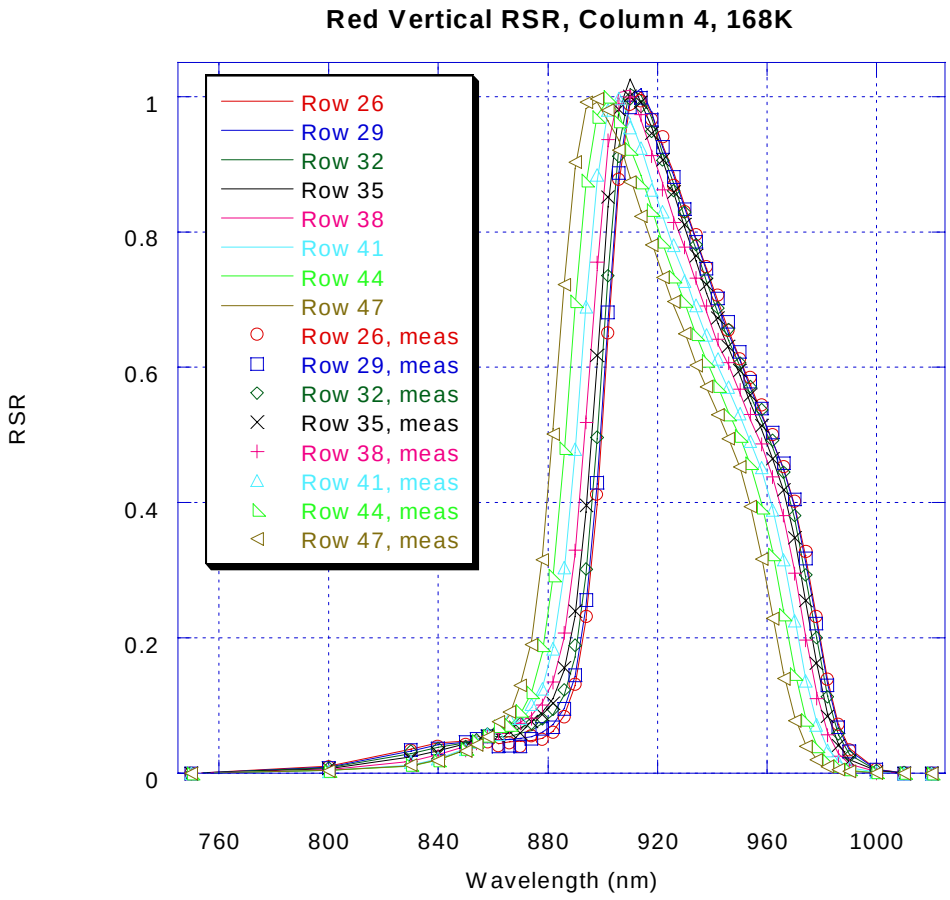
Red Vertical RSR, Column 4, 168K
RSR
Wavelength (nm)
Row 26
Row 29
Row 32
Row 35
Row 38
Row 41
Row 44
Row 47
Row 26, meas
Row 29, meas
Row 32, meas
Row 35, meas
Row 38, meas
Row 41, meas
Row 44, meas
Row 47, meas
0
0.2
0.4
0.6
0.8
1
760
800
840
880
920
960
1000

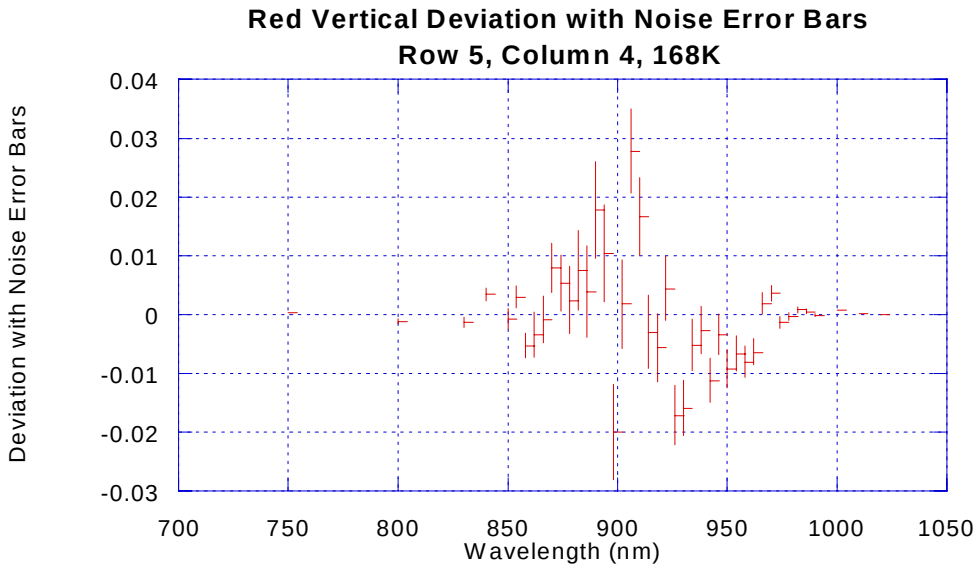
Red Vertical Deviation with Noise Error Bars
Row 5, Column 4, 168K
Deviation with Noise Error Bars
Wavelength (nm)
0.04
0.03
0.02
0.01
0
-0.01
-0.02
-0.03
700
750
800
850
900
950
1000
1050

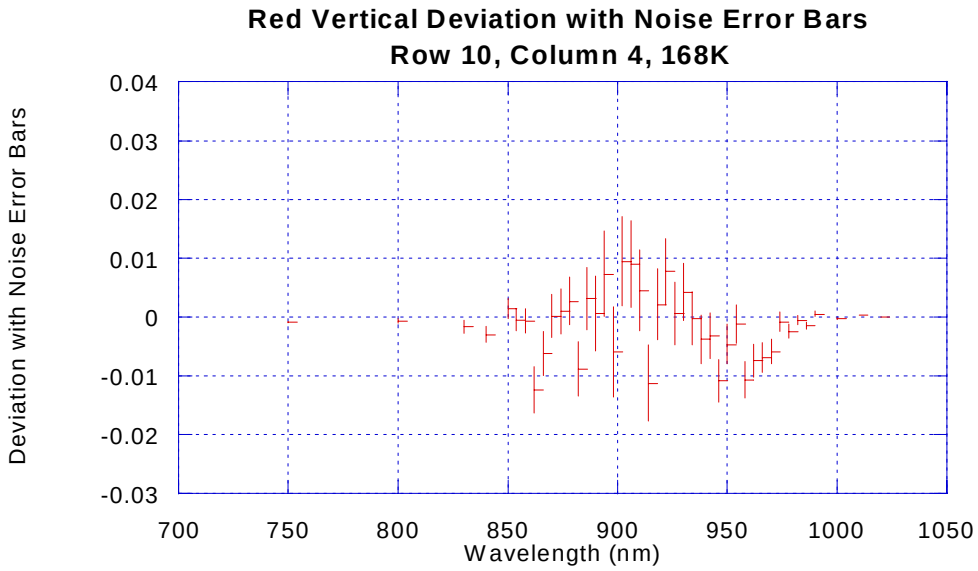
Red Vertical Deviation with Noise Error Bars
Row 10, Column 4, 168K
Deviation with Noise Error Bars
0.04
0.03
0.02
0.01
0
-0.01
-0.02
-0.03
700
750
800
850
900
950
1000
1050
Wavelength (nm)

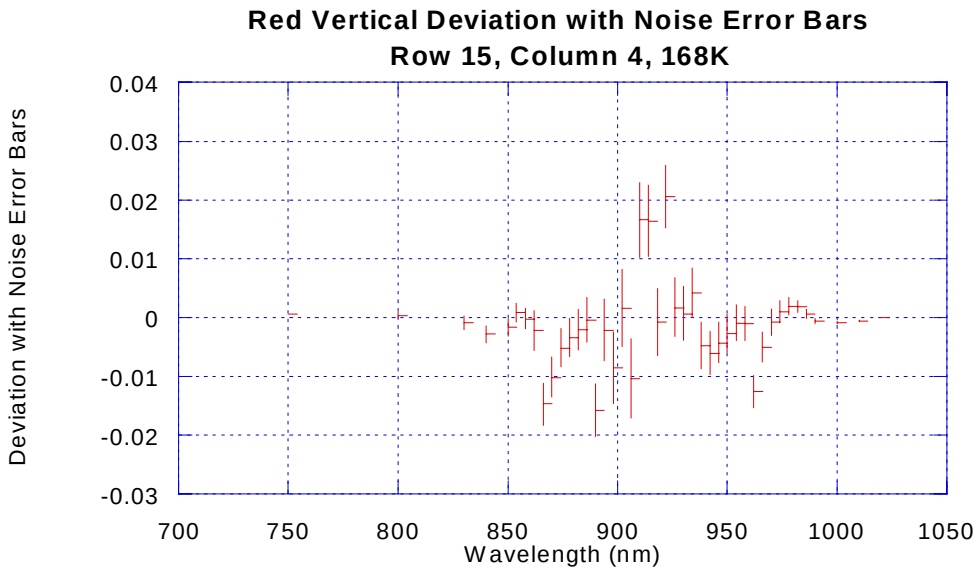
Red Vertical Deviation with Noise Error Bars
Row 15, Column 4, 168K
Deviation with Noise Error Bars
0.04
0.03
0.02
0.01
0
-0.01
-0.02
-0.03
700
750
800
850
900
950
1000
1050
Wavelength (nm)

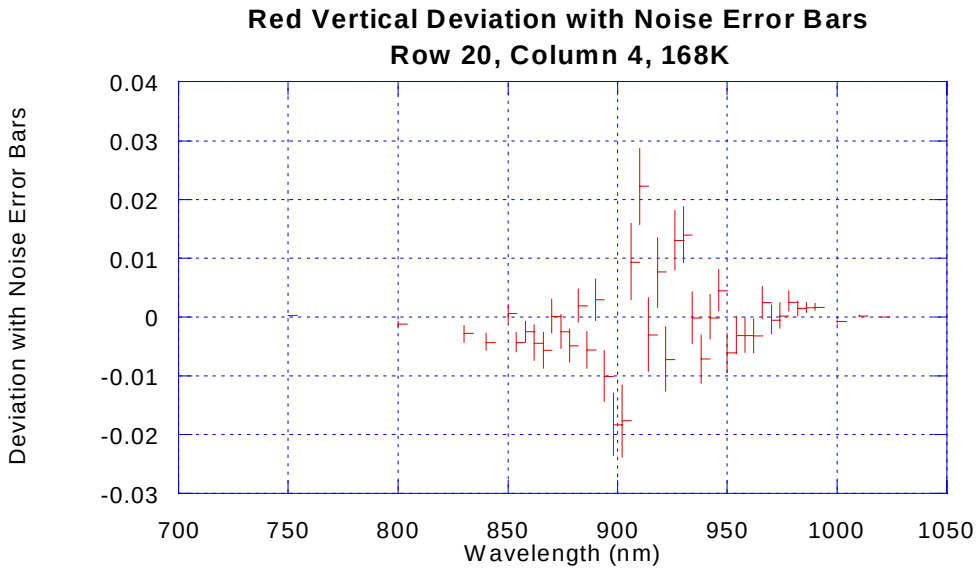
Red Vertical Deviation with Noise Error Bars
Row 20, Column 4, 168K
Deviation with Noise Error Bars
0.04
0.03
0.02
0.01
0
-0.01
-0.02
-0.03
700
750
800
850
900
950
1000
1050
Wavelength (nm)

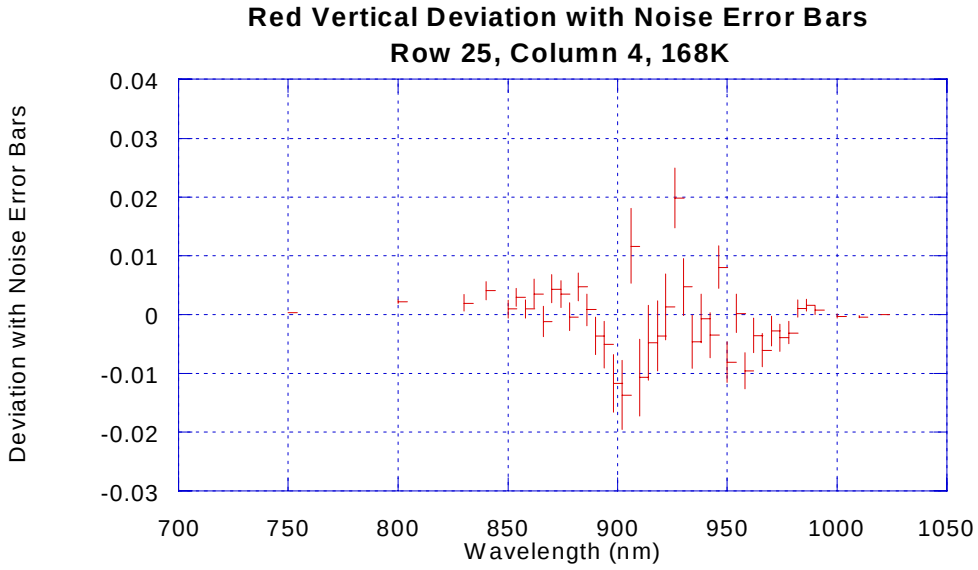
Red Vertical Deviation with Noise Error Bars
Row 25, Column 4, 168K
Deviation with Noise Error Bars
0.04
0.03
0.02
0.01
0
-0.01
-0.02
-0.03
700
750
800
850
900
950
1000
1050
Wavelength (nm)

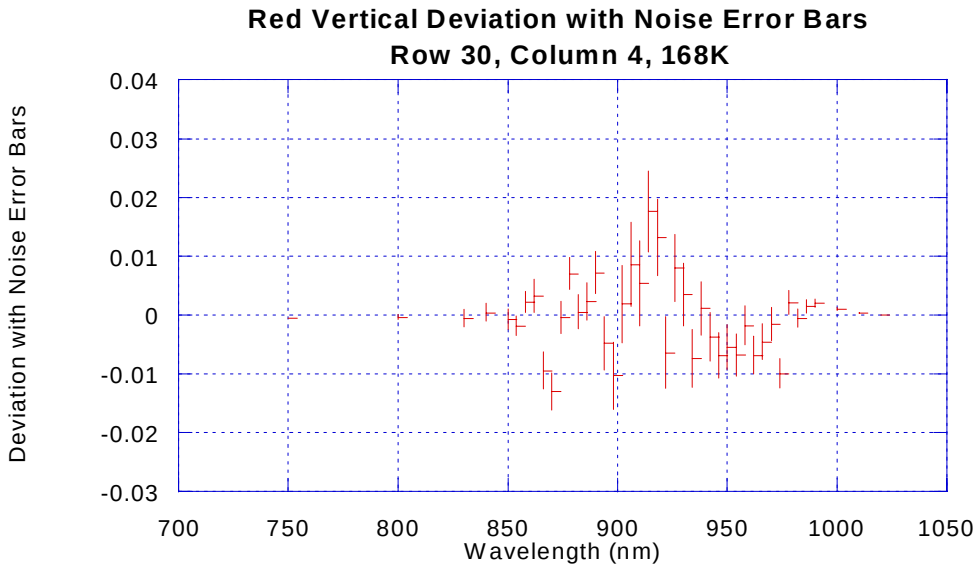
Red Vertical Deviation with Noise Error Bars
Row 30, Column 4, 168K
Deviation with Noise Error Bars
0.04
0.03
0.02
0.01
0
-0.01
-0.02
-0.03
700
750
800
850
900
950
1000
1050
Wavelength (nm)

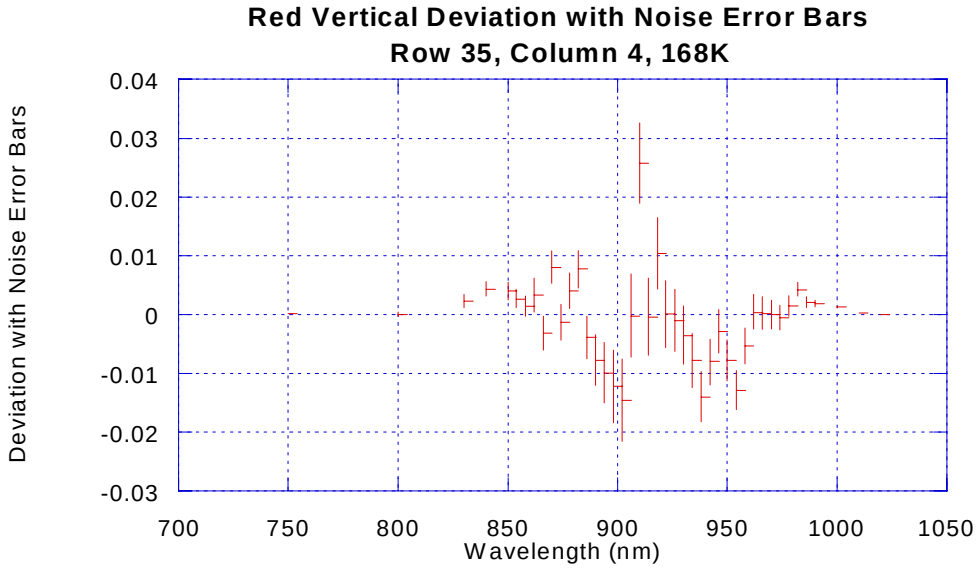
Red Vertical Deviation with Noise Error Bars
Row 35, Column 4, 168K
Deviation with Noise Error Bars
0.04
0.03
0.02
0.01
0
-0.01
-0.02
-0.03
700
750
800
850
900
950
1000
1050
Wavelength (nm)

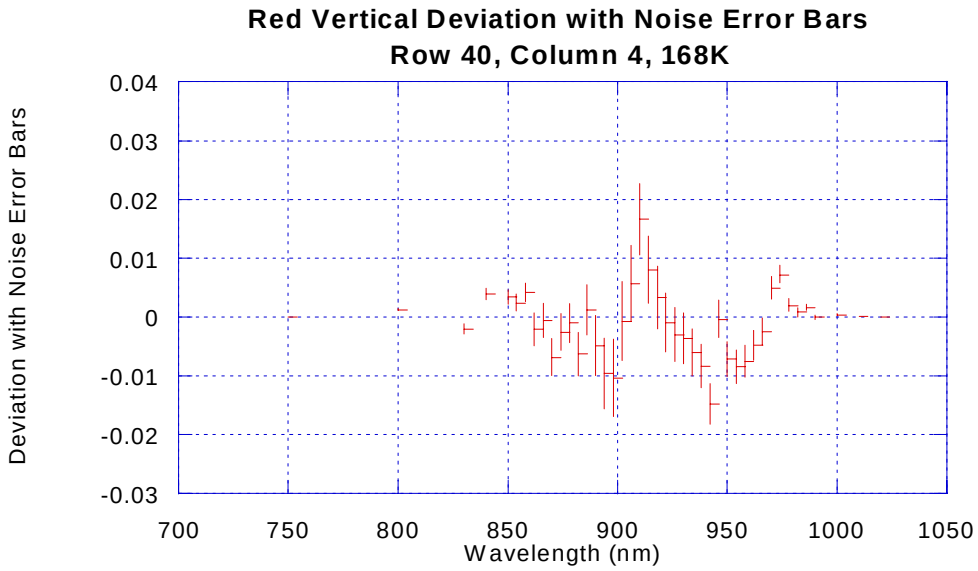

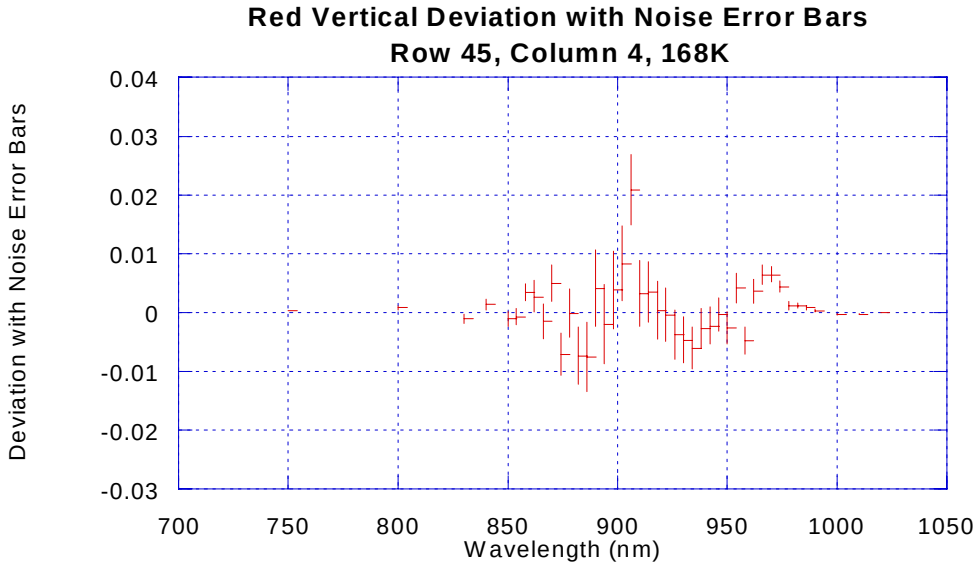

13.4.3.9 Appendix about the Fliers

"RSR fliers" are defined as pixels whose root-mean-square deviation of the modeled RSR from the measured RSR is greater than 1% at some temperature.

13.4.3.9.1 Test Conditions

The following plot shows the total number of fliers versus temperature for each channel. It is interesting to note the similarities in the relative number of fliers for each channel and to recall the order in which the data was taken, designated in text on the plot. The notes files from each of the tests indicate the possibility of systematic differences introduced into the data.

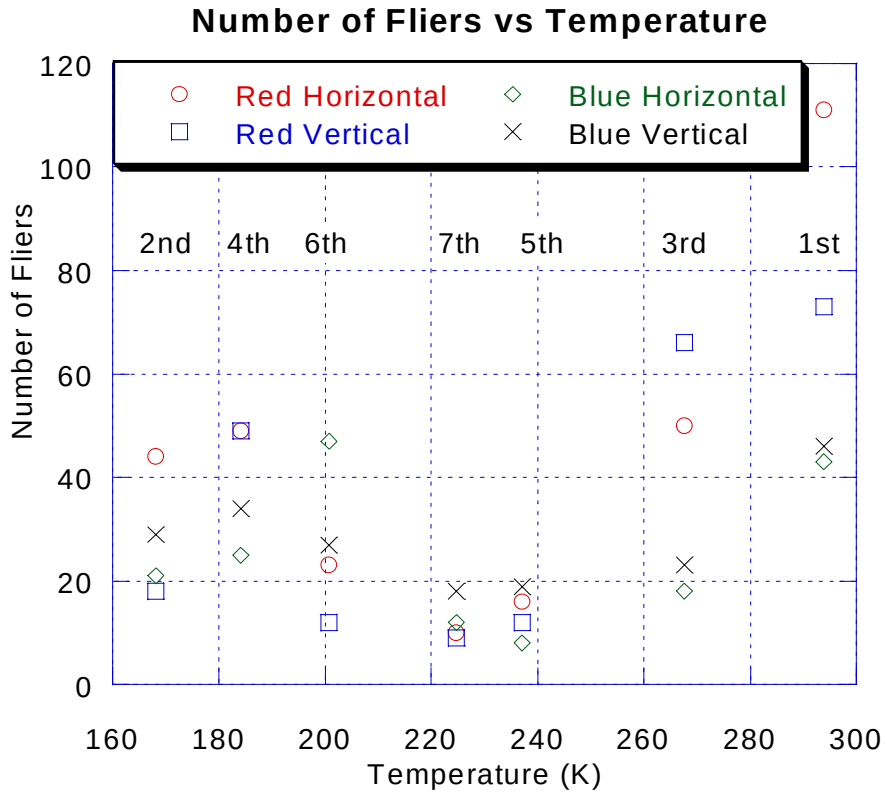

Figure 13-53 Number of Relative Spectral Response Fliers versus Temperature

For example, at 293K where each channel has its highest number of fliers, the injection baffle was present at port 5 (the high intensity lamp port), but it was not present for the other tests. It is hard to see how the presence of this baffle would change the measured RSR shape in the SA channels, but it is worthy of note.

At 267K, the maximum counts in the red channels were roughly 2200dN, the point at which the non-linearity occurs for some cable configurations. Therefore, some saturation could have occurred in the red channels for that temperature, causing readings slightly off from the true readings.

At 184K, the three slits in the system were slightly different from the other tests – 5:5:2.5 versus 2.5:5:2.5 for the others. Notes files indicate that at 184K and possibly at 267K there were different exit slits than the rest of the days. As in the injection baffle case, it is not obvious how this would change the readings, but the difference in the test condition was worthy of mention.

Also at 184K, the note is found, “We turned off the lamp providing a heat source under the integrating sphere. The light seemed to contaminate the SA darks.” If contamination of the dark readings had occurred, this would certainly have changed the resultant measured RSR. It

is unclear whether this lamp condition was in effect for the test at 184K and other tests, or just at 184K.

By the last three days of testing, the setup had stabilized and the system was working smoothly. These latter three test days show the fewest fliers, and there is indication that the higher numbers of fliers for the other temperatures could be due partially to systematic test variations. Coincidentally, the RSR model reference data was taken on the last day of test.

13.4.3.9.2 Which Pixels Are Fliers

Given the possibility that the test setup variations created some of the fliers, it is helpful to determine which pixels have root-mean-square deviations greater than 1% consistently over temperature and which pixels have a larger deviation only once or twice (i.e., at one or two temperatures).

The following four plots show the total number of times each pixel has a root-mean-square deviation greater than 1%. There are 7 possible times.

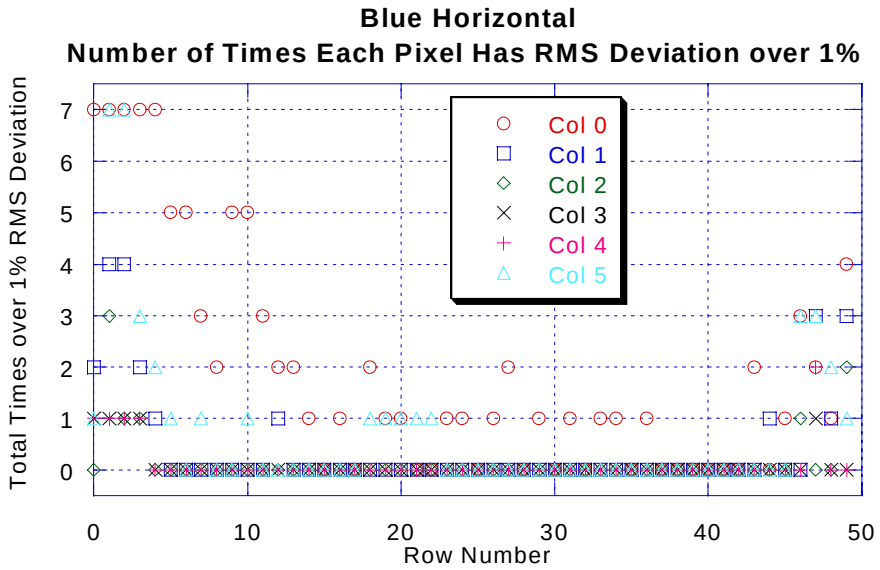

Figure 13-54 Frequency of Blue Horizontal Pixels Having RSR with RMS Deviation over 1%

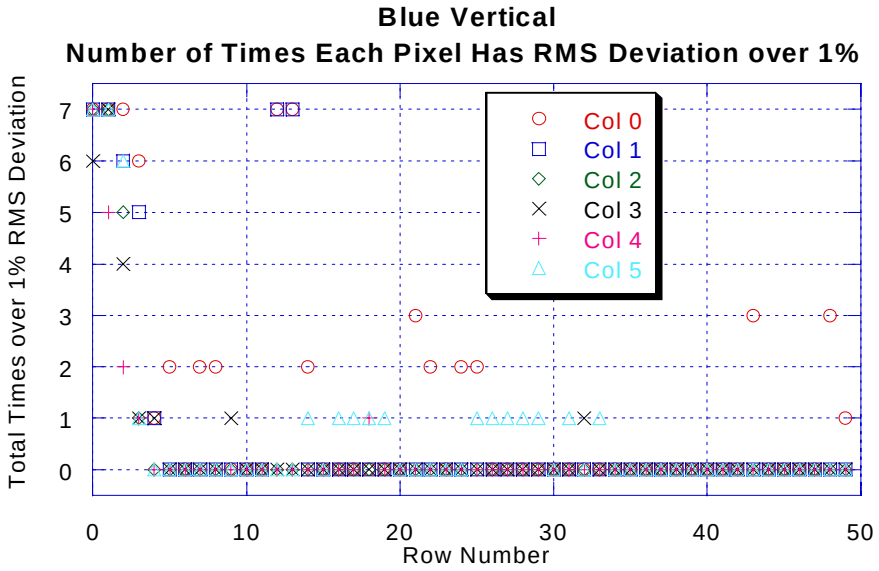

Figure 13-55 Frequency of Blue Vertical Pixels Having RSR with RMS Deviation over 1%

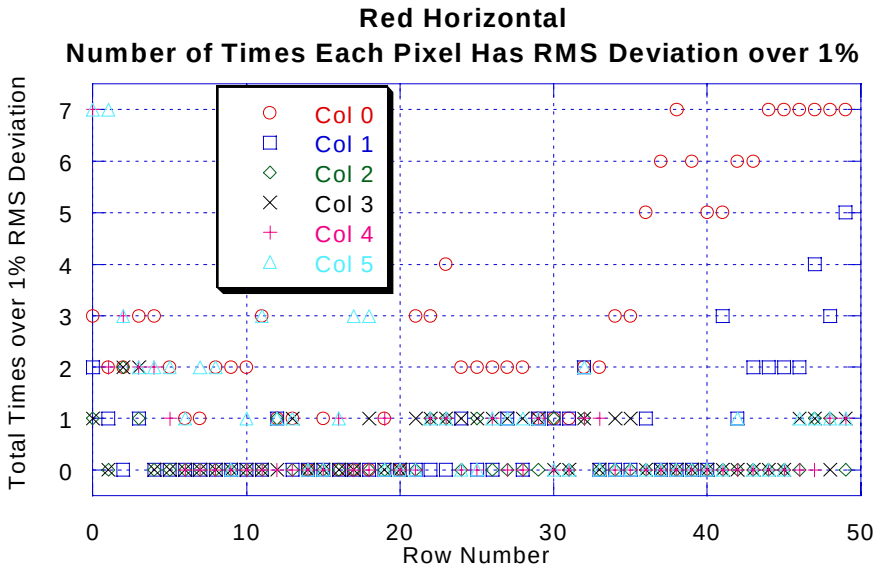

Figure 13-56 Frequency of Red Horizontal Pixels Having RSR with RMS Deviation over 1%

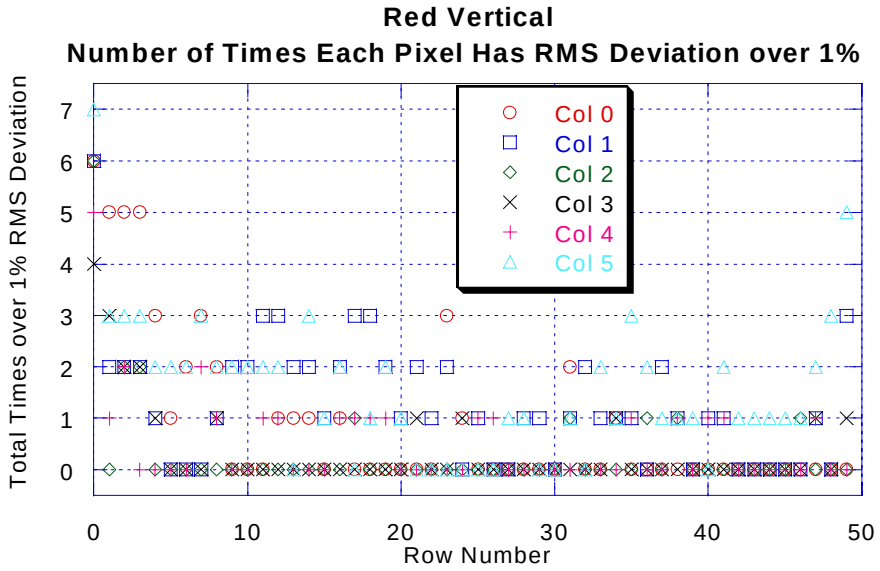

Figure 13-57 Frequency of Red Vertical Pixels Having RSR with RMS Deviation over 1%

While these plots show the detail perhaps better than an image of the SA channel, it is often useful to see this data in image form. Displays were generated of the number of times each pixel has root-mean-square deviation greater than 1%. From these displays, the following conclusions were drawn.

It is clear that the blue horizontal channel has some questionable RSR matches in the corners and on the edges, but fits well in the central region. There are a total of 14 pixels that are fliers for 4 or more temperatures out of 7. If one were to mask out or disregard data from the first few rows of column 0, there would be only 5.

The blue vertical channel has a chip in the fiber ribbon on the left side causing a few poor fits, and the bottom rows are out of family, but the central region fits well. There are a total of 23 pixels that are fliers for 4 or more temperatures out of 7. If one were to mask out or disregard data from the first 3 rows, there would be only 6.

The red horizontal channel column 0 has a number of pixels with out of family response, and several scattered throughout the channel with questionable RSR shape. There are a total of 20 pixels that are fliers for 4 or more temperatures out of 7. If one were to mask out or disregard data from the latter rows of column 0, there would be only 6.

The red vertical channel is similar, with most variations in the bottom and corners. There are a total of 10 pixels that are fliers for 4 or more temperatures out of 7. If one were to mask out or disregard data from the first row, there would be only 4.

Thus, there are specific regions on each SA channel that have RSR shapes that do not match the rest of the arrays. This is largely due to fiber ribbon misalignment on the CCD camera regions. Outside of these specific regions, each channel has 4 to 6 out of family pixels.

13.4.3.9.3 Signal to Noise Ratios of Relative Spectral Response Measurements

The misalignment of the SA fiber ribbon on the CCD array causes pixels that are only partially illuminated. The partial illumination also results in poorer signal levels. It is interesting to note the signal to noise ratio of the measurements, and to fold that noise band back into the analysis.

Any given pixel at a given temperature and wavelength has a known signal level and therefore a known theoretical noise. It is reasonable to say that the measured data fits the model if it matches the model to within this noise value. If the root-mean-square deviation of a pixel at a given temperature is greater than 1%, one can loop through the measurements at every wavelength, testing for the noise level. If the measured data matches the model within the noise, the deviation at that wavelength is defined to be zero. Then one can compute a new root-mean-square deviation for the pixel at that temperature. This gives a bound on how much the incorporation of the noise information can aid the model fidelity figure of merit.

The number of times a given pixel has greater than 1% root-mean-square deviation from the model when the noise is incorporated as described above was plotted in image format and compared with the fliers results.

The results are left largely unchanged. The pixels that are identified as having some out of family shape are classified as such whether noise based error bars are included or not. This is also seen in the deviations with error bars plotted in the detailed results section of this report. While some deviations at some wavelengths can be attributed to noise, there is genuine deviation between the measured data and the modeled results at other wavelengths.

Fortunately the models match the measured data remarkably well over column and temperature, most of the time to within 1%.

13.5 Absolute Responsivity

13.5.1 Introduction

The count rate generated in the Solar Aureole Cameras can be computed with the following equation.

$$Counts/_{\sec}(T,col,row) = Abs(T,col,row)\int_{\lambda} I(\lambda)RSR(T,\lambda,col,row)d\lambda$$

where :

$Counts/_{\sec}$ = Count rate generated in the SA pixels (counts/sec)

T = Temperature of the measurement

col = SA pixel column number

row = SA pixel row number

Abs = Absolute Response of that pixel at that temperature (W/sqm – sr)

I = Input Intensity (W/sqm - sr - μ)

λ = wavelength

RSR = SA Relative Spectral Response at that temperature for that pixel

73.

This section derives the Solar Aureole Absolute Responsivity, Abs(T,col,row).

13.5.2 Approach for Absolute Response Computation at One Temperature

On July 24, 1996 the SA absolute response measurement test was performed with the DISR#3 sensor head in the integrating sphere. A broadband lamp illuminated the integrating sphere, and the calibrated monochromator viewed the sphere as a spectrum analyzer to determine the input intensity. A broadband silicon detector monitored the interior of the sphere throughout.

The derivation of the SA absolute response is given by the following equation.

$$Abs(T,col,row) = \frac{Counts/_{\sec}(T,col,row)}{\int_{\lambda} I(\lambda)RSR(T,\lambda,col,row)d\lambda}$$

where :

$I(\lambda)$ = Input Intensity during the absolute response measurement

74.

13.5.2.1 Count Rate

The absolute response was measured at 31 temperatures in two separate logs listed below. The data sets for temperatures below 260K are in test log *.1, and those for temperatures over 260K are in test log *.4.

/disr3_cal/24Jul96/Log/absresp_cold_24Jul96.1
/disr3_cal/24Jul96/Log/absresp_cold_24Jul96.4

For each one of 31 temperatures, there are six data sets – one each for bright and bright with 0 ms integration time, and two each for dark and dark with 0 ms integration time. The basic integration time was always less than a second, so the electronic shutter effect is significant. The 0 ms integrations remove any electronic shutter effect in the measurement. The two

darks were taken on either side of the bright data sets. The temperature difference between each dark and its bright is under 0.5K, so the two are averaged to form an average dark measurement for each bright. The case at 205.3K is different, and the darks with temperatures closest to the bright are used. For each temperature, all data sets are taken within 90 seconds.

If one sorts the files in the Solar Aureole directory of the log by mission time, one determines the sequence of the data set formation. The sequence numbers identifying the data sets for analysis are in the following table.

Figure 13-58 Sequence Numbers of Data Sets Used in Absolute Responsivity Derivation

Temperature	Bright	Dark #1	Dark #2	Bright, 0ms	Dark, 0ms, #1	Dark, 0ms, #2
171.260	5	0	6	3	2	8
171.390	11	6	12	9	8	14
174.560	20	15	21	18	17	23
175.050	26	21	27	24	23	29
179.440	35	30	36	33	32	38
180.050	41	36	42	39	38	44
186.030	50	45	51	48	47	53
186.390	56	51	57	54	53	59
191.030	65	60	66	63	62	68
191.760	71	66	72	69	68	74
205.300	80	75	none	78	none	77
205.670	86	81	87	84	83	89
209.210	95	90	96	93	92	98
209.690	101	96	102	99	98	104
218.600	110	105	111	108	107	113
219.330	116	111	117	114	113	119
225.800	125	120	126	123	122	128
226.410	131	126	132	129	128	134
233.000	140	135	141	138	137	143
233.480	146	141	147	144	143	149
240.680	155	150	156	153	152	158
241.410	161	156	162	159	158	164
250.080	170	165	171	168	167	173
250.690	176	171	177	174	173	179
260.200	5	0	6	3	2	8
260.450	11	6	12	9	8	14
270.690	20	15	21	18	17	23
270.820	26	21	27	24	23	29
280.820	35	30	36	33	32	38
280.940	41	36	42	39	38	44
289.600	50	45	51	48	47	53

It can be observed that two sets of data were taken at close to the same temperature throughout the test. Averaging the two sets reduces the statistical noise before using them to generate a model. Additionally, including the data sets taken at 186.39K and 191.03K caused

errors in the models, so these data sets are discarded in the model generation. They are included below in the model performance section.

The lamp illuminating the integrating sphere drifts over the course of the calibration and data collection, so normalization must occur. A broadband silicon detector monitored the sphere intensity throughout the test. One can reference all measurements to the intensity at a given time by computing a drift factor as follows.

$$Drift\_Factor(t) = \frac{Si_b(t) - Si_d(t)}{Si_b(t_0) - Si_d(t_0)}$$

$$\begin{aligned} where: & \\ t &= \text{time} \\ t_o &= \text{standard time} \\ Si_b &= \text{Silicon reading at time t, bright} \\ Si_d &= \text{Silicon reading at time t, dark} \end{aligned} \qquad 75.$$

The count rate for a pixel is then computed by the following equation.

$$Counts/\text{sec} = \frac{(Bright - AvgDark) - (Bright0 - AvgDark0)}{\text{exposure time}} * Drift\_factor$$

$$\begin{aligned} where: & \\ Bright &= \text{Data numbers for the bright data set with appropriate exposure time} \\ \text{AvgDark} &= \text{Average data numbers for the dark data sets with same exposure time as bright} \\ \text{Bright0} &= \text{Data numbers for the bright data set with 0ms exposure time} \\ \text{AvgDark0} &= \text{Average data numbers for the dark data sets with 0 ms exposure time} \\ \text{exposure time} &= \text{Time (sec) for the exposures} \end{aligned} \qquad 76.$$

13.5.2.2 Relative Spectral Response

The SA RSR has been derived above. The model SA RSR is used in this analysis for each temperature and pixel.

13.5.2.3 Sphere Intensity

The sphere intensity must now be computed before the absolute response can be derived. The following equation is used.

$$I(\lambda, r, c) = \frac{1}{2}\frac{Mono(\lambda)}{C(\lambda)} * Drift\_factor * \frac{rb(r,c)}{0.987988} \qquad (77.)$$

where:

I = Sphere intensity (W/sqm – μ – sr) at wavelength λ and location in the sphere viewed by pixel at row r and column c

Mono = Monochromator reading for a given wavelength (Amps)

C = Monochromator calibration function (Amps/(W/sqm - μ - sr))

rb(r, c) = Brightness of integrating sphere at the location viewed by pixel at row r and column c relative to the brightness at the front of the integrating sphere

0.987988 = Relative brightness (rb) at location viewed by the monochromator

The factor of one-half in the equation is because the monochromator responds to all polarization states in the sphere, but the intensity entering each SA channel is that in one polarization state alone. The monochromator calibration function, C(λ), in units of Amps/(W/sqm-μ-sr), is in the file /local/cal.cal/Si_resp_5_5_5ap_dry_new.txt. The lamp drift must also be included. No dark values are available during the monochromator scan of the sphere, so the standard reference dark measurement is used. The integrating sphere spatial structure is included in the relative brightness ratio, rb/0.987988.

The four tables below give rb(r,c) for every pixel in the Solar Aureole.

Table 13-19 Relative Brightness at the Location of Blue Horizontal Pixel to the Brightness at the Front of the Integrating Sphere

Row	Col 0	Col 1	Col 2	Col 3	Col 4	Col 5
0	0.9813	0.9804	0.9792	0.9781	0.9772	0.9764
1	0.9817	0.9805	0.9792	0.9782	0.9775	0.9771
2	0.9814	0.9802	0.9790	0.9783	0.9780	0.9779
3	0.9807	0.9797	0.9789	0.9787	0.9786	0.9785
4	0.9801	0.9795	0.9792	0.9791	0.9789	0.9786
5	0.9799	0.9795	0.9792	0.9789	0.9785	0.9782
6	0.9798	0.9794	0.9789	0.9783	0.9778	0.9775
7	0.9794	0.9792	0.9788	0.9781	0.9774	0.9770
8	0.9790	0.9791	0.9789	0.9783	0.9775	0.9770
9	0.9786	0.9791	0.9794	0.9787	0.9779	0.9775
10	0.9788	0.9797	0.9800	0.9794	0.9787	0.9784
11	0.9797	0.9806	0.9809	0.9804	0.9800	0.9800
12	0.9810	0.9818	0.9820	0.9819	0.9820	0.9825
13	0.9825	0.9833	0.9838	0.9843	0.9850	0.9858
14	0.9843	0.9851	0.9859	0.9870	0.9879	0.9885
15	0.9866	0.9872	0.9878	0.9880	0.9887	0.9899
16	0.9889	0.9893	0.9898	0.9902	0.9902	0.9899
17	0.9910	0.9911	0.9915	0.9923	0.9925	0.9923
18	0.9926	0.9926	0.9929	0.9938	0.9945	0.9944
19	0.9937	0.9937	0.9940	0.9948	0.9957	0.9961
20	0.9944	0.9946	0.9948	0.9955	0.9964	0.9972
21	0.9950	0.9951	0.9954	0.9959	0.9968	0.9977
22	0.9954	0.9955	0.9957	0.9961	0.9969	0.9977
23	0.9959	0.9960	0.9961	0.9963	0.9968	0.9976
24	0.9965	0.9965	0.9965	0.9966	0.9970	0.9975
25	0.9971	0.9970	0.9969	0.9969	0.9971	0.9975
26	0.9979	0.9975	0.9973	0.9972	0.9973	0.9975
27	0.9986	0.9982	0.9978	0.9976	0.9975	0.9976
28	0.9993	0.9990	0.9985	0.9980	0.9978	0.9978
29	1.0000	0.9997	0.9992	0.9986	0.9982	0.9980
30	1.0007	1.0004	0.9999	0.9993	0.9987	0.9984
31	1.0013	1.0010	1.0006	1.0000	0.9993	0.9989
32	1.0018	1.0016	1.0012	1.0006	1.0000	0.9995
33	1.0023	1.0022	1.0018	1.0013	1.0007	1.0001
34	1.0028	1.0028	1.0025	1.0020	1.0014	1.0008
35	1.0034	1.0034	1.0032	1.0027	1.0021	1.0016
36	1.0040	1.0040	1.0039	1.0035	1.0030	1.0024
37	1.0045	1.0046	1.0045	1.0043	1.0038	1.0033
38	1.0051	1.0053	1.0052	1.0050	1.0047	1.0042
39	1.0056	1.0059	1.0059	1.0057	1.0055	1.0051
40	1.0061	1.0065	1.0065	1.0064	1.0062	1.0060
41	1.0064	1.0069	1.0071	1.0071	1.0069	1.0067
42	1.0070	1.0074	1.0076	1.0077	1.0076	1.0075
43	1.0078	1.0083	1.0085	1.0085	1.0084	1.0082
44	1.0088	1.0094	1.0096	1.0096	1.0094	1.0091
45	1.0096	1.0103	1.0107	1.0107	1.0104	1.0099
46	1.0101	1.0110	1.0115	1.0115	1.0111	1.0102
47	1.0102	1.0112	1.0117	1.0117	1.0110	1.0098
48	1.0097	1.0108	1.0113	1.0111	1.0102	1.0091
49	1.0089	1.0099	1.0102	1.0099	1.0091	1.0084

Table 13-20 Relative Brightness at the Location of Blue Vertical Pixel to the Brightness at the Front of the Integrating Sphere

Row	Col 6	Col 7	Col 8	Col 9	Col 10	Col 11
0	0.9777	0.9772	0.9766	0.9758	0.9748	0.9738
1	0.9792	0.9786	0.9778	0.9769	0.9759	0.9749
2	0.9805	0.9796	0.9786	0.9776	0.9766	0.9757
3	0.9812	0.9800	0.9788	0.9778	0.9770	0.9764
4	0.9812	0.9798	0.9787	0.9780	0.9775	0.9772
5	0.9806	0.9794	0.9786	0.9783	0.9781	0.9781
6	0.9800	0.9792	0.9789	0.9788	0.9787	0.9786
7	0.9797	0.9794	0.9792	0.9790	0.9787	0.9784
8	0.9797	0.9793	0.9789	0.9785	0.9781	0.9779
9	0.9794	0.9791	0.9785	0.9779	0.9774	0.9773
10	0.9792	0.9790	0.9785	0.9777	0.9771	0.9770
11	0.9791	0.9791	0.9787	0.9779	0.9772	0.9771
12	0.9792	0.9795	0.9793	0.9784	0.9778	0.9777
13	0.9798	0.9803	0.9800	0.9793	0.9789	0.9789
14	0.9809	0.9813	0.9811	0.9807	0.9806	0.9810
15	0.9823	0.9827	0.9827	0.9829	0.9834	0.9840
16	0.9839	0.9845	0.9852	0.9859	0.9866	0.9871
17	0.9859	0.9866	0.9874	0.9881	0.9890	0.9892
18	0.9881	0.9885	0.9887	0.9890	0.9896	0.9903
19	0.9901	0.9905	0.9911	0.9910	0.9906	0.9908
20	0.9918	0.9921	0.9929	0.9933	0.9931	0.9926
21	0.9932	0.9934	0.9941	0.9950	0.9951	0.9948
22	0.9941	0.9944	0.9950	0.9959	0.9966	0.9964
23	0.9948	0.9951	0.9956	0.9965	0.9974	0.9976
24	0.9953	0.9955	0.9960	0.9968	0.9977	0.9983
25	0.9957	0.9958	0.9962	0.9968	0.9977	0.9984
26	0.9962	0.9962	0.9964	0.9969	0.9976	0.9983
27	0.9967	0.9967	0.9968	0.9970	0.9975	0.9982
28	0.9972	0.9971	0.9970	0.9972	0.9975	0.9981
29	0.9978	0.9975	0.9974	0.9973	0.9976	0.9980
30	0.9985	0.9981	0.9977	0.9976	0.9977	0.9980
31	0.9992	0.9987	0.9982	0.9979	0.9978	0.9981
32	1.0000	0.9994	0.9988	0.9983	0.9981	0.9982
33	1.0006	1.0001	0.9995	0.9989	0.9986	0.9984
34	1.0013	1.0008	1.0001	0.9995	0.9991	0.9987
35	1.0018	1.0014	1.0008	1.0001	0.9996	0.9991
36	1.0025	1.0020	1.0014	1.0008	1.0003	0.9997
37	1.0031	1.0027	1.0022	1.0015	1.0010	1.0005
38	1.0037	1.0035	1.0030	1.0023	1.0018	1.0013
39	1.0043	1.0041	1.0038	1.0032	1.0027	1.0022
40	1.0050	1.0048	1.0046	1.0041	1.0036	1.0031
41	1.0057	1.0055	1.0053	1.0050	1.0045	1.0041
42	1.0063	1.0063	1.0060	1.0058	1.0055	1.0051
43	1.0069	1.0069	1.0068	1.0066	1.0063	1.0061
44	1.0074	1.0075	1.0074	1.0073	1.0071	1.0070
45	1.0083	1.0083	1.0082	1.0080	1.0079	1.0078
46	1.0094	1.0095	1.0093	1.0090	1.0087	1.0085
47	1.0105	1.0106	1.0104	1.0100	1.0094	1.0089
48	1.0113	1.0115	1.0113	1.0105	1.0095	1.0090
49	1.0116	1.0118	1.0113	1.0102	1.0092	1.0090

Table 13-21 Relative Brightness at the Location of Red Vertical Pixel to the Brightness at the Front of the Integrating Sphere

Row	Col 12	Col 13	Col 14	Col 15	Col 16	Col 17
0	0.9735	0.9737	0.9737	0.9734	0.9727	0.9719
1	0.9755	0.9754	0.9751	0.9745	0.9738	0.9729
2	0.9772	0.9768	0.9764	0.9758	0.9750	0.9741
3	0.9787	0.9783	0.9777	0.9770	0.9762	0.9752
4	0.9802	0.9796	0.9789	0.9780	0.9770	0.9761
5	0.9814	0.9806	0.9796	0.9785	0.9775	0.9766
6	0.9820	0.9809	0.9797	0.9787	0.9777	0.9770
7	0.9818	0.9807	0.9795	0.9785	0.9779	0.9775
8	0.9811	0.9801	0.9791	0.9786	0.9784	0.9783
9	0.9804	0.9796	0.9792	0.9790	0.9789	0.9787
10	0.9800	0.9796	0.9793	0.9791	0.9789	0.9786
11	0.9798	0.9795	0.9792	0.9787	0.9783	0.9780
12	0.9796	0.9793	0.9789	0.9783	0.9777	0.9773
13	0.9792	0.9791	0.9789	0.9783	0.9775	0.9770
14	0.9788	0.9791	0.9792	0.9786	0.9777	0.9772
15	0.9787	0.9794	0.9796	0.9791	0.9783	0.9778
16	0.9794	0.9801	0.9805	0.9800	0.9793	0.9790
17	0.9806	0.9813	0.9815	0.9811	0.9807	0.9808
18	0.9821	0.9827	0.9829	0.9830	0.9833	0.9838
19	0.9838	0.9845	0.9851	0.9858	0.9865	0.9870
20	0.9859	0.9865	0.9871	0.9875	0.9885	0.9893
21	0.9883	0.9886	0.9890	0.9891	0.9893	0.9897
22	0.9904	0.9905	0.9911	0.9914	0.9912	0.9909
23	0.9922	0.9921	0.9926	0.9933	0.9935	0.9932
24	0.9934	0.9934	0.9938	0.9946	0.9953	0.9952
25	0.9943	0.9944	0.9947	0.9955	0.9964	0.9967
26	0.9949	0.9950	0.9953	0.9960	0.9969	0.9976
27	0.9954	0.9955	0.9957	0.9963	0.9971	0.9980
28	0.9958	0.9959	0.9960	0.9964	0.9971	0.9980
29	0.9963	0.9963	0.9964	0.9966	0.9971	0.9979
30	0.9969	0.9968	0.9968	0.9969	0.9972	0.9978
31	0.9975	0.9973	0.9971	0.9971	0.9973	0.9977
32	0.9982	0.9978	0.9975	0.9974	0.9974	0.9977
33	0.9990	0.9985	0.9980	0.9977	0.9976	0.9978
34	0.9997	0.9992	0.9986	0.9982	0.9979	0.9980
35	1.0004	0.9999	0.9993	0.9987	0.9983	0.9982
36	1.0010	1.0006	1.0000	0.9993	0.9988	0.9986
37	1.0016	1.0012	1.0006	0.9999	0.9994	0.9990
38	1.0021	1.0018	1.0012	1.0006	1.0000	0.9995
39	1.0027	1.0024	1.0019	1.0013	1.0007	1.0002
40	1.0033	1.0031	1.0026	1.0020	1.0014	1.0009
41	1.0039	1.0038	1.0034	1.0028	1.0022	1.0017
42	1.0046	1.0044	1.0041	1.0036	1.0031	1.0026
43	1.0052	1.0051	1.0048	1.0045	1.0040	1.0035
44	1.0058	1.0058	1.0055	1.0053	1.0049	1.0044
45	1.0064	1.0065	1.0063	1.0060	1.0057	1.0054
46	1.0069	1.0070	1.0070	1.0068	1.0065	1.0063
47	1.0075	1.0076	1.0076	1.0074	1.0073	1.0071
48	1.0084	1.0084	1.0083	1.0082	1.0080	1.0079
49	1.0095	1.0096	1.0094	1.0092	1.0089	1.0086

Table 13-22 Relative Brightness at the Location of Red Horizontal Pixel to the Brightness at the Front of the Integrating Sphere

Row	Col 18	Col 19	Col 20	Col 21	Col 22	Col 23
0	0.9787	0.9782	0.9775	0.9767	0.9758	0.9749
1	0.9800	0.9793	0.9785	0.9775	0.9766	0.9757
2	0.9810	0.9800	0.9789	0.9779	0.9771	0.9764
3	0.9814	0.9801	0.9790	0.9781	0.9774	0.9770
4	0.9811	0.9799	0.9788	0.9782	0.9779	0.9778
5	0.9805	0.9795	0.9788	0.9786	0.9786	0.9785
6	0.9800	0.9794	0.9791	0.9790	0.9789	0.9787
7	0.9798	0.9795	0.9792	0.9789	0.9786	0.9783
8	0.9797	0.9794	0.9789	0.9784	0.9779	0.9776
9	0.9795	0.9792	0.9788	0.9781	0.9775	0.9771
10	0.9792	0.9790	0.9789	0.9781	0.9774	0.9770
11	0.9789	0.9791	0.9791	0.9785	0.9777	0.9773
12	0.9789	0.9795	0.9797	0.9791	0.9784	0.9780
13	0.9794	0.9802	0.9805	0.9800	0.9795	0.9794
14	0.9805	0.9813	0.9815	0.9812	0.9811	0.9814
15	0.9819	0.9827	0.9830	0.9832	0.9838	0.9845
16	0.9835	0.9843	0.9851	0.9859	0.9868	0.9875
17	0.9856	0.9863	0.9871	0.9876	0.9885	0.9895
18	0.9879	0.9883	0.9888	0.9891	0.9894	0.9895
19	0.9901	0.9902	0.9908	0.9914	0.9914	0.9912
20	0.9919	0.9919	0.9923	0.9931	0.9937	0.9935
21	0.9932	0.9932	0.9935	0.9943	0.9952	0.9955
22	0.9941	0.9942	0.9944	0.9951	0.9960	0.9968
23	0.9947	0.9948	0.9951	0.9956	0.9965	0.9974
24	0.9952	0.9953	0.9955	0.9959	0.9967	0.9976
25	0.9957	0.9957	0.9958	0.9961	0.9967	0.9975
26	0.9962	0.9962	0.9962	0.9964	0.9968	0.9974
27	0.9968	0.9967	0.9967	0.9967	0.9970	0.9974
28	0.9975	0.9973	0.9971	0.9971	0.9971	0.9974
29	0.9983	0.9979	0.9976	0.9974	0.9974	0.9975
30	0.9990	0.9987	0.9982	0.9979	0.9977	0.9976
31	0.9997	0.9994	0.9989	0.9984	0.9981	0.9979
32	1.0004	1.0001	0.9997	0.9991	0.9986	0.9983
33	1.0010	1.0008	1.0004	0.9998	0.9992	0.9988
34	1.0015	1.0014	1.0011	1.0005	0.9999	0.9994
35	1.0020	1.0020	1.0017	1.0012	1.0006	1.0000
36	1.0026	1.0026	1.0023	1.0018	1.0013	1.0007
37	1.0031	1.0031	1.0030	1.0026	1.0020	1.0014
38	1.0036	1.0037	1.0036	1.0033	1.0028	1.0023
39	1.0042	1.0043	1.0043	1.0041	1.0037	1.0032
40	1.0047	1.0050	1.0049	1.0048	1.0045	1.0041
41	1.0052	1.0056	1.0056	1.0055	1.0053	1.0050
42	1.0057	1.0061	1.0063	1.0062	1.0060	1.0058
43	1.0060	1.0066	1.0069	1.0069	1.0068	1.0066
44	1.0065	1.0070	1.0074	1.0075	1.0074	1.0073
45	1.0072	1.0078	1.0081	1.0082	1.0082	1.0081
46	1.0081	1.0088	1.0092	1.0093	1.0092	1.0091
47	1.0090	1.0098	1.0103	1.0105	1.0104	1.0101
48	1.0095	1.0105	1.0112	1.0114	1.0113	1.0107
49	1.0095	1.0107	1.0115	1.0118	1.0116	1.0106

13.5.2.4 Computation of SA Absolute Response

The SA absolute response is then computed for every pixel at every temperature. This is the true, measured absolute response of the Solar Aureole.

13.5.3 Thermal Modeling

13.5.3.1 Mean Absolute Response

Because the absolute response varies with temperature, it is helpful to have a thermal model. As a base for the model, the mean absolute response for each channel is computed versus CCD chip temperature, and it is fit with a fifth or sixth order polynomial. Column 0 is excluded from the mean because it lies at the edge of the fiber ribbon illumination and is impacted by mechanical changes with temperature that are different from the rest of the array. Creating a thermal model using the detector temperature for the mean and initial pixel map derivation, but using the optics temperature for pixel-to-pixel variations over temperature (which makes more physical intuitive sense), resulted in a model with poorer performance than just using CCD temperature. The pixel-to-pixel variation with temperature is likely due to thermal variance of the separation between the CCD and the fiber ribbon, which is better modeled by the CCD temperature than the optics temperature since that temperature sensor is closer than the one on the optical bench.

The results are in the following plot and table.

Table 13-23 Polynomial Coefficients for the Mean Absolute Response versus CCD Temperature

	Blue Horizontal	Blue Vertical	Red Horizontal	Red Vertical
A0	-1.320628900000e+8	-1.043157230000e+8	-6.342293175000e+7	-4.764707846875e+7
A1	3.439118281250e+6	2.708450062500e+6	1.392982078125e+6	1.053106603516e+6
A2	-3.693190771484e+4	-2.898806738281e+4	-1.200406482697e+4	-9.126064826965e+3
A3	2.100620784760e+2	1.643101100922e+2	5.120302107930e+1	3.914550912380e+1
A4	-6.678061112761e-1	-5.205441340804e-1	-1.080477217911e-1	-8.309265802382e-2
A5	1.125490496634e-3	8.742839563638e-4	9.032962566380e-5	6.989951356218e-5
A6	-7.858712436359e-7	-6.084150783181e-7	0.000000000000e+0	0.000000000000e+0

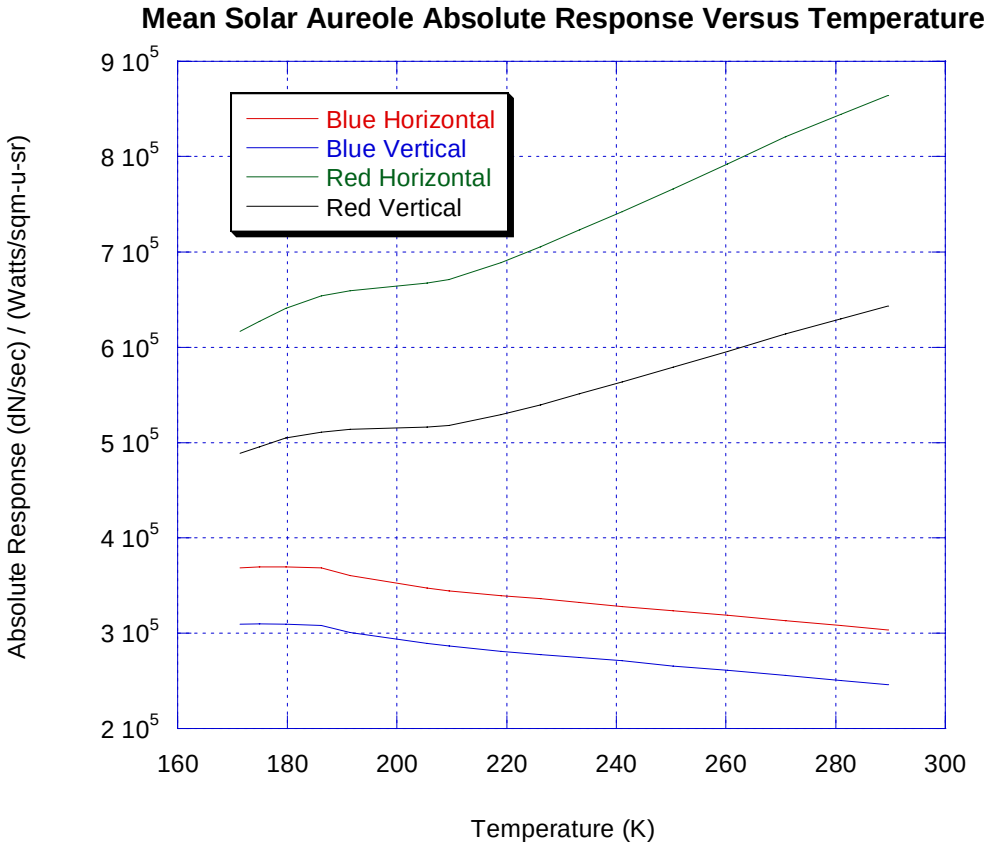

Figure 13-59 Mean Absolute Response versus Temperature

13.5.3.2 Pixel Maps

The next step in the generation of a thermal model is the formation of a pixel map at the coldest temperature. This map is the computed absolute response from the previous sections divided by the polynomial fit at the coldest temperature. This map then represents the pixel-to-pixel variations.

$$Map(col,row) = \frac{Abs(T_0,col,row)}{A0 + A1*T_0 + A2*T_0^2 + A3*T_0^3 + A4*T_0^4 + A5*T_0^5 + A6*T_0^6} \qquad 78.$$

13.5.3.3 Thermal Variation in Pixel Maps

If the pixel-to-pixel variations were thermally invariant, one could then compute the absolute response of any pixel at any temperature by the following equation.

$$Abs(T,col,row) = Map(col,row)* \left(A0 + A1*T_0 + A2*T_0^2 + A3*T_0^3 + A4*T_0^4 + A5*T_0^5 + A6*T_0^6\right) \qquad 79.$$

Unfortunately, this is not the case. The pixel-to-pixel variations do vary also with temperature. Several physical mechanisms may be contributing to this variation, but one effect is that the separation between the fiber ribbon bundle and the CCD appears to vary slightly with temperature.

The pixel-to-pixel variation with temperature is modeled by an additional set of polynomial coefficients for each pixel in the map. Two temperatures were considered in this polynomial fit – the detector temperature and the optics temperature. The detector temperature yields the better performance, probably because the detector temperature sensor is closer to the gap between the fiber ribbon and CCD and thus models the temperature of that gap more accurately. In this way, the absolute response for any pixel at any temperature can be computed by the following equation.

$$\begin{aligned} Abs(T,col,row) = Map(col,row) * \\ (p0(col,row) + p1(col,row) * T + p2(col,row) * T^2 + p3(col,row) * T^3) * \\ \left(A0 + A1 * T_0 + A2 * T_0^2 + A3 * T_0^3 + A4 * T_0^4 + A5 * T_0^5 + A6 * T_0^6\right) \end{aligned} \quad 80.$$

This equation can be simplified by multiplying the Map and the "p" polynomial coefficients to result in the final model for the thermal variation of the absolute response.

$$\begin{aligned} Abs(T,col,row) = \left(M0(col,row) + M1(col,row) * T + M2(col,row) * T^2 + M3(col,row) * T^3\right) * \\ \left(A0 + A1 * T_0 + A2 * T_0^2 + A3 * T_0^3 + A4 * T_0^4 + A5 * T_0^5 + A6 * T_0^6\right) \end{aligned} \quad 81.$$

The "M" coefficients for the thermal variation of the pixel map are in the tables in the main body of this document.

13.5.4 Model Results

A figure of merit for the thermal model is the model divided by the true absolute response.

Before applying this figure of merit to the model, the measurement uncertainty can be incorporated in the analysis by applying the theoretical signal to noise ratio for the original measurements of the absolute response. The measured "value" is actually a measured "band" consisting of the value plus and minus the noise. The model matches the measured absolute response if it falls within the band defined by the true absolute response and the measurement noise. The following table lists the portion of modeled pixels and temperatures (6*50*31 total samples for each channel) that match the measured values to within the measurement noise.

Table 13-24 Portion of Modeled Data that Match Measured to within Noise

Blue Horizontal	Blue Vertical	Red Horizontal	Red Vertical
0.7045	0.7191	0.6043	0.6135

If one then adds an error band to the model to find the portion of the pixels that lie within a given percentage of the noise banded measured data, one gets the following plots. (Figs 13_5_4_A thru 13_5_4_M). The plots show the model performance overall, as well as broken out by column and by temperature. In the blue channels, 96% of the pixel/temperature

combinations using the model are within 1% of the measured absolute response, and over 99% of the modeled pixels are within 1.7% of the measured data. In the red channels, over 99% are within 1%, and all are within 1.5%.

In most cases, no particular column or temperature is worse performing than the others. However, in the blue channels, the data at 186K is not well modeled. There are two measurements at 186K, but they do not match the models well. The red horizontal column 0 is also poorly modeled.

Figures 13.5.4A through 15.5.4M...

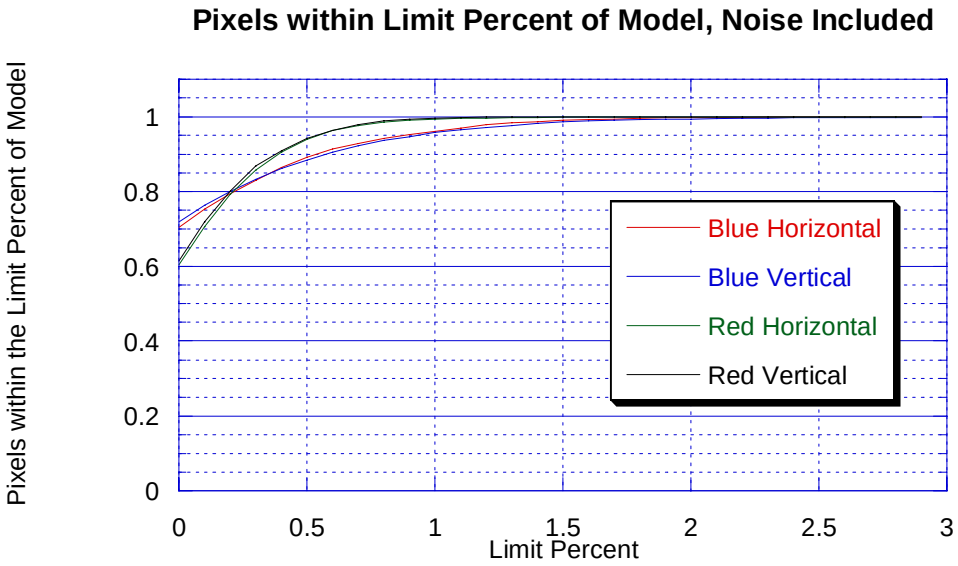

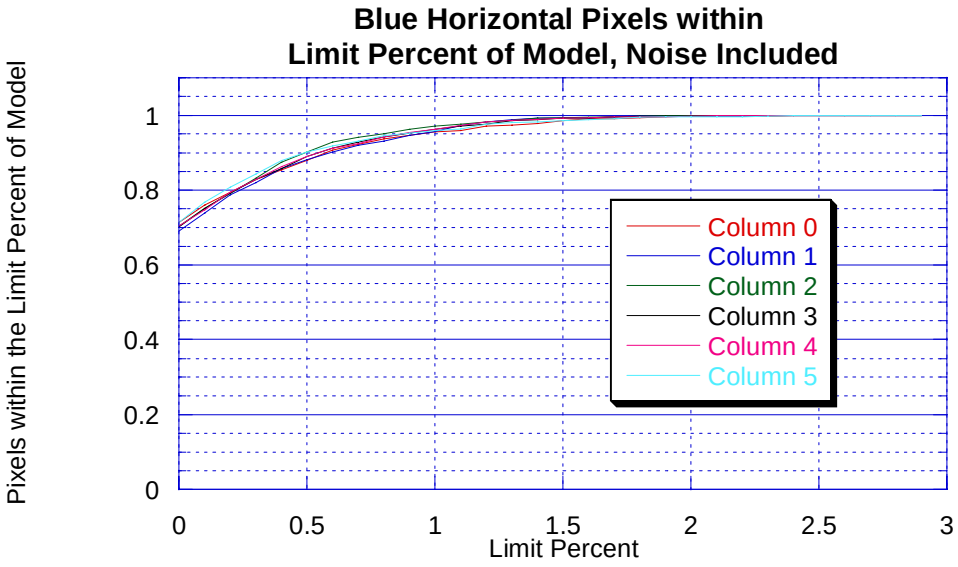

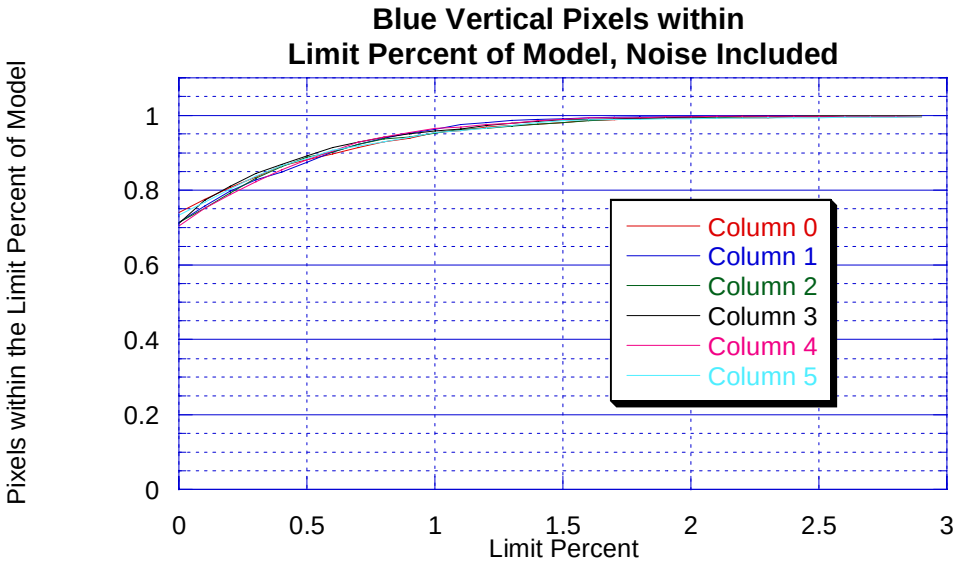
Blue Vertical Pixels within
Limit Percent of Model, Noise Included
Pixels within the Limit Percent of Model
Limit Percent
0
0.2
0.4
0.6
0.8
1
0
0.5
1
1.5
2
2.5
3
Column 0
Column 1
Column 2
Column 3
Column 4
Column 5

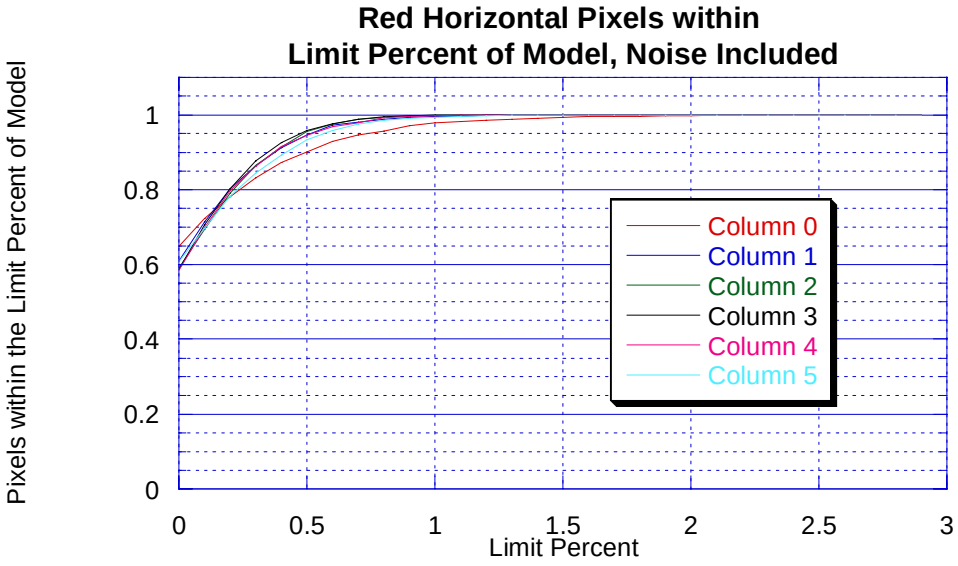
Red Horizontal Pixels within
Limit Percent of Model, Noise Included
Pixels within the Limit Percent of Model
Limit Percent
0
0.2
0.4
0.6
0.8
1
0
0.5
1
1.5
2
2.5
3
Column 0
Column 1
Column 2
Column 3
Column 4
Column 5

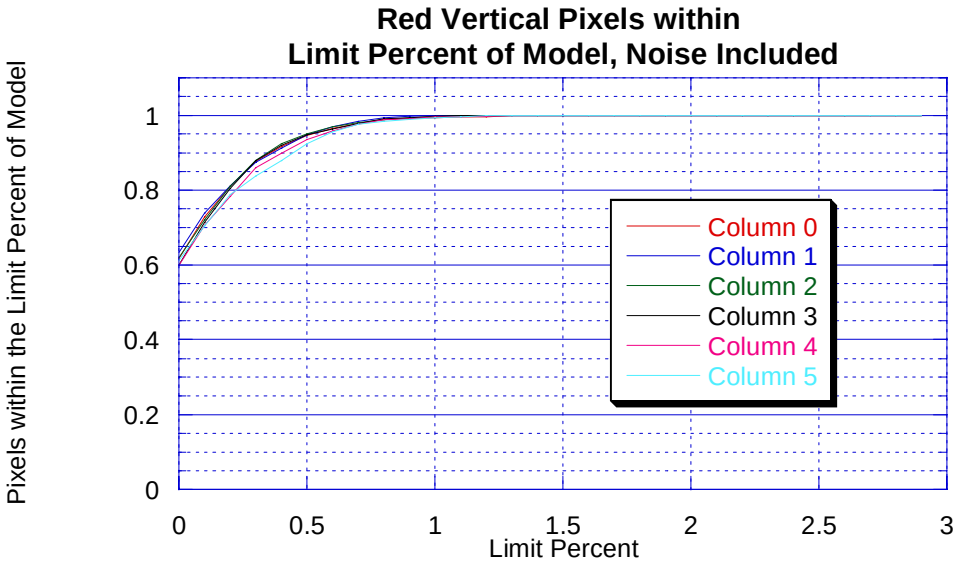
Red Vertical Pixels within
Limit Percent of Model, Noise Included
Pixels within the Limit Percent of Model
Limit Percent
0
0.2
0.4
0.6
0.8
1
0
0.5
1
1.5
2
2.5
3
Column 0
Column 1
Column 2
Column 3
Column 4
Column 5

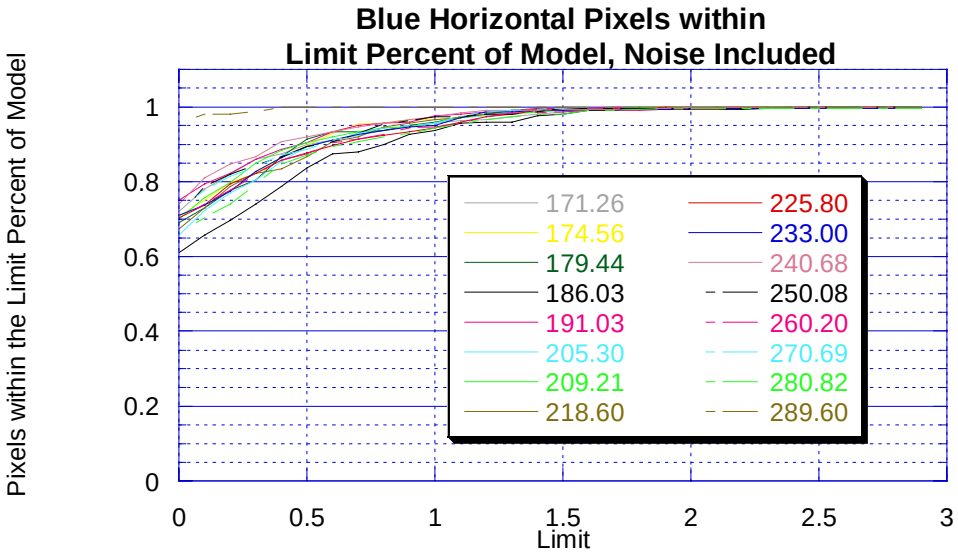
Blue Horizontal Pixels within
Limit Percent of Model, Noise Included
Pixels within the Limit Percent of Model
Limit
0
0.2
0.4
0.6
0.8
1
0
0.5
1
1.5
2
2.5
3
171.26
174.56
179.44
186.03
191.03
205.30
209.21
218.60
225.80
233.00
240.68
250.08
260.20
270.69
280.82
289.60

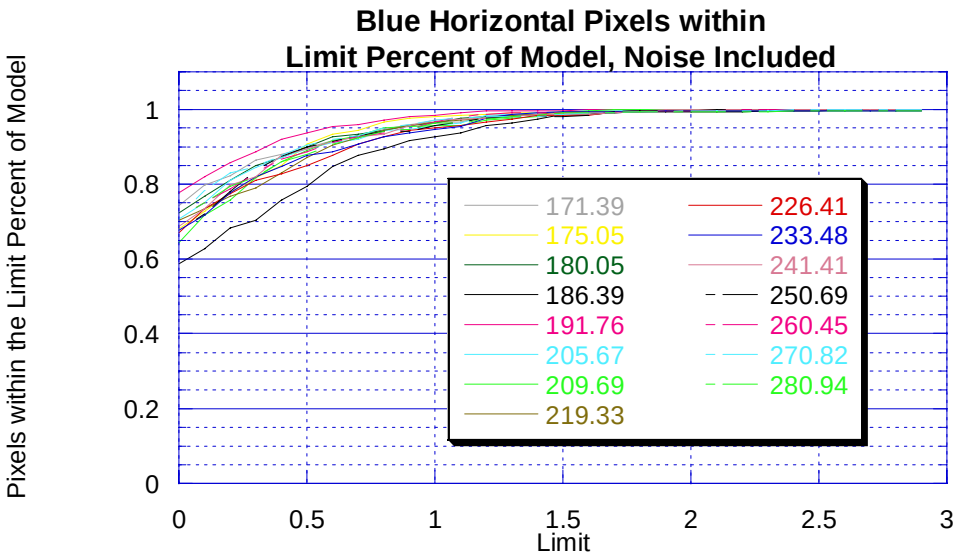
Blue Horizontal Pixels within
Limit Percent of Model, Noise Included
Pixels within the Limit Percent of Model
Limit
0
0.2
0.4
0.6
0.8
1
0
0.5
1
1.5
2
2.5
3
171.39
175.05
180.05
186.39
191.76
205.67
209.69
219.33
226.41
233.48
241.41
250.69
260.45
270.82
280.94

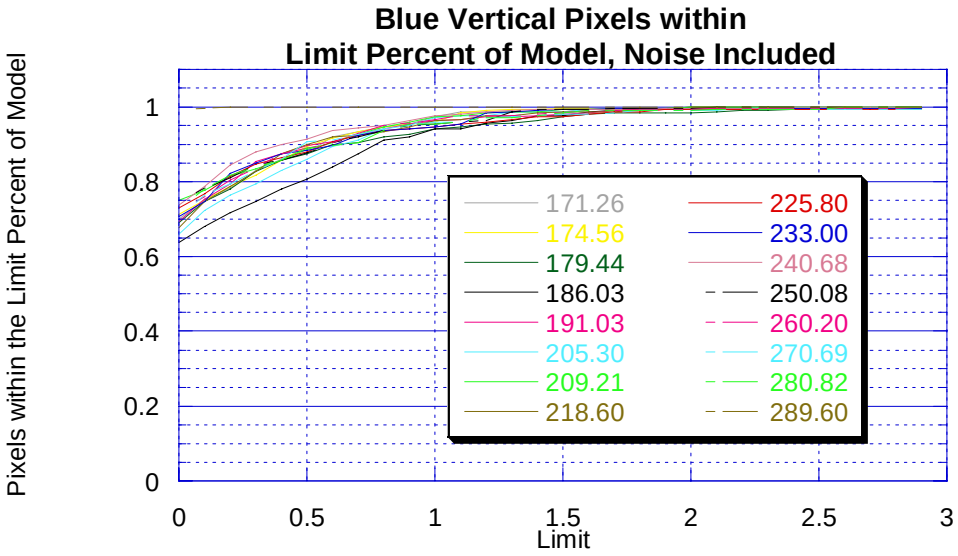
Blue Vertical Pixels within
Limit Percent of Model, Noise Included
Pixels within the Limit Percent of Model
Limit
0
0.2
0.4
0.6
0.8
1
0
0.5
1
1.5
2
2.5
3
171.26
174.56
179.44
186.03
191.03
205.30
209.21
218.60
225.80
233.00
240.68
250.08
260.20
270.69
280.82
289.60

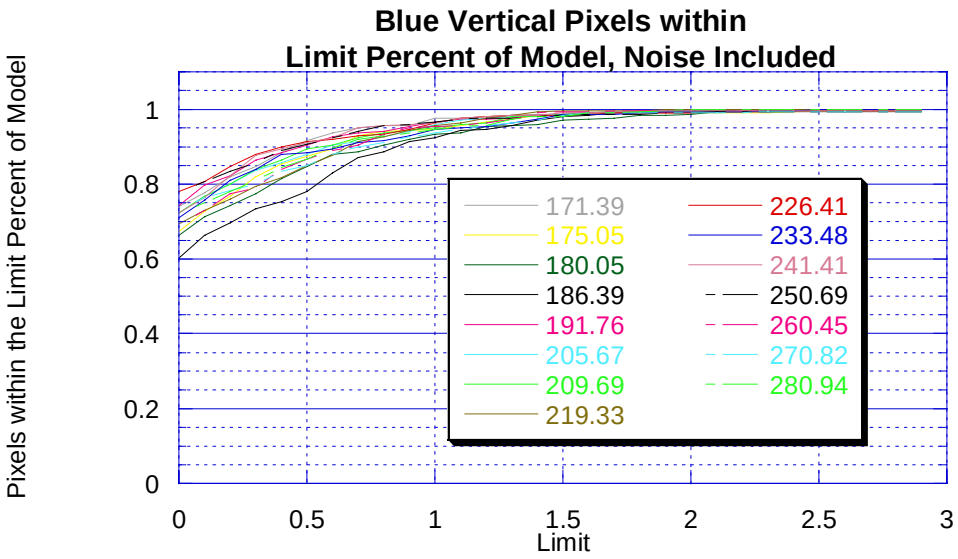
Blue Vertical Pixels within
Limit Percent of Model, Noise Included
Pixels within the Limit Percent of Model
Limit
0
0.2
0.4
0.6
0.8
1
0
0.5
1
1.5
2
2.5
3
171.39
175.05
180.05
186.39
191.76
205.67
209.69
219.33
226.41
233.48
241.41
250.69
260.45
270.82
280.94

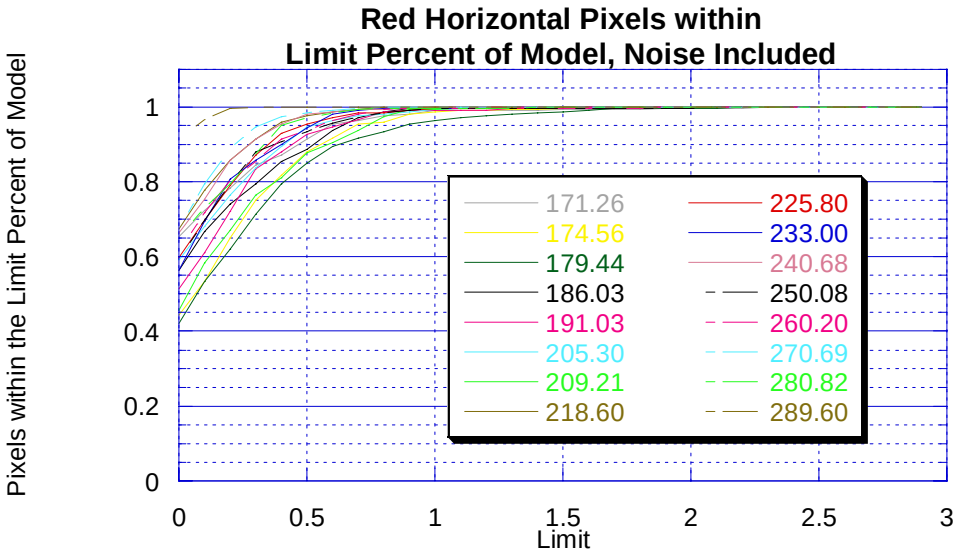
Red Horizontal Pixels within
Limit Percent of Model, Noise Included
Pixels within the Limit Percent of Model
Limit
0
0.2
0.4
0.6
0.8
1
0
0.5
1
1.5
2
2.5
3
171.26
174.56
179.44
186.03
191.03
205.30
209.21
218.60
225.80
233.00
240.68
250.08
260.20
270.69
280.82
289.60

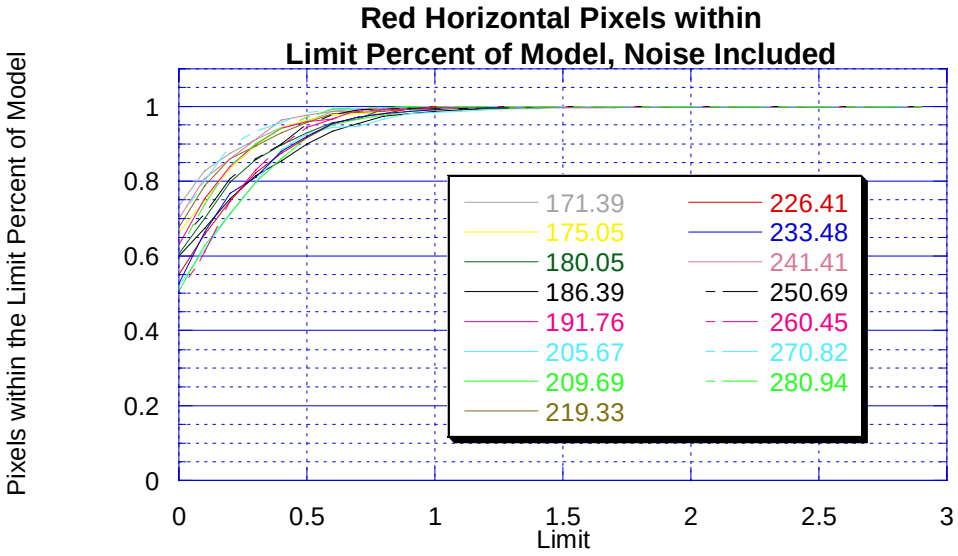
Red Horizontal Pixels within
Limit Percent of Model, Noise Included
Pixels within the Limit Percent of Model
Limit
0
0.2
0.4
0.6
0.8
1
0
0.5
1
1.5
2
2.5
3
171.39
175.05
180.05
186.39
191.76
205.67
209.69
219.33
226.41
233.48
241.41
250.69
260.45
270.82
280.94

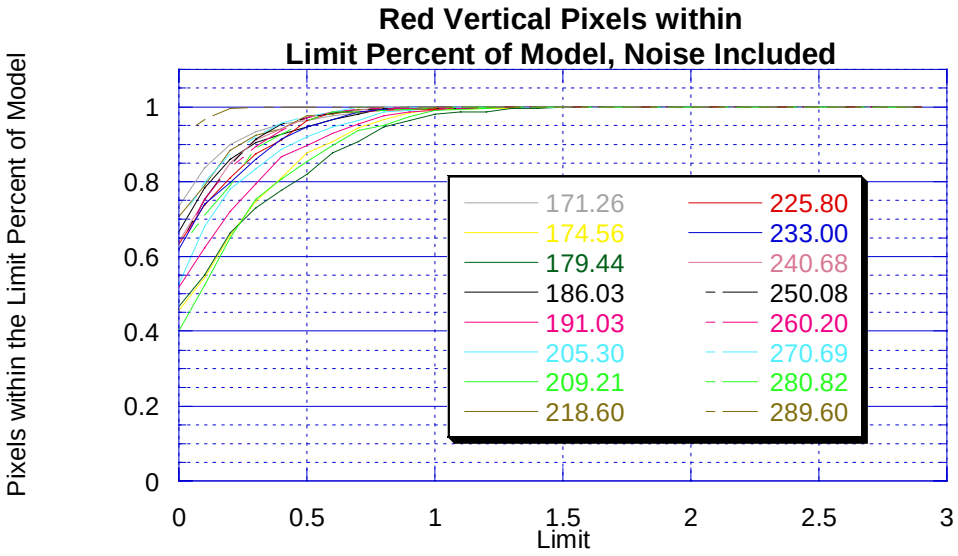
Red Vertical Pixels within
Limit Percent of Model, Noise Included
Pixels within the Limit Percent of Model
Limit
0
0.2
0.4
0.6
0.8
1
0
0.5
1
1.5
2
2.5
3
171.26
174.56
179.44
186.03
191.03
205.30
209.21
218.60
225.80
233.00
240.68
250.08
260.20
270.69
280.82
289.60

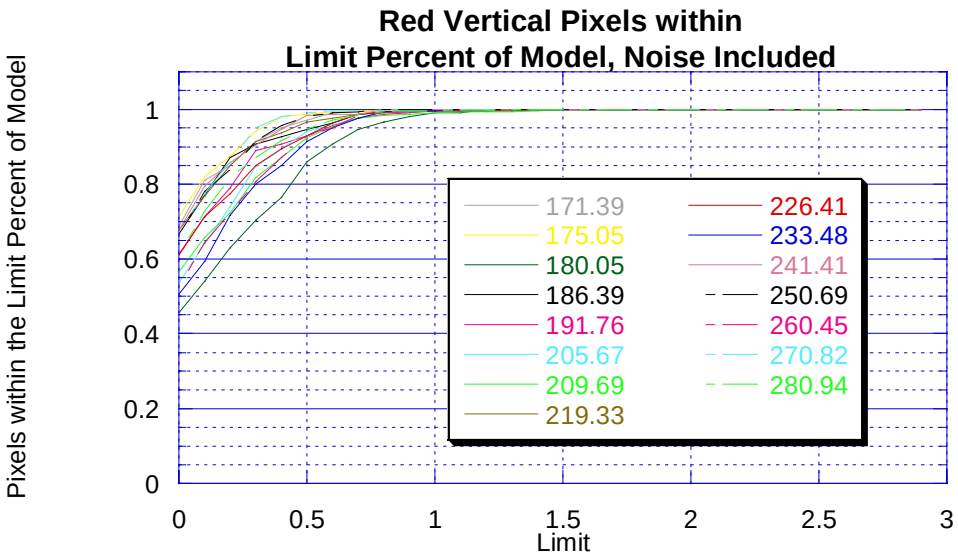

Following are four plots (Figs 13.5.4 N thru Q) of the root-mean-square deviation over temperature of the model from the measured absolute response, divided by the average response over temperature, for every pixel in each SA camera. For each plot the legend is the same.

Point Style	Column Number
+	0
*	1
diamond	2
triangle	3
square	4
X	5

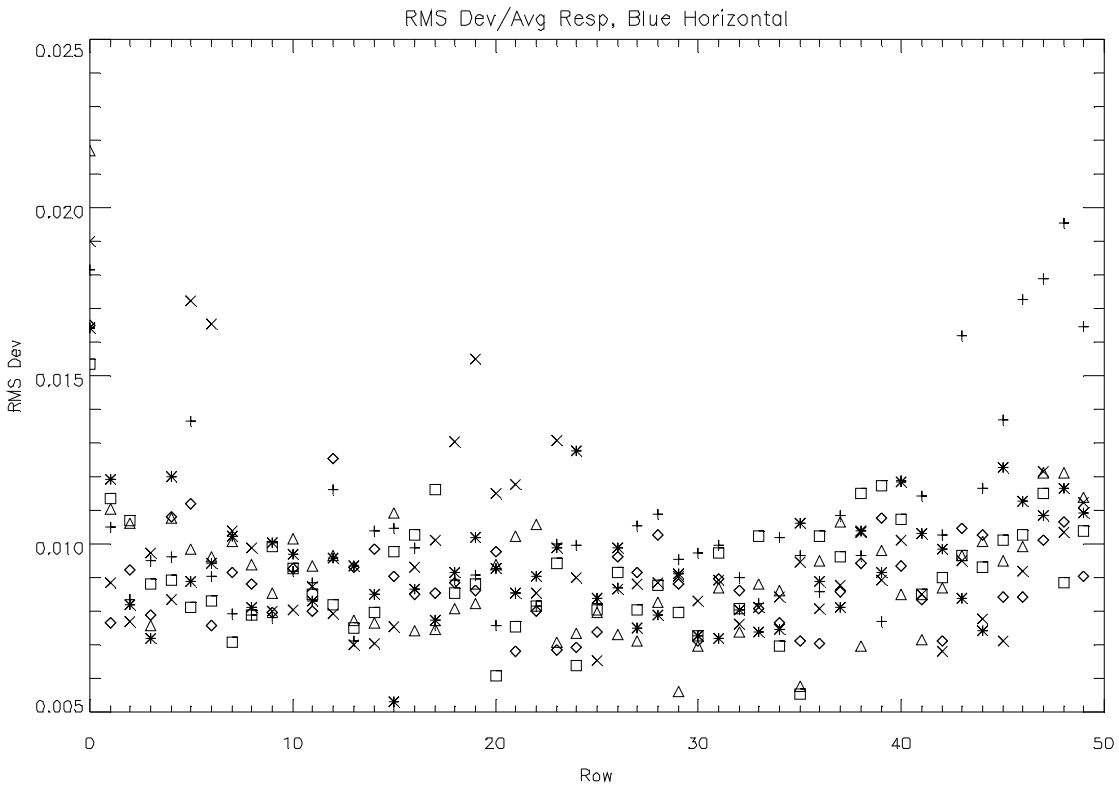
RMS Dev/Avg Resp, Blue Horizontal
RMS Dev
0.025
0.020
0.015
0.010
0.005
0
10
20
30
40
50
Row

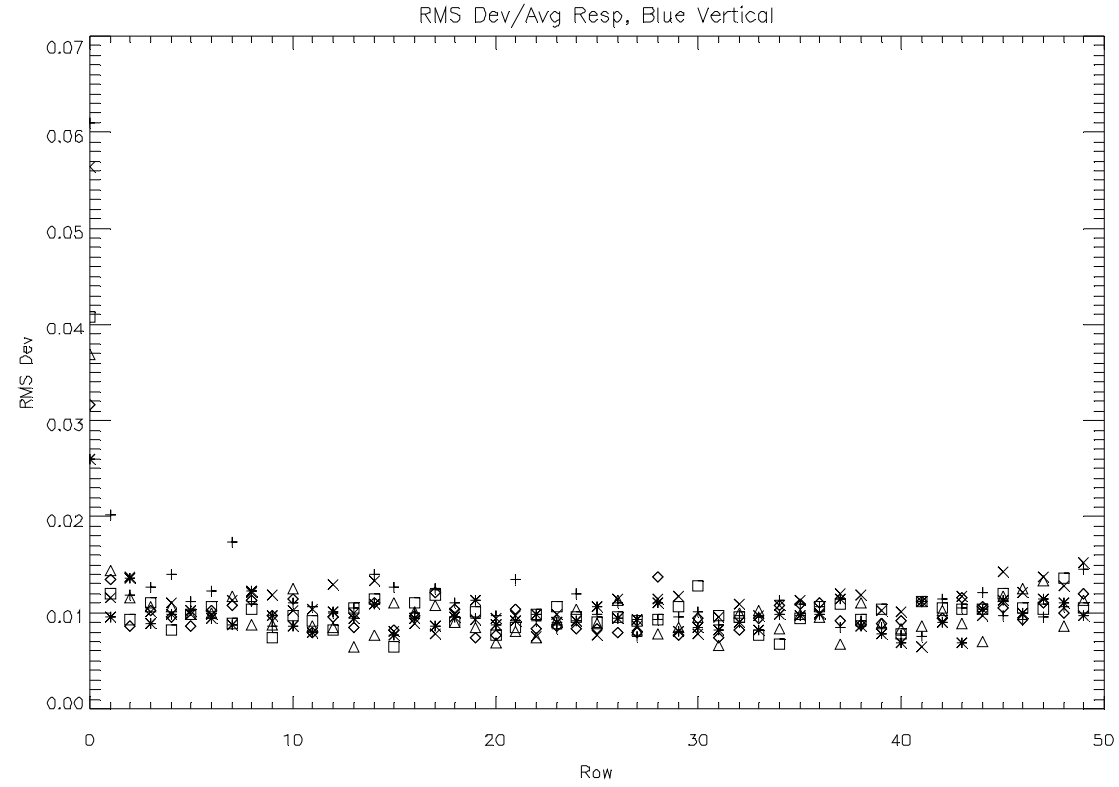
RMS Dev/Avg Resp, Blue Vertical
RMS Dev
0.07
0.06
0.05
0.04
0.03
0.02
0.01
0.00
0
10
20
30
40
50
Row

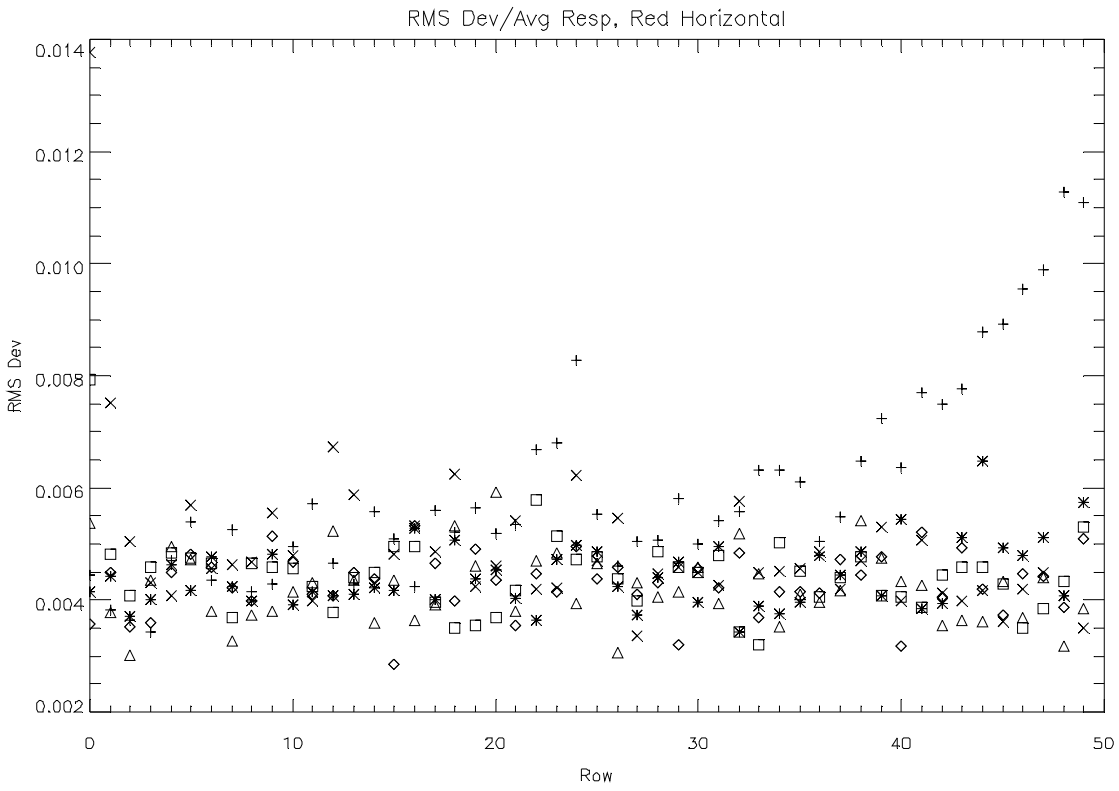
RMS Dev/Avg Resp, Red Horizontal
RMS Dev
0.014
0.012
0.010
0.008
0.006
0.004
0.002
0
10
20
30
40
50
Row

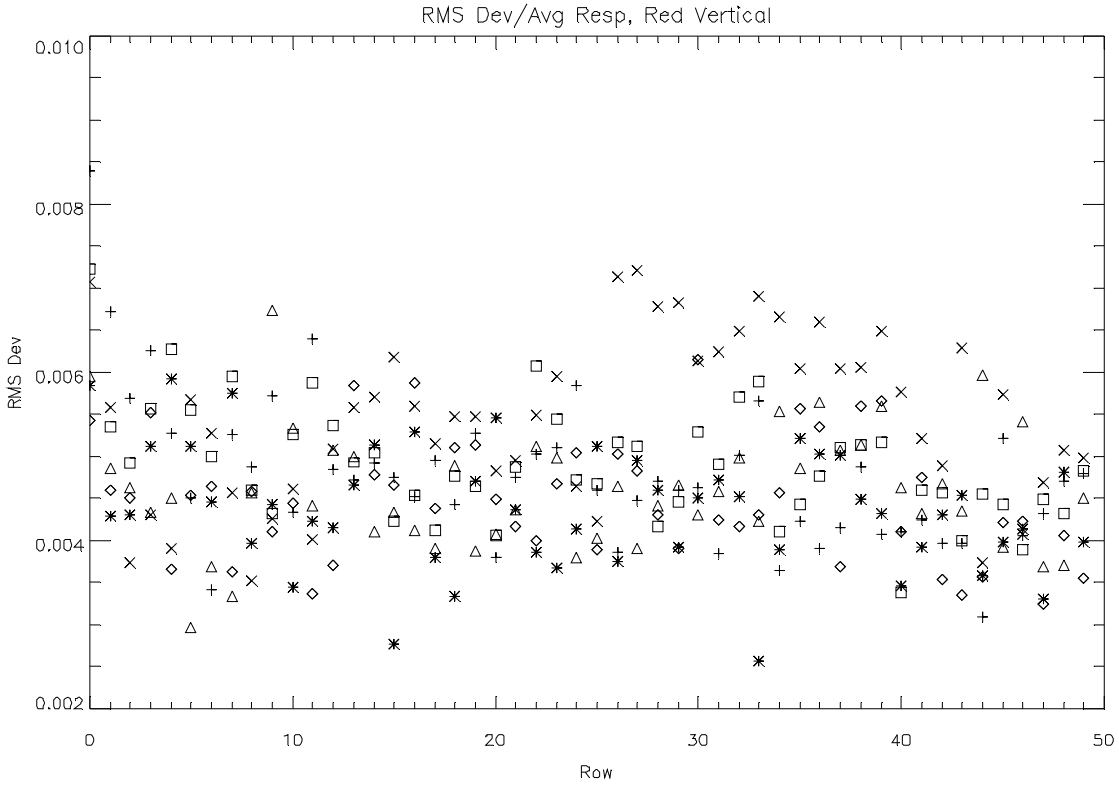
RMS Dev/Avg Resp, Red Vertical
RMS Dev
0.010
0.008
0.006
0.004
0.002
0
10
20
30
40
50
Row

The blue channels are modeled to about 1% accuracy, and the red are modeled to about half that, with the exception of the red horizontal column 0, which has known fiber ribbon chips.

13.6 Polarization Sensitivity

13.6.1 Test Configuration

The Solar Aureole portion of the flight sensor head (SN03) was illuminated by a test setup in which the orientation of linearly polarized light could be changed. In this setup, light from the high intensity lamp passed through a spectral filter and then through a Glan-Thompson prism. The prism was mounted in a motor-driven rotating mount so the direction of linearly polarized light emerging from the prism could be changed during the test. The light emerging from the prism was turned through 90 degrees by reflection from a front surface mirror and was directed to an 8-inch diameter spherical mirror. Light reflected from the spherical mirror produced a collimated beam. The flight sensor head was mounted in a motor driven altitude-azimuth mount and was placed in this beam. A series of measurements was made while the Glan-Thompson prism was rotated. This series was repeated as the instrument was tipped so different columns and rows in the Solar Aureole camera were illuminated by the collimated beam. The instrument was removed from the beam and replaced by the standard silicon detector. This measured any variations in intensity presented to the instrument while the Glan-Thompson prism was rotated. Significant variations in intensity were measured at the location of the DISR sensor head. The DISR counts per second were divided by the signal of the standard detector to remove this modulation.

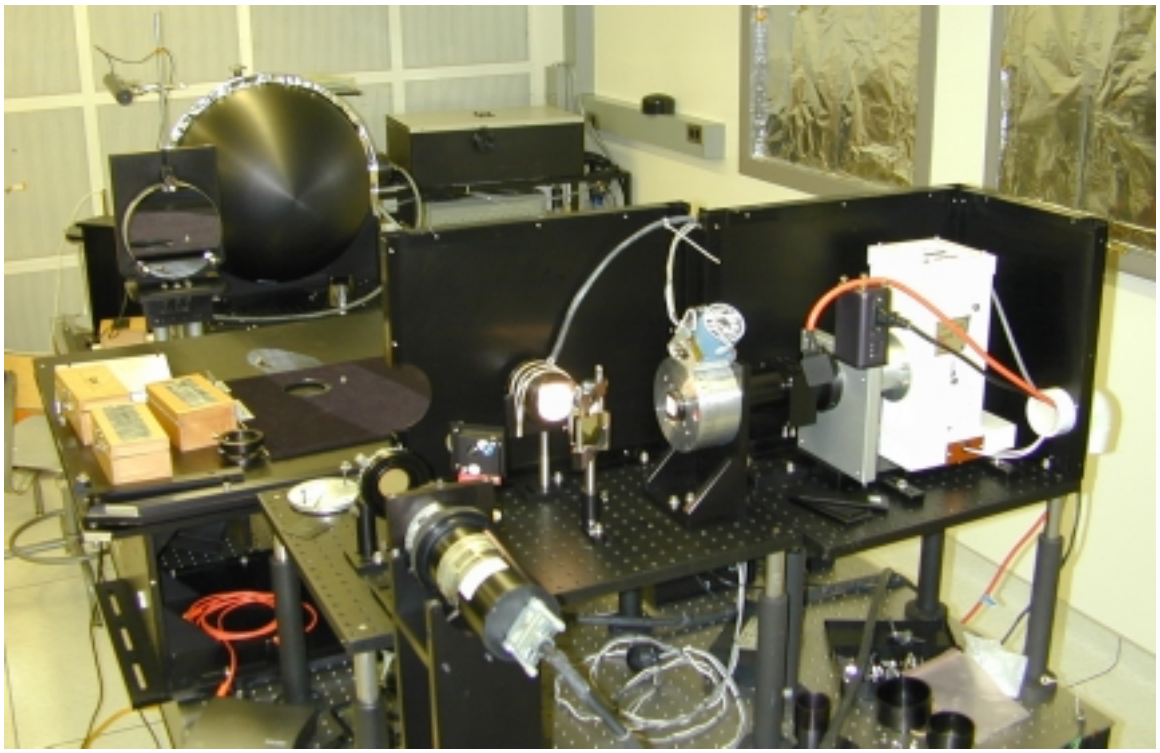

Figure 13-60 The setup used to measure the polarization of the SH03 Flight Instrument.

A second form of correction factor was also applied. The measurements made with the DISR instrument were separated in time from the measurements made using the standard detector in

the collimated beam. It was possible that the brightness of the lamp might have drifted between these times. A partially-silvered beam splitter (actually an nd=1 neutral density filter) was used to pick off a portion of the beam emerging from the Glan-Thompson prism. This portion of the beam was measured by a second silicon detector. The ratio of the brightness measured by this detector at the times when the DISR measurements were taken and when the standard detector measurements were made was used to correct for drifts in the lamp with time. The test setup is shown in the figure.

13.6.2 Polarization Calibration of the 500 nm SA Channels

Unfortunately, the partially silvered beam splitter and the front silvered mirror used to turn the direction of the beam acted to change the state of polarization of the light presented to the DISR instrument as a function of the rotation angle of the Glan-Thompson prism. The fact that this occurred can be seen in the corrected DISR intensities plotted as a function of the Glan-Thompson rotational position in Figure 13-61 and Figure 13-62. In these figures the points represent the measured intensities after the two correction factors were applied. The curves are attempts to fit the data with a cosine- squared law. Note that the fits are not very good. Also, it is not apparent why the peak intensity does not occur at the same Glan-Thompson angle regardless of row number of the SA instrument. In these measurements, a Glan-Thompson angle of 29.5 degrees corresponds to horizontally polarized light and 119.5 degrees corresponds to vertically polarized light. In both the vertical and horizontal channels the phase of apparent polarization varies significantly with row number in a manner that was totally unexpected. Further, at some rows (especially at small or large row numbers far off axis of the center of the SA field) the measurements seem to not go to zero for any orientation of the Glan-Thompson prism.

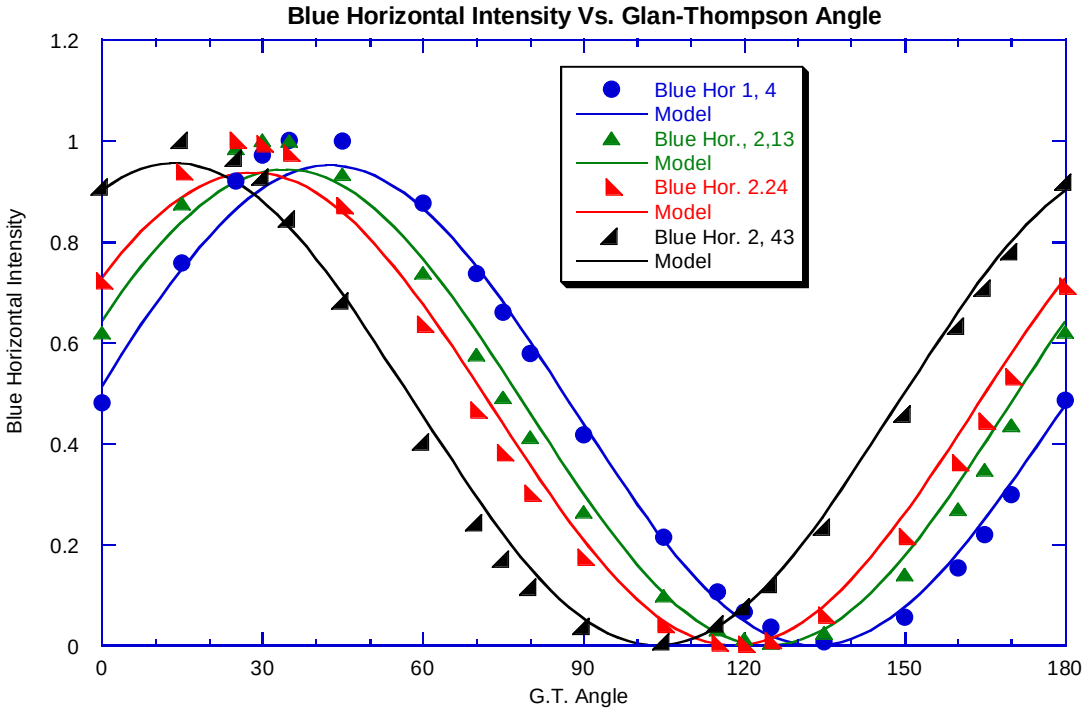

Figure 13-61 The intensity measured in the Blue Horizontal Channel as a function of the orientation of the polarization of the incident light as measured by the angle of the Glan-Thompson prism. The points are the observations at the columns 1 or 2 and at rows 4, 13, 24, and 43. The curves are cosine squared models that do not fit the observations well.

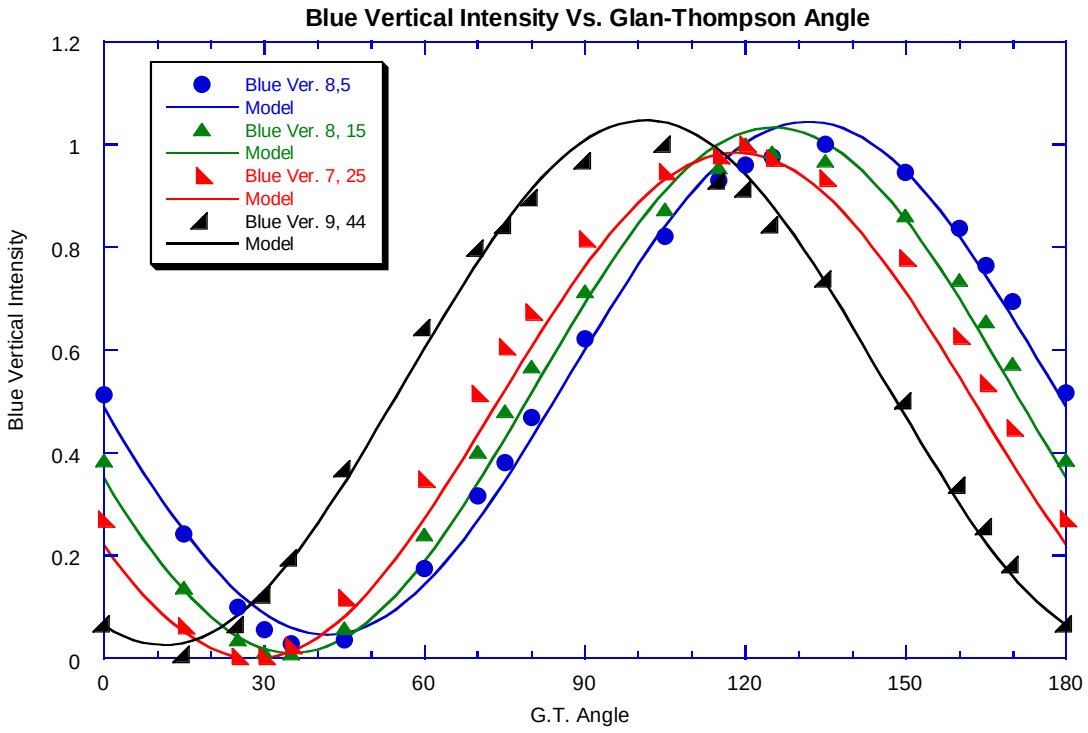

Figure 13-62 Same as Figure 13-61 but for the Blue Vertical channel.

Even though the test setup likely produced light that was not completely linearly polarized at exactly the orientation of the Glan-Thompson polarizer, the shift of phase with location in the field (row number) was so striking and unexpected that a special set of measurements was made. These consisted of illuminating a spare beamsplitter of the type installed in the flight instrument by linearly polarized light and measuring the intensity emerging from the beam splitter as a function of the angular position of a sheet polarizer placed after the beam splitter. The test setup for this test is shown in Figure 13-63.

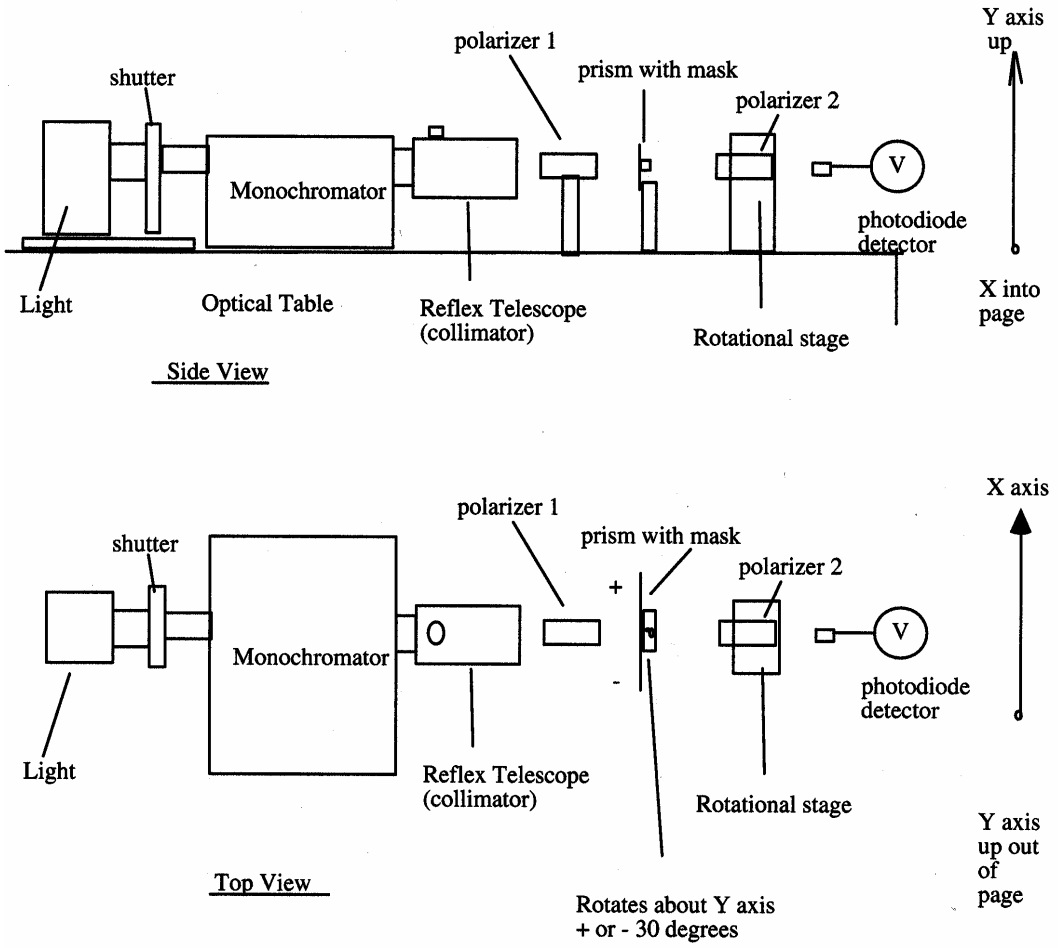

Figure 13-63 Diagram of test setup for measuring the properties of a spare prism of the type used in the flight model of the DISR Solar Aureole system. Polarizer 1 was set to introduce linearly polarized at an angle of 0, 45, or 90 degrees from the horizontal direction. The intensity is measured by the photodiode detector after the light is passed through polarizer 2. The orientation of polarizer 2 is varied in 10 degree steps from the horizontal increasing in the CCW direction looking toward the source. Data were collected with the prism oriented perpendicular to the incident beam or at an angle of + or – 30 degrees from the direction. At a reading of 29.5 degrees on polarizer 2 the plane of polarization is oriented parallel to the Y axis (vertical).

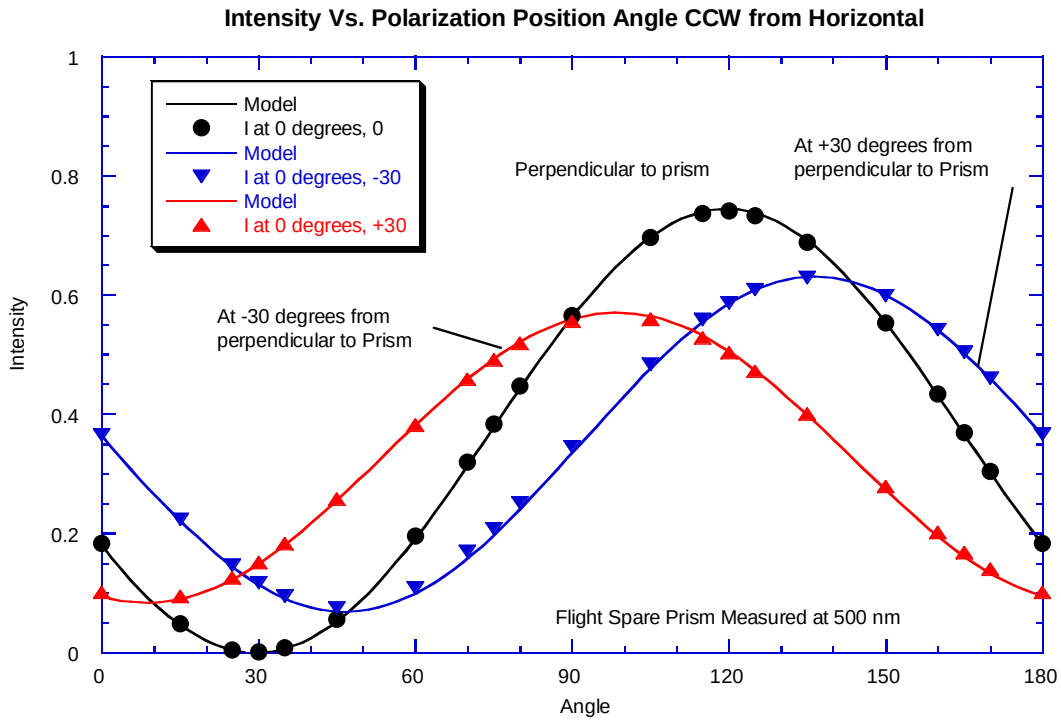

Figure 13-64 The intensity as a function of position angle when the spare Solar Aureole prism was illuminated by horizontally polarized light. The Glan-Thompson analyzer is positioned after the light passes through the flight prism. Note that a reading of 29.5 degrees corresponds to vertically polarized light. The points are observations, and the curves are models for a retardance, tau, and position angle, psi, of the incident light from the principal axis of the retarder that arises from the partially silvered beam splitter in the prism. Note that the fits are quite good.

In this test, horizontally polarized light was sent to the flight prism, and the state of polarization of the light that passed through the prism was measured by measuring the intensity that passed through the Glan-Thompson prism for each of many orientations of the prism. This test was repeated with the flight prism rotated so the light struck the prism perpendicular to the long axis of the prism, and also at + and – 30 degrees from this direction. The intensities measured as a function of Glan-Thompson analyzer orientation are shown in Figure 13-64.

In addition to sending horizontally polarized light to the flight prism, the orientation of the sheet polarizer in front of the prism was rotated so that vertically polarized light could be used to illuminate the prism, and an orientation 45 degrees between horizontal and vertically polarized light could also be used. Figure 13-65 and Figure 13-66 show the results for these different orientations.

The results for the 45 degree orientation of the incident beam are particularly revealing. Note that when light at 45 degrees orientation strikes the prism at 0 degrees from the perpendicular to the long axis of the prism that the light intensity is only very slightly modulated as a function of the orientation of the Glan-Thompson analyzer. For purely linearly polarized incident light to emerge almost unmodulated by the orientation of an analyzer requires the flight prism to act nearly as a quarter-wave retarder! In Figure 13-64, Figure 13-65, and Figure 13-66 the points are the measured intensities while the curves are the intensities

expected from an ideal retarder with variable retardance and variable orientation of the incident polarized light from the principal axis of the retarder.

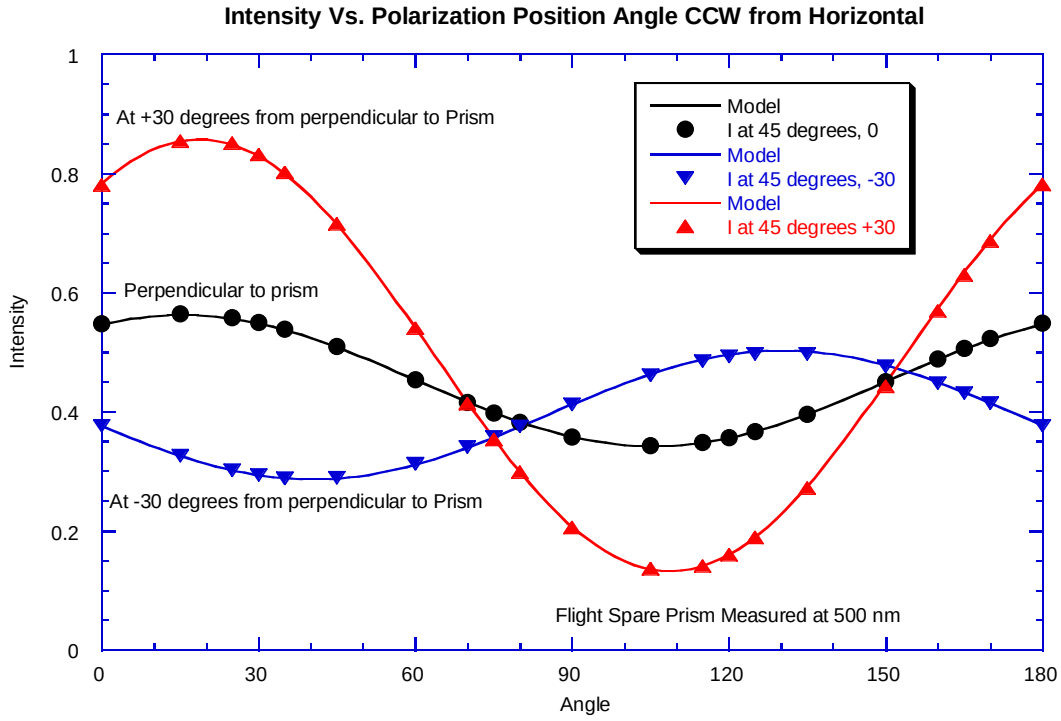

Figure 13-65 Same as Figure 13-62 but for light initially polarized at an angle of 45 degrees from the vertical. Note that when this purely polarized light is incident perpendicular to the prism (black curve) the output intensity is only modulated by some 10% after passing through the Glan-Thompson prism. This is an indication that the input polarized light is converted to a significant component of circular polarization in passing through the flight prism. The retardance of the flight prism must be nearly 90 degrees in this case.

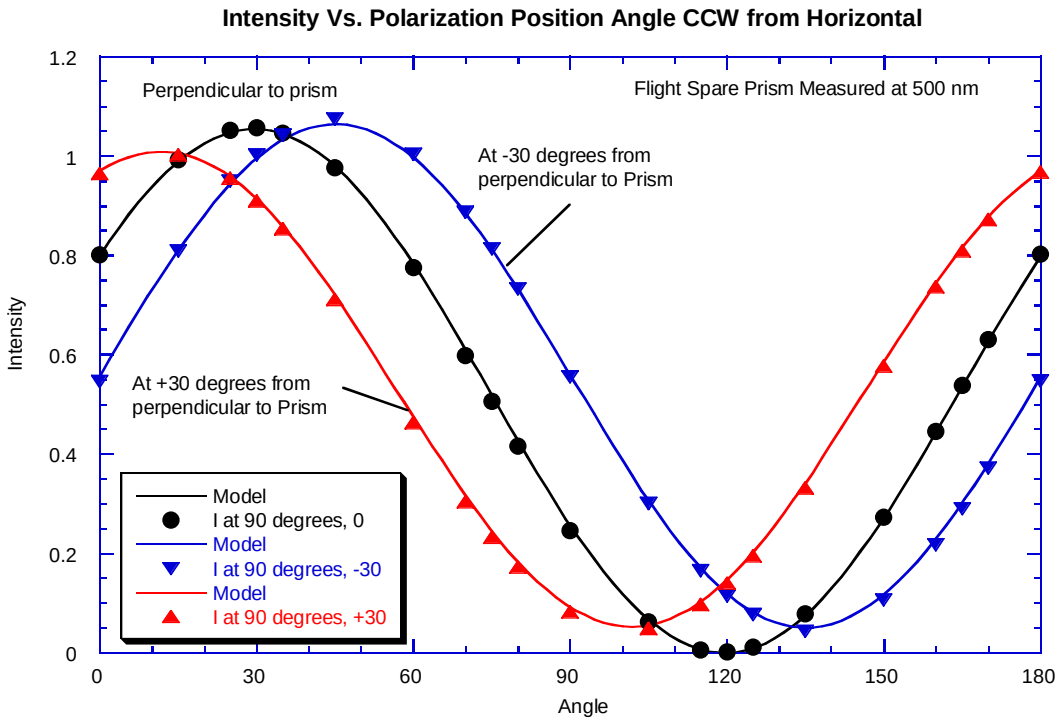

Figure 13-66 Like Figure 13-65 but for vertically polarized light incident on the flight prism. While the light is highly modulated, the phase of the light is shifted, again indicating strong retardance in the flight prism.

Figure 13-67 shows the retardance of the spare prism for the three orientations of the incident polarization and for the three angles of incidence of the light relative to the long axis of the prism. Note that the retardance is nearly 90 degrees in all cases.

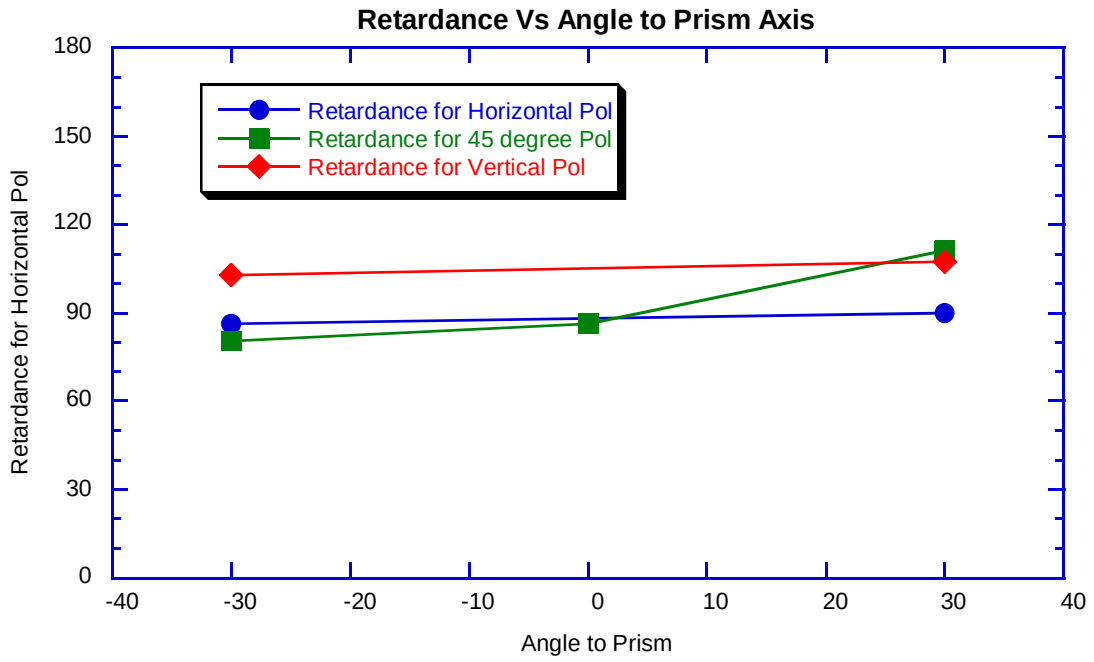

Figure 13-67 This figure shows the retardance of the flight prism necessary to fit the observations in the last three figures as a function of the angle of the incident light to the perpendicular to the prism. Note that the retardance is near 90 degrees, and the flight prism acts similar to a quarter-wave plate.

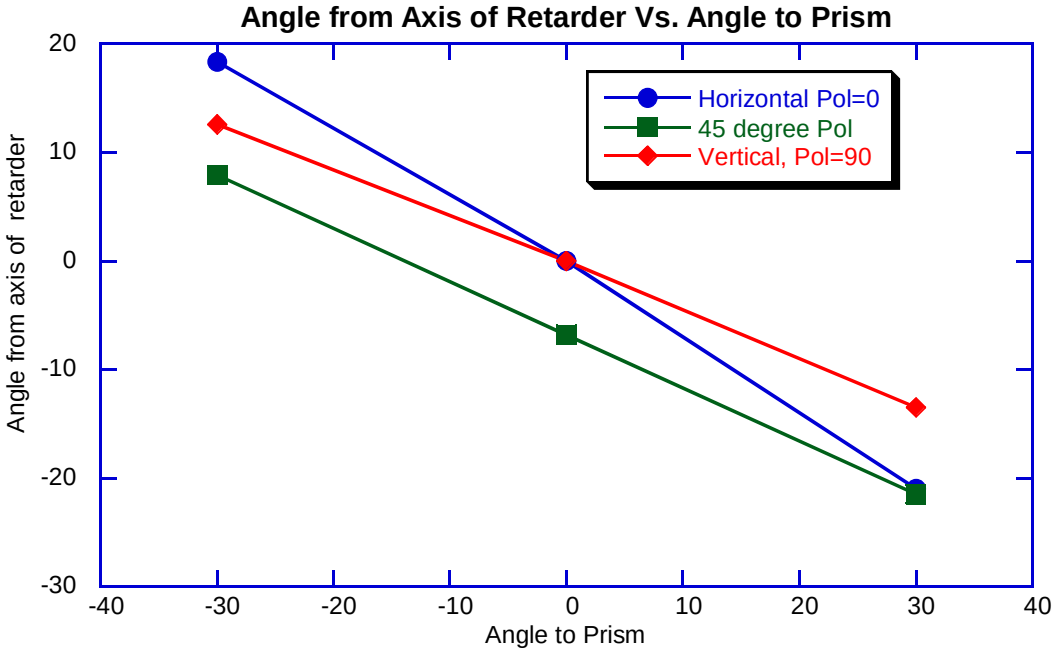

Figure 13-68 This figure shows the angle of the polarized light from the principal axis of the retarder as a function of the angle of the beam from the perpendicular to the prism. In the flight configuration, light in each row of the detector will enter the prism at a different angle, spanning the range from about -25 to + 25 degrees.

Figure 13-68 shows the angle of the polarized light from the principal axis of the retarder as a function of the angle of the incident beam from the perpendicular to the flight prism. The field of view in row number corresponds to angles within about + and – 25 degrees in this figure. Thus, the action of the flight prism corresponds to a roughly quarter wave plate with variable angles relative to the principal axes with different row numbers. This seems to be how the phase was shifted with row number in the original measurements in the test setup.

In order to make use of the measurements made on the flight model before delivery, it is necessary to measure the properties of the test setup. This setup was reconstructed in the spring of 2004. We installed a sheet polarizer followed by the standard silicon detector at the location where the DISR sensor head had been placed in the collimated beam. We recorded the corrected intensity in this location for each orientation of the Glan-Thompson prism as a function of the orientation of the sheet polarizer. The results are shown in Figure 13-69 below.

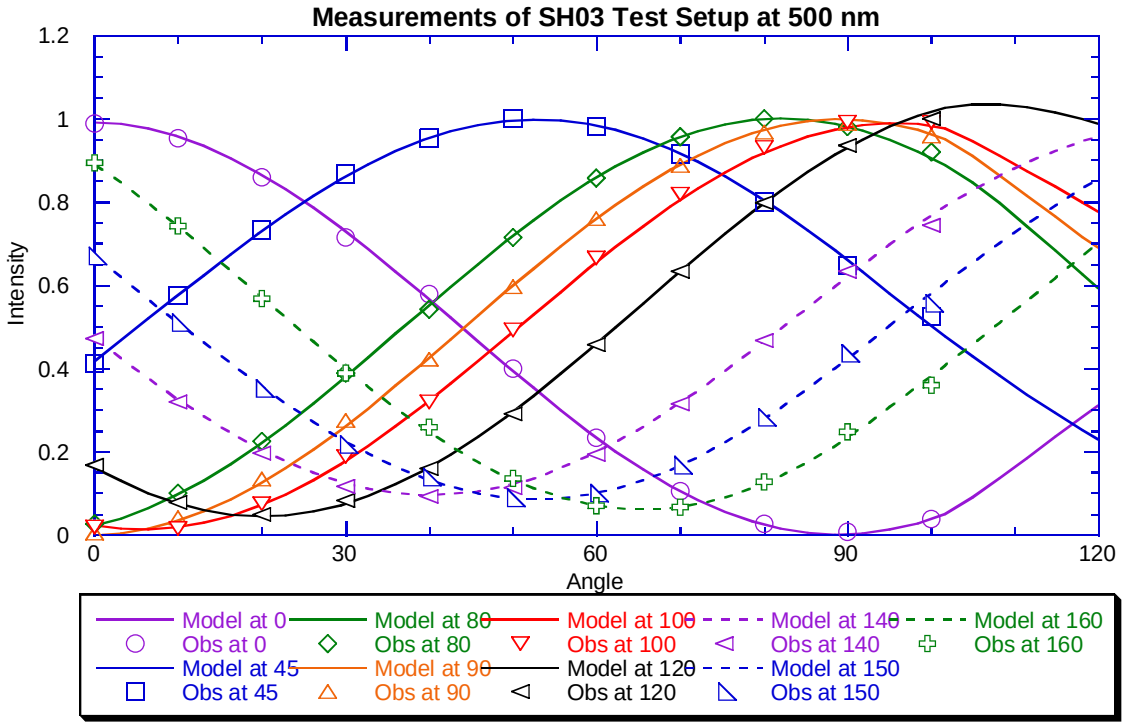

Figure 13-69 We show the modulation of intensity caused by a rotated analyzer at the location of DISR in the test setup used for polarization measurements for different orientations of the plane of polarization of the input light. Note that for some orientations of the incident polarization a significant intensity leaks through the analyzer at the output of the test setup, indicating that a significant conversion from linear to circular polarization is occurring in the test setup is some orientations.

Note that the intensity does not go to zero for any orientation of the sheet when the input polarization orientation is near 45 degrees from the horizontal. Near 0 and 90 degrees, the intensity does go to zero at the expected orientation of the sheet polarizer. In Figure 13-69, the points are the measured intensities and the curves are for an ideal retarder for fitted retardance and position angle relative to the principal axis of the retarder. The results are shown in Figure 13-70 and Figure 13-71. Figure 13-70 shows the variation of the position angle relative to the principal axis of the retarder as a function of the input polarization

orientation. Figure 13-71 shows the retardance as a function of input polarization orientation. Note that the retardance is well constrained at input polarization angles of 45 and 135 degrees, and is poorly constrained near 0, 90, and 180 degrees since the polarization is nearly aligned with the principal axis of the retarder for these orientations. The retardance is approximately 60 degrees where it is well constrained.

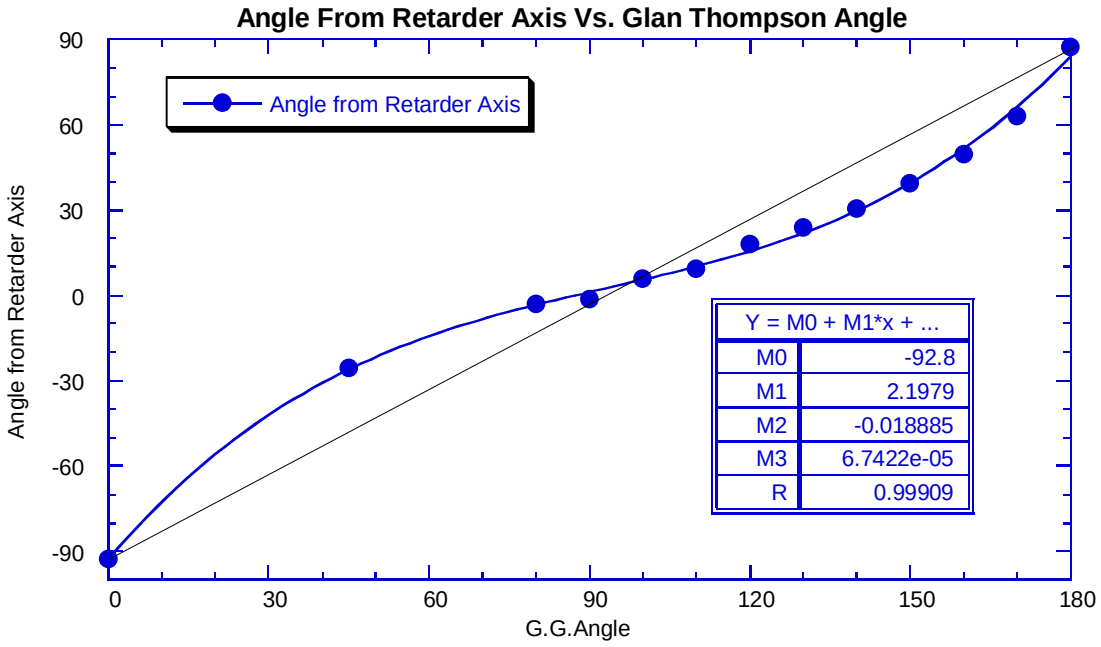

Figure 13-70 We show the angle of the polarized light relative to the principal axis of the retarder in the test setup for different orientations of the Glan-Thompson prism at the input to the test setup. The angle is near 0 or 90 degrees when the Glan-Thompson prism polarizes the light vertically or horizontally, but at intermediate angles, significant angles from the axis of the retarder are reached.

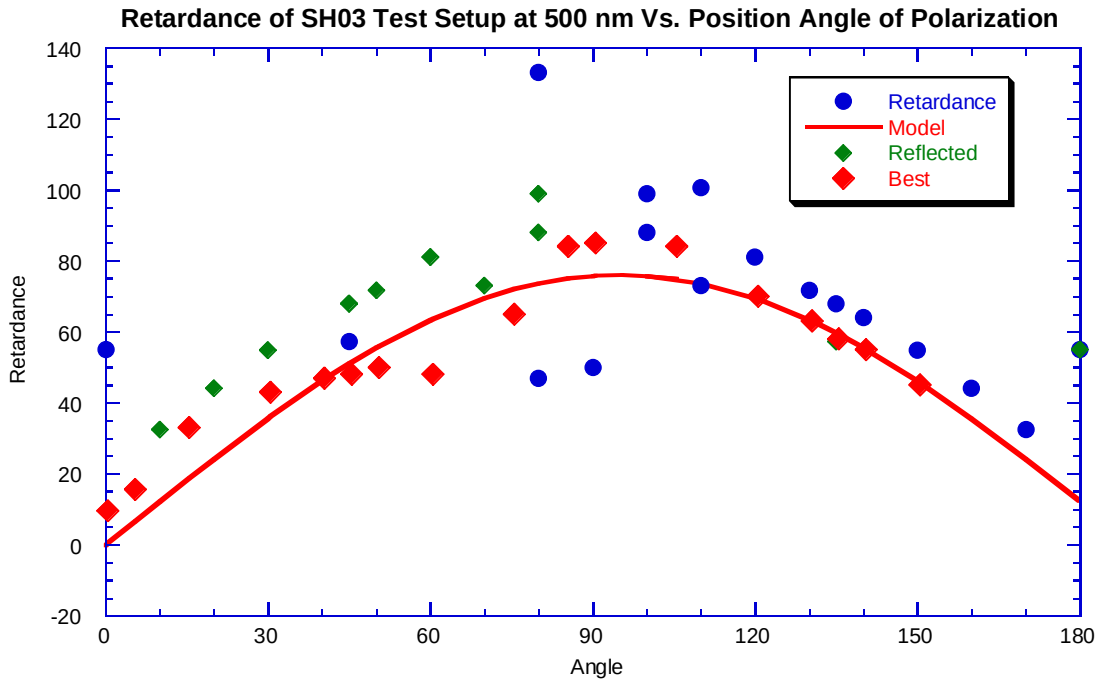

Figure 13-71 The retardance introduced by the test setup is shown as a function of the angle of the Glan-Thompson prism. There is little sensitivity at angles near 0 or 90 degrees, but near 45 or 135 degrees the retardance is some 50 or 60 degrees.

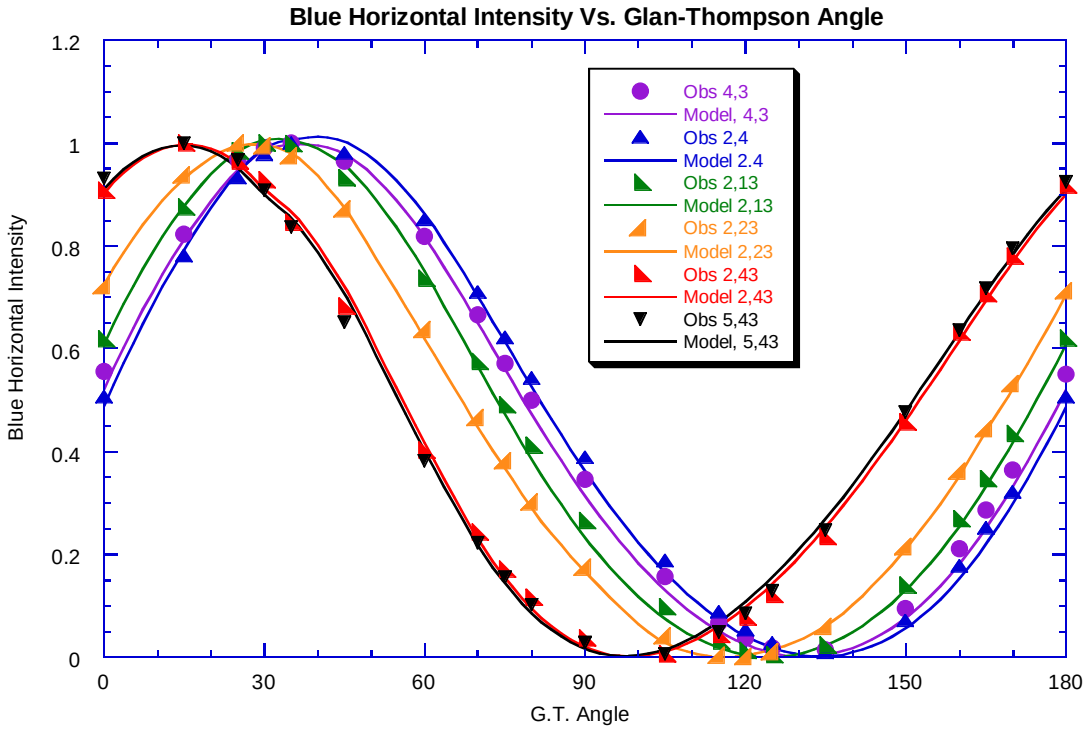

Figure 13-72 The measured variation in intensity of the Blue Horizontal channel as a function of the setting of the Glan-Thompson prism is shown for various columns and rows. The curves are functions including the retardance of the test setup as well as a variable retardance and position angle of the flight prism. Note that the fits are much better than in Figure 13-61.

Now that the characteristics of the test setup have been determined, it is possible to solve for the degree of retardance of the beam splitter in the flight model SA unit and the angle of the input polarization relative to the principal axis of the retarder as a function of row number in the blue horizontal and vertical channels. The best fits of the data to the observations are shown in Figure 13-72 and Figure 13-73. The points are the measurements while the curves are for a model of the sensor head. The fits are quite good.

Figure 13-74 shows the position angle relative to the principal axis of the retarder of the sensor head as a function of row number in the blue vertical and horizontal channels. This angle varies from +10 to some – 15 degrees as the row number increases from 0 to 49 in the flight unit. Quadratic fits to the position angles as functions of row number in each blue channel are also given.

It is interesting to understand how the instrument came to have these properties. One requirement of the in flight calibration system was that it pass light through all the optical elements of a system except for the front window. This requirement allowed for accurate tracking of any radiation darkening of optics or changes in alignments over the launch or cruise environments. However, because of the design of the Solar Aureole optical system, it implied a beamsplitter to introduce the calibration signal.

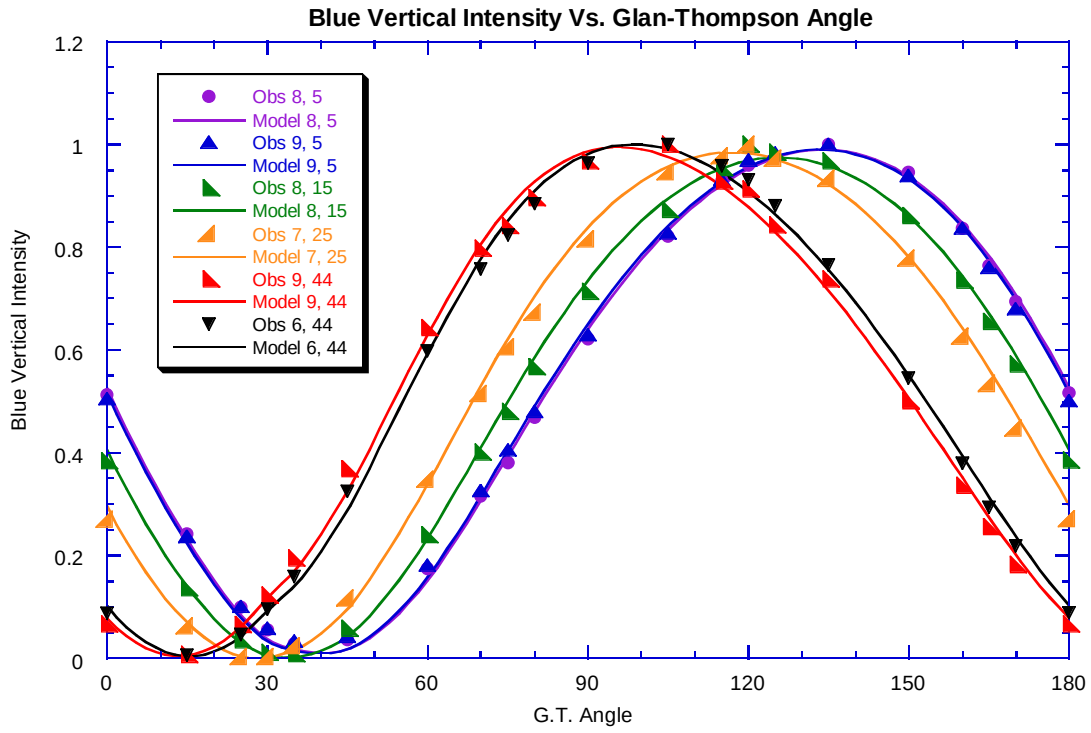

Figure 13-73 Same Figure 13-72 but for the Blue Vertical channel. Again note the improved quality of the fit compared to Figure 13-62.

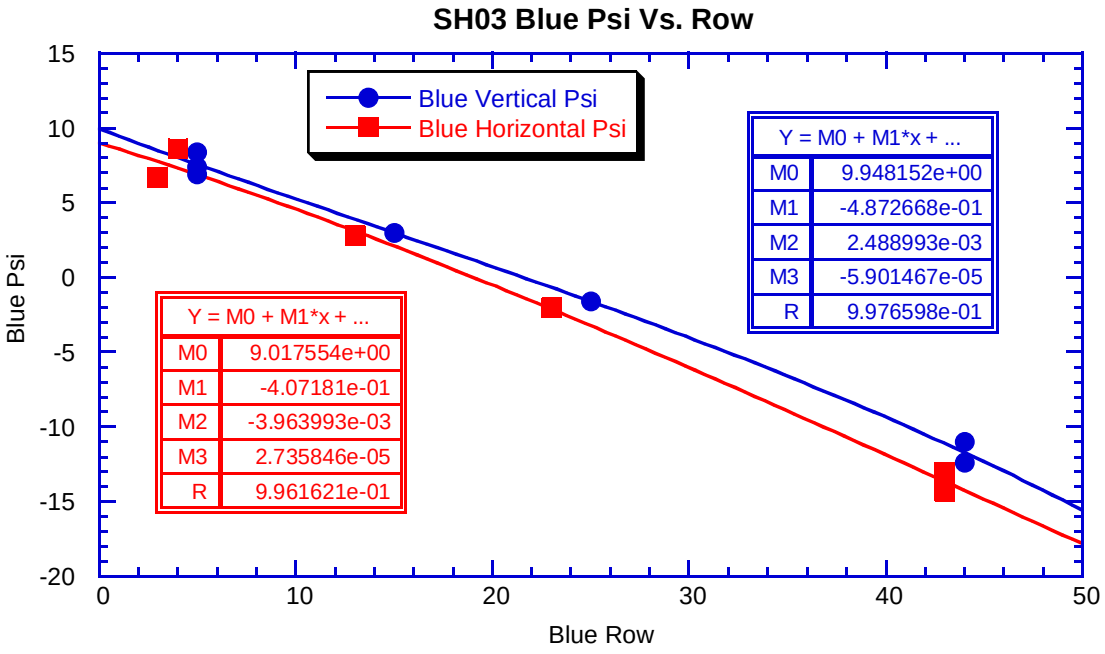

Figure 13-74 We show the position angle as a function of row number for the Blue Vertical and Horizontal channels in the SH03 flight Solar Aureole system. The retardance is taken as 90 degrees for the flight prism in the blue channel.

13.6.3 Polarization Calibration of the 935 nm SA Channels

A similar set of measurements of the full flight instrument as well as for the prism alone was made in the red Solar Aureole channel. Again, the measurements did not fit the corrected measurements made in the full instrument test. Measurements on the spare prism alone were repeated in the red channel using the test setup shown in Figure 13-63. The results for incident light at 45, 0, and 90 degrees from the horizontal are shown in Figure 13-75, Figure 13-76, and Figure 13-77. Points are measurements and the curves are fits for variable retardance and angle relative to the principal axis of the retardance introduced by the prism.

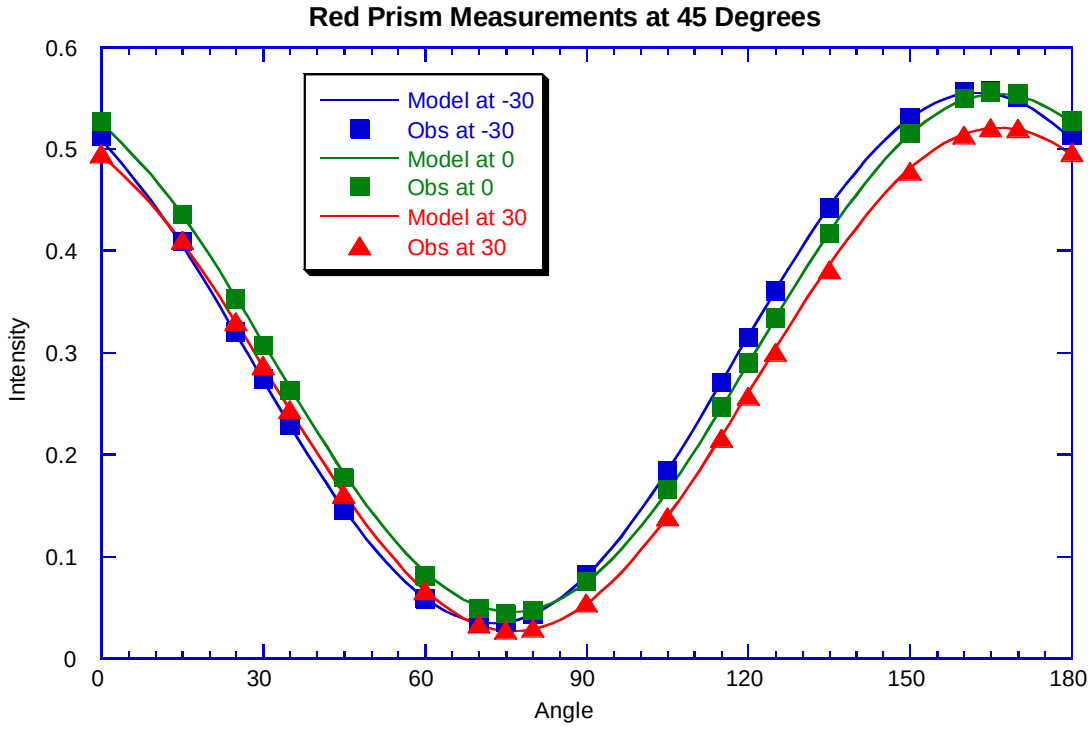

Figure 13-75 Intensity as a function of analyzer angle when spare prism is illuminated with linearly polarized light at an angle of 45 degrees.

Note that the curve for 45 degrees incidence is much more highly modulated in the red channel than in the blue, indicating that the retardance of the flight prism is less in the red than in the 500 nm channel. Again, good fits are possible with adjustments of the retardance of the prism and the position angle. Results are shown in Figure 13-79.

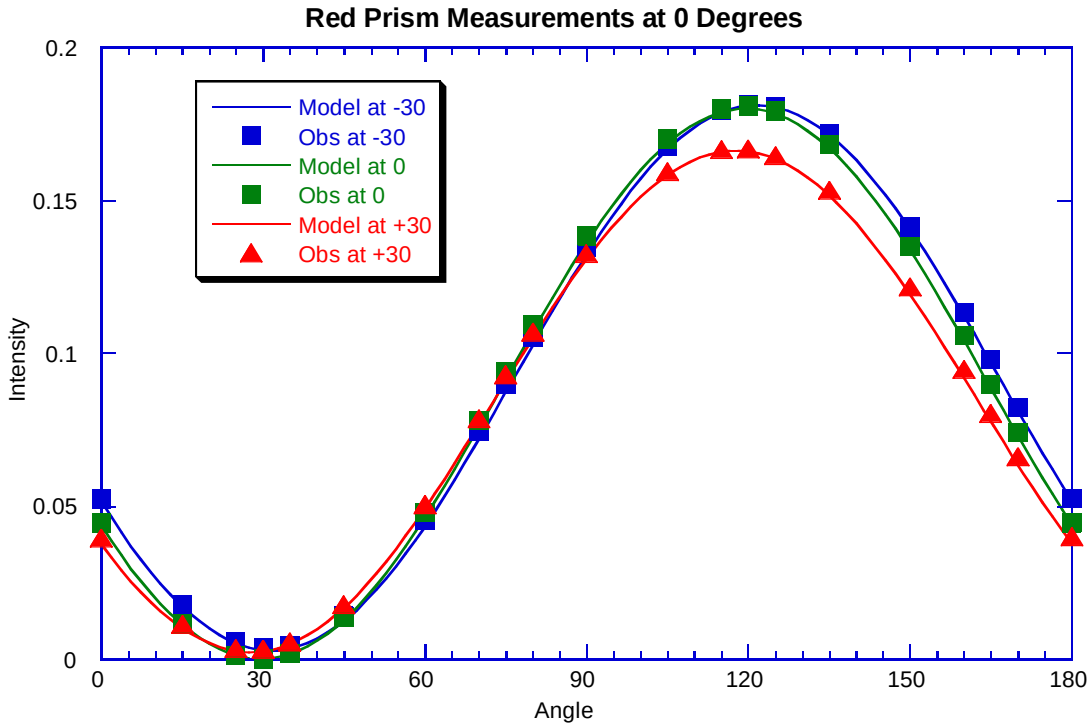

Figure 13-76 Like Figure 13-75 but for incident light polarized at an angle of 0 degrees (parallel to long axis of prism.)

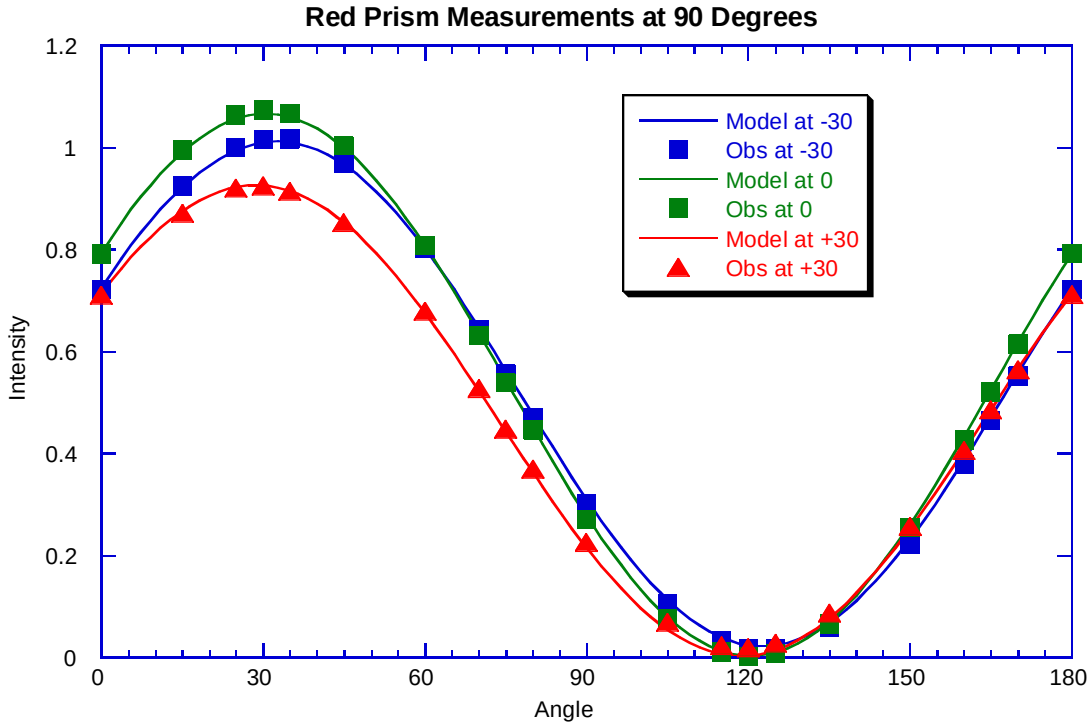

Figure 13-77 Like Figure 13-76 but for light polarized at an angle of 90 degrees (perpendicular to long axis of prism).

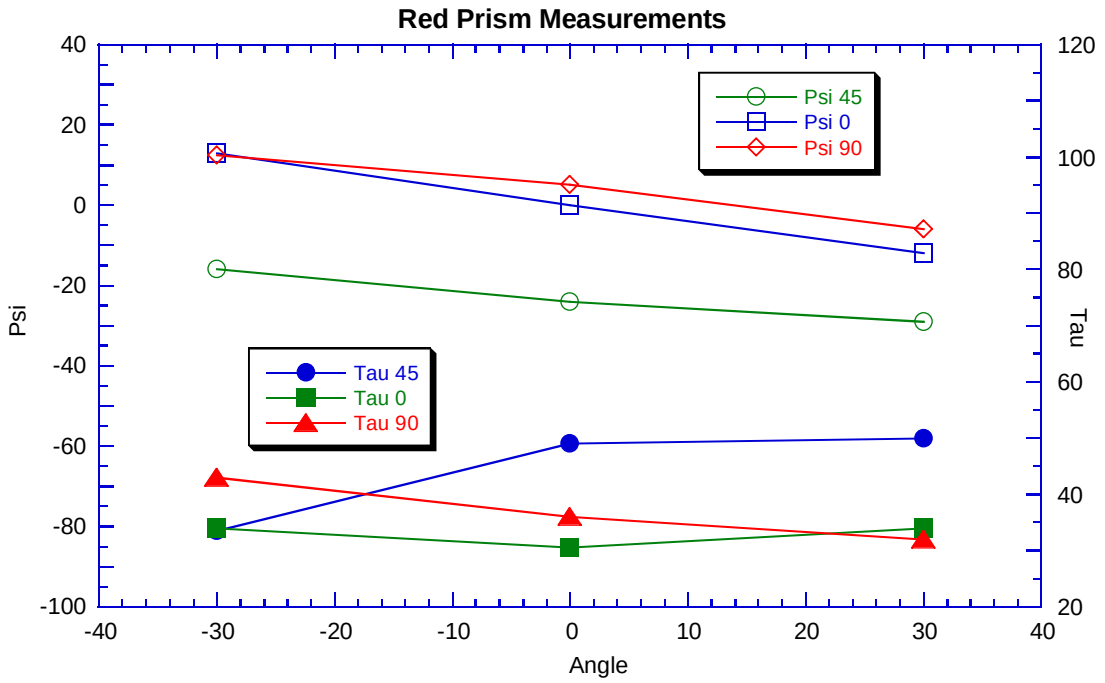

Figure 13-78 Position angle of polarization relative to principal axis of retarder as a function of angle of illumination relative to perpendicular to spare prism (left scale and open symbols.) Right scale shows the degree of retardance of the spare prism as a function of the angle of illumination to the perpendicular to the prism. Note that the retardance of the prism is some 30 degrees, much less than the prism as measured in blue light.

Note that the retardance of the prism alone in the red channels is approximately 30 degrees compared to the 90 degrees measured in the 500 nm channel. Since the dichroic beam splitter is much more reflective in the 500 nm channel than in the red channel, this is not surprising. Also, the position angle relative to the principal axis of the retarder varies with row number in a similar manner to that measured for the measurements on the blue prism.

Figure 13-79 shows the measurements made at the red channel wavelength on the test setup used for the measurements on the full flight Solar Aureole instrument. Again, the curves do not go to zero intensity near 45 and 135 degrees. The reduced position angle and retardance of the test setup in red light are shown in Figure 13-80 and Figure 13-81. With these measurements of the characteristics of the test setup in red light, the measurements made on the flight unit in this test can be analyzed.

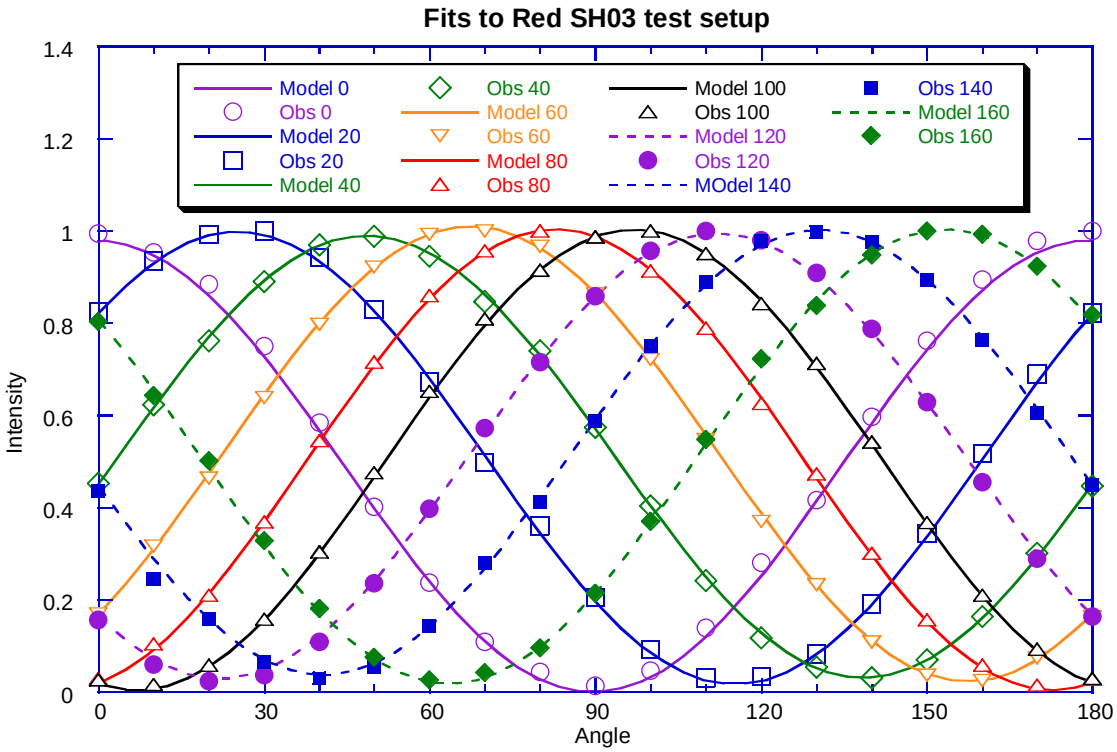

Figure 13-79 Intensity as a function of angle from horizontal direction when the test setup used to measure the flight instrument in red light is illuminated by linearly polarized light oriented as shown in the caption (caption angle is from horizontal increasing CCW looking toward the source.) Note that the intensity does not go to zero near 45 and 135 degrees indicating some amount of circular polarization in the beam under these conditions.

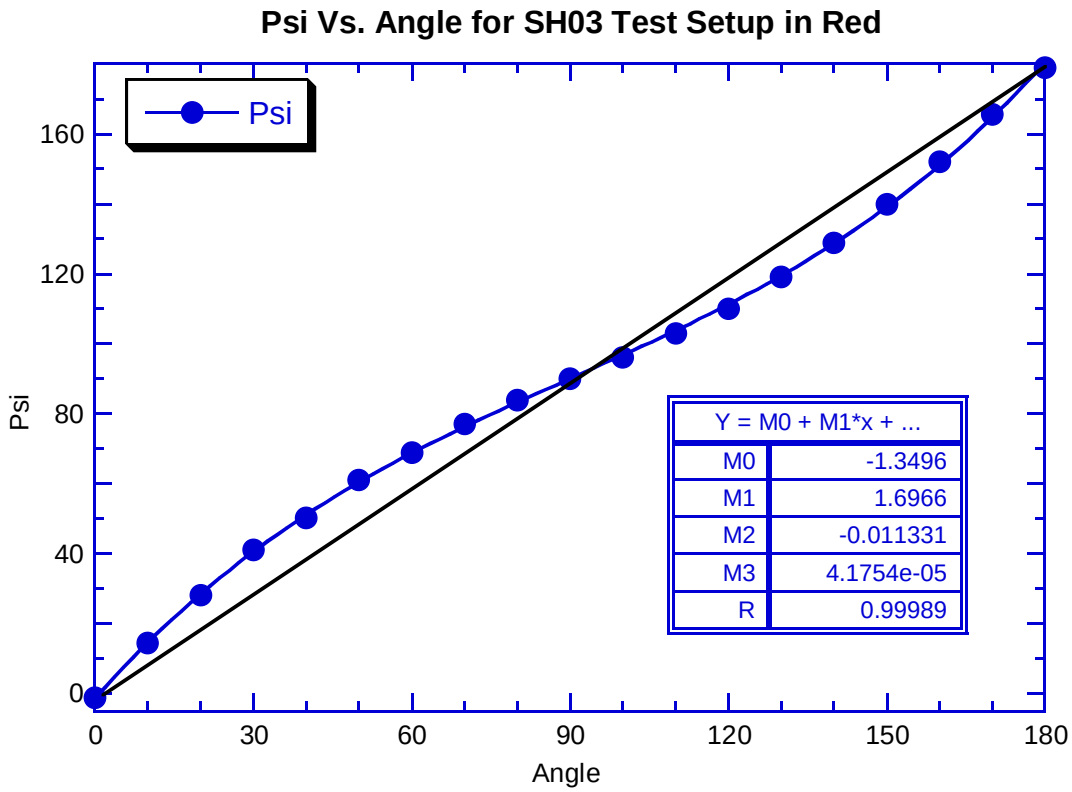

Figure 13-80 The angle of the polarized beam relative to the principal axis of the retarder in the test setup used to measure the flight SA instrument in red light.

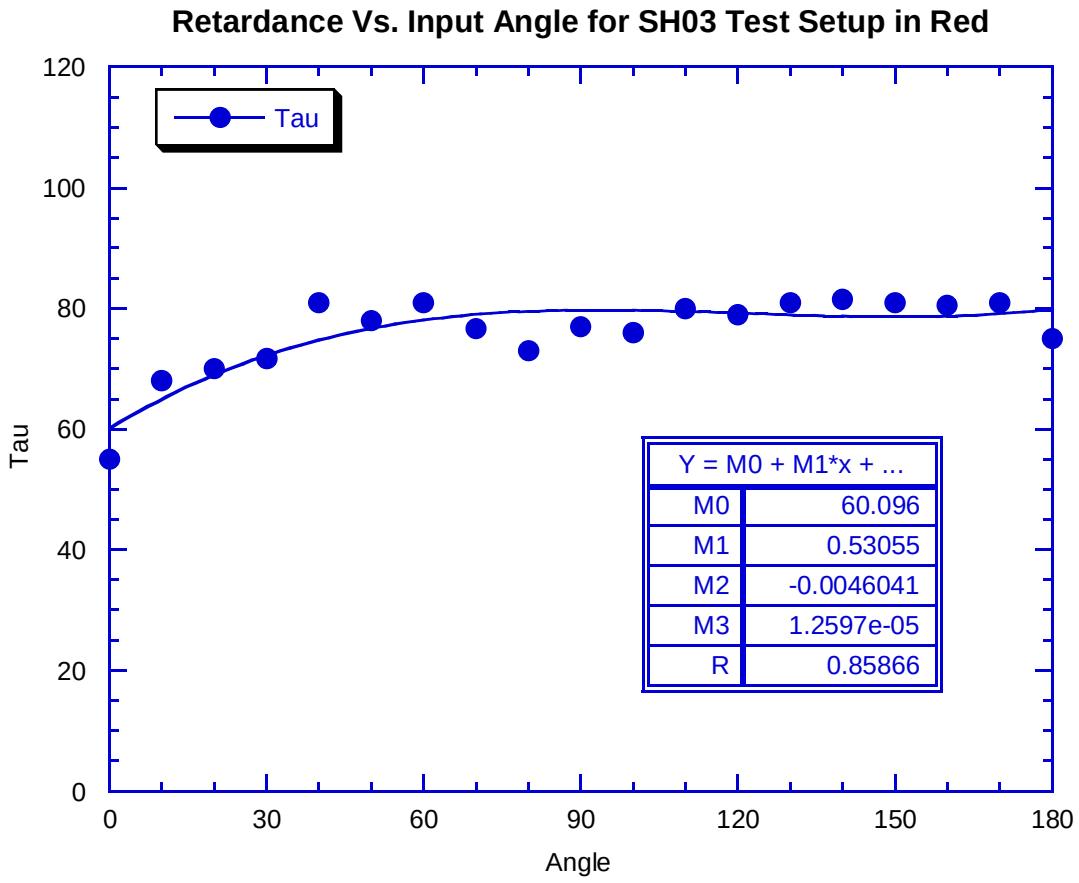

Figure 13-81 The retardance of the test setup used to measure the properties of the flight SA instrument as a function of the angle of polarization produced by the Glan-Thompson prism. The polarization angle is measured CCW from horizontal looking toward the source.

The resulting position angle (Psi) and degree of retardance (Tau) as functions of row number are shown in Figure 13-82 and Figure 13-83 for red horizontal and vertical channels, respectively. The retardance is about 30 degrees, as measured for the prism alone. The position angle varies from some 80 degrees to near 20 degrees from row 0 to row 49 in both red channels. These values are slightly different than the values measured for the prism alone, but the full instrument is included in these tests. It seems necessary to accept these values of Psi as functions of row in the full flight assembly. Note that with a smaller degree of retardance in the prism in the red than the blue, more drastic values of Psi must be chosen to make the test measurements agree with the calculations. It may be that other portions of the optical system included in the full optical assembly require these values for the position angles in the red channels.

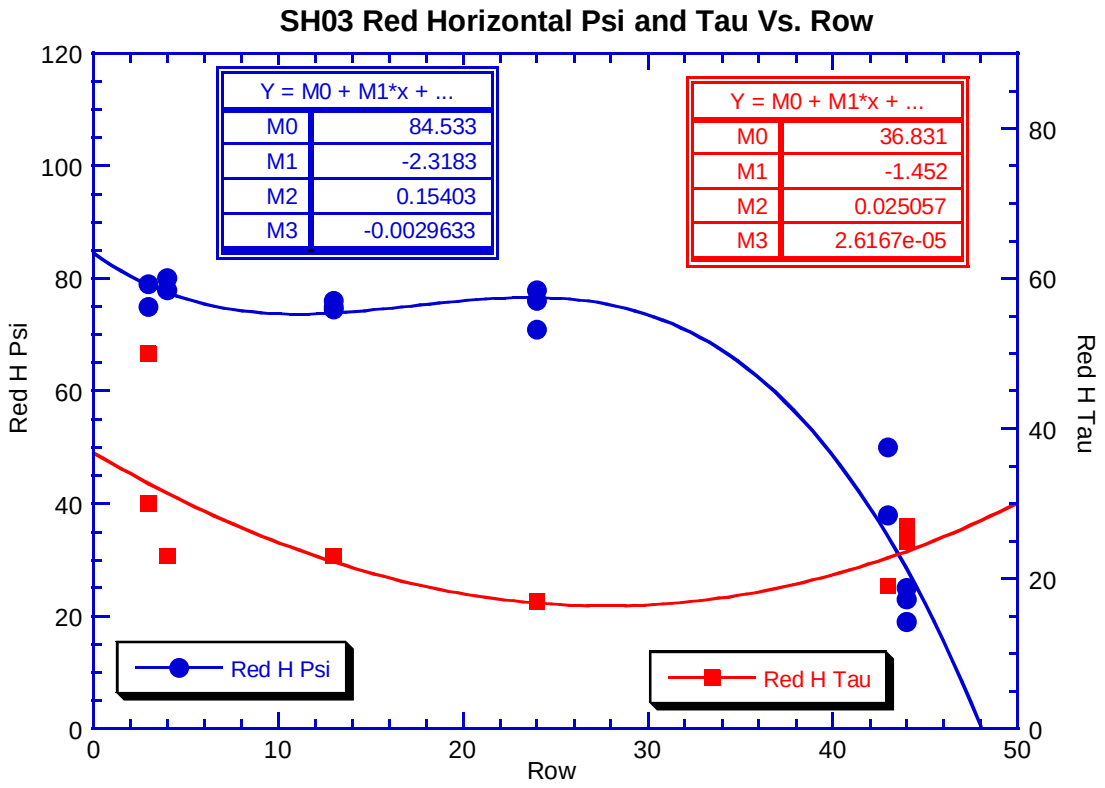

Figure 13-82 The position angle (Psi, left scale, blue dots) and the degree of retardance (tau, right scale, red squares) as functions of row in the horizontal channel of the flight sensor head.

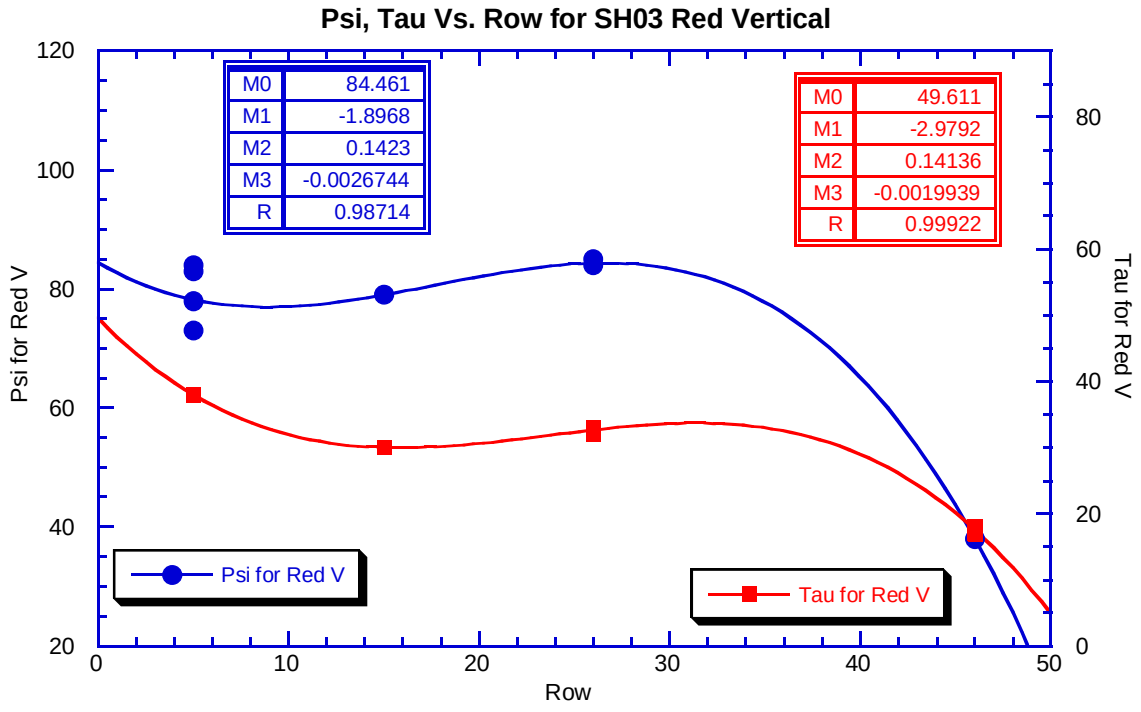

Figure 13-83 Like Figure 13-82 but for the vertical channel of the flight SA in the red.

The results of the model (curves) are compared to the observations made in the red full-instrument test setup are shown in Figure 13-84 and Figure 13-85 below. Again, the fits are quite good in both channels. Thus, it seems that the full flight Solar Aureole system can be modeled by an ideal variable retarder with position angle and retardance dependant on row number followed by an analyzer in the vertical or horizontal orientation. With this model, the intensity in the two instrument channels can be predicted for any orientation and degree of linear polarization in the incident light. Also, if the orientation of the polarization of the incident light is assumed, the total intensity and the degree of polarization can be found.

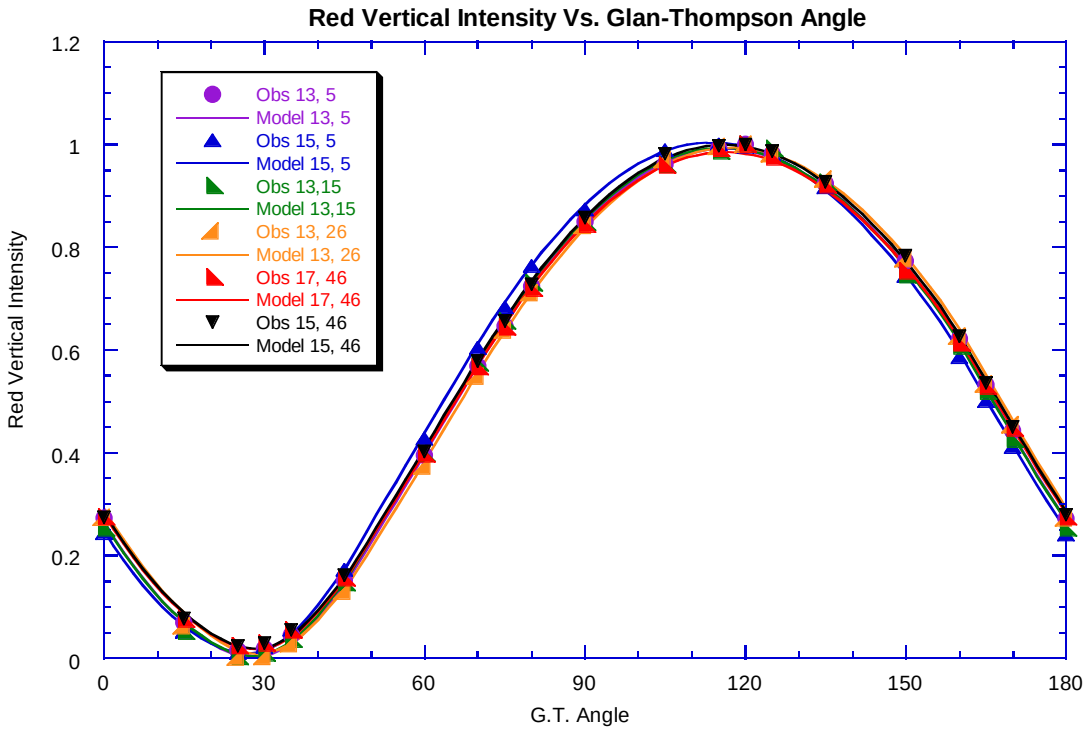

Figure 13-84 The intensity measured by the flight SA in the red vertical channel as a function of the setting of the Glan-Thompson prism in the test setup when different rows were illuminated as indicated. Note that the curves are in good agreement with the measured points.

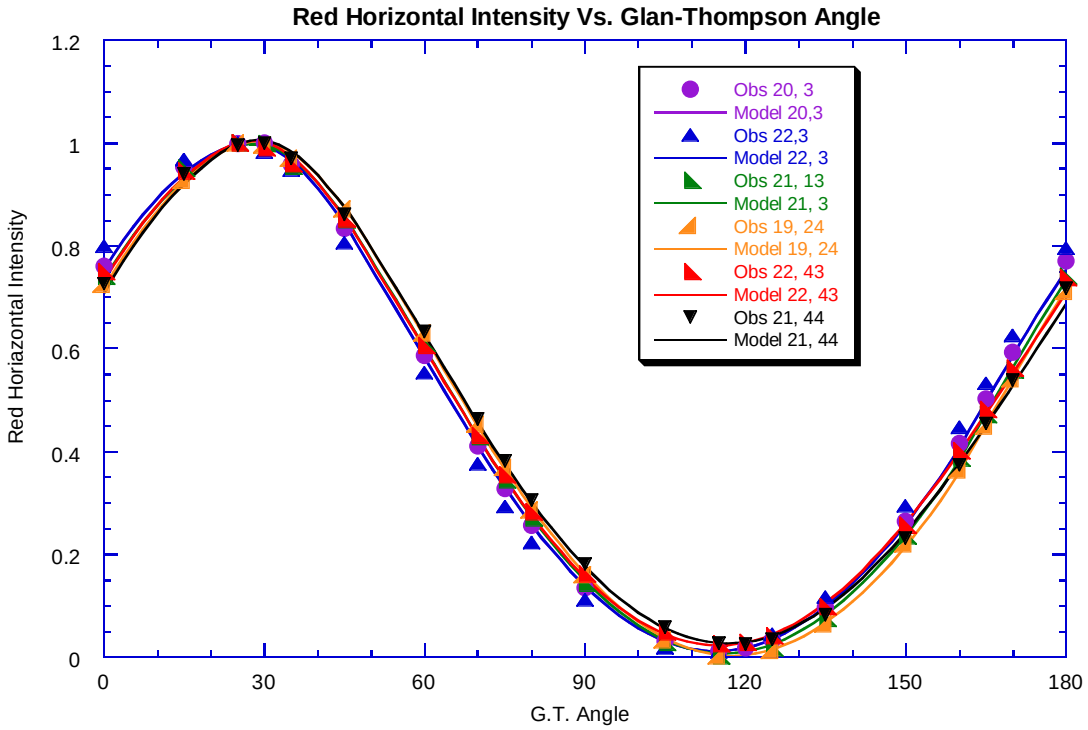

Figure 13-85 Like Figure 13-84 but for the red horizontal channel of the flight SA instrument. The fits are quite good except for the extreme corner of the field of view (column 22, row 3). Since the instrument will be used near the peak of the curve (near 30 degree Glan-Thompson angle), the agreement of the curves with the measured points is considered acceptably good.